

INFORMATION TO USERS

This manuscript has been reproduced from the microfilm master. UMI films the text directly from the original or copy submitted. Thus, some thesis and dissertation copies are in typewriter face, while others may be from any type of computer printer.

The quality of this reproduction is dependent upon the quality of the copy submitted. Broken or indistinct print, colored or poor quality illustrations and photographs, print bleedthrough, substandard margins, and improper alignment can adversely affect reproduction.

In the unlikely event that the author did not send UMI a complete manuscript and there are missing pages, these will be noted. Also, if unauthorized copyright material had to be removed, a note will indicate the deletion.

Oversize materials (e.g., maps, drawings, charts) are reproduced by sectioning the original, beginning at the upper left-hand corner and continuing from left to right in equal sections with small overlaps. Each original is also photographed in one exposure and is included in reduced form at the back of the book.

Photographs included in the original manuscript have been reproduced xerographically in this copy. Higher quality 6" x 9" black and white photographic prints are available for any photographs or illustrations appearing in this copy for an additional charge. Contact UMI directly to order.

U·M·I

University Microfilms International
A Bell & Howell Information Company
300 North Zeeb Road, Ann Arbor, MI 48106-1346 USA
313 761-4700 800 521-0600

Order Number 9131720

**Upper-mantle structure of the Cascadia subduction zone from
nonlinear teleseismic travel-time inversion**

VanDecar, John Callaway, Ph.D.

University of Washington, 1991

Copyright ©1991 by VanDecar, John Callaway. All rights reserved.

U·M·I
300 N. Zeeb Rd.
Ann Arbor, MI 48106

**Upper-mantle Structure of the Cascadia Subduction Zone
from Non-linear Teleseismic Travel-time Inversion**

by

John Callaway VanDecar

A dissertation submitted in partial fulfillment
of the requirements for the degree of

Doctor of Philosophy

University of Washington

1991

Approved by Robert L. Crosson
(Chairperson of Supervisory Committee)

Program Authorized
to Offer Degree Geophysics Program

Date 06/14/91

© Copyright by
JOHN CALLAWAY VANDECAR
1991

Doctoral Dissertation

In presenting this dissertation in partial fulfillment of the requirements for the Doctoral degree at the University of Washington, I agree that the Library shall make its copies freely available for inspection. I further agree that extensive copying of this dissertation is allowable only for scholarly purposes, consistent with "fair use" as prescribed in the U.S. Copyright Law. Requests for copying or reproduction of this dissertation may be referred to University Microfilms, 300 North Zeeb Road, Ann Arbor, Michigan 48106, to whom the author has granted "the right to reproduce and sell (a) copies of the manuscript in microform and/or (b) printed copies of the manuscript made from microform."

Signature

John Van Deren

Date

14 June 1991

University of Washington

Abstract

**Upper-mantle Structure of the Cascadia Subduction Zone
from Non-linear Teleseismic Travel-time Inversion**

by John Callaway VanDecar

Chairperson of Supervisory Committee: Professor Robert S. Crosson
Graduate Program in Geophysics

The tectonic evolution of the Juan de Fuca plate system has undergone dramatic changes over the past several million years as evidenced by seafloor geomagnetic data. If there are large geodynamic forces active in the subduction of oceanic lithosphere, corresponding changes in the structure of the Cascadia subduction zone should also be dramatic. In light of the seismic hazard normally presented by active subduction zones and the Pacific Northwest population centers potentially affected by such a hazard, it is important that we understand this subduction zone structure in order to properly evaluate the seismic potential of the region. We have approximated a non-linear inversion for variations in seismic wave speed over the upper-mantle portion of the Cascadia subduction zone by alternately performing linear travel-time inversions, via an efficient conjugate gradient method, and three-dimensional ray tracing. We employ regularization through minimizing the Laplacian of the final solution. We parameterize the three-dimensional model at over 10,000 knots with velocities between knots represented by spline interpolation. The culled data set consists of approximately 10,000 relative arrival times of teleseismic P and PKP waves recorded from 1980 to 1990 at

146 station locations of a short-period vertical-component seismic network in Washington and Northern Oregon. We obtain accurate relative arrival-time data (standard errors ≈ 0.01 sec) and associated data covariance estimates via the use of a new multi-channel cross-correlation technique. The most prominent and robust characteristic of our models is a 3-4% fast, planar feature that dips steeply to the east (at $\approx 60^\circ$) with a width of approximately 100 km. We infer this to be the seismic manifestation of a thermal and compositional anomaly associated with the subducting Juan de Fuca oceanic plate. At shallow depths (≈ 80 km) this feature is consistent with the projections of models of shallow slab structure. The high velocity zone is located at a depth of 100-120 km beneath the Cascade volcanos, consistent with other subduction zones. Under central Washington the slab extends to depths of 400 km or more, while there is an apparent lack of deep slab material beneath southern Washington and northern Oregon. The latter, when taken together with the tectonic history of the region and other geophysical observations, is consistent with a deep slab that has torn away from the shallow portion of the slab.

Table of Contents

	Page
List of Figures	iv
List of Tables	vi
Chapter 1 Introduction	1
1.1 Objectives	1
1.2 Tectonic Framework.....	4
1.3 Previous Structural Studies	6
1.3.1 Shallow Structure.....	6
1.3.2 Deep Structure.....	7
1.4 Procedure Outline.....	10
Chapter 2 Teleseismic Data Set	16
2.1 Introduction.....	16
2.2 Selection of Data.....	18
Chapter 3 Multi-channel Cross Correlation	24
3.1 Introduction.....	24
3.2 Cross Correlation Analysis	27
3.3 Least Squares and Uncertainty Estimation.....	32
3.4 Selection of Parameters and Waveform Coherency.....	39
3.5 Examples.....	44
Chapter 4 Travel-time Inversion Procedure	51
4.1 Introduction.....	51
4.2 Least-squares Inversion.....	51
4.3 Linearization of the Travel-time Equation	53
4.4 Parameterization	54
4.5 Inverse Problem Formulation.....	59
4.6 Iterative Procedure.....	66
Chapter 5 Inversion Results for the Cascadia Subduction Zone.....	69
5.1 Introduction.....	69
5.2 Resolution Analysis.....	70
5.2.1 Ray Distribution.....	72
5.2.2 Spike Resolution Tests	75
5.2.3 Resolution of a Synthetic Slab Model	84

5.3 Slowness Perturbation Models	90
5.3.1 First Iteration ‘Linear’ Model UW91F1	93
5.3.2 Second Iteration Model UW91F2	102
5.3.3 Third Iteration Model UW91F3	107
Chapter 6 P-wave Amplitude Analysis	114
6.1 Introduction.....	114
6.2 Inversion for Site Amplitude Responses	114
6.3 Observed Amplitude Signature over the WRSN	117
6.4 Amplitude Response of Cascadia Subduction Zone	123
Chapter 7 Summary and Conclusions	126
Bibliography	133
Appendix A : Station Locations	154
Appendix B : Event Locations	159
Appendix C : Three-dimensional Ray Tracing	163

List of Figures

	Page
Figure 1.1 Map view of Cascadia subduction zone tectonic structure	2
Figure 1.2 Absolute plate motions over past 7 million years	5
Figure 1.3 Cross section of Puget Sound seismicity	8
Figure 1.4 Contour map of shallow subduction geometry	9
Figure 1.5 Upper mantle velocity structure from previous studies.....	11
Figure 1.6 Flow chart of data analysis procedure.....	14
Figure 2.1 Map view of the Washington regional seismograph network.....	17
Figure 2.2 Locations of events resulting in P phases	19
Figure 2.3 Locations of events resulting in core phases	21
Figure 2.4 Statistical distribution of events.....	22
Figure 3.1 Example traces from event in Kamchatka region.....	28
Figure 3.2 Example cross-correlation.....	31
Figure 3.3 Statistics from multi-channel cross-correlation procedure.....	33
Figure 3.4 Aligned windows of unfiltered traces.....	37
Figure 3.5 Aligned windows of filtered traces.....	38
Figure 3.6 Three-dimensional perspective of cross-correlation coefficients	40
Figure 3.7 Cross-correlation coefficients as function of station separation.....	42
Figure 3.8 Residuals to least-squares solution as function of station separation ..	43
Figure 3.9 Contour map of P phase relative arrival times	45
Figure 3.10 Contour maps of P phase relative arrival time residuals.....	46
Figure 4.1 One-dimensional example of spline under tension interpolation	56
Figure 4.2 Perspective view of model's spline knot distribution.....	58
Figure 5.1 Latitudinal cross-sections of ray number density	73
Figure 5.2 Three-dimensional plots of rays effecting selected knots.....	76
Figure 5.3 Latitudinal cross-sections of multiple spike resolution test.....	80
Figure 5.4 Latitudinal cross-sections of subducting slab resolution tests.....	85
Figure 5.5 Longitudinal variation of slab models at 250 km depth.....	91
Figure 5.6 Trade-off curve for linear model UW91F1	94

Figure 5.7	Latitudinal cross-sections of slowness perturbation model UW91F1..	96
Figure 5.8	Map view at 200 km depth through model UW91F1	100
Figure 5.9	Latitudinal cross-sections through entirety of model UW91F1	101
Figure 5.10	Latitudinal cross-sections of slowness perturbation model UW91F2..	103
Figure 5.11	Map view at 200 km depth through model UW91F2	105
Figure 5.12	Latitudinal cross-sections through entirety of model UW91F2	106
Figure 5.13	Latitudinal cross sections of slowness perturbation model UW91F3..	108
Figure 5.14	Map view at 200 km depth through model UW91F3	110
Figure 5.15	Latitudinal cross-sections through entirety of model UW91F3	111
Figure 5.16	Longitudinal variation of slowness models at 200 km depth.....	112
Figure 6.1	Weighting function used for robust iterative inversion	118
Figure 6.2	Site and instrument amplitude calibration for WRSN.....	119
Figure 6.3	Uncalibrated amplitude response from SE azimuth events	121
Figure 6.4	Calibrated amplitude response from SE azimuth events	122
Figure 6.5	Amplitude response from SE azimuth events for model UW91F1	124
Figure 6.6	Amplitude response from SE azimuth events for model UW91F2	125
Figure 7.1	Three-dimensional perspective views of model UW91F3.....	128

List of Tables

	Page
Table 3.1. Example events used in cross-correlation analysis	29
Table A.1. Washington Regional Seismograph Network (WRSN) station locations and elevations	154
Table B.1. Epicentral parameters of teleseisms used in this study and locations with respect to WRSN.....	159

Acknowledgements

I gratefully acknowledge Dr. Robert Crosson for providing the impetus and support necessary to accomplish the work presented in this manuscript. Drs. John Booker and Ken Creager, both through classes they have taught and many discussions, have provided much of the insight that formed the inversion philosophy I have used. Dr. Creager also generously provided the code used as a basis for the three-dimensional ray tracing essential to this work. All my colleagues and office mates over the years and in particular Torquil Smith, Yvan Orsolini, Ling-Yun Chiao, David Lapp, Brad Baker, Mike Schwitter and Kim Edlund have provided stimulating discussion and a fertile working environment. Ruth Ludwin's wry wit and keen eye as an editor was always appreciated. Special thanks go to my good friends and fellow workers in geophysical tomography Jonathan Lees and Jennifer Scott for many productive exchanges and their challenging of my (sometimes dogmatic) views on inverse theory, tomography and literature. The support of my family and long-time friends Ken Cooper, Alan Crouch and Bob Hendricks was unflagging and is greatly appreciated. I thank NATO and the National Science Foundation for the opportunity to participate in the 1988 Les Houches Ecole d'été de Physique Théorique on geophysical tomography where much was learned and many friendships made. I owe my timely progression through graduate school in no small part to the entire staff of the Geophysics Program and in particular Lisa Peterson, Cathy Sharpe and Connie Wright, who cheerfully went well beyond the line of duty to make matters right. The untiring efforts of Dr. Steve Malone, Rick Benson, Laurens Engel, Jim Ramey, and others to maintain the Washington Regional Seismic Network at peak performance is appreciated by myself and all who take advantage of the data they supply. This work was supported by U.S. Geological Survey contracts 14-08-0001-G-1390 and 14-08-0001-G1803. Portions of the computing were carried out on a Cray Y-MP4/464 system supported by the National Center for Supercomputing Applications, University of Illinois at Urbana-Champaign, and on an IBM 3090-3E system supported by the University of Washington Academic Computing Center.

Chapter 1

Introduction

1.1 Objectives

An objective of this dissertation is to investigate methods of optimizing resolution and accuracy in travel-time inversion for velocity structure and in particular analyze the reliability of the inversion of teleseismic arrival-time data recorded on large-aperture regional seismic arrays. The specific impetus for this research was to better define the upper-mantle structure of the Cascadia subduction zone (Figure 1.1). In most subduction zones the upper-mantle structure, or at least the position of the subducting lithosphere, is constrained by a Wadati-Benioff zone - a region where deep earthquakes regularly occur - extending to several hundred km depth. In the case of Cascadia, however, the lack of a well-defined Wadati-Benioff zone outside of the shallow Puget Sound region (where it extends to only 100 km) leaves a distinct void in our knowledge of the regional structure and tectonics. This void may be especially critical in light of recent debate over potential earthquake hazards in the region.

A recent study of strain accumulation in the region [*Savage and Lisowski* 1991] provides a direct piece of evidence suggesting stress buildup in the region, while geologic studies along the present-day coast have uncovered circumstantial evidence of past large to great earthquakes. Given the known average rate of convergence of the subducting Juan de Fuca and overriding North American plates along with the age of the subducting lithosphere, comparison with other subduction zones [*e.g. Heaton and Kanamori*, 1984] indicates that the Cascadia subduction zone should be prone to subduction-type earthquakes in the magnitude range 8 to 8.5. Is this comparison valid? Knowledge of other factors such as the subduction of sediments, heat flow, phase-changes and the overall controlling geometry of the subducting lithosphere will be critical to the successful prediction of the degree of elastic coupling between these plates and how this coupling might vary along the strike of the zone.

Our knowledge of shallow subduction structure (depths < 80-100 km) is improving through the use of several geophysical and geologic data sets (§1.3.1) but the only data set that has been found to resolve upper-mantle Cascadia subduction

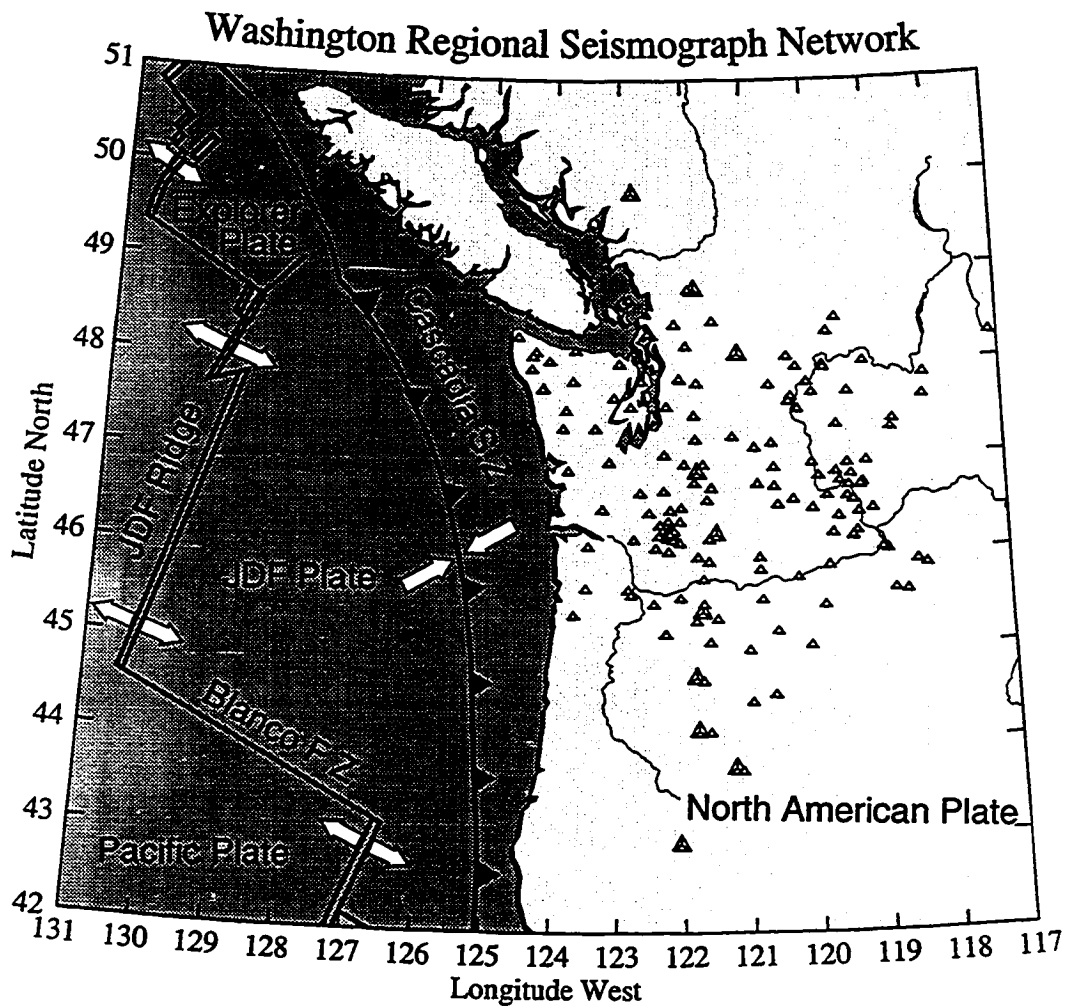


Figure 1.1 Lambert conformal projection of the tectonic structure of the Juan de Fuca plate system and Cascadia subduction zone. Arrows indicate direction of current relative motion along plate boundaries. Small triangles indicate stations of the Washington Regional Seismic Network used in this study. Large triangles are locations of Quaternary strato-volcanos. (JDF = Juan de Fuca, F.Z. = fracture zone, and S.Z. = subduction zone.)

structure with appreciable resolution is that of teleseismic arrivals recorded on the Washington Regional Seismograph Network (WRSN). The WRSN, operated by the University of Washington and composed primarily of short-period vertical-component seismometers, was put in place in the 1960s and has been recording approximately 120 channels of data digitally (on a triggered basis) since 1980. Not all stations were in place over the entire time period, so the configuration of the network was time dependent. This resulted in 146 station positions being occupied for a long enough time period to be used in this study (Figure 1.1). Although its primary purpose has been to monitor regional seismicity, the system also triggers on and archives teleseismic arrivals. It is this data set that we exploit in the current study.

In order to obtain a high resolution, well constrained upper mantle structure in the Cascadia region we delineated three distinct areas of research where improvements were deemed necessary and attainable. The large digital data set that has been accumulating at the WRSN over the past 10+ years is of high quality and spans ranges of azimuth and distance heretofore unexploited by teleseismic studies. The culling of this vast data set (over 3200 events) to obtain an optimal distribution of the highest quality events was the first area of improvement sought (Chapter 2). Next, we developed a novel technique for extracting both accurate relative arrival times and quantitative uncertainty estimates (for use in weighting data in inversion). The method combines a multi-channel cross-correlation procedure with adjustment by least squares which exploits the random character of errors present in cross-correlation derived relative arrival time estimates (Chapter 3). While with these improvements alone (expanded data set, higher quality data and quantitative estimates of data covariance) we expect a marked improvement in model resolution, we also felt that the currently used methodology of obtaining velocity estimates from large arrival-time data sets needed improvement. In this regard we have developed a pseudo-nonlinear (iterative linear) inversion technique employing full three-dimensional ray tracing and the inversion for optimally smooth final models (Chapter 4).

After discussing each of these developments, we examine the result of their application to the Cascadia subduction zone in Chapter 5. We also investigate the

resolution capabilities of the data set and provide a method of clarifying the effects of the non-linearity of our problem on linear inversions. In Chapter 6 we investigate the use of first-arrival *P*-wave amplitudes and a robust means by which to empirically calibrate a regional array for site and instrument response. The sensitivity of these amplitudes to velocity *gradients* may provide us with a means of distinguishing between ambiguous features of the travel-time derived velocity structure.

1.2 Tectonic Framework

The tectonic structure of the Juan de Fuca plate system has received a great deal of attention dating back to the initial development of sea-floor spreading theory [Vine and Wilson 1965, Vine 1966] and continues to be one of the most well documented tectonic regions. The present-day structure of the system is shown schematically in Figure 1.1 with arrows to represent relative plate motions. The evolution of the ridge system is reviewed in detail by Wilson *et al.* [1984]. They propose two distinct shifts in the Juan de Fuca Ridge rotation pole occurring at 8.5 and 5.0 Ma (million years before present) causing clockwise shifts of 10° and 15° respectively in the direction of relative motion. The disagreement between magnetic anomalies on the Juan de Fuca and Explorer plates after 5.0 Ma led to the conclusion that it was at this time that the Explorer plate broke from the Juan de Fuca. It had been suggested by Rogers [1983] and others that the Explorer plate is now distinct from the Juan de Fuca and Riddihough [1984] came to the conclusion that the Explorer plate is no longer subducting but instead rotating in a clockwise fashion.

Through the use of sea-floor magnetic anomalies both relative and absolute motions of the Juan de Fuca, Pacific, and North American plates dating back 7 Ma are calculated by Riddihough [1984]. Reproduced in Figure 1.2 are those motions relative to the 'hot-spot' reference frame. It can be seen that the magnetic data indicate drastic changes in the Juan de Fuca/North American pole of rotation over the past 7 Ma. The implications of this complicated tectonic history must be taken into account in order to predict what sort of structure one should expect for the *subducted* portion of the Juan de Fuca plate. A reduction in subduction rate of 45% or more over these time periods should have effects at depth. Does the deep slab also

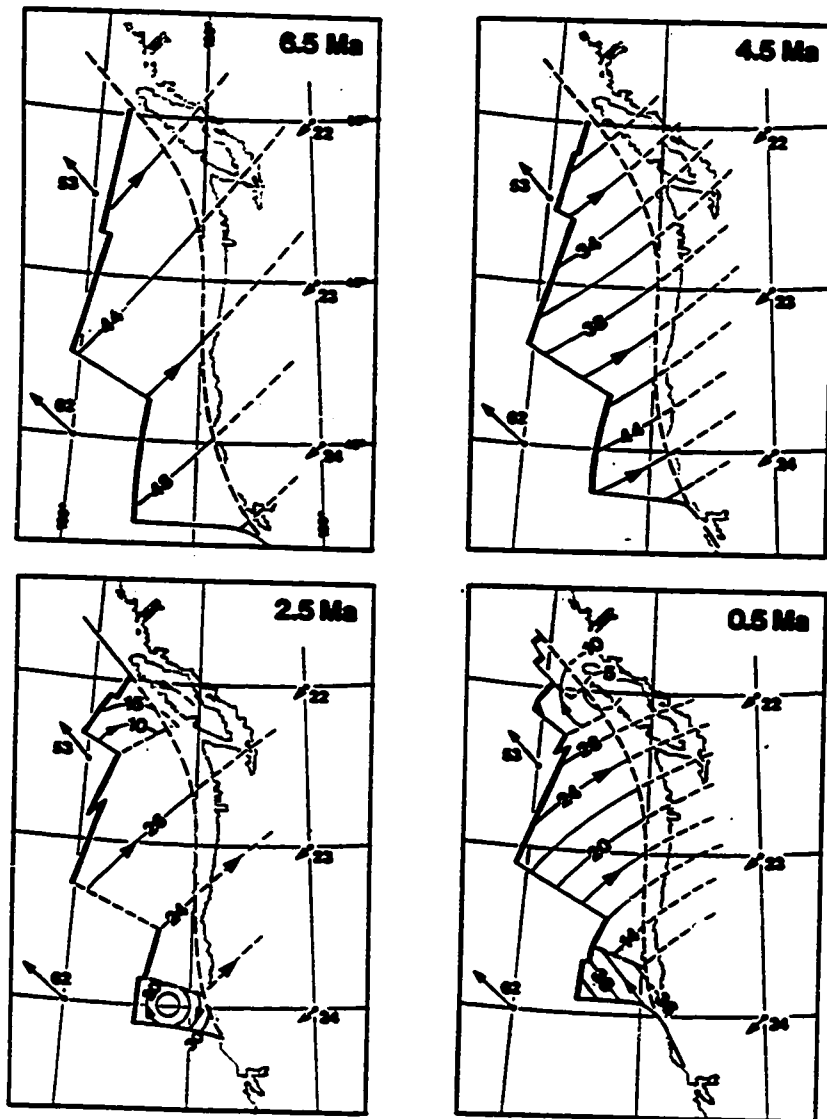


Figure 1.2 Absolute motions of the Juan de Fuca, North American, and Pacific plates over the past 6.5 Ma derived by Riddihough [1984] from the analysis of geomagnetic anomalies. The pole of rotation between the North American and Juan de Fuca plates has moved from being northwest of the system to now lying to the southeast. The evolution is such that subduction of the Juan de Fuca plate has slowed along the entire subduction zone, most dramatically in the southern portion.

slow by 45%? If 'slab pull' is the dominant driving force of subduction, then we might expect this deeper portion of the slab to exert a sizable tensional stress on the upper part, possibly enough to even pull it apart. We might even expect a positive feedback process in that once the deep part of the slab is no longer providing a downward force, the upper portions will have that much more of a tendency to slow down. In this thesis we attempt to shed light on these questions by obtaining a high-resolution image of the current state of Cascadia subduction structure - an instantaneous 'snap-shot' of what appears to be an evolving system.

1.3 Previous Structural Studies

As noted in the preceding section the interest in the Juan de Fuca plate system dates back to the initial research on plate tectonic and sea-floor spreading theory. Since *McKenzie and Parker* [1967] and *Atwater* [1970] first identified Cascadia as a convergent margin, it also has received much attention. In the following two sections we review findings from such studies as they pertain to the shallow and deep structure, respectively, of the Cascadia subduction zone.

1.3.1 Shallow Structure

The shallow structure of the Cascadia subduction zone has been extensively investigated both with many geophysical techniques and on many scales. A special issue of the *Journal of Geophysical Research* (November 1990) chronicles research performed in connection with the crustal structure of the Cascade mountain range while *Hyndman et al.* [1990] give a review of crustal structure in southwestern Canada. Crustal seismic tomography has been performed in several regions both with the use of local travel-time data alone [*Lees and Crosson*, 1989; 1990] and travel-time data along with constraints imposed by the regional gravity field [*Lees and VanDecar*, 1991]. It was recognized by *Dickinson* [1970] that crustal structure could provide a clue to recent shallow subduction structure. By examining the petrology of the Cascade volcanics he was able to infer approximate depth contours to the subducting Juan de Fuca plate. Those contours indicated an arch structure around the Olympic Peninsula consistent with the bend observed in the off-shore deformation front.

Seismicity defines well a subducting Juan de Fuca plate only beneath Puget sound and only to depths of approximately 100 km [Crosson 1983, Taber and Smith 1985, Weaver and Baker 1988]. Outside of this region the number of events inferred to lie within the subducted plate is relatively small. In Figure 1.3 a cross section of contemporary earthquake activity clearly shows the division of hypocenters into crustal and sub-crustal regimes. These sub-crustal events are inferred to lie within the subducting Juan de Fuca plate and are consistent with the position of the plate estimated from other geophysical measurements. Other measurements of regional velocity structure include seismic reflection and refraction studies [Green *et al.* 1986, Keach *et al.* 1986, Zervas and Crosson 1986, Taber and Lewis 1986, Clowes 1987], and receiver function experiments employing three component broadband seismometer stations [Langston 1981, Hendrickson 1986, Owens and Crosson 1988, Owens *et al.* 1988, Lapp *et al.* 1990]. A synthesis of some of these results is illustrated in Figure 1.4 [after Crosson and Owens 1987] where depth contours mark the inferred position of the subducting Juan de Fuca plate. Mundal *et al.* [1991] have modeled the arrival of anomalous slab phases from selected sub-crustal events and found them to also be consistent with this model.

Work has recently been done on computer simulations of the structure of the shallow subducting plate which minimizes the overall amount of in-plane strain resulting from plate deformation [Chiao and Creager 1990]. A dramatic feature of the sub-crustal seismicity within the subducted plate is its localization near the inferred arch structure. The use of such modeling seems to indicate that this is a natural consequence of the unusual concave oceanward trend of the trench and volcanic arc. What then is the effect of 'slab pull' on the shallow Juan de Fuca plate and why is it failing to induce earthquakes all along the Cascadia subduction zone? This is a question that we attempt to answer through the imaging of deep slab structure.

1.3.2 Deep Structure

Previous attempts to image deep Cascadia subduction structure have centered around the use of the relative travel-times of teleseismic phase recorded on the WRSN. In 1973 it was found, through forward modeling, that a subducting slab

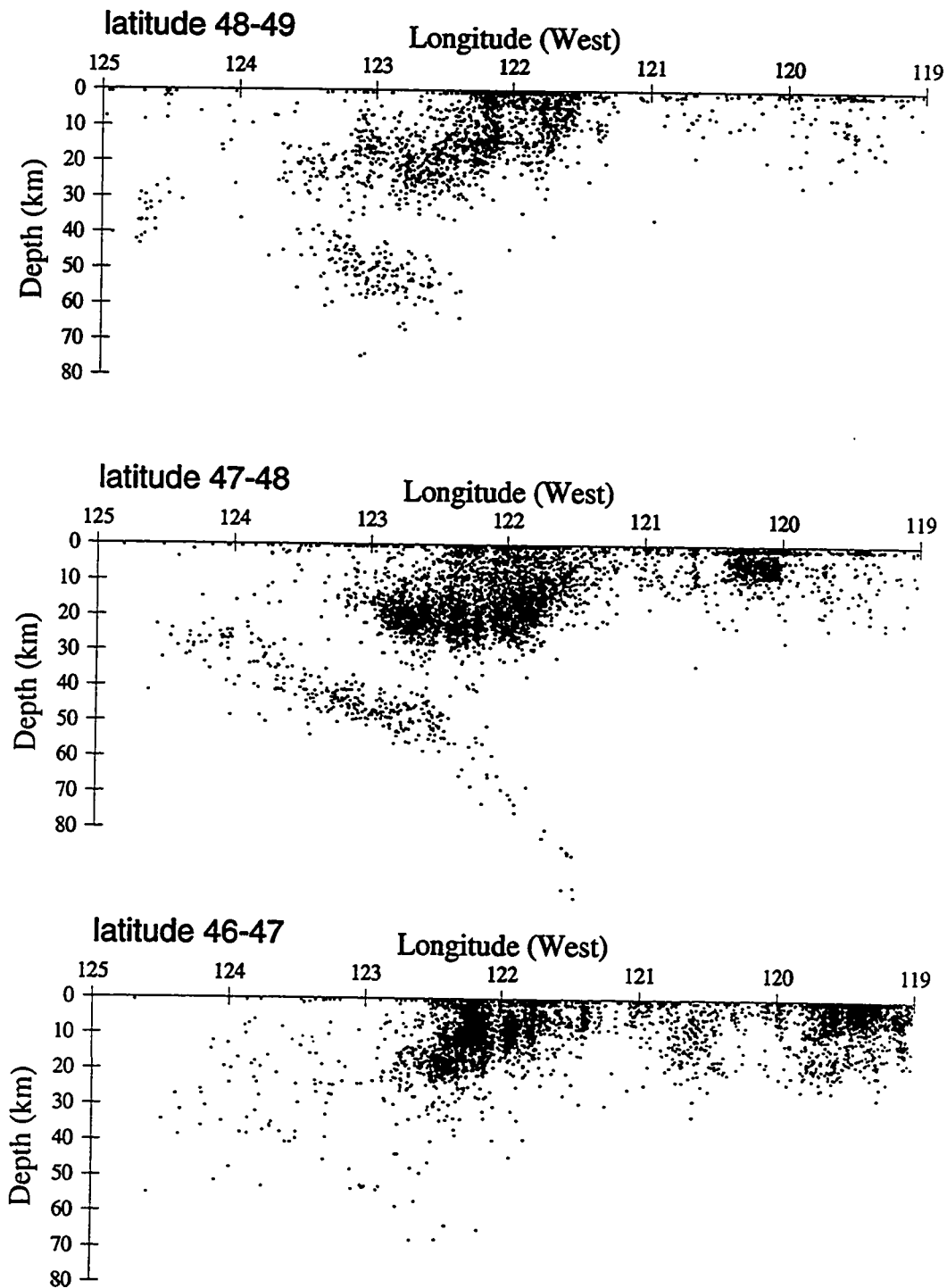


Figure 1.3 Cross-sections of seismicity in Western Washington. Each cross-section represents all earthquakes recorded from 1970 through April 1991 within the indicated degree of latitude. Vertical exaggeration is 2:1.

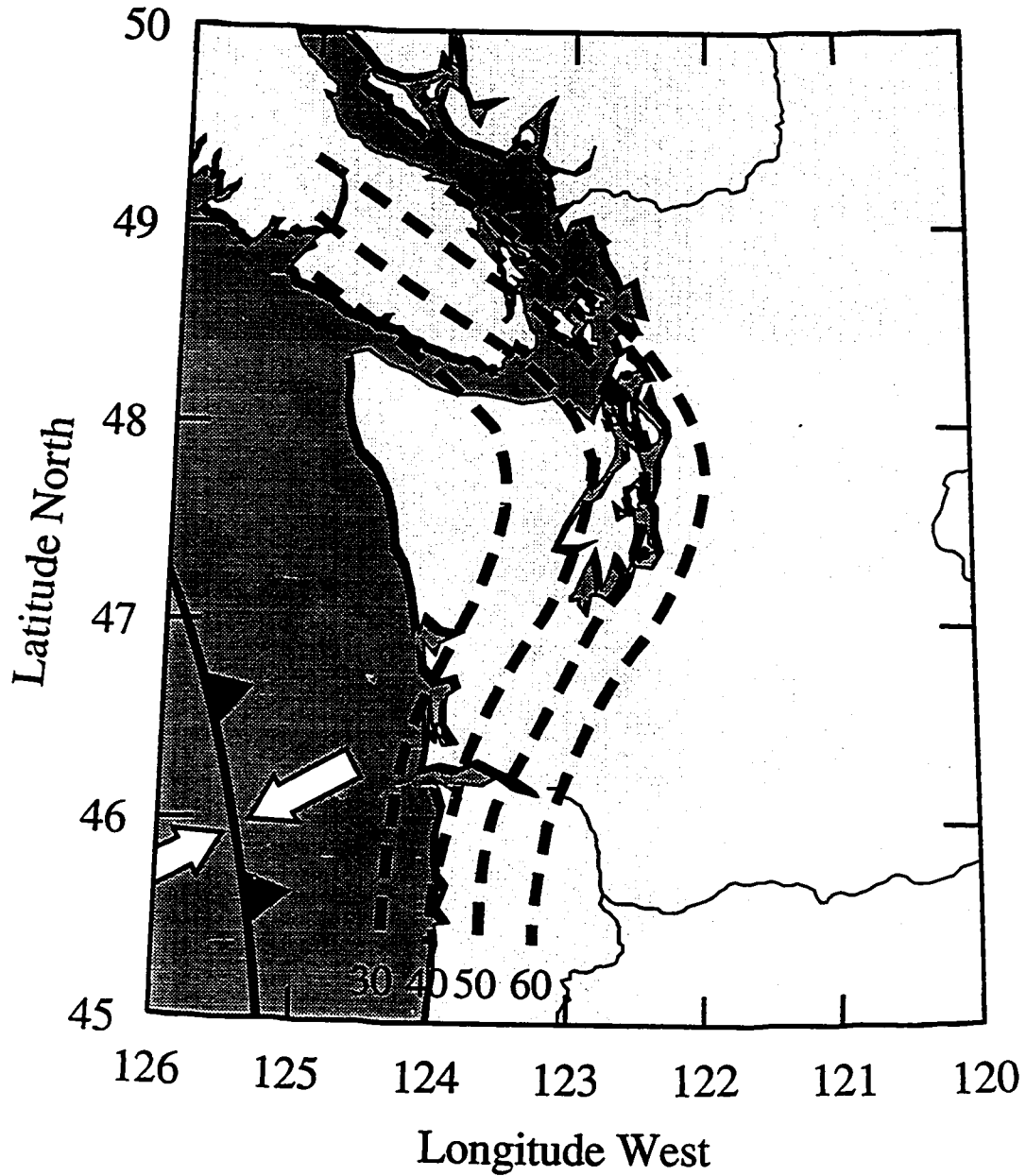


Figure 1.4 Contour map of shallow subducted slab structure overlain by Lambert conformal projection of Pacific Northwest map. The contours were inferred with the use of seismicity as well as other data sets including P-coda studies [after Crosson and Owens, 1987]. Depth to contours, in km, is shown at the bottom of the figure.

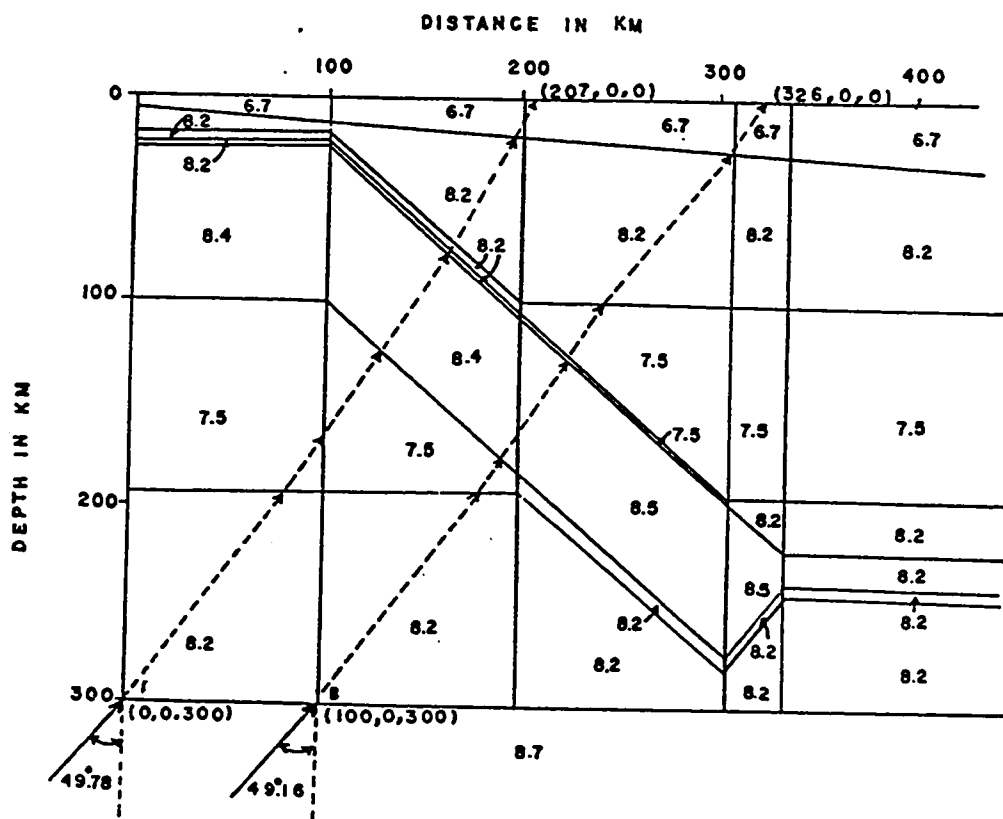
with a dip of approximately 50° was consistent with observed azimuthally dependent teleseismic arrival time anomalies [Lin 1973, Lin and Crosson 1974]. The data used for this analysis consisted of visually-chosen arrival times from analog records of the 13 seismometers of the WRSN present in the early 1970s. Figure 1.5a is an example of a velocity structure used by Lin [1973] along with two-dimensional ray tracing to model the observed teleseismic travel-time patterns.

Michaelson and Weaver [1986] further quantified these results by performing a three-dimensional linear least-squares inversion for blocks of constant velocity. They used 104 stations and 67 events resulting in 4160 visual picks from data recorded digitally from 1980-1982. Figure 1.5b illustrates their results in the form of cross sections through the model of velocity perturbations. *Rasmussen and Humphreys* [1988] applied the method of back-projection tomography to the same data set supplemented by several core phases and data recorded on temporary stations in southern Oregon (altogether ≈ 4900 visual arrival time picks). Their results were essentially the same as that of *Michaelson and Weaver* [1986] and are reproduced in Figure 1.5c for comparison.

1.4 Procedure Outline

The procedure followed to construct models of Cascadia subduction zone structure as well as the structure of the following chapters of this thesis, is illustrated in the flow chart in Figure 1.6. We begin with the selection and archiving of events recorded on the WRSN. The next step in the data-analysis stream is the extraction of parameters from the teleseismic data that we need in order to accomplish a weighted least-squares travel-time inversion. Once these parameters have converged to an acceptable database of travel times and travel-time covariances, we move on to the numerically intensive portions of our procedure.

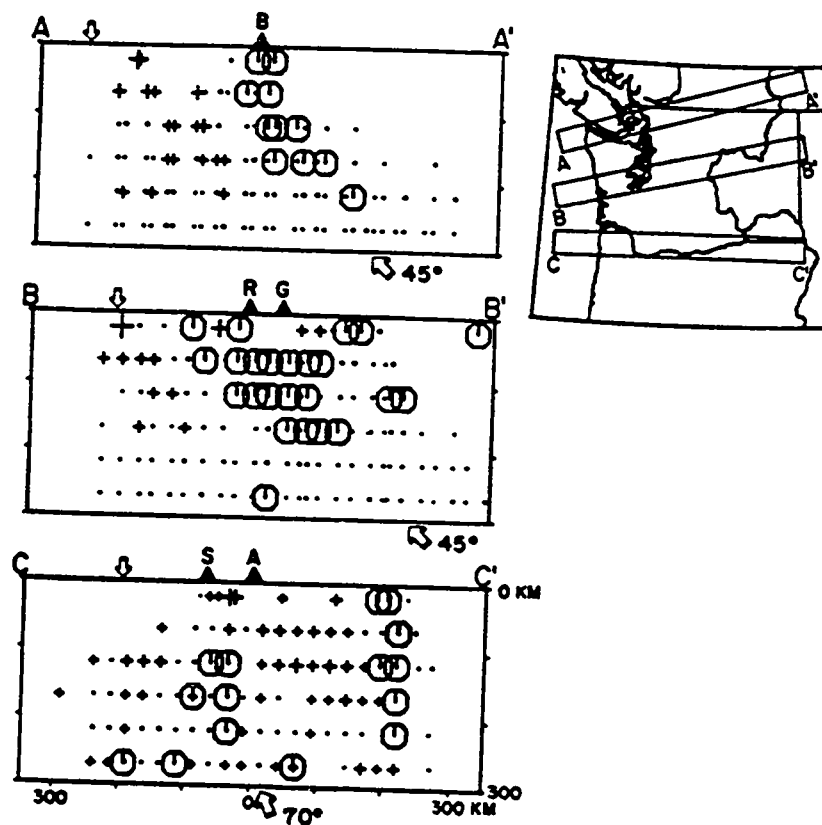
If our reference model is laterally varying we will need to perform three-dimensional ray tracing to obtain ray paths through this structure. At the first iteration of our method, however, our reference model is radially symmetric therefore the appropriate take-off angles and azimuths of each ray are known and this step is trivial. In order to formulate our inverse problem we must calculate the effect on travel times of perturbations to our current model of velocity. After compiling



(a)

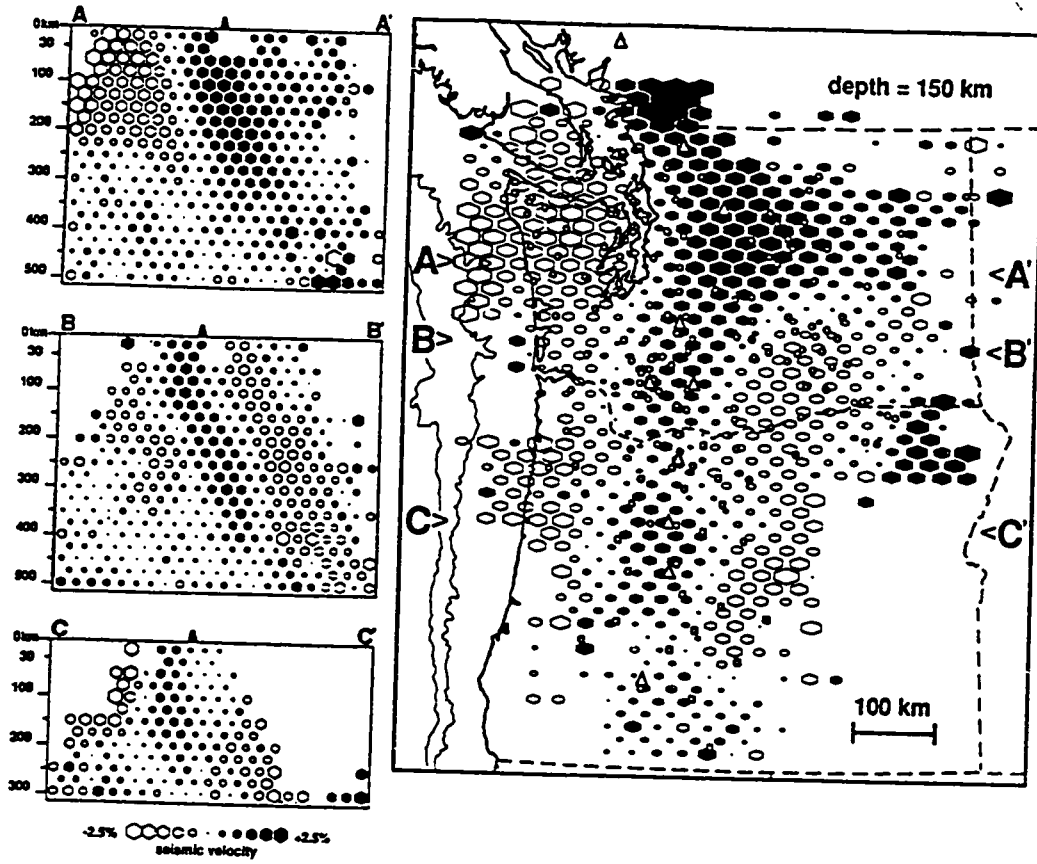
Figure 1.5a-c Results from previous studies employing teleseismic data recorded on the WRSN. (a) cross-section through velocity structure used in forward modeling data by Lin [1973], (b) velocity anomalies from linear block inversion performed by Michealson and Weaver [1986] (with open symbols representing low velocity), and (c) velocity anomalies derived by Rasmussen and Humpheries [1988] with approximately the same data set as in (b) but employing back-projection tomography.

Figure 1.5 (continued)



(b)

Figure 1.5 (continued)



(c)

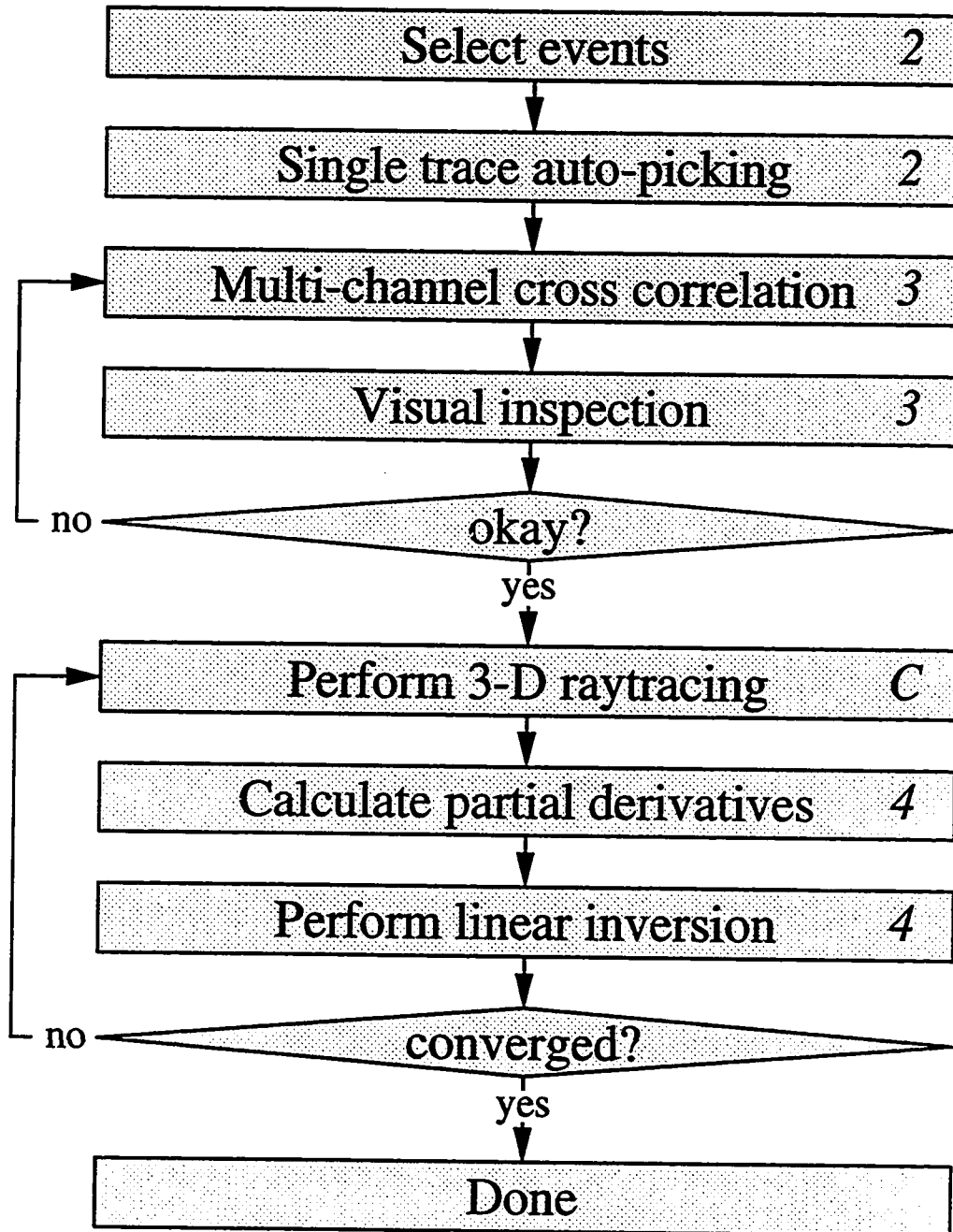


Figure 1.6 Flow chart of data reduction and non-linear travel-time inversion procedures. Numbers on right indicate chapter in which full descriptions of each topic may be found.

these partial derivatives along with the theoretical travel times through the reference velocity structure, we are ready to perform a linear inversion of the resulting system. The method we have chosen for inverting this system is that of conjugate gradients. Due to the nonlinearity of our problem we then iterate our inversion method as shown in the lower half of Figure 1.6.

Chapter 2

Teleseismic Data Set

2.1 Introduction

The Washington Regional Seismograph Network (WRSN, shown in Figure 2.1 and tabulated in Appendix A) has been in operation since the late 1960's. It has been recording approximately 120 channels digitally since January 1980 on a triggered basis at a 100 samples/sec digitization rate. The triggering algorithm is based on a standard STA/LTA[†] criterion combined with a set of rules based on subsets of the network used to suppress false triggers. The primary mission of the WRSN is to monitor local and regional seismicity in order to evaluate local seismotectonic structure and to aid in seismic hazard analysis. It also, however, triggers on many teleseismic arrivals which are flagged as such by an analyst and subsequently archived. In order to minimize the necessary storage space, the data are often decimated by two after the application of a low pass filter to avoid aliasing. Since short-period teleseismic data is usually dominated by frequencies of 1-4 Hz, a sampling frequency of 50 Hz (corresponding to a Nyquist frequency of 25 Hz) is more than sufficient to define the signal.

Although several different seismometer types are used within the network, all their response functions near 1 Hz are reasonably similar even though their gains differ. Due to the band-limited nature of short-period teleseismic data just mentioned, we therefore do not expect significant waveform distortion of the teleseismic signal due to differing instrument response. To analyze the amplitudes of the signals we will, however, need to quantify these differences (as well as site effects) which is discussed in §6.2. A comprehensive review of network operations and triggering is given in *Qamar et al.* [1986]. In the next section we discuss the catalog of teleseismic events recorded by the WRSN from January 1980 through December 1989, the subset of events selected for this study, and the selection procedure.

[†] (short-term average energy) / (long-term average energy)

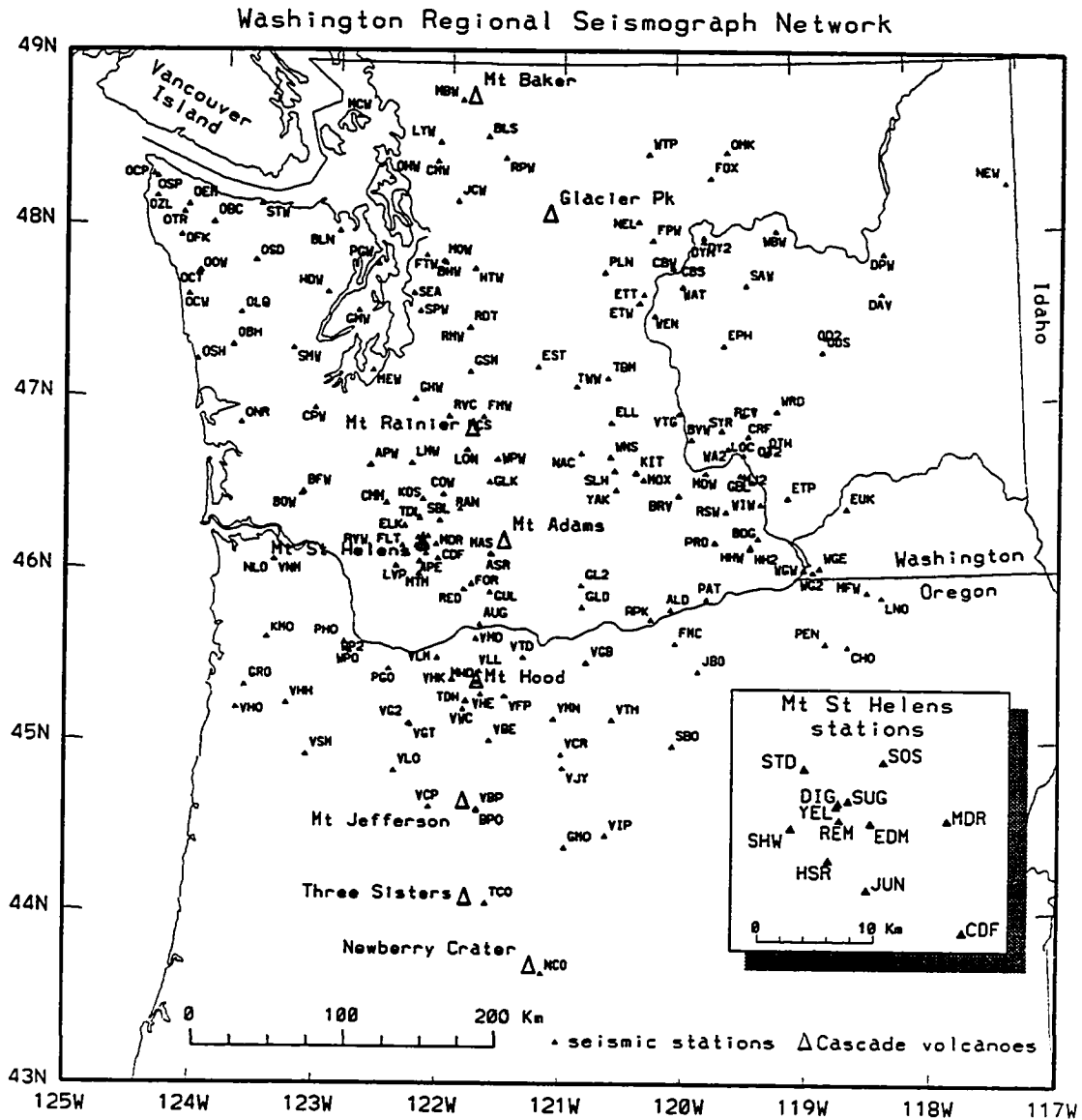


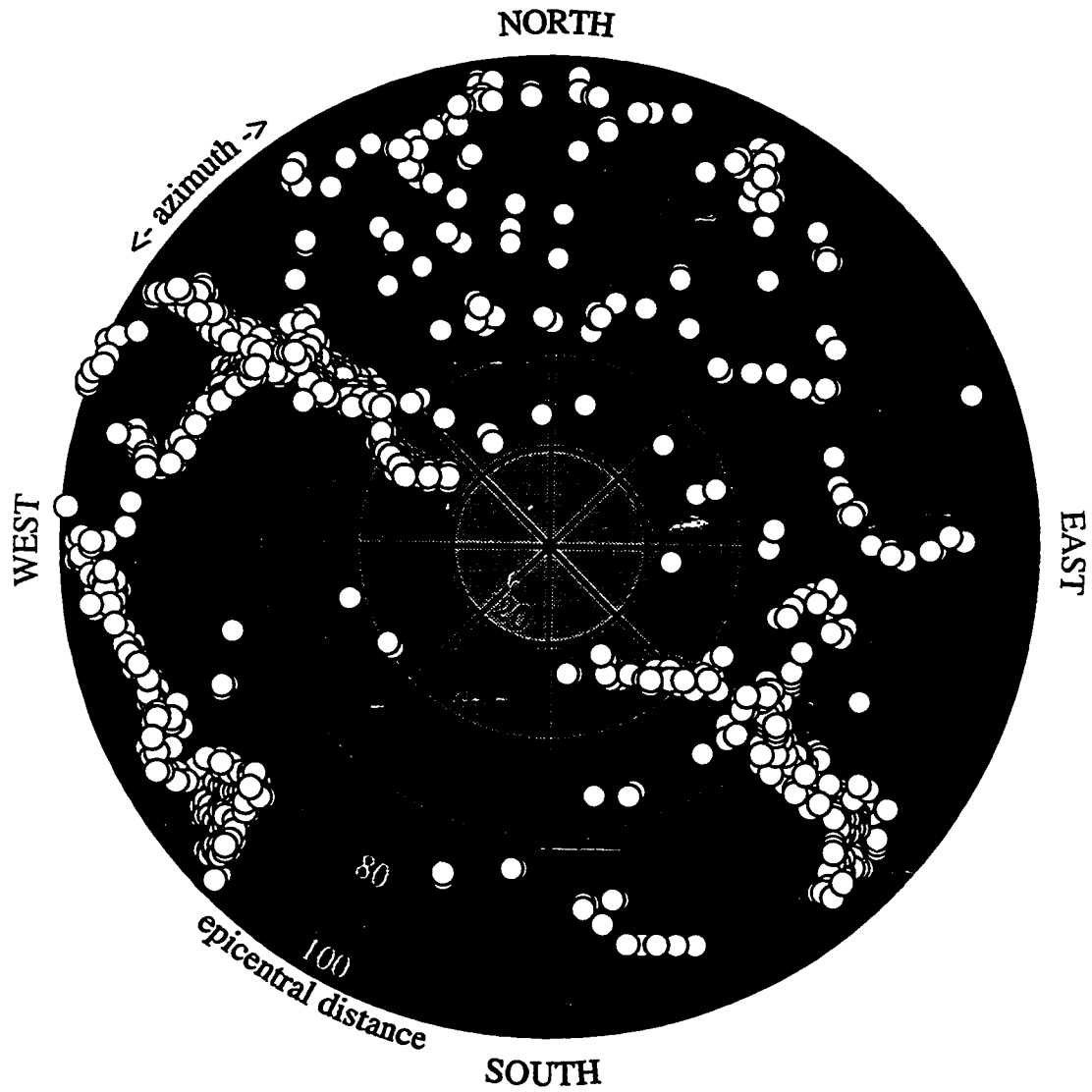
Figure 2.1 Stations of the Washington Regional Seismograph Network (WRSN). Inset is of stations in the Mt. Saint Helens region. The network has been recording approximately 120 channels digitally since 1980. The projection is Lambert conformal.

2.2 Selection of Data

The data considered for this study consisted of approximately 3200 teleseismic events recorded digitally on the WRSN from January 1980 through December 1989. In order to sort the data by origin region and phase we first developed an automated scheme to determine event hypocenters from the trigger times of a large number of events. We match each trigger time to a hypocenter cataloged by the National Earthquake Information Center (NEIC) by comparing the trigger time to the combined origin time plus Herrin radial earth travel time [Herrin, 1968] from the reported hypocenter. From this procedure the event triggers were found to arise from the arrival of *P* phases for 3100, core phases for 82, and later phases (e.g. PP, pP and S) for 32 of the triggers.

The event locations resulting in *P*-phase data are shown in Figure 2.2a as a function of azimuth and angular distance with respect to the WRSN. Figure 2.2b is the same type of plot showing the distribution of events that were finally chosen for use with the procedure described below. The corresponding events which resulted in core-phase data are plotted in Figures 2.3a,b. These distributions are represented in histogram form in Figure 2.4. Most of the range of possible teleseismic locations has been filled over this time period, but it can be seen in Figure 2.2a that several regions are still sparsely populated (most notably SSW azimuths) so that the minimum 'acceptable quality' of data needs to be varied as a function of location. It is obvious that if one were to simply take a random subset of these data (e.g. all the events from a given time window) the distribution of events would be heavily skewed toward certain source areas. This would result in highly heterogeneous ray coverage within our model region, therefore we attempted to mitigate this factor in our selection procedure. The result of using heterogeneous ray coverage in travel-time inversion can lead to the overweighting of rays traveling in particular directions over different parts of the model, resulting in spurious structure [e.g. Humphreys and Clayton 1985, Lees 1989].

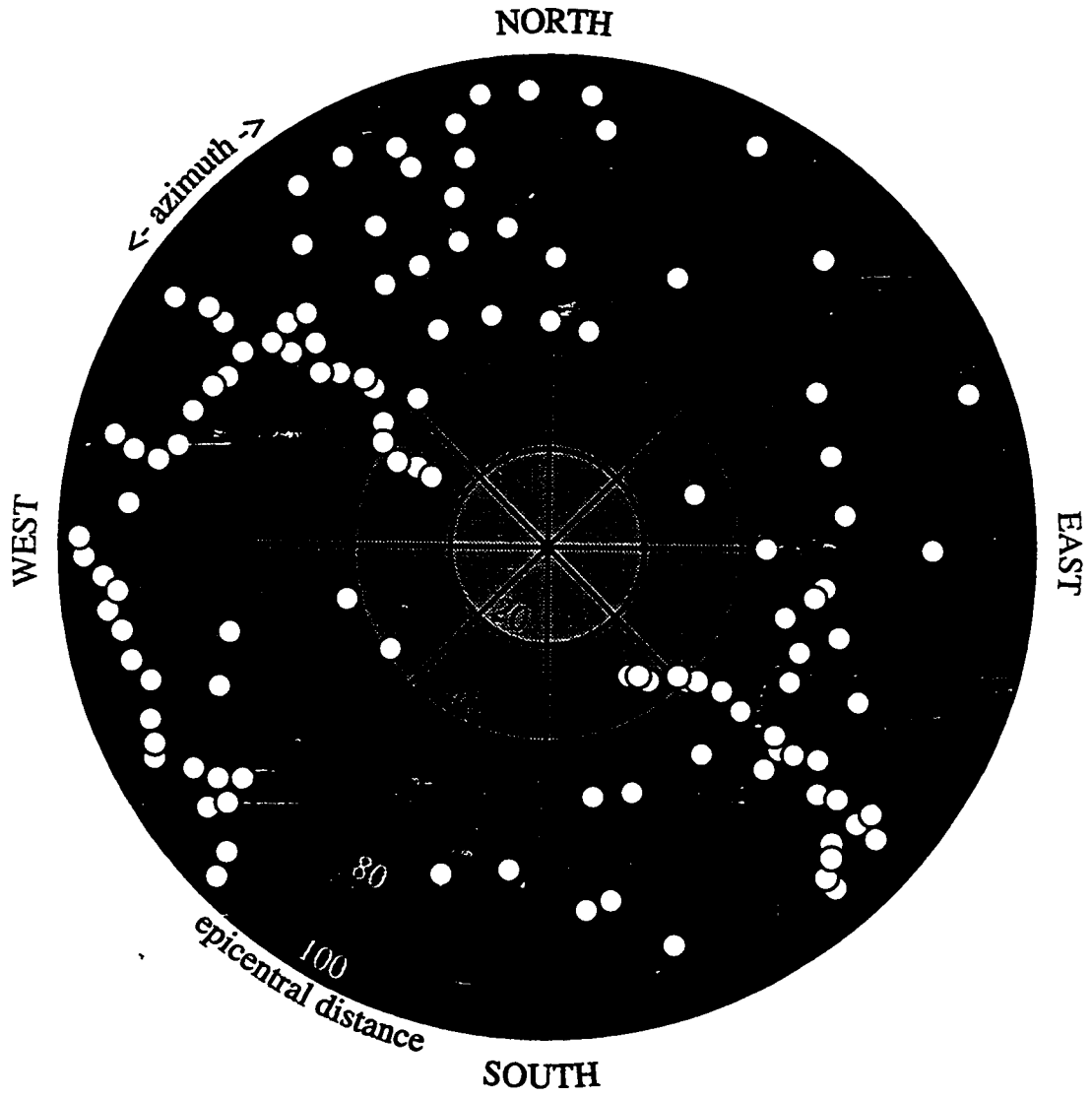
When much of the data set described above was archived it was mixed with local and regional data and placed on 9-track tape, therefore one of the first tasks necessary to providing adequate access to the data set was to extract the teleseismic data and place it on several high capacity exabyte tape cartridges. This was



(a)

Figure 2.2a,b Event locations with respect to the WRSN for events which resulted in P-phase data for (a) the complete set of data recorded between January 1980 and January 1990 and (b) for data used in travel-time inversion procedure.

Figure 2.2(continued)



(b)

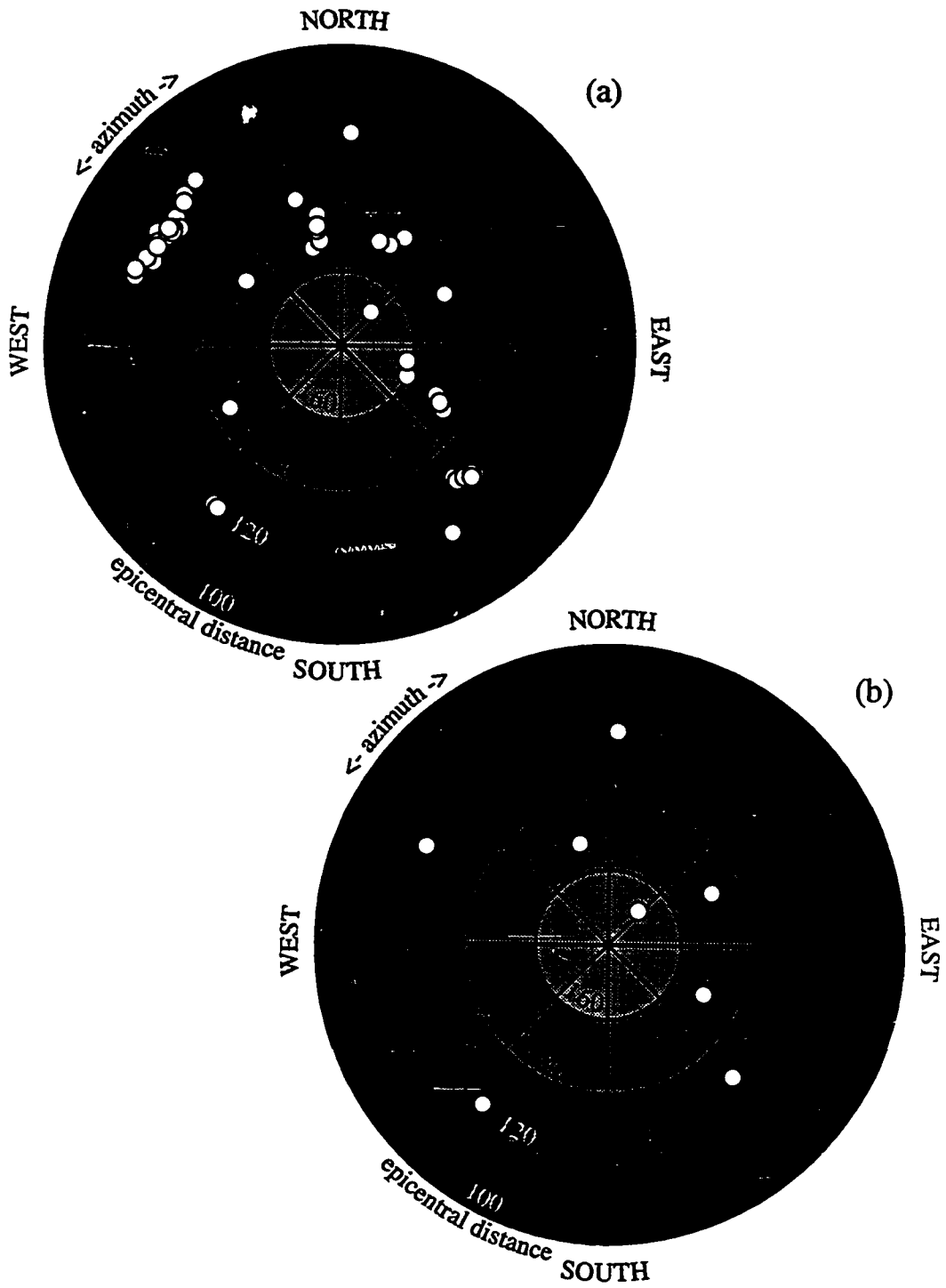


Figure 2.3a,b Event locations with respect to the WRSN for events which resulted in core-phase data for (a) the complete set of data recorded between January 1980 and January 1990 and (b) for data used in travel-time inversion procedure.

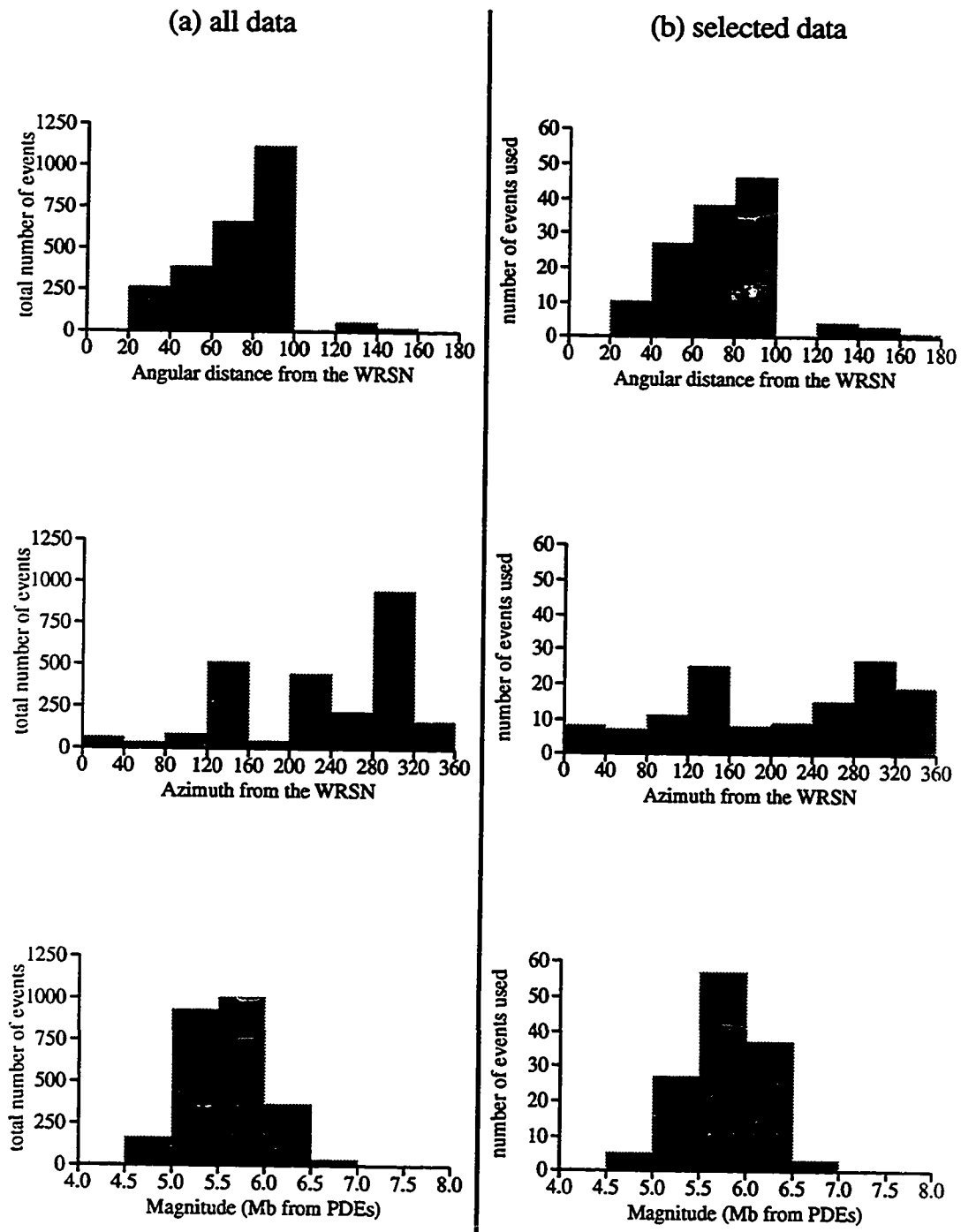


Figure 2.4a,b Histograms of event parameters with respect to the Washington Regional Seismic Network for (a) all events which were recorded from January 1980 to January 1990 and (b) events used in travel-time inversion procedure

necessary since we wished to extract the highest quality data available from *each* range of azimuth and distance covered by the data set. The procedure we enacted to do so was the following:

- divide all events into small subsets within natural groups or clusters (we chose to use 32 subsets),
- extract to disk all events from a given subset,
- choose candidate events from subset by quick visual inspection of data quality performed by plotting events on a computer workstation,
- perform multi-channel cross correlation procedure (§3.1) on candidate events collecting relevant statistics,
- make final selection based on signal quality, locations spanning the subset, and statistics,

In this manner all 3100 *P* phase and 82 core phase arrivals were examined in at least a cursory fashion in order to cull out the highest quality events from each region. At the end of this process 129 events had survived with 121 resulting in *P*-phase data and 8 in core phase data (Figures 2.2*b* and 2.3*b*, respectively). These are events tabulated in Appendix B. There were at least 9 events recorded at each station with most recording more than 40 and many over 100.

Core phases which could not be distinguished by angular distance and arrival time alone were found by plotting travel-time residual contour maps[†] assuming a different candidate phase for the theoretical times of each plot. Since the apparent velocities of the different core phases differ substantially, the proper phase was easily distinguished in this manner. Of the core phases shown in Figure 2.3*b*, the three events at approximately 150° angular distance resulted in *PKP_{BC}* triggers while the rest resulted in *PKIKP* phases. This was consistent with the theoretical amplitudes of these phases.

[†] Travel-time residual contour maps are described in §3.5 along with several examples.

Chapter 3

Multi-channel Cross Correlation [†]

3.1 Introduction

Our goal in this chapter is to improve on methods of relative arrival time estimation in order to provide a high quality set of data for imaging the deep structure of the Cascadia subduction zone. In addition to insufficient data coverage and approximations due to model parameterizations, three problems that degrade resolution and accuracy in travel-time inversion are (1) errors in arrival time measurement, (2) the lack of quantitative uncertainty estimates for use in weighting observations during inversion, and (3) the rejection of possibly useful data perceived to have too low a signal to noise ratio. The last problem is especially critical in studies which have poor data coverage from certain azimuths since often the sparse number of events from these regions have low magnitudes and shallow hypocenters resulting in recorded waveforms of relatively low quality. When large velocity perturbations are present in the region to be modeled and nonlinear methods are required, problems (1) and (2) may even act to preclude solution convergence [Nakanishi and Yamaguchi 1986]. The need to improve in these three areas together with the constraints imposed by the large volume of data regularly acquired by networks of up to a hundred or more stations makes it apparent that there is need for an efficient, effective and automated method of relative arrival-time estimation. While single-trace phase-picking algorithms [e.g. Allen 1978, Allen 1982, Crosson and Crosson 1988] are objective and have proven to be useful for the analysis of local and regional data, they are not normally suitable for use with teleseismic phases due primarily to the relatively emergent character of teleseismic waveforms.

The similarity of teleseismic waveforms leads naturally to the use of correlation methods [e.g. Bungum and Husebye 1971] and even manual methods using first breaks, peaks, troughs, or zero crossings make qualitative use of signal correlation [e.g. Iyer et al. 1981, Achauer et al. 1986]. In this chapter we present a novel

[†] This chapter was published in part as: VanDecar, J.C. and R.S. Crosson (1990). Determination of teleseismic relative phase arrival times using multi-channel cross correlation and least squares, *Bull. Seis. Soc. Amer.*, 80, pp. 150-169.

method for determining relative arrival times which provides both high quality relative arrivals and dependable uncertainty estimates. We use a multi-channel cross-correlation procedure with adjustment by least squares which allows us to make quantitative estimates of the uncertainty in relative arrival times as well as to make use of data that may be unusable with visual methods. Previous studies using large aperture arrays such as the Swedish Seismograph Network [*Husebye and Jansson 1966*], the Norwegian Seismic Array (NORSAR) [*Jansson and Husebye 1968, Bungum et al. 1971*] and the Large Aperture Seismic Array of Montana (LASA) [*Archambeau et al. 1965, Mack 1969*] have shown that teleseismic waveforms remain suitably coherent for cross-correlation analysis. These studies found that the waveform coherency between stations as a function of station separation decreases somewhat to distances of 10 to 20 km, beyond which there is virtually no change. When stations are separated by over 10 to 20 km (as is the case with many regional networks) the waveform distortion induced by multi-pathing appears as uncorrelated noise. We have confirmed this result for the Washington Regional Seismograph Network (WRSN, Figure 2.1), and later in this chapter demonstrate the lack of dependence on station separation of both waveform coherency and rms timing uncertainty.

Clearly when considering only a single station and therefore each waveform as a sample from a multiple number of events, waveform distortion cannot be thought of as a purely random process. This is due to the fact that at least some waveform distortion will undoubtedly arise from multipathing - multiple reverberations in the upper crust - and therefore a contribution to waveform distortion will vary predictably with respect to the azimuth and distance of each source. Likewise, given two stations, the cross-correlation function between their traces will not be distorted in a purely random manner when considering multiple events from similar azimuth and distance. However, when considering a single event recorded on a multiple number of stations (separated by sufficient distances) the distortions in the cross-correlation functions, and therefore shifts induced in the positions of cross-correlation maxima, manifest themselves as nearly random uncorrelated noise. This is due to structural complexity and resulting incoherence of multi-pathing between stations (as opposed to between events) and is the statistical property that we seek to exploit.

A simple and effective method of obtaining the time lag between two traces with similar waveforms is to locate the offset of the maximum of their cross-

correlation function. One way to apply this approach to more than two traces would be to choose a single channel with a characteristic waveform and then cross correlate it with remaining channels to find their relative time shifts. A possible problem with this method is that waveform distortions from both multipathing and even random noise (since the time series used are necessarily of finite length) may introduce first-order distortions into each cross-correlation function and therefore first order errors into the relative arrival time estimates. Even the relative magnitudes of these errors are difficult, if not impossible, to reliably estimate and are a function of which trace was chosen as the standard to cross correlate against. As an alternative to selecting a single representative trace, *Bungum and Husebye* [1971] developed a procedure which cross correlates each trace against a summed beam trace. They then generate a new beam with the resultant relative delay times and iterate on this process. Although superior to simply choosing a single trace to correlate against, their method may still be influenced in a first-order manner by the non-random distortions present in individual cross-correlation functions and does not converge in all cases. Neither of these procedures are capable of detecting cycle skipping - the selection of an incorrect maximum of a cross-correlation function - nor of producing quantitative uncertainty estimates.

To achieve our stated goal of improving relative arrival time estimates we have developed a straight-forward, semi-automated procedure which uses the cross correlations between all possible pairs of traces and estimates both accurate delays and quantitative timing uncertainties. We assume that errors in cross-correlation derived delay times, when taken between many different stations, are primarily random in nature; and therefore an improved estimate of waveform relative arrival times can be made through an over-determined system of equations and least squares. Our procedure can be broken into three major parts: (1) estimation of the relative delay time between each pair of traces via a search of their cross-correlation function, (2) minimizing the inconsistencies between all delay time estimates in a least squares sense in order to eliminate cycle skipping and invert for a single waveform arrival time on each trace, and (3) final interactive optimization of the solution to eliminate signals of unacceptably low quality. In this chapter we describe each of these steps in detail. Using examples from the WRSN, we explore the optimization of correlation and least squares weighting parameters and analyze the validity of our uncertainty estimation procedure. Finally, some examples of the

application of the method are presented.

3.2 Cross Correlation Analysis

Prior to any multi-channel processing we remove both the high and very low frequency energy present in the data by applying a zero-phase, band-pass Chebyshev filter with corner frequencies of 0.5 and 5.0 Hz. Although the precise filter specifications are not important, we find that band-pass filtering increases the reliability of our signal quality and timing uncertainty estimates while also making waveforms more recognizable during visual inspection. We have found by experiment that filtering has little effect on our optimized solution indicating that, for our purposes, high frequency energy may be considered incoherent noise. Figure 3.1 shows an example of *P*-wave arrivals for data so filtered, recorded on 85 WRSN stations. This event, originating near the east coast of Kamchatka, will be used as an example throughout the analysis portions of this chapter and referred to as Event I (see Table 3.1 for event parameters). It is of relatively low quality compared to many teleseisms recorded at the WRSN, and of lower quality than any events chosen for the travel-time inversion procedure (see Chapter 2).

For each trace we normally calculate a preliminary arrival time using a single-trace phase-picking algorithm developed at the University of Washington [Crosson and Crosson 1988]. This method, which was designed primarily for regional and local earthquake phase picking, estimates approximate arrival times. With Event I, for purposes of comparison, we have used visual picks of the first minimum which are indicated on Figure 3.1 by single vertical lines. Any picking procedure that locates the approximate onset of the major energy packet of the phase may be used. In discrete form, the truncated estimate of the cross-correlation function between the i^{th} and j^{th} traces is

$$\phi_{ij}(\tau) = \frac{\delta t}{T} \sum_{k=1}^{T/\delta t} x_i(t_i^P + t_0 + k\delta t + \tau) x_j(t_j^P + t_0 + k\delta t) \quad (3.2.1)$$

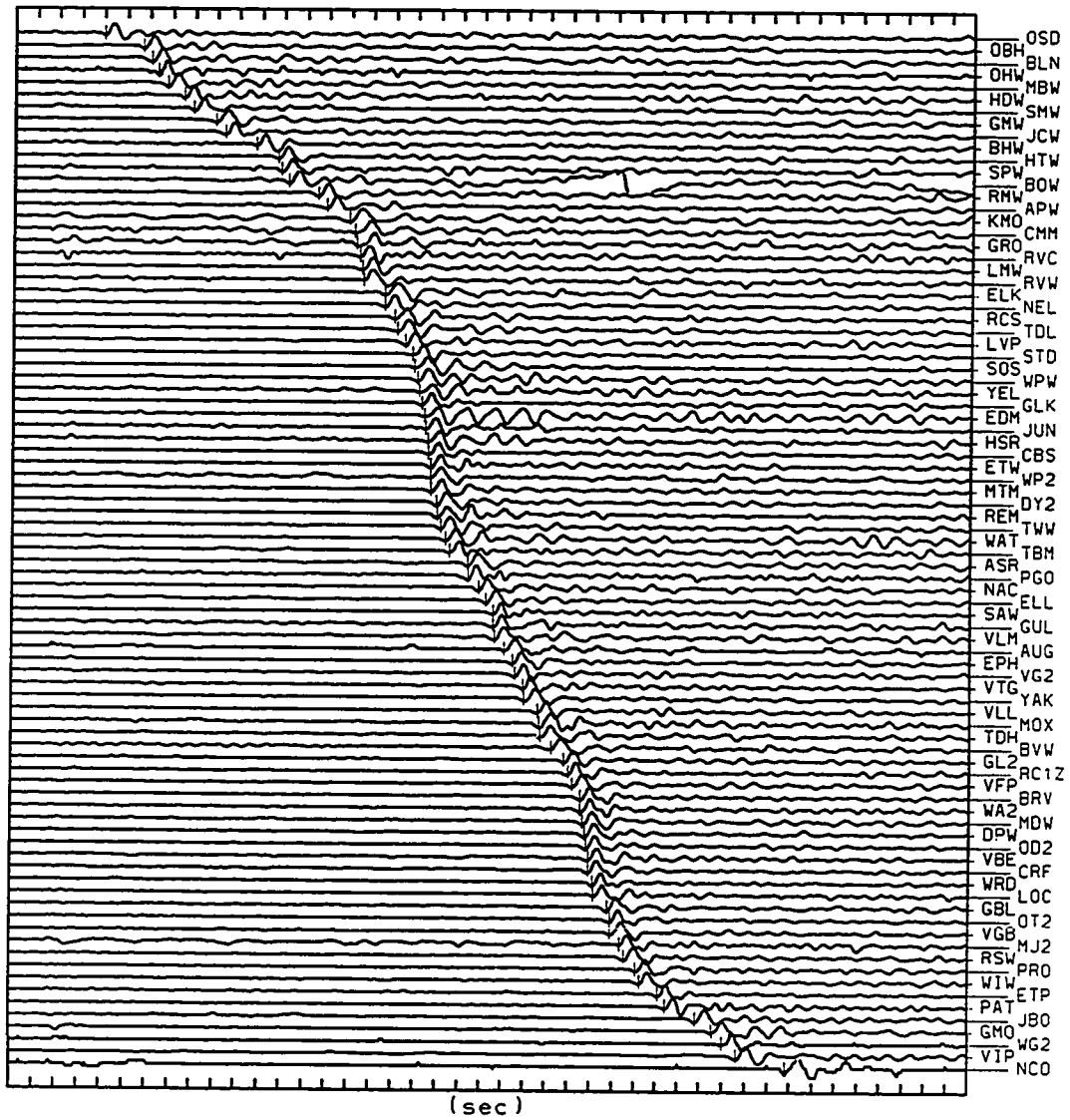


Figure 3.1 Bandpass-filtered seismic traces recorded on 85 WRSN stations illustrating the direct P-phase waveform of event I (see Table 3.1 for event parameters). Traces are ordered by arrival time with vertical line markers denoting preliminary arrival-time estimates made with visual picks of the first minimum. Each trace is individually scaled to the signal energy around the initial pick.

Table 3.1: Event parameters from the NOAA data base for the earthquakes used as examples in Chapter 3. The back azimuth and epicentral distance (Δ) to each event are calculated with respect to WRSN (latitude 46 N and longitude 121 W).

Example Events Used in Chapter 3									
Event Number	Date yy/mm/dd	Time (UTC)	Location		Depth (km)	Magnitude		Back azimuth Δ (from WRSN)	
			Latitude	Longitude		m_b	M_{sz}		
I	89/07/18	10:41	53.4N	160.4E	24	5.4	5.0	311°	51°
II	89/06/25	11:15	32.9N	39.6W	10	5.2	4.6	70°	63°
III	89/05/29	22:22	23.8S	70.3W	43	5.5	4.9	134°	81°
IV	89/05/28	09:46	16.4S	173.4W	51	5.7		232°	76°

where

x_i = digital data from i^{th} trace,

t_i^P = i^{th} trace's preliminary arrival time estimate,

τ = lag time relative to preliminary arrival time estimates,

T = length of correlation window (sec),

t_0 = time between t_i^P and when correlation window begins,

δt = sample interval (≈ 0.01 sec for WRSN, or 0.02 for decimated data).

Two traces to be cross correlated, with the parameters T and t_0 depicted, are shown at the top of Figure 3.2. Since on a routine basis we are only interested in the position of the maximum and its magnitude, the entire cross-correlation function need not be calculated. We speed up the search for the maximum's position, τ_{ij}^{max} , through the use of coarse estimates of the function. These estimates are performed by ranging lag times in steps of m sample intervals and multiplying only every m^{th} datum. We proceed through two levels of coarseness ($m = 10$ and 5) before performing the full resolution cross correlation ($m = 1$). In each case the next finer portion of the function is calculated within only $\pm m$ sample intervals of the current estimate. For instance with $T = 3$ sec and lag time, τ , ranging ± 1 sec this method results in a reduction in computation time to 1/15 of that for computing the same range at full resolution thereby making multi-channel cross correlation feasible for use in routine analysis. The bottom of Figure 3.2 illustrates the cross-correlation function of the two traces above showing both the coarse estimates of the function and a detail of the higher resolution portions. Negative extrema of the cross-correlation functions can be ignored by correcting the polarity of each trace before processing. This eliminates the possibility of large negative side-lobes being erroneously identified as the desired cross-correlation maximum.

Combining these lag times with the preliminary arrival time estimates defines the *cross-correlation derived relative delay time* between the i^{th} and j^{th} traces:

$$\Delta t_{ij} = t_i^P - t_j^P - \tau_{ij}^{\text{max}} \quad (3.2.2)$$

From the maximum magnitude of the cross-correlation function, $\phi_{ij}(\tau_{ij}^{\text{max}})$, an estimate of the *cross-correlation coefficient* between the i^{th} and j^{th} traces is given by

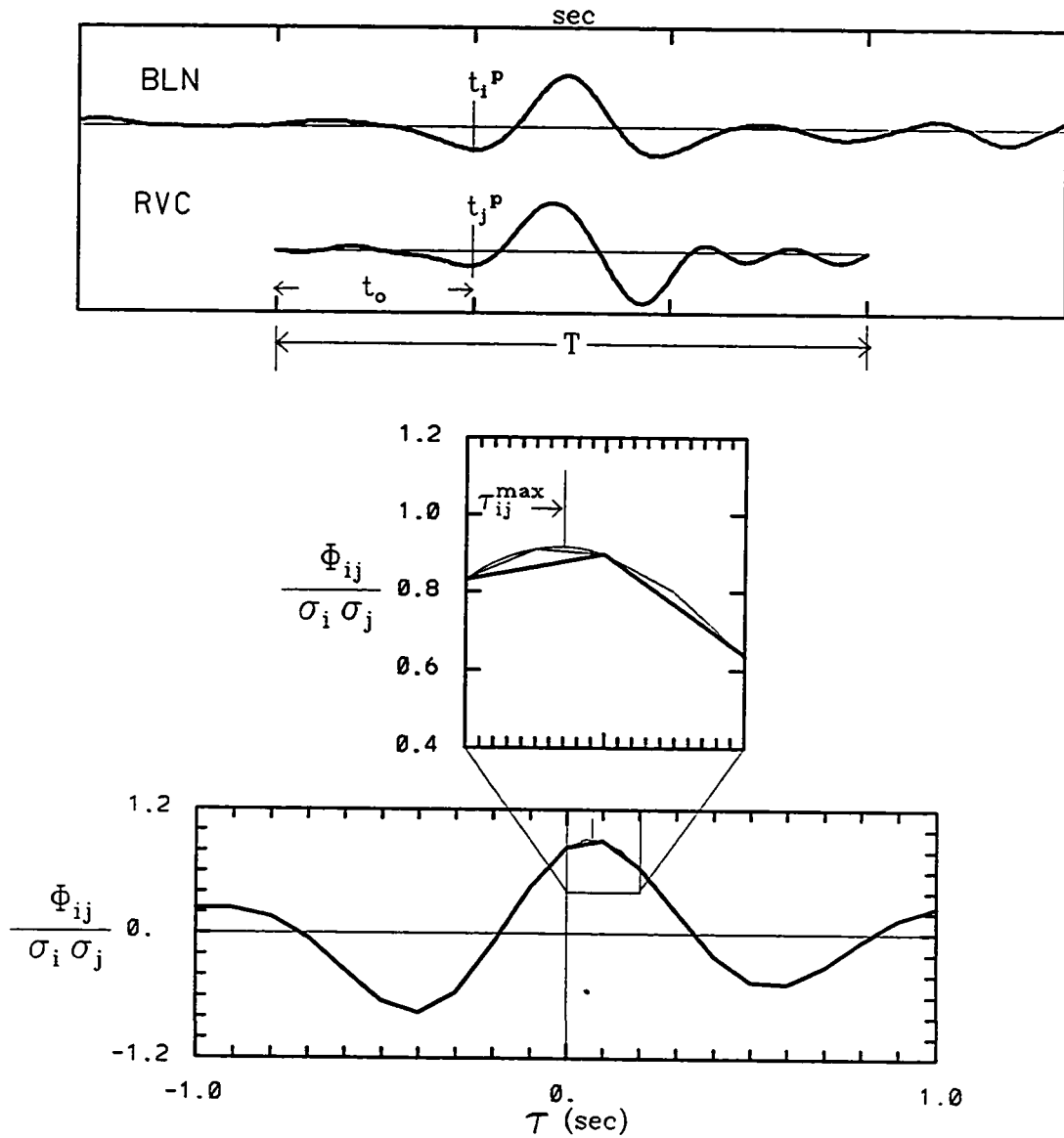


Figure 3.2 Estimate of the (normalized) cross-correlation function between trace data from stations BLN and RVC for Event I. At the top of the figure are the portions of the trace data used for the cross correlation. Below are the coarse estimate and a detail of the higher resolution portion.

$$r_{i j} = \frac{\phi_{i j} (\tau_{i j}^{\max})}{\sigma_i \sigma_j} \quad (3.2.3)$$

where $\phi_{i j}$ is defined in equation (3.2.1) and σ_i^2 represents the sample variance of the i^{th} trace data computed over the appropriate correlation window (when $\tau = \tau_{i j}^{\max}$). Since r is bounded by unity and therefore not normally distributed we introduce Fisher's transform [e.g. *Snedecor* 1956]:

$$z = \frac{1}{2} \ln \left[\frac{(1+r)}{(1-r)} \right]. \quad (3.2.4)$$

This new random variable, z , is almost normal, thereby allowing for the calculation of appropriate means, variances and confidence intervals which are then inverse transformed for use in analysis. All cross-correlation coefficient statistics which we refer to below have been calculated in this manner.

We initially quantify the relative signal quality of a given trace by using the sample mean and standard deviation of all cross-correlation coefficients associated with that trace. These statistics are plotted at the bottom of Figure 3.3 for the filtered traces of Event I. For data of moderate quality the sample means range from 0.80 to 0.95, corroborating our assertion from visual inspection that the majority of waveforms are highly coherent across the WRSN. The cross-correlation statistics provide useful keys in assessing a trace's relative quality and for spotting any large errors that may have been made during the preliminary picking process. For example, if a poor initial pick causes some of the cross-correlation functions associated with a trace to not include the true maximum while others do, the sample variance will be abnormally high. If a waveform is badly distorted or completely missed by the initial picking, that trace will produce consistently low cross-correlation coefficients usually with a small variance.

3.3 Least Squares and Uncertainty Estimation

Since waveforms are never completely coherent from station to station and there is always noise present, the cross-correlation derived relative delay times are not perfectly consistent (i.e. $\Delta t_{12} + \Delta t_{23} \neq \Delta t_{13}$). For n stations this inconsistency

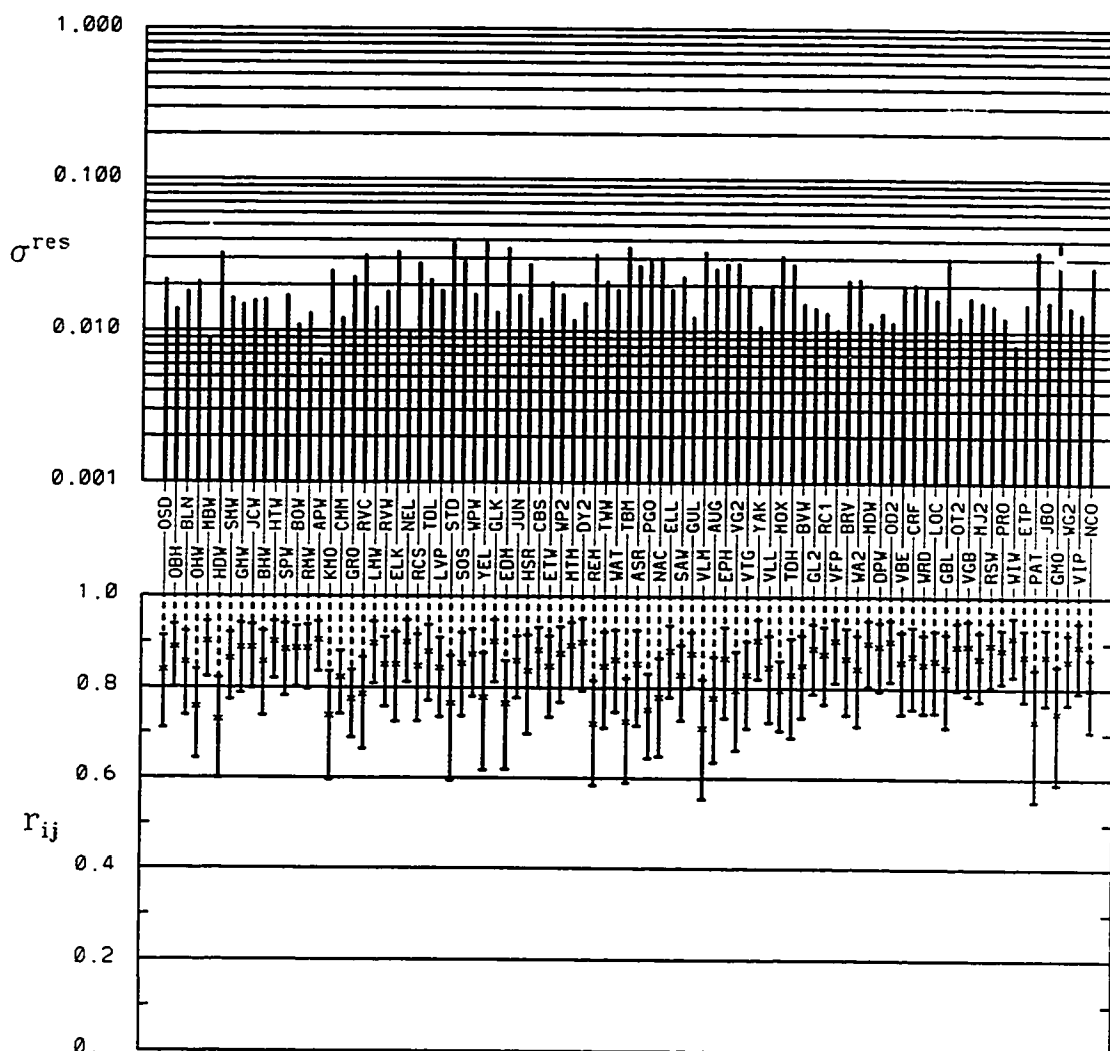


Figure 3.3 Statistics associated with each trace of the filtered version of Event I. Above are plotted the rms timing errors associated with each trace (equation 3.3.5) and below are the mean and standard deviation of the maximum cross-correlation coefficients associated with each trace (equation 3.2.3). The standard deviations are not symmetric about the mean since the cross-correlation coefficients were calculated from the Fisher-transformed values (equation 3.2.4) and then inverse transformed for analysis.

allows us to generate a system of $\frac{n(n-1)}{2}$ over-determined equations given by

$$t_i - t_j = \Delta t_{i,j} \quad i = 1, 2, \dots, n-1; \quad j = i+1, i+2, \dots, n \quad (3.3.1a)$$

to which we add the constraint equation

$$\sum_{i=1}^n t_i = 0 \quad (3.3.1b)$$

to force the arbitrary mean of the optimized relative arrival times, t_i , to zero. This system may be expressed symbolically as $\mathbf{A}\mathbf{t} = \Delta\mathbf{t}$ where the n length solution vector \mathbf{t} represents the optimized relative arrival time of the waveform on each trace (with zero mean), $\Delta\mathbf{t}$ is the $\frac{n(n-1)}{2}+1$ length data vector of cross-correlation derived relative delay times, and \mathbf{A} is a sparse $\frac{n(n-1)}{2}+1 \times n$ coefficient matrix.

For the simple case of only 5 traces this system would take the form

$$\begin{bmatrix} 1 & -1 & 0 & 0 & 0 \\ 1 & 0 & -1 & 0 & 0 \\ 1 & 0 & 0 & -1 & 0 \\ 1 & 0 & 0 & 0 & -1 \\ 0 & 1 & -1 & 0 & 0 \\ 0 & 1 & 0 & -1 & 0 \\ 0 & 1 & 0 & 0 & -1 \\ 0 & 0 & 1 & -1 & 0 \\ 0 & 0 & 1 & 0 & -1 \\ 0 & 0 & 0 & 1 & -1 \\ 1 & 1 & 1 & 1 & 1 \end{bmatrix} \begin{bmatrix} t_1 \\ t_2 \\ t_3 \\ t_4 \\ t_5 \end{bmatrix} = \begin{bmatrix} \Delta t_{12} \\ \Delta t_{13} \\ \Delta t_{14} \\ \Delta t_{15} \\ \Delta t_{23} \\ \Delta t_{24} \\ \Delta t_{25} \\ \Delta t_{34} \\ \Delta t_{35} \\ \Delta t_{45} \\ 0 \end{bmatrix} \quad (3.3.2)$$

For the more typical case of 90 or more stations the number of equations grows to over 4000.

Adding the zero-mean constraint makes the system non-singular and allows us to analytically calculate the least squares solution $\mathbf{t}^{est} = (\mathbf{A}^T \mathbf{A})^{-1} \mathbf{A}^T \Delta\mathbf{t}$ [e.g. Menke, 1984]. Since $\mathbf{A}^T \mathbf{A} = n \mathbf{I}$ (where \mathbf{I} is the identity matrix), and therefore

$(\mathbf{A}^T \mathbf{A})^{-1} = \frac{1}{n} \mathbf{I}$, it follows that $\mathbf{t}^{est} = \frac{1}{n} \mathbf{A}^T \Delta \mathbf{t}$, or explicitly the simple sum

$$t_i^{est} = \frac{1}{n} \left[- \sum_{j=1}^{i-1} \Delta t_{j i} + \sum_{j=i+1}^n \Delta t_{i j} \right]. \quad (3.3.3)$$

If we wish to weight the equations to reflect varying quality of observations, then we must instead perform a numerical inversion of the system $\mathbf{t}_w^{est} = (\mathbf{A}^T \mathbf{W} \mathbf{A})^{-1} \mathbf{A}^T \mathbf{W} \Delta \mathbf{t}$ (where \mathbf{W} represents an $\frac{n(n-1)}{2} + 1 \times \frac{n(n-1)}{2} + 1$ diagonal weighting matrix). Due to the sparseness of \mathbf{A} and its regular form it is possible to calculate $\mathbf{A}^T \mathbf{W} \mathbf{A}$ without constructing its component matrices, thereby limiting the maximum storage requirement to a size $n \times n$ matrix

We have tested two different weighting schemes. The first involves weighting each equation by its associated cross-correlation coefficient and the second via a weighted function of equation residuals from the previously determined un-weighted estimate,

$$res_{i j} = \Delta t_{i j} - (t_i - t_j) \quad (3.3.4)$$

These weighting schemes have little effect on the solution itself except when large outliers are present in which case they make the inversion more robust by down-weighting those equations. The weighting does, however, make the uncertainty estimates more realistic since outliers have a strong effect on variance estimation. Since, for the un-weighted case, the least-squares solution to (3.3.1) is simply a normalized sum of cross-correlation derived relative delay times given by (3.3.3), the standard deviation of the residuals associated with the i^{th} trace,

$$\sigma_i^{res} = \sqrt{\frac{1}{n-2} \left[\sum_{j=1}^{i-1} res_{i j}^2 + \sum_{j=i+1}^n res_{i j}^2 \right]}, \quad (3.3.5)$$

represents an estimate of its rms timing uncertainty. We have found that these residuals are nearly normally distributed with a tendency to have slightly heavy tails. Their standard deviation therefore provides a reliable, if somewhat pessimistic, estimate of rms timing uncertainty (not accounting for possible biases). At the top of Figure 3.3 we plot rms timing uncertainty for the filtered traces of Event I associated with the un-weighted least-squares inversion.

Timing uncertainty, σ_i^{res} , normally has a strong inverse correlation with mean cross-correlation coefficient, as one would expect, but under certain circumstances this correlation breaks down. The breakdown occurs when relatively high frequency noise (4-10 Hz) is present in an otherwise undistorted waveform. The result is low cross-correlation coefficients but highly consistent and accurate delay times producing low timing uncertainties. Therefore the least squares derived timing uncertainty, rather than correlation coefficient, gives the most reliable estimate of arrival time accuracy.

We have found that very large equation residuals ($res_{i,j} > .5$ sec) are usually the result of cycle skipping occurring during the cross-correlation analysis. To alleviate this problem our procedure automatically computes a new delay time, $\Delta t_{i,j}$, for each cross-correlation function associated with one of these large equation residual. In order to choose the correct maximum we now search only the region of the cross-correlation function near the time lag predicted by the least-squares solution ($\tau = t_i^{est} - t_j^{est}$). This method has proven to be effective when the number of cases of cycle-skipping is less than 10-20% of the total number of cross correlations with a given trace. In the rare case when cycle skipping is more prevalent the initial least-squares solution is likely to be thrown off too far to be useful, and manual correction by an analyst is required.

The first manual intervention with our algorithm normally occurs on a computer workstation after the first round of least-squares optimized picks have been made. Adjustments may be made in several ways. The analyst may delete dead or highly distorted traces and re-run only the least squares portion of the procedure. This is accomplished in several seconds. If excessive cycle skipping has occurred or an improper phase has been chosen, the analyst may move one or more traces into alignment within visual accuracy and then re-run the full cross-correlation and least-squares procedures with a short range of lag times (e.g. $-0.25 \leq \tau \leq 0.25$ sec). Figures 3.4 and 3.5 show details of unfiltered and filtered traces, respectively, of Event 1 aligned on the left by preliminary arrival time estimates, t_i^P , and on the right by their respective least-squares optimized arrival times, t_i^{est} .

When examining the various maximas in the waveforms of Event I it can be seen that any one of these features vary substantially from the optimized alignment in Figures 3.4 and 3.5. For the highest quality data all the methods that we tested

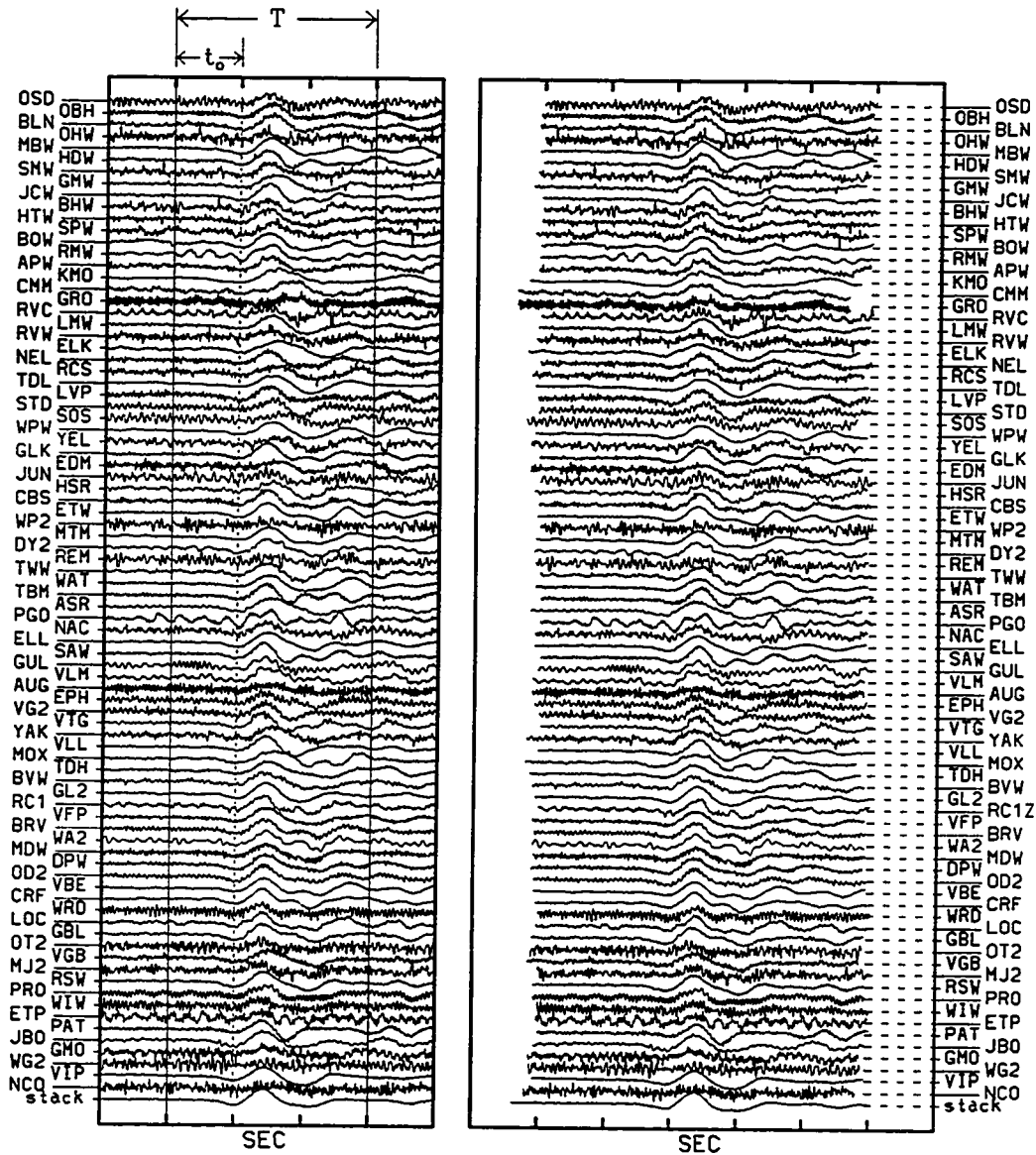


Figure 3.4 Portions of unfiltered waveforms of Event I used for cross-correlation analysis aligned by preliminary arrival-time estimates (visual) on the left and least-squares optimized relative arrival times on the right. The alignment was obtained with unfiltered data. Each trace is individually scaled by the signal energy within the window of data shown.

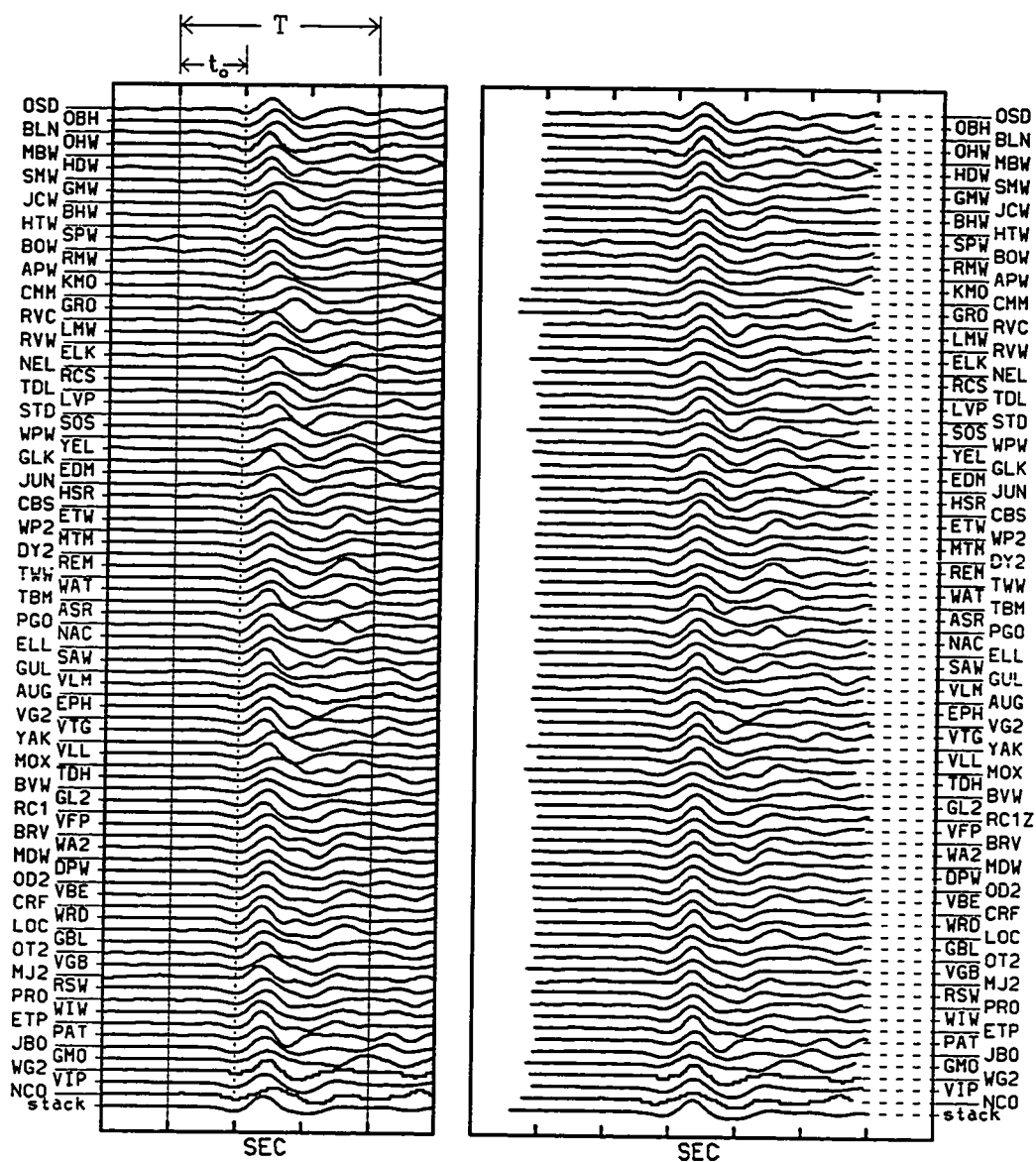


Figure 3.5 Portions of filtered waveforms of Event I used for cross-correlation analysis aligned by preliminary arrival-time estimates (visual) on the left and least-squares optimized relative arrival times on the right. The alignment was obtained with filtered data. Each trace is individually scaled by the signal energy within the window of data of data shown.

yielded similar results. For slightly lower quality events, if the visually obtained arrival times from several features are averaged, the result once again approximates that of the least-squares optimized relative times. For yet lower quality data, however, such as in Event I, the major features are distorted to such an extent that even averaged times may be severely biased for many of the traces.

3.4 Selection of Parameters and Waveform Coherency

The adjustable parameters in our cross-correlation analysis are the cross-correlation window length (T), the maximum lag time ($\Delta\tau$), and the position of the correlation window starting time (t_o , see Figure 3.2). As long as the true maximum is included in the estimated cross-correlation function, lag time range has no effect on our results, thus this parameter need only be chosen large enough to guarantee inclusion of that maximum. The global statistic that we use to evaluate the quality of the relative arrival times determined with a given set of parameters is the mean cross-correlation coefficient. We find that the most consistent and computationally efficient results are obtained with window lengths of 2-4 sec beginning at the onset of the first major energy packet of the phase. Figure 3.6 illustrates the three-dimensional representation of mean cross-correlation coefficient as a function of window length, T , and window starting position, t_o . Plotted beneath for reference is the stacked trace for this event, computed by

$$x_{sum}(k \delta t) = \sum_{j=1}^n x_j (t_{ref}^p - t_{ref}^{est} + t_j^{est} + k \delta t) \quad (3.4.1)$$

where the subscript *ref* indicates times associated with an arbitrary reference station. The stacked trace illustrates how the coefficient means are influenced by the signal energy at a given position in the waveform. Bands of high coefficient means that trend diagonally across the plot represent major packets of coherent waveform energy being reached with shorter window lengths as the window position moves down the trace. These correlation coefficient means are all calculated with respect to the optimized alignment at $t_o = -1.0$ sec and $T = 3.0$ sec (indicated by an * on the plot) so that each point represents the amount of waveform energy coherent with that alignment. It can readily be seen from both the short window length means ($T = 0.5$ sec) and the stacked trace that there is a considerable amount of coherent energy out 2 to 2.5 sec beyond the initial correlation window starting

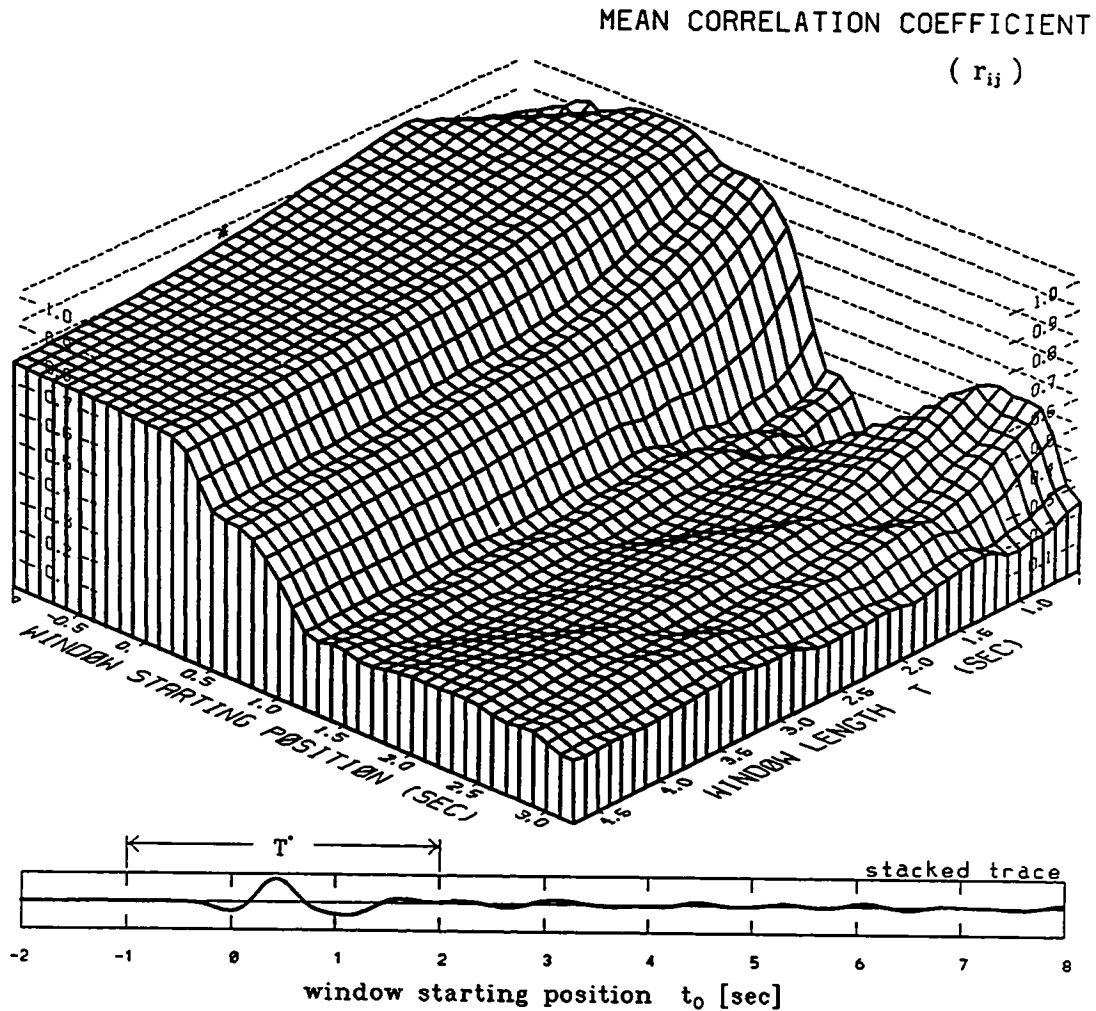


Figure 3.6 Three-dimensional perspective of mean cross-correlation coefficient as a function of window position, and window length for sample Event I. Plotted below for reference is the stacked trace for Event I (equation 3.4.1). T^* represents the window length used to obtain the least-squares optimized trace alignment. The corresponding point on the diagram is also indicated by an *. The rest of the diagram represents the amount of energy coherent with this alignment (obtained with $T=3.0$ sec).

position ($t_0 = -1.0$ sec). For larger magnitude events this length of coherency extends later into the traces as one would expect, since larger events tend to have longer source time functions. It is therefore the source time function, or equivalently magnitude of the earthquake, which controls the optimum window length for any particular event. Extending the correlation windows beyond this region has little effect on our solution but does increase the computer time necessary to process each event. Using small windows ($T < 2$ sec) generates solutions which tend to be unstable and highly sensitive to parameter changes. This is due in part to the edge effect arising from the truncation inherent in the windowing process. The effect can be partially alleviated with the use of tapering, but only at the expense of discarding a sizable portion of the information contained in the (already small) window. We do not taper our windows which are normally of lengths of 3 to 4 sec. By examining plots such as in Figure 3.6, we are able to judge what minimum length of correlation window is appropriate for a given event. By following a line of equal t_0 we can see that once we reach a certain critical window length the amount of coherent energy drops dramatically. This is presumably due to the effect of the initial source function response ending at this point and multi-pathing energy dominating the rest of the signal.

We have found that there is little if any correlation between station separation and waveform coherence for the WRSN. To quantify this result we have examined the coherence, as measured by the maximum cross-correlation coefficient, as a function of station separation. The correlation coefficients, r_{ij} as defined in equation (3.2.3) are plotted in Figure 3.7 as a function of station separation for both the unfiltered and filtered traces of Event I. Also shown in Figure 3.7 is a running mean and one standard deviation from that mean ($\pm \sigma$), once again calculated from Fisher-transformed coefficients (equation (3.2.4)) and then inverse transformed. Likewise, Figure 3.8 illustrates the dependence of solution residuals on station separation. If there were coherence in multi-pathing on scale lengths spanned by the network, then one would expect to see both a definite decline in waveform coherence and increase in residual magnitude with station separation. We have found that these dependencies are small (if at all existent) and change from event to event showing no general trend. This outcome is consistent with the findings of *Archambeau et al.* [1965] and also those of *Mack* [1969] who concluded that there was coherent multi-pathing within LASA sub-arrays (.5-7 km scale lengths) but that

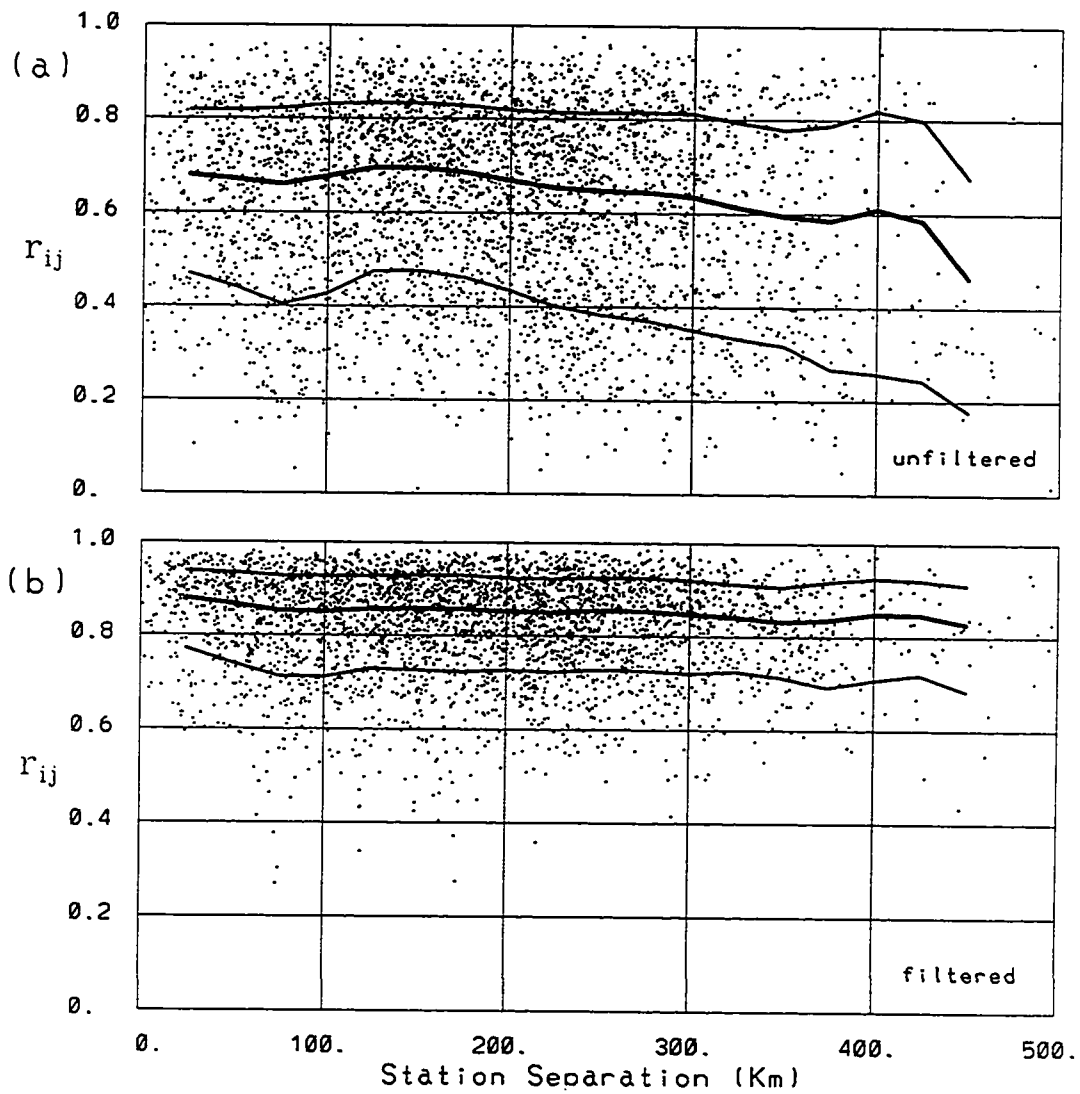


Figure 3.7 Maximum correlation coefficients as a function of station separation for (a) the unfiltered and (b) the filtered traces of Event I. The heavy line represents a running mean (sample window = 50 km) calculated from the Fisher-distributed coefficients (equation 3.2.4) with lighter lines representing one standard deviation from the mean.

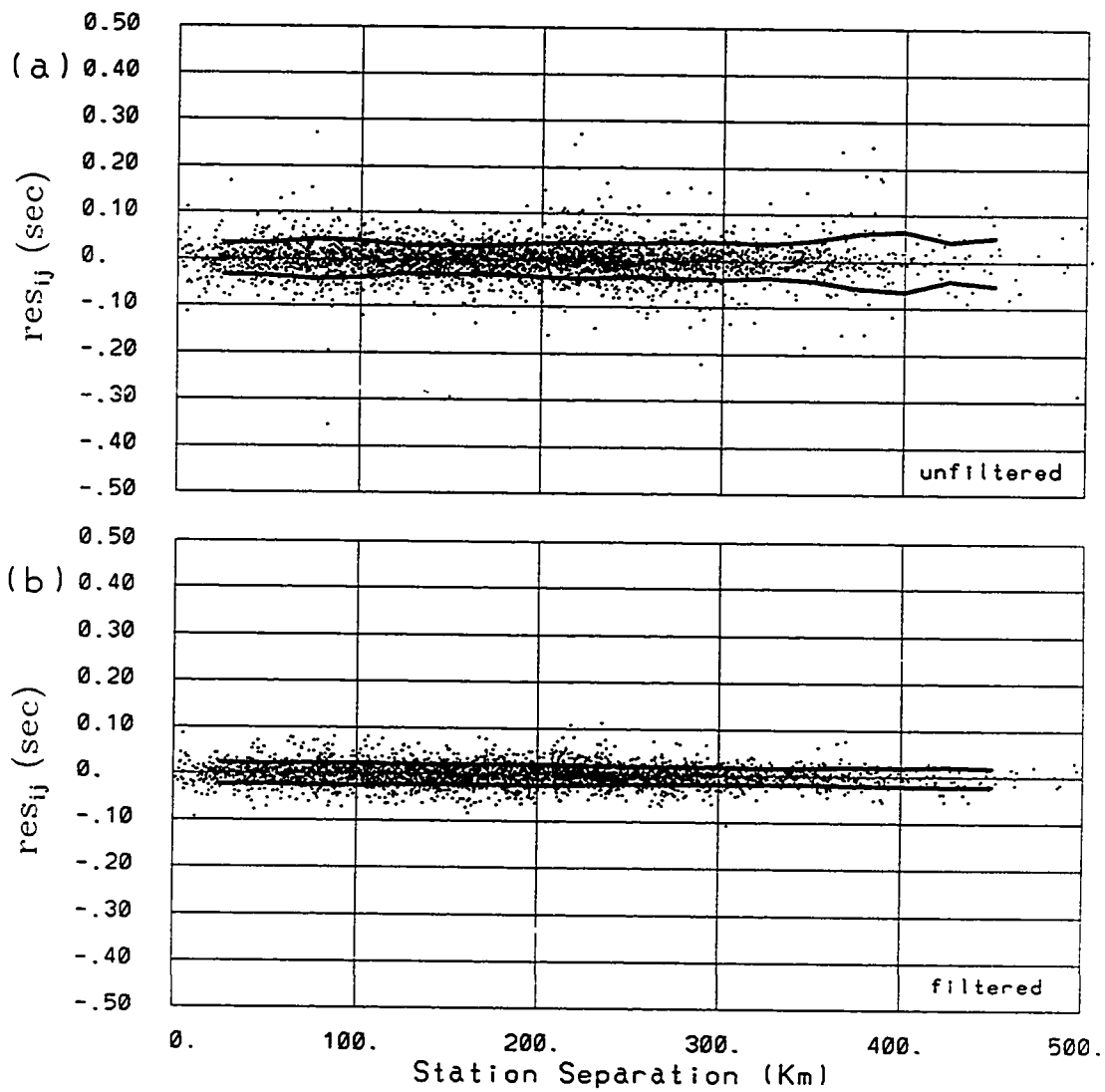


Figure 3.8 Residuals to least-squares solution (equation 3.3.4) as a function of station separation for (a) the unfiltered and (b) the filtered traces of Event I. The heavy line represents a running standard deviation of this data (sample window = 50 km). Means are in general indistinguishable from zero.

between the sub-arrays (10-200 km span) multiples were in-coherent so that “phased summation tends to cancel them.”

3.5 Examples

As with studies relying on visually chosen arrival times [e.g. *Michaelson and Weaver*, 1986; *Rasmussen and Humphreys*, 1988] we have found that the delay residual patterns over the WRSN vary greatly with azimuth and angular distance. Figure 3.9 shows relative arrival times across WRSN for Event I (see Table 3.1 for example event parameters). The overall pattern is one of a plane wave crossing the array but distortions can be seen even in these raw arrival times. To obtain the relative arrival residual patterns we subtract expected times calculated from PDE locations and the Herrin radial earth model [*Herrin*, 1968]. We calculate the expected arrival time at each station, remove the mean of those times, and then subtract them from our zero-mean optimized relative arrival times. Figure 3.10a is a map of these residuals contoured for Event I. The relatively small magnitude of many features of this pattern (.2 to .6 sec) points out the need for accurate relative arrival times in order to resolve this signal. The signal dramatically changes with azimuth as is illustrated in Figures 3.10a-d. The degree of reproducibility of these residual patterns is very high, even for low amplitude features, with statistical correlations between events from similar regions commonly ranging from 0.96 to 0.99.

The large variation of residual pattern with azimuth indicates that deep structure plays an important role in their generation. Some features such as the late arrivals over the north Puget Sound lowlands and the early arrivals over the North Cascades are relatively constant and depend only moderately on azimuth possibly reflecting fairly shallow structure. On the other hand features such as the band of large magnitude early arrivals from eastern azimuths (Events II and III) are certainly not present in data from the west, most likely reflecting deep slab structure.

We point out here that the arrival times that we measure with our procedure are those of the major phase arriving in each time window. If a low amplitude earlier phase is present it will not necessarily represent the measured arrival time. This is a problem with any method of arrival time estimation for teleseismic data and should caution users of travel-time data to make sure that both the amplitude of the earliest phase is indeed sufficiently large and its arrival sufficiently separated

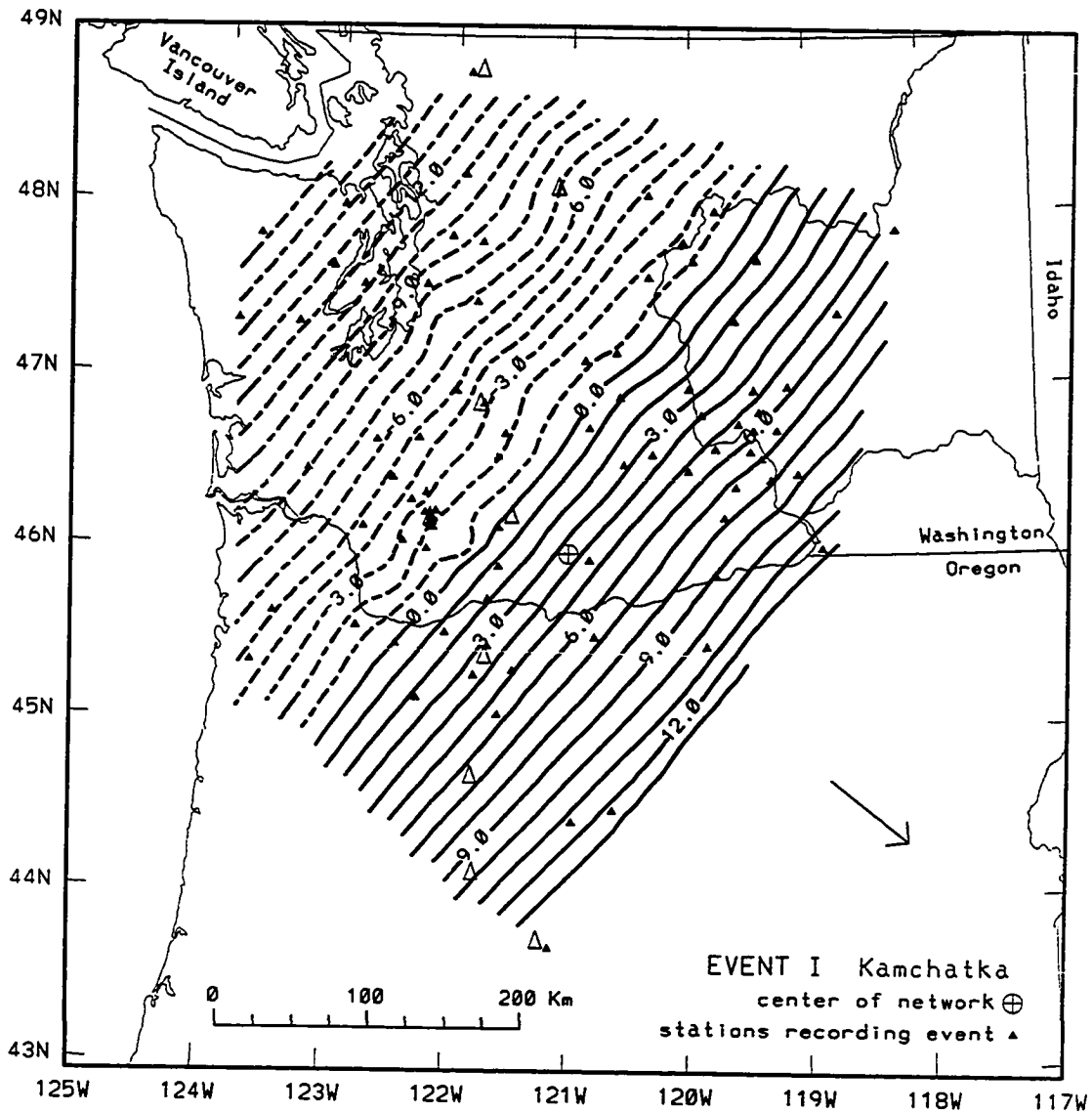


Figure 3.9 Contour map of P-phase relative arrival times for sample Event I. Contour interval is 1.0 sec. Arrow represents azimuthal direction with length proportional to the indicated epicentral distance from center of network. Azimuth to Event I is 311 degrees and distance is 51 degrees (see Table 3.1 for additional parameters).

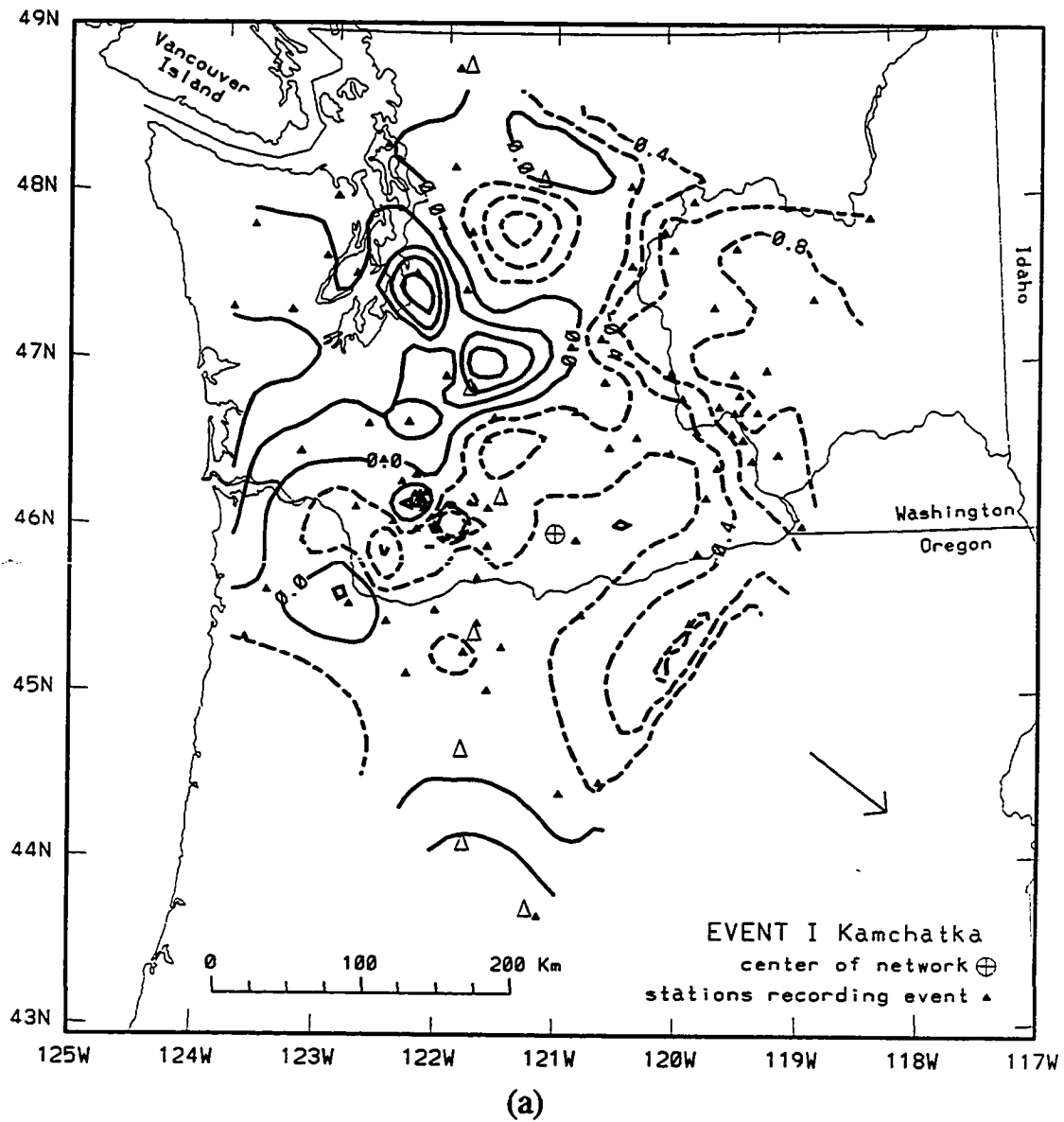
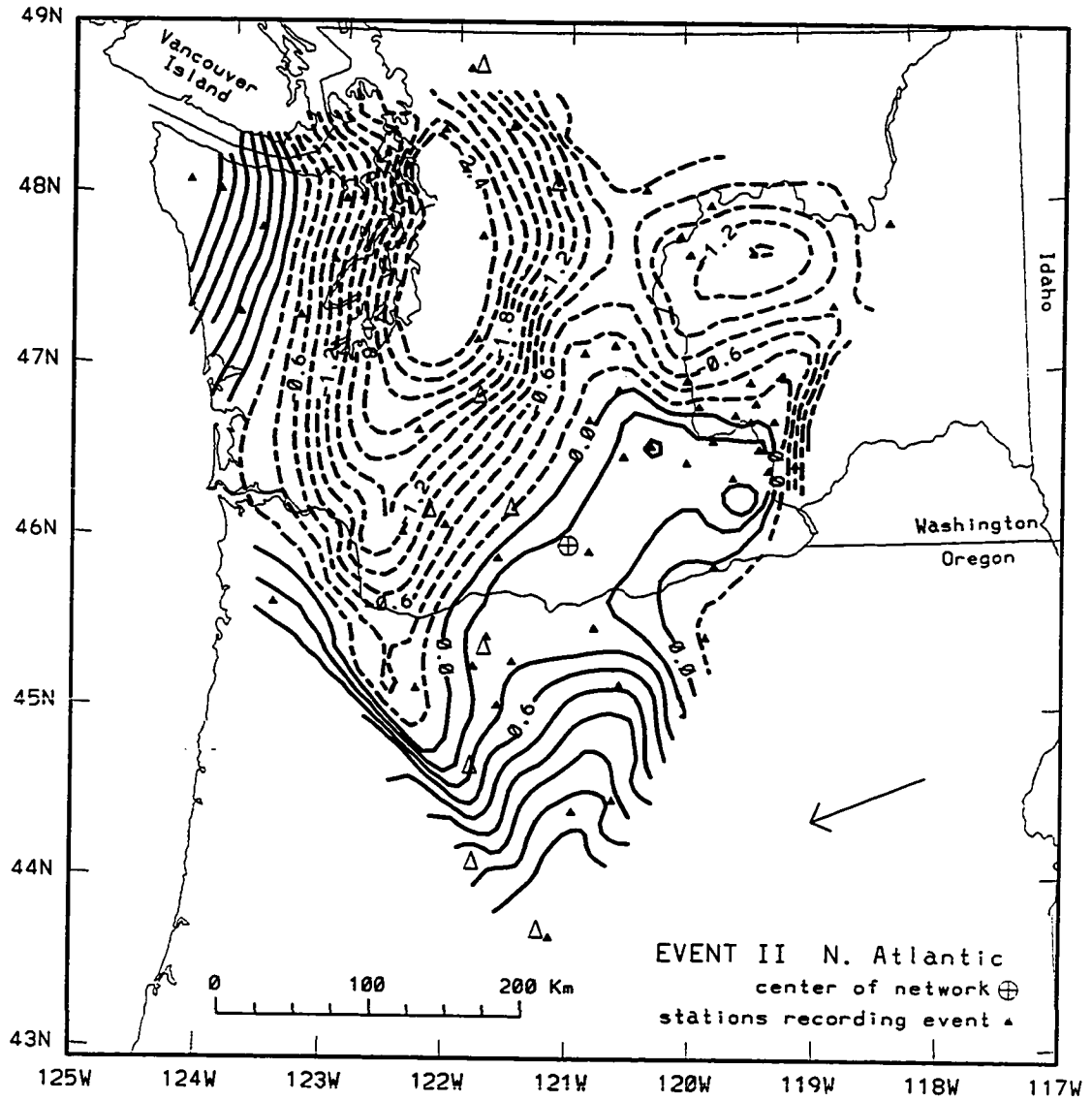


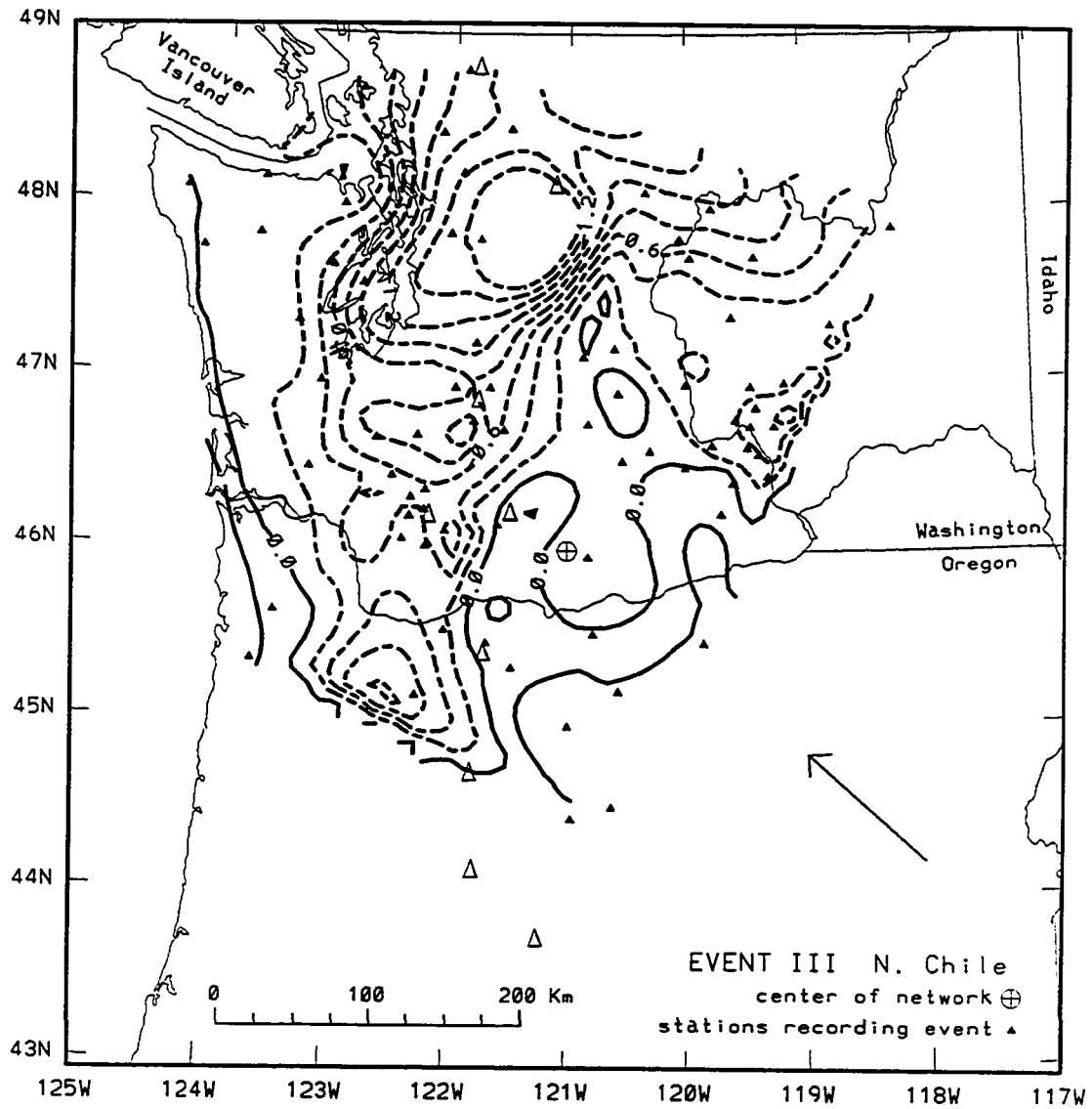
Figure 3.10a-d Contour maps of P-phase relative arrival-time residuals for (a) sample Event I, (b) Event II, (c) Event III and (d) Event IV. Residuals are the difference between the least-squares optimized relative arrival times and those predicted from PDE locations and the Herrin radial earth model [Herrin, 1967]. Contour interval is 0.2 sec with dashed lines representing negative contours. See Table 3.1 for additional event parameters.

Figure 3.10 (continued)



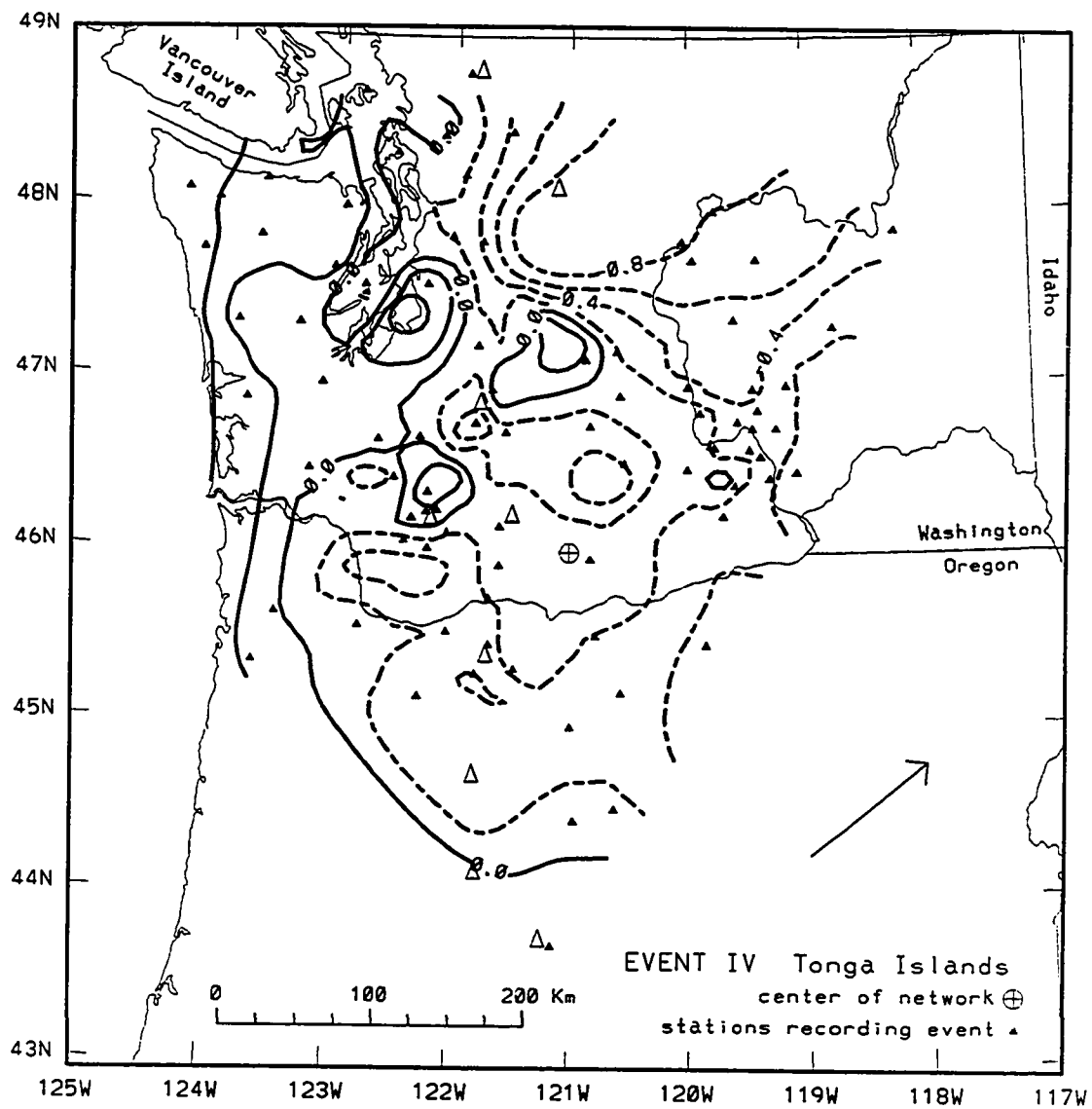
(b)

Figure 3.10 (continued)



(c)

Figure 3.10 (continued)



(d)

from other phases to have been picked.

Chapter 4

Non-linear Inversion Procedure

4.1 Introduction

In this chapter we will discuss the basis for least-squares inversion (§4.2), the linearization and discretization of the two point seismic-wave travel-time equation (§4.3, §4.4), the formulation of the appropriate linear inverse problem and its conjugate gradient solution (§4.5), and finally the procedure that we employ to iterate on these procedures (§4.6). The sections on least-squares inversion is a brief review to put into context further discussion in this and following chapters. References to appropriate texts and review papers are given in each section for more detailed discussions of these topics.

4.2 Least-squares Inversion

The prediction of a measurement given a theoretical basis for its generation (i.e. the appropriate physics) and a model of the parameters on which the theory is sensitive is known as a *forward problem*. Conversely, the mapping of measured quantities back into the space of model parameters is known as an *inverse problem*. Both forward and inverse mappings (theory) may be either linear or non-linear. When this mapping is linear with respect to the model we may represent such systems as sets of integral equations

$$\int g_i(\mathbf{r})m(\mathbf{r})d\mathbf{r} = d_i \quad i = 1,2\dots n \quad , \quad (4.2.1)$$

where the d_i represent n discrete measurements, $m(\mathbf{r})$ functions of model parameters, g_i functionals that map the model into data space, and \mathbf{r}^\dagger a vector of independent variables (for instance spatial coordinates). In general d itself will be a continuous function but in practice measurements are made at discrete points. For linear problems there is well developed and efficient theory for performing inversions and analyzing the resulting models. However for non-linear problems concepts such as uniqueness and resolution/covariance tradeoff take on new

† Throughout this thesis, vectors will be represented by emboldened lower-case letters (e.g. \mathbf{d} , \mathbf{t} and \mathbf{m}) and second-order matrices by emboldened upper-case letters (e.g. \mathbf{G} and \mathbf{C}).

complexity. In the following sections we will briefly review the basic concepts of linear and linearized inversion as they will be treated in the following sections. For a more comprehensive treatment of these subjects the reader is directed to standard texts such as *Menke* [1984] and *Tarantola* [1987a], or review articles such as *Parker* [1977b] or *Sabatier* [1977a].

The most studied and well-understood inverse problems are those that are linear (i.e. can be expressed as a set of linear equations). In such a case, if we discretize the model into m parameters, we may then represent the system in 4.2.1 in the form of a sum,

$$\sum_{j=1}^m G_{ij} m_j = d_i \quad i = 1, 2 \dots n, \quad (4.2.2)$$

or symbolically as $\mathbf{Gm} = \mathbf{d}$, where \mathbf{m} is a vector of model parameters, \mathbf{d} a vector of measurements (i.e. data), and \mathbf{G} is the mapping that relates the two. The forward problem consists of calculating \mathbf{d} given \mathbf{G} and \mathbf{m} . This operation is trivial and exact (within computational precision). Conversely, the calculation of \mathbf{m} given \mathbf{G} and a realization of \mathbf{d} is generally more challenging.

We refer to \mathbf{d} as a *realization* since real measurements are never exact and therefore we only work with a limited number of data sampled from a (usually unknown) probability distribution. In general we are forced to make strict assumptions about the shapes of these distributions (e.g. assume Gaussian distributions) due to our lack of knowledge concerning the true probability structure. Even with the simplification of assuming a given *shape* for this distribution, its characteristic width is rarely known with any degree of certainty. This is the most basic and perhaps most important level at which to seek an improvement if one wishes to increase the reliability and accuracy of a modeling procedure.

Given a set of measurements \mathbf{d} and an estimate of the probability functions from which they were derived, we now wish to infer which types of models \mathbf{m} are likely to have generated these measurements. If we assume that the probability distributions from which our measurements were drawn are Gaussian in shape with the matrix \mathbf{C} describing the covariance of these distributions then the *maximum likelihood estimator* of \mathbf{m} will be the one that minimizes the function

$$\begin{aligned}\phi &= \frac{1}{2}(\mathbf{C}^{-1/2}\mathbf{G}\mathbf{m} - \mathbf{C}^{-1/2}\mathbf{d})^T(\mathbf{C}^{-1/2}\mathbf{G}\mathbf{m} - \mathbf{C}^{-1/2}\mathbf{d}) \\ &= \frac{1}{2}(\mathbf{G}\mathbf{m} - \mathbf{d})^T\mathbf{C}^{-1}(\mathbf{G}\mathbf{m} - \mathbf{d}),\end{aligned}\quad (4.2.3)$$

where superscript T indicates transpose and superscript -1 indicates matrix inverse (assuming the inverse exists, which will be discussed in §4.5). This minimization leads to the well-known *weighted least-squares* estimator [see *Menke, 1984*],

$$\hat{\mathbf{m}} = (\mathbf{G}^T\mathbf{C}^{-1}\mathbf{G})^{-1}\mathbf{G}^T\mathbf{C}^{-1}\mathbf{d} . \quad (4.2.4)$$

The simplicity of this solution has great power, in that the maximum likelihood estimate may now be efficiently computed. For large problems, however, the construction of the "Gramm matrix", $\mathbf{G}^T\mathbf{C}^{-1}\mathbf{G}$, of the so-called "normal equations", in main computer memory remains prohibitive, therefore it is often necessary to resort to making *estimates* of the least-squares solution through the use of storage efficient procedures (e.g. conjugate gradients, §4.5).

4.3 Linearization of the Travel-time Equation

The travel time, t , of a seismic wave through an inhomogeneous but isotropic elastic solid may be calculated (in the high frequency approximation) with the line integral,

$$t = \int_{L_o} \frac{1}{v_o(\mathbf{r})} dl , \quad (4.3.1)$$

where $v_o(\mathbf{r})$ represents intrinsic seismic wave velocity, L_o defines a *ray path*, dl is an element of path length, and \mathbf{r} is a vector of spatial coordinates. *Ray paths* in an isotropic medium remain perpendicular to wavefronts and are, through *Fermat's Principle*, paths of stationary time. As a forward problem it is a simple matter to calculate the travel-time, t , knowing the velocity field and ray path but, unfortunately, we usually do not *a priori* know this path. In general the ray path must be computed numerically. There are many ways to formulate the ray path search, the most popular of which break into the two categories of *shooting* and *bending*. The former of these groups formulates the resulting set of differential equations as an initial value problem, while the latter solves the associated boundary value

problem [*Julian and Gubbins 1977, Appendix C*].

Since (4.3.1) is nonlinear (due to the fact that the path of integration depends on the integrand itself) we must resort to perturbation theory in order to form a set of linear differential equations suitable for inversion. First we define slowness, s , as

$$s_o(\mathbf{r}) = \frac{1}{v_o(\mathbf{r})} \quad (4.3.2)$$

in order to simplify the algebra of our problem. We then consider a second model, $s + \Delta s$, close to s , and the resulting travel time, $t + \Delta t$. Since a ray path represents a position of stationary time, by definition small perturbations in the ray path will produce only second order changes in the travel time, t . We may therefore, to first order, substitute the perturbed values into (4.3.1) without changing the path of integration, L_o . Using relation (4.3.2) and substituting in the perturbed values gives us,

$$t + \Delta t \approx \int_{L_o} (s_o(\mathbf{r}) + \Delta s(\mathbf{r})) dl . \quad (4.3.3)$$

Finally, subtracting (4.3.1) from (4.3.3) we arrive at a first-order linear relation between travel-time perturbations and slowness perturbations,

$$\Delta t \approx \int_{L_o} \Delta s(\mathbf{r}) dl . \quad (4.3.4)$$

In order to formulate this as a matrix equation we must first choose a suitable form to represent the slowness field, Δs , as a set of discrete parameters.

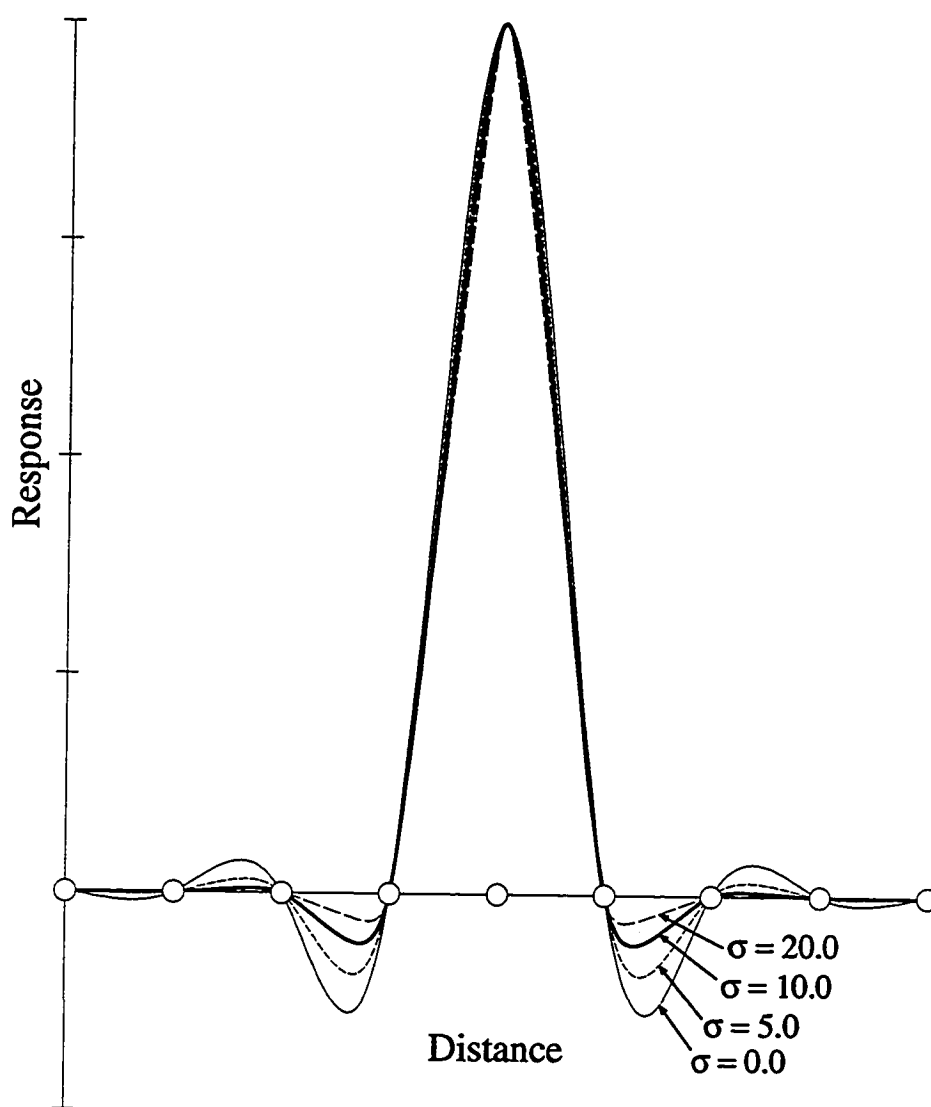
4.4 Parameterization

The parameterization we have chosen to represent the slowness is that of splines under tension constrained at a series of regular knots [*Cline, 1981*]. This interpolation scheme is achieved by first calculating a one-dimensional b-spline basis in each direction (r, θ, ϕ) and then the tensor product of this basis. Hermite interpolation coefficients are then calculated and stored for each knot so that interpolated values along with continuous first and second derivatives may be quickly obtained for any point within the grid (we require only first derivatives for our application). The tension of the splines is controlled through the parameter σ . A σ

equal to zero represents purely cubic spline interpolation and a large σ (e.g. 50) results in approximately tri-linear interpolation. A series of one-dimensional interpolation examples with various σ 's is shown in Figure 4.1 for a spike of unit magnitude at the central knot. In order to minimize the effect of negative side lobes and create the most localized possible interpolation (while at the same time producing a relatively smooth structure) a σ of 10.0 was chosen (heavy line in Figure 4.1).

The knots at which these splines are pinned are shown in perspective view in Figure 4.2 with each line crossings representing a knot position. There are 18 knots in depth, 25 in longitude, and 24 in latitude, resulting in a total of 10,800. The grid extends from sea level to 900 km depth with knots every 25 km in the first 150 km, every 50 km on down to 500 km, and every 100 km from 500 to 900 km. In latitude, knots are spaced every 1/3 of a degree from 44°N to 50°N, and every degree on down to 42°N and up to 53°N. In longitude, knots are spaced every 1/2 degree from 116°W to 125°W, and every 1 1/2 degrees on out to 128°W and back to 110°W.

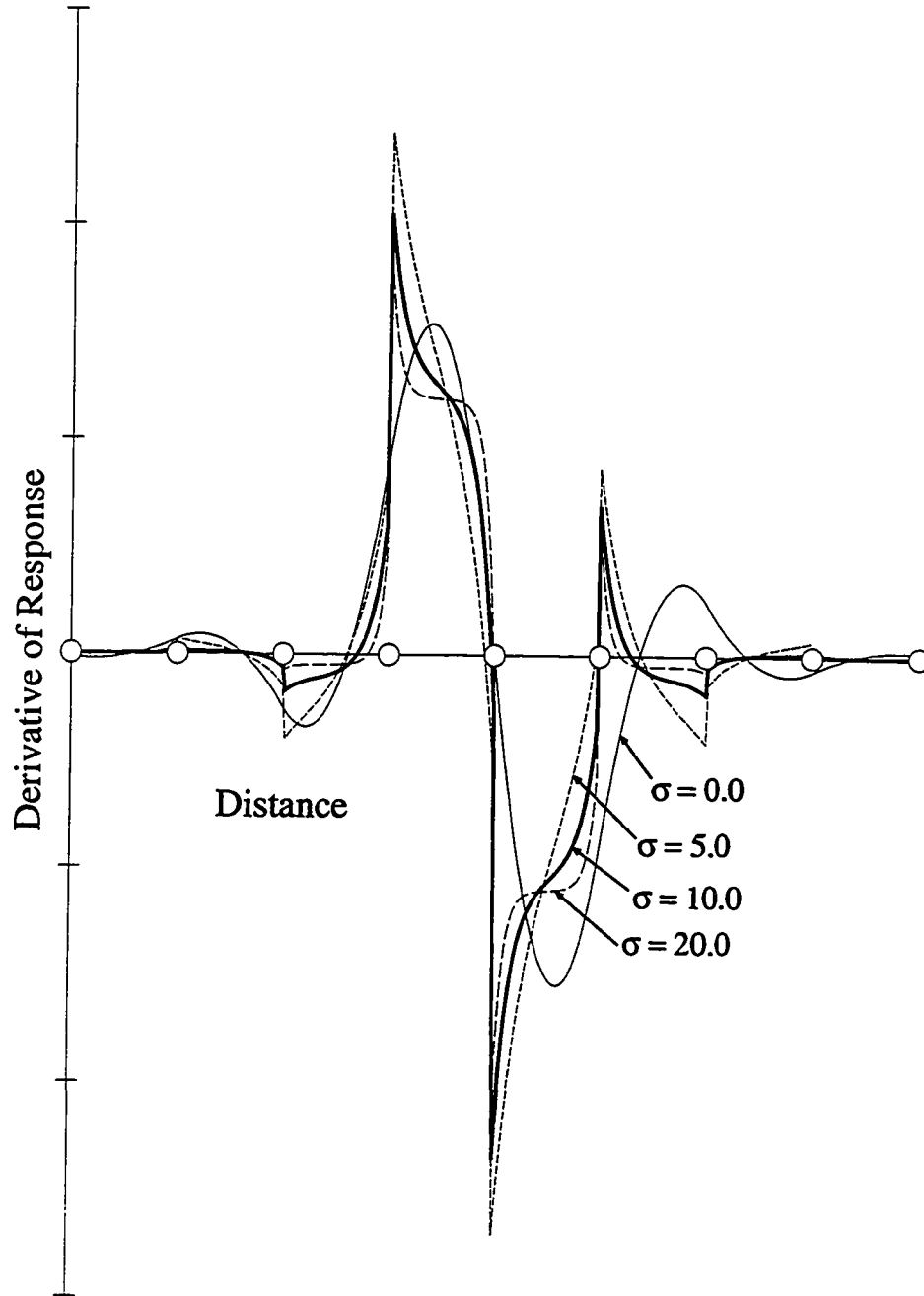
The central region outlined by darker lines on the surface (with projections out to the sides of the model region) is the portion of the model in which we expect to obtain appreciable resolution from the teleseismic data set. We will concentrate our analysis in Chapter 5 on this region. Our rationale for inverting for knots beyond this grid is twofold; for practical purposes it is necessary to smoothly damp both the three-dimensional slowness perturbations and their derivatives to zero at the edges of our model for three-dimensional ray tracing stability; also we wish to allow structure to fall outside of our region of resolution if the data are best fit by such models. While this may remove some structure from our model region that rightfully belongs there, we consider it preferable to forcing all possible outside structure into our model. In this regard we are already pushing ourselves toward models containing the minimum amount of structure necessitated by the data. We will follow this philosophy throughout the construction of our inverse problem. The outside knots (with the exception of the top layer) are therefore always forced to represent zero perturbation in order for the three-dimensionally varying model to smoothly merge into the outside radial Earth model. This is accomplished by heavily damping these parameters in the inversion process through the inclusion of an extra constraint equation, $\kappa\Delta s_i = 0.0$, for each i that represents an outside model element (where κ is a relatively large number compared to the scale of the other



(a)

Figure 4.1a,b One-dimensional example of (a) spline under tension interpolation and (b) its spatial derivative. The open circles represent knots constraining the splines. The tension that we use for our models is 10.0 (thick line).

Figure 4.1 (continued)



(b)

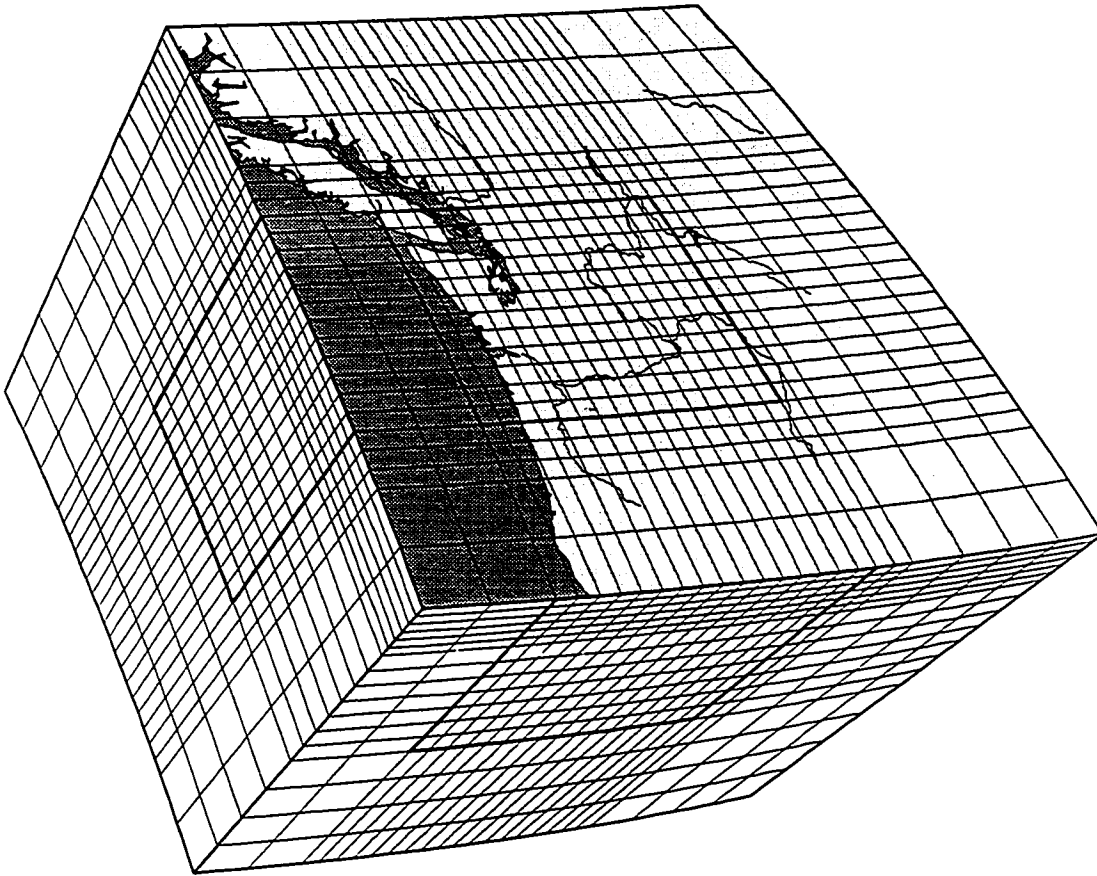


Figure 4.2 Three-dimensional perspective view of positions of knots which constrain the perturbation slowness model. Knots range in depth from 0 to 900 km, in latitude from 41 to 51 degrees and in longitude from 127 to 112 degrees East. See text for a more detailed description.

equations).

The functional values and Hermite interpolation coefficients corresponding to the slowness perturbation model (relative to the Herrin radial Earth model), are saved at knots in a spherical polar coordinate system (r, θ, ϕ) . Since the splines we use are relatively local and our grid spacing dense, the portion of the grid used for the interpolation of any given point spans a small angular distance and is therefore locally very close to a Cartesian system. We take advantage of this to use the efficient spline under tension package developed by *Cline* [1981] and capable of handling regular three-dimensional grids with variable spacing. The effect of this distortion varies over our grid depending on position and the relative distance between knots. For the central, high resolution, portion of our model the distortion in line lengths between a position directly in the center of a cell and the knots at opposite corners is 0.38 percent while at the lower corners of our model region it rises to 0.84 percent. Since this distortion is less than a percent over our grid its effect will be negligible compared to other errors, but to use the same interpolation scheme for a larger region (with correspondingly larger knot spacing) one would need to take the curvature into account. To do so could, however, negate one of the primary advantages of the method, its efficiency.

4.5 Inverse Problem Formulation

By inverting for structure beyond the region where we expect to obtain appreciable resolution, we are attempting to allow into our interior model only the minimum amount of structure required by the data. Since we have no reason to believe that there is *not* structure in this exterior region and since such structure could have an appreciable effect on the measured relative arrival times, inverting for only the interior portion could lead to the introduction of spurious structure. In a similar vein, we simultaneously invert for station parameters to compensate for local shallow structure and avoid projecting such short wavelength features into the long wavelength upper mantle model. We also invert for a relative arrival time correction for each event to account for first order uncertainties in event origin time and location, and large-scale velocity heterogeneities in the source region and lower mantle. Note that setting the mean of each event's relative arrival times to zero, as is often done [e.g. *Robinson and Iyer* 1981, *Achauer et al.* 1986, *Michaelson and*

Weaver 1986, Rasmussen and Humphreys 1988], is *not* justified since there is no reason to believe that arrivals from every angle will have zero mean residual. Setting the mean relative arrival times to zero is imposing an unnecessary and unwarranted *a priori* assumption (this assumption would presumably have less of an effect when modeling only shallow crustal structure).

The formulation of the un-weighted travel-time equation for the i^{th} ray is, [†]

$$P_{ij}^{(k-1)} \Delta s_j^{(k)} + h_r^{(k)} + e_q^{(k)} = \Delta t_i^{(k-1)} \quad (4.5.1)$$

where,

$$P_{ij}^{(k-1)} = \left[\frac{\partial t_i}{\partial s_j} \right]_{\mathbf{s} = \mathbf{s}^{(k-1)}} ,$$

$\Delta s_j^{(k)}$ = slowness perturbation to $\mathbf{s}^{(k-1)}$ at knot j ,

$h_r^{(k)}$ = time correction for station r at iteration k ,

$e_q^{(k)}$ = time correction for event q at iteration k , and

$\Delta t_i^{(k-1)}$ = travel-time residual for i^{th} ray relative to the $(k-1)^{\text{st}}$ model,

with r and q completely determined by i . The travel-time residuals are calculated as the difference between the measured relative arrival times obtained in the manner described in Chapter 3 and those predicted by ray tracing through the reference model, $\mathbf{s}^{(k-1)}$ (which will be discussed in §4.6). Since we allow for an un-damped mean time for each event through the inclusion of the e_q in (4.5.1) the starting mean of the residual times for each event is unimportant and is arbitrarily set to zero.

To this set of travel-time equations we then add constraints to regularize the inversion (this would be the identity matrix for the choice of simple damping, see Levenberg 1944, Marquardt 1963, Lawson and Hanson 1981). The quantity we have chosen to minimize is a 7-point finite element approximation to the Laplacian operator in order to penalize the roughness (second derivative) of our final slowness perturbation model [e.g. Menke 1984, Lees 1989, Lees and Crosson 1989]. To

[†] summation convention is always assumed for subscripted variables unless otherwise stated. Superscripted variable in parentheses represents iteration number and is never subject to implicit summation.

describe this operator we consider the vector \mathbf{f} to be the row of the regularization matrix \mathbf{F} associated with knot (h, i, j) in the polar coordinate system (r, θ, ϕ) . Subscripts to \mathbf{f} indicate the column associated with the subscripted model element. We then have, for the nearest neighbors to element (h, i, j) , (with no implicit summation)

$$f_{(h-1, i, j)} = \frac{-2}{(r_h - r_{h-1})(r_{h+1} - r_{h-1})}, \quad (4.5.2a)$$

$$f_{(h+1, i, j)} = \frac{-2}{(r_{h+1} - r_h)(r_{h+1} - r_{h-1})}, \quad (4.5.2b)$$

$$f_{(h, i-1, j)} = \frac{-2}{r_h^2 (\theta_i - \theta_{i-1})(\theta_{i+1} - \theta_{i-1})}, \quad (4.5.2c)$$

$$f_{(h, i+1, j)} = \frac{-2}{r_h^2 (\theta_{i+1} - \theta_i)(\theta_{i+1} - \theta_{i-1})}, \quad (4.5.2d)$$

$$f_{(h, i, j-1)} = \frac{-2}{r_h^2 \sin^2(\theta_i)(\phi_j - \phi_{j-1})(\phi_{j+1} - \phi_{j-1})}, \quad (4.5.2e)$$

$$f_{(h, i, j+1)} = \frac{-2}{r_h^2 \sin^2(\theta_i)(\phi_{j+1} - \phi_j)(\phi_{j+1} - \phi_{j-1})}, \quad (4.5.2f)$$

and for the element (h, i, j) itself,

$$f_{(h, i, j)} = - \left[f_{(h-1, i, j)} + f_{(h+1, i, j)} + f_{(h, i-1, j)} + f_{(h, i+1, j)} + f_{(h, i, j-1)} + f_{(h, i, j+1)} \right] \quad (4.5.2g)$$

with all other f equal to zero. This operator calculates distances in terms of spherical coordinates but calculates the Laplacian assuming that, locally, the system is close to being Cartesian. For the sizes of our knot spacing this is a small distortion. On the edges of our model this becomes the corresponding two-dimensional 5-point finite element operator (simply zero out the coefficients in the appropriate direction). For the case of equally spaced knots (with spacing Δ), $f_{(h, i, j)}$ would be equal to $\frac{6}{\Delta^2}$ with the values of its nearest neighbors equal to $\frac{-1}{\Delta^2}$. Note that this constraint is completely satisfied by any linear gradient and therefore only penalizes model roughness as defined by higher derivatives. *Constable et al.* [1987] appropriately term inversions with regularization such as this *Occam's inversion* in reference

to obtaining the least amount of model structure necessary to explain the data.

Our weighted system of linear equations at iteration k may now be written as

$$\begin{bmatrix} \mathbf{WP} & \mathbf{WH} & \mathbf{WE} \\ \lambda \mathbf{F} & \mathbf{0} & \mathbf{0} \end{bmatrix} \begin{bmatrix} \Delta \mathbf{s}^{(k)} \\ \mathbf{h}^{(k)} \\ \mathbf{e}^{(k)} \end{bmatrix} = \begin{bmatrix} \mathbf{W}\Delta \mathbf{t}^{(k-1)} \\ -\lambda \mathbf{F} \left\{ \sum_{i=0}^{k-1} \Delta \mathbf{s}^{(i)} \right\} \end{bmatrix}, \quad (4.5.3)$$

where,

$$W_{ij} = \begin{cases} \frac{1}{\sigma_i^{res}} & \text{if } i = j \\ 0 & \text{if } i \neq j \end{cases} \quad n \times n \text{ matrix,}$$

$$H_{ir} = \begin{cases} 1 & \text{if ray } i \text{ was recorded at station } r \\ 0 & \text{otherwise} \end{cases} \quad n \times (\# \text{ station}) \text{ matrix,}$$

$$E_{iq} = \begin{cases} 1 & \text{if ray } i \text{ originated from earthquake } q \\ 0 & \text{otherwise} \end{cases} \quad n \times (\# \text{ event}) \text{ matrix,}$$

$$F_{ij} = \begin{cases} \delta_{ij} & \text{for simple damping} \\ filter_{ij} & \text{otherwise} \end{cases} \quad m \times m \text{ matrix,}$$

λ = weight of damping or smoothing, n = number of rays, and m = number of model knots. A $\mathbf{0}$ in (4.5.3) represents a null matrix of appropriate size. The σ_i in the weighting matrix are determined via the multi-channel cross correlation procedure of arrival time estimation described in Chapter 3.

The Laplacian operator, \mathbf{F} , minimizes the roughness of the *final* model by setting the right hand side of (4.5.3) equal to the negative roughness of the previous model's perturbations (or to the previous model if we wish to smooth the entire model rather than the perturbations). The constraint imposed for smoothing the final *total* model at iteration k is obtained by setting the roughness of the model (weighted by λ) equal to zero. We therefore have

$$\lambda \mathbf{F} \mathbf{s}^{(k)} = 0 \quad (4.5.4a)$$

or, since $\mathbf{s}^{(k)} = \Delta \mathbf{s}^{(k)} + \mathbf{s}^{(k-1)}$,

$$\lambda \mathbf{F}(\Delta \mathbf{s}^{(k)} + \mathbf{s}^{(k-1)}) = 0 . \quad (4.5.4b)$$

Using the distributive property of the linear operator and rearranging gives

$$\lambda \mathbf{F} \Delta \mathbf{s}^{(k)} + \lambda \mathbf{F} \mathbf{s}^{(k-1)} = 0 , \quad (4.5.4c)$$

and

$$\lambda \mathbf{F} \Delta \mathbf{s}^{(k)} = - \lambda \mathbf{F} \mathbf{s}^{(k-1)} . \quad (4.5.4d)$$

To smooth the final *perturbation* from $\mathbf{s}^{(0)}$ we similarly have

$$\lambda \mathbf{F} \sum_{i=0}^k \Delta \mathbf{s}^{(i)} = 0 , \quad (4.5.5a)$$

or, since $\sum_{i=0}^k \Delta \mathbf{s}^{(i)} = \Delta \mathbf{s}^{(k)} + \sum_{i=0}^{k-1} \Delta \mathbf{s}^{(i)}$,

$$\lambda \mathbf{F} (\Delta \mathbf{s}^{(k)} + \sum_{i=0}^{k-1} \Delta \mathbf{s}^{(i)}) = 0 . \quad (4.5.5b)$$

Once again applying distributivity and rearranging (4.5.5b) becomes

$$\lambda \mathbf{F} \Delta \mathbf{s}^{(k)} + \lambda \mathbf{F} \sum_{i=0}^{k-1} \Delta \mathbf{s}^{(i)} = 0 , \quad (4.5.5c)$$

and

$$\lambda \mathbf{F} \Delta \mathbf{s}^{(k)} = - \lambda \mathbf{F} \sum_{i=0}^{k-1} \Delta \mathbf{s}^{(i)} , \quad (4.5.5d)$$

which we have used in (4.5.3). An iterative inversion that smooths the total model through the addition of constraints such as in (4.5.4) has been termed a "jumping" procedure by *Shaw* [1986] [c.f. *Shaw and Orcutt* 1985, *Chapman and Orcutt* 1985, *Constable et al.* 1987, and *Sambridge* 1990] as opposed to a "creeping" procedure that simply constrains perturbations relative to the previous iteration's result. By constraining the final model (or the final perturbation model) to be smooth we are allowing roughness that may be introduced at early iterations of the inversion procedure to be eliminated if our improved knowledge of the partial derivative matrix \mathbf{P} is consistent with such a model. Conversely, if we had only constrained the perturbations to the previous iteration to be smooth, we may retain unnecessary roughness in our final model.

In a trivial sense (4.5.3) is still singular since we may add an arbitrary constant to all earthquake time corrections if we simply subtract the same constant from all station time corrections. We alleviate this by arbitrarily adding a constraint to set the mean of the station time corrections to zero. Although portions of the model space may be over-constrained by the unregularized system (4.5.1), large sections may also be under-constrained. There is no reason, however, to reduce our parameterization when we can increase the rank of our system through regularization such as we have described above. Such regularization can provide a much more intuitive and flexible constraint than under-parameterization. The addition of F in (4.5.3) creates a system of rank n and allows us to potentially obtain its least squares solution (to within the numerical stability of our inversion procedure). For subsequent discussion we will represent the system of (4.5.3) symbolically as

$$\tilde{\mathbf{A}}\mathbf{x} = \tilde{\mathbf{b}}, \quad (4.5.6)$$

where,

$$\tilde{\mathbf{A}} = \begin{bmatrix} \mathbf{WP} & \mathbf{WH} & \mathbf{WE} \\ \lambda\mathbf{F} & \mathbf{0} & \mathbf{0} \end{bmatrix}, \quad \mathbf{x} = \begin{bmatrix} \Delta s^{(k)} \\ \mathbf{c}^{(k)} \\ \mathbf{e}^{(k)} \end{bmatrix}, \quad \text{and } \tilde{\mathbf{b}} = \begin{bmatrix} \mathbf{W}\Delta t^{(k-1)} \\ -\lambda\mathbf{F}\left\{\sum_{i=0}^{k-1} \Delta s^{(i)}\right\} \end{bmatrix}, \quad (4.5.7)$$

and the covariance of the new 'data' vector $\tilde{\mathbf{b}}$ is assumed to be the identity operator times a scalar. We will also reference a form of (4.5.6) that is not regularized (i.e. where $\lambda = 0$) as \mathbf{A} and \mathbf{b} where then

$$\mathbf{A} = \begin{bmatrix} \mathbf{WP} & \mathbf{WH} & \mathbf{WE} \\ \mathbf{0} & \mathbf{0} & \mathbf{0} \end{bmatrix} \quad \text{and} \quad \mathbf{b} = \begin{bmatrix} \mathbf{W}\Delta t^{(k-1)} \\ \mathbf{0} \end{bmatrix}. \quad (4.5.8)$$

Obtaining the least-squares solution to equation (4.5.6) in a straight-forward fashion would require a prohibitive amount of computer memory. This is due to the fact that, although the matrix $\tilde{\mathbf{A}}$ is sparse (few of its elements are non-zero), the matrix $\tilde{\mathbf{A}}^T\tilde{\mathbf{A}}$ is relatively dense. Therefore, in order to take advantage of the sparseness of (4.5.3), we will turn to a method of solution that can act directly on $\tilde{\mathbf{A}}$ and that does not require the storage of the entire matrix (such as the method of singular value decomposition does). The conjugate gradient method we use was originally developed for the solution of large sparse systems by *Hestenes and Stiefel* [1952].

Golub and Van Loan [1983], and *Scales* [1987] provide reviews of its derivation and use. In one form or another the method of conjugate gradients is widely used at present to solve large geophysical inverse problems (the LSQR algorithm of *Paige and Saunders* [1982] being a popular derivative of the method [see *Nolet* 1987]). The convergence of the method of conjugate gradients to the least-squares solution is discussed in *Golub and Van Loan* [1983].

In all of the inversions that we discuss in this thesis, we have performed 500 iterations of the conjugate gradient procedure. We have found that, for our problem, the solution has converged (i.e. the model is no longer significantly changing) after 200-300 iterations. We have occasionally performed up to 2000 iterations and found that there is negligible change beyond approximately 300. The 500 iterations we regularly perform consume only 5 minutes of CPU time (on an IBM 3090 3E), so it is economical to invert for many different models (e.g. with various levels of regularization) for a given partial derivative matrix, \mathbf{P} .

There are several features that make the conjugate gradient procedure particularly attractive. We are able to calculate iterations recursively and therefore do not need to store information from all previous iterations, only the preceding. Also, the only operations required are matrix-vector and vector-vector products. First of all, this limits memory requirements for we do not have to save the previous direction vectors nor even store the entire matrix $\tilde{\mathbf{A}}$ (since for the matrix-vector products we may take advantage of sparse matrix techniques and only store its non-zero elements). Also, due to the lack of matrix-matrix products and the sparseness of $\tilde{\mathbf{A}}$ the number of necessary multiplications is limited.

To take advantage of the sparseness of $\tilde{\mathbf{A}}$ we simply need to supply an algorithm for multiplying only non-zero elements when performing matrix-vector products in the above algorithm. This may be accomplished with the use of only a small amount of memory by storing the non-zero elements of $\tilde{\mathbf{A}}$ in a vector along with one integer vector representing the number of non-zero elements in each row and one to keep track of the column position of each non-zero element. It is then a simple matter to avoid multiplication by zero.

4.6 Iterative Procedure

As described in §4.5, while the system (4.5.3) is linear, it depends on our knowledge of the matrix of partial derivatives \mathbf{P} , and therefore an iterative improvement of this aspect of our problem may be necessary. Our initial estimate of \mathbf{P} comes from our knowledge of the ‘average’ radial velocity structure of the Earth. There are several models commonly used in seismological studies of travel times (e.g. *Jeffreys and Bullen* [1940], *Herrin* [1968], *Dziewonski and Anderson* [1981]) but for our purposes of investigating only rays at teleseismic distances ($\Delta > 25^\circ$) the differences are not severe. To be consistent with both previous studies in the region [*Michaelson and Weaver* 1986, *Rasmussen and Humphreys* 1988] and our choice of searching for a *smooth* model to fit our data we have chosen the smooth Herrin model (which contains no mantle velocity discontinuities, but does contain a Mohorovicic discontinuity at 40 km depth) to represent our reference model. The shallow discontinuities have little effect on our models since all the rays traverse this region nearly vertically and we allow for each event to have an arbitrary mean arrival time. We therefore construct our initial \mathbf{P} matrix from this model by calculating the effect of the model perturbation parameters on the rays traveling through the radial structure. We already know the correct take off angle and azimuth for these rays for the radial Earth model, so the determination of the partial derivative matrix is the only numerically intensive procedure necessary for the first iteration of our procedure.

The first step in calculating the matrix of partial derivatives is to determine which knots appreciably affect each ray. Since our spline under tension interpolation scheme acts on a relatively local scale (see Figure 4.1) any knots more than two grid intervals away from a given interpolation point have little effect on the interpolated value. We tabulate the knots that affect a given ray by shooting the ray through the three-dimensional structure, at each integration step switching ‘on’ all knots within two grid intervals of that position (of course, at any given step, many of these 64 nearest knots will have already been switched on at previous steps). We also keep track of the linearly interpolated position (r, θ, ϕ) between each integration step and the distance between the steps. This then allows us to approximate the travel time along a ray path as a simple dot product between the

lengths of these straight line segments and the velocities at the center points. We use an integration step of approximately 2.0 sec so that these straight line segments match closely the true ray path. In any case, to obtain partial derivatives it is differential times that we are interested in (as discussed below) and we have found that the errors produced with this level of time step are on the order of 0.01 sec. The calculation of partial derivatives is a computationally intensive procedure so we do not wish to integrate with time steps any smaller than necessary.

After accumulating both the ray-path parameters and the knots affecting each ray (on the order of 300-500 knots are identified as possibly contributing to each ray's travel time), we then begin our calculation of partial derivatives by working through all 10,800 knots (column-wise):

- we perturb the slowness at a single knot (with an arbitrary perturbation),
- calculate the spline coefficients for the resulting new slowness structure,
- perform the dot-product between the previously calculated ray lengths and the interpolated values at the tabulated ray positions for all rays affected by this knot,
- subtract the perturbed time from the unperturbed (calculated from the same ray lengths and positions, through the un-perturbed model),
- divide the time-difference by the slowness perturbation to obtain the estimated partial derivative, and
- save the partial derivative if its magnitude is greater than 0.05 (i.e. $\frac{\partial t}{\partial s} > 0.05$ km. This value would correspond to 'ray length' in a block inversion).

Approximately 50% of the potentially significant partial derivatives have magnitudes exceeding this limit which corresponds to a knot in the center of our model being 'hit' along approximately 0.1% of its region of influence. This method is substantially more efficient than acting on single rays at a time (a row-action procedure) since the time to calculate the spline coefficients for each new model is approximately the same as performing 40 of the above partial derivative calculations.

Given the partial derivative matrix and travel times for each ray from the Herrin radially symmetric Earth model [Herrin 1968] we can now proceed to implement the inversion procedure as described in §4.5. The slowness perturbation model obtained from this inversion, $\Delta s^{(1)}$ can then be added to the radial slowness

model $s^{(0)}$ in order to perform a further iteration of this process. Now that the new 'reference model', $s^{(1)}$, is no longer radially symmetric, we must perform three-dimensional ray-tracing in order to locate the correct ray paths through this slowness field. Our solution to the two-point ray tracing problem is adapted from a method developed by K. C. Creager [Creager 1984, Creager and Jordan 1984] using a ray shooting algorithm developed and coded by B. R. Julian [Julian and Gubbins 1977]. We have altered these procedures for our fully three-dimensional problem, incorporating spline under tension interpolation and several minor adjustments but, in essence, the methods are identical. A review of this process is given briefly in Appendix C and in detail by Creager [1984]. We do not perform three-dimensional ray tracing for the 517 rays (5.6% of the total) that are associated with core phases ($PKIKP$ and PKP_{BC}) due to the difficulty of obtaining correct ray paths for these phases. We do include these rays at each iteration, but do not improve our estimates of ray paths. We have found that our inversions are not highly sensitive to the inclusion or exclusion of these rays, due in part to the general lower quality of the arrival-time estimates associated with them (and therefore the down-weighting of these equations in the inversion process) and also to fact that events at distances of 80-90 degrees (of which there are many, see Figure 2.2) also result in ray paths traveling at high angles through our model region.

The iterative nature of this process was illustrated in the lower half of the chart in Figure 1.6. To summarize this iterative process we:

- (1) obtain ray paths and travel times with three-dimensional ray tracing,
- (2) calculate partial derivatives empirically, and
- (3) invert the resulting system of equations, with smoothing constraints, to produce the next solution approximation.

These steps are repeated until the new ray paths are no longer substantially changing. Since Fermat's principle tells us that travel times are relatively insensitive to first order deviations in ray paths, we expect that only a few iterations will be necessary to obtain ray paths close to being self-consistent with the travel-time data. The ray paths may still be far from being the 'true' ray paths, but since travel times are not sensitive to relatively large deviations of these paths, the best that we can hope to find are rays that are internally consistent with our resulting models. This, therefore, is what we mean when we speak of the *convergence* of our non-linear procedure.

Chapter 5

Inversion Results for the Cascadia Subduction Zone

5.1 Introduction

In this chapter we examine the results of applying the theory of Chapters 3 and 4 to the teleseismic data set compiled on the Washington Regional Seismic Network (described in Chapter 2). First, in §5.2, we estimate the inherent resolution capabilities of the data set both for the standard purely linear problem (i.e. assuming the radial earth ray paths are correct) and including possible biases due to our incomplete knowledge of an appropriate starting model (i.e. performing full three-dimensional ray tracing in the forward problem). We examine not only the standard resolution estimates of single model parameters, but also the resolution capabilities of the data set for a more complicated model (a phantom model of a subducting slab) where non-linearities are likely to become important.

In §5.2.1 we examine examples of the ray distribution and the spatial density of rays. These will be used to help us interpret the origin of resolution variation across the model. Then, in §5.3, we traverse a series of inversions beginning with the first iteration 'linear' model UW91F1, and proceeding on through the third iteration model UW91F3. At each level we will sample a series of models obtained with varying degrees of regularization (smoothness) in order to decide which features of the model are most robust and therefore required by the data. Since our resolution varies significantly across the region modeled, the optimum trade-off parameter or level of regularization will vary also. In lieu of presenting models which have such a variation as a function of position, we will examine several models with constant levels of regularization realizing that no one level is optimum for the entire model.

Throughout this chapter we will be viewing series of cross sections taken at positions of equal latitude. They contain no vertical exaggeration but are slightly distorted due to being square images of slightly trapezoidal regions. This effect also changes slightly with latitude across the different model images. These viewing distortions are slight and do not effect our interpretations. We will, at times, plot sections through the entire model but usually concentrate on the interior region where our resolution is highest. These regions were delineated in Figure 4.2 and

the rationale for inverting for model elements beyond this interior is discussed in §4.3. The second type of image we examine will be cross-sections through the model at equal depth. For reference, we superimpose on these plots a map of features present at the Earth's surface at the same latitude and longitude (coastlines and major rivers) and also contours of shallow slab structure described in §1.3.1 (first shown in Figure 1.4).

5.2 Resolution Analysis

When solving problems of the type

$$\mathbf{Ax} = \mathbf{b} \dagger \quad (5.2.1)$$

through least-squares, the means of relating our model estimate, $\hat{\mathbf{x}}$, to the 'truth', \mathbf{x} , is through the relation

$$\hat{\mathbf{x}} = \mathbf{G}^{-1}\mathbf{Ax} = \mathbf{Rx} \quad (5.2.2)$$

where \mathbf{G}^{-1} is known as the *generalized inverse* [e.g. Menke 1984]. \mathbf{R} , the *resolving kernel*, may be viewed as the window or filter through which we, in the best case, view the 'truth.' The generalized inverse replaces $(\mathbf{A}^T\mathbf{A})^{-1}\mathbf{A}^T$ since this inverse in general does not exist (i.e. $\mathbf{A}^T\mathbf{A}$ is usually singular). We could obtain the generalized inverse by performing a singular value decomposition of \mathbf{A} but this would require the storing of a prohibitively large matrix in main computer memory and therefore a prohibitively large amount of computer time. Another way of obtaining a *pseudo-inverse* is to regularize \mathbf{A} through the addition of auxiliary constraints as in (4.5.3) (the regularized system we have simply termed $\tilde{\mathbf{A}}$). For this new system we then have,

$$\hat{\mathbf{x}} = (\tilde{\mathbf{A}}^T\tilde{\mathbf{A}})^{-1}\tilde{\mathbf{A}}^T\mathbf{Ax} = \tilde{\mathbf{R}}\mathbf{x}, \quad (5.2.3)$$

where $\tilde{\mathbf{R}}$ represents the resolution kernel for our regularized system. Unfortunately, since we never form the inverse in (5.2.3), we cannot directly compute $\tilde{\mathbf{R}}$. It is clear, however, that if we were to replace \mathbf{x} in (5.2.3) with a spike (i.e. set $\mathbf{x} = \mathbf{I}_i$, where \mathbf{I}_i is the i^{th} column of an $n \times n$ identity matrix), we would then retrieve in

† The terminology of this section as it relates to our inverse problem formulation is given in §4.5. Basically the travel-time equations without regularization are represented as \mathbf{A} , and with regularization as $\tilde{\mathbf{A}}$.

$\hat{\mathbf{x}}$ the i^{th} column of the resolution matrix, $\tilde{\mathbf{R}}_i$. If we now write (5.2.3) as

$$\tilde{\mathbf{R}}_i = (\tilde{\mathbf{A}}^T \tilde{\mathbf{A}})^{-1} \tilde{\mathbf{A}}^T \mathbf{A} \mathbf{I}_i, \quad (5.2.4)$$

or equivalently,

$$\tilde{\mathbf{A}}^T \tilde{\mathbf{A}} \tilde{\mathbf{R}}_i = \tilde{\mathbf{A}}^T \mathbf{A} \mathbf{I}_i, \quad (5.2.5)$$

we then have a form amenable to our conjugate gradient procedure (see §4.5). We would need to perform this operation n times (once for each model element) in order to construct the entire resolution matrix, but since we do not expect the resolution to vary dramatically over nearby elements, we can obtain what information we desire by skipping over several knots at a time. Also, if the spiked knots are sufficiently separated, we may assume that to first order they are non-interfering, and therefore solve for multiple spikes simultaneously. This will be illustrated in §5.2.2.

The preceding was based on the assumption that the system is, for practical purposes, linear. To test the resolvability of structures which *do* significantly deflect ray paths, however, we must perform the forward problem properly in order to achieve meaningful results. In deriving (5.2.2) we simply started with our formula for the least-squares estimator, $\hat{\mathbf{x}} = (\tilde{\mathbf{A}}^T \tilde{\mathbf{A}})^{-1} \tilde{\mathbf{A}}^T \mathbf{b}$, and substituted for \mathbf{b} with our original set of linear equations, $\mathbf{b} = \mathbf{A} \mathbf{x}$. But now consider if our *a priori* assumption of the partial derivative matrix \mathbf{P} (and therefore \mathbf{A}) was incorrect, and a different operator was more representative of the true forward problem (i.e. the correct ray paths). In order to obtain this new operator to test this effect, we must ray trace through each model of interest in order to locate the correct ray paths. For models such as \mathbf{I}_i , with sufficiently small-scale perturbations, the ray bending should be minimal and therefore the standard linear resolution estimate is valid and useful. If, however, the models which we seek are *not* isolated spikes of energy, we then should test the linearity of our problem to make sure that estimates of linear resolution are in fact useful.

Models in which we do need to worry about non-linearity becoming important (i.e. the true ray paths being *very* different from those initially assumed) are ones which contain structure which has strong coherent velocity gradients perpendicular or sub-perpendicular to the ray paths. This has been found to be the case, for instance, in borehole tomography experiments [Stork, 1988] and also in the

dependence of regional ray paths on reference velocity model [e.g. *van der Hilst and Spakman* 1989, *Zielhuis et al.* 1989]. In our case, we have ray paths traversing a subducting slab (presumably cold, fast material). Rays traveling in a direction sub-parallel and near to the slab sense strong lateral gradients in velocity and therefore may diverge far from their associated radial Earth model trajectories. In order to test the effect that such a structure would have on a linear inversion we simply need to substitute a suitable velocity model of a subducting slab into (5.2.5) for I_i . This is done by performing full three-dimensional ray tracing through the synthetic model to obtain realistic estimates of travel times that such a model would produce. The results of this exercise for a simple slab model are explored in §5.2.3 along with the results that would have been obtained with a purely linear resolution experiment.

Since, for a given data variance (and therefore optimal smoothing weight), the resolution is completely determined by the distribution of ray paths, it is instructive to study both the ray number density and distribution of rays within a given region (i.e. the degree to which there are crossing paths). We will turn to this topic in the following section.

5.2.1 Ray Distribution

Since the resolution of a travel-time inversion is heavily dependent on ray distribution, investigators have often turned to ray number density [e.g. *Spakman* 1988, *Spakman and Nolet* 1988, *Sambridge* 1990], and higher order moments characterizing local ray directions [e.g. *Kissling* 1988, *Lees* 1989] to quantify which parts of the model are to be believed and where smearing of structure is likely to occur. For the data set described in Chapter 2 we will examine the ray number density (number of rays per volume) in the following figures. We plot this parameter in Figures 5.1*a* for the Herrin radial Earth model (used as a reference throughout this work), and for the three-dimensionally varying model, UW91F2 (with a regularization of 3200), in Figure 5.1*b* (model UW91F2 will be discussed in detail in §5.3).[†]

The difference between the ray distributions resulting from the two models is not dramatic and therefore the interpretation of the spatial variation of resolution is

[†] latitudinal cross-section plots are described in §5.1.

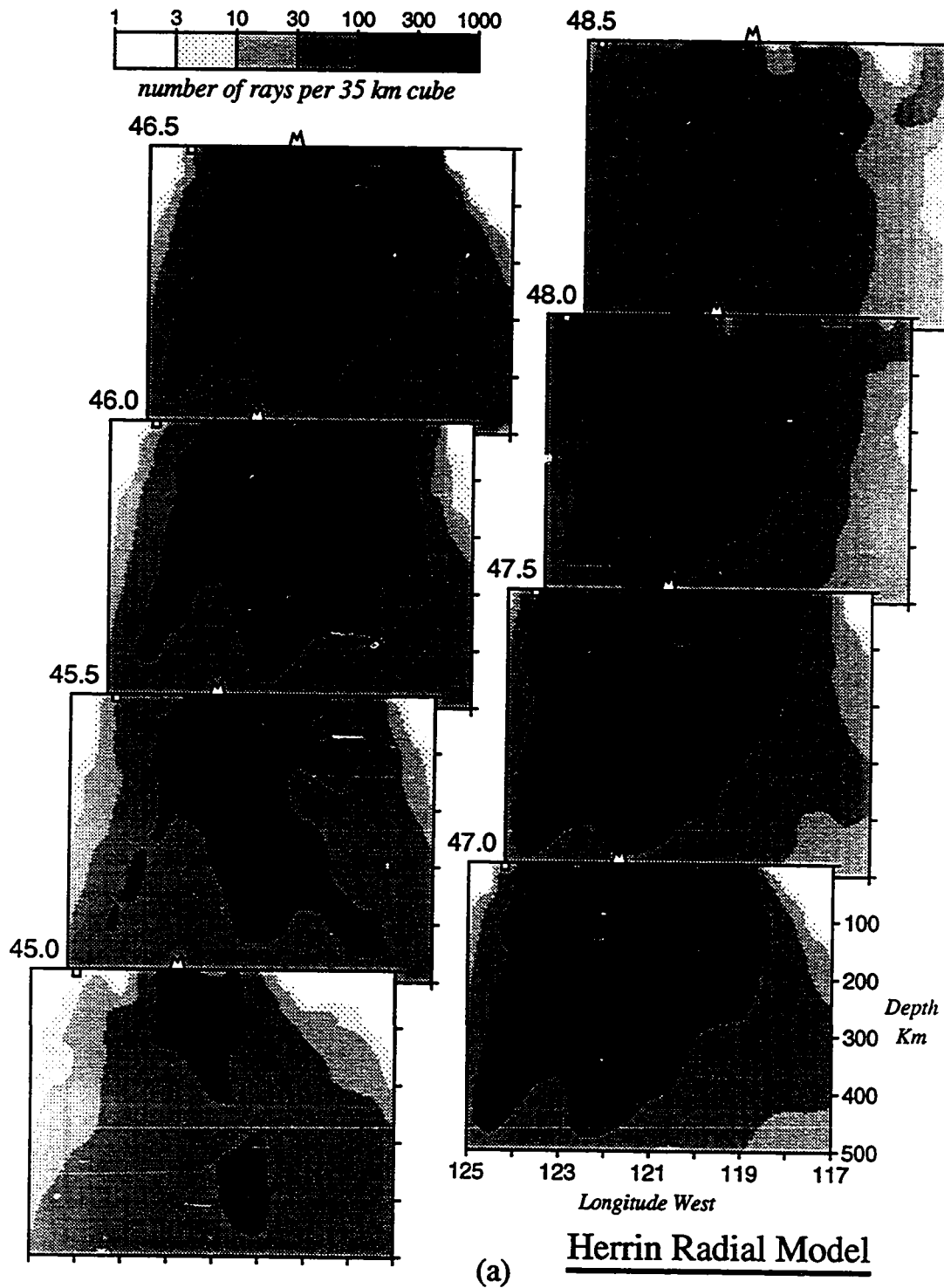
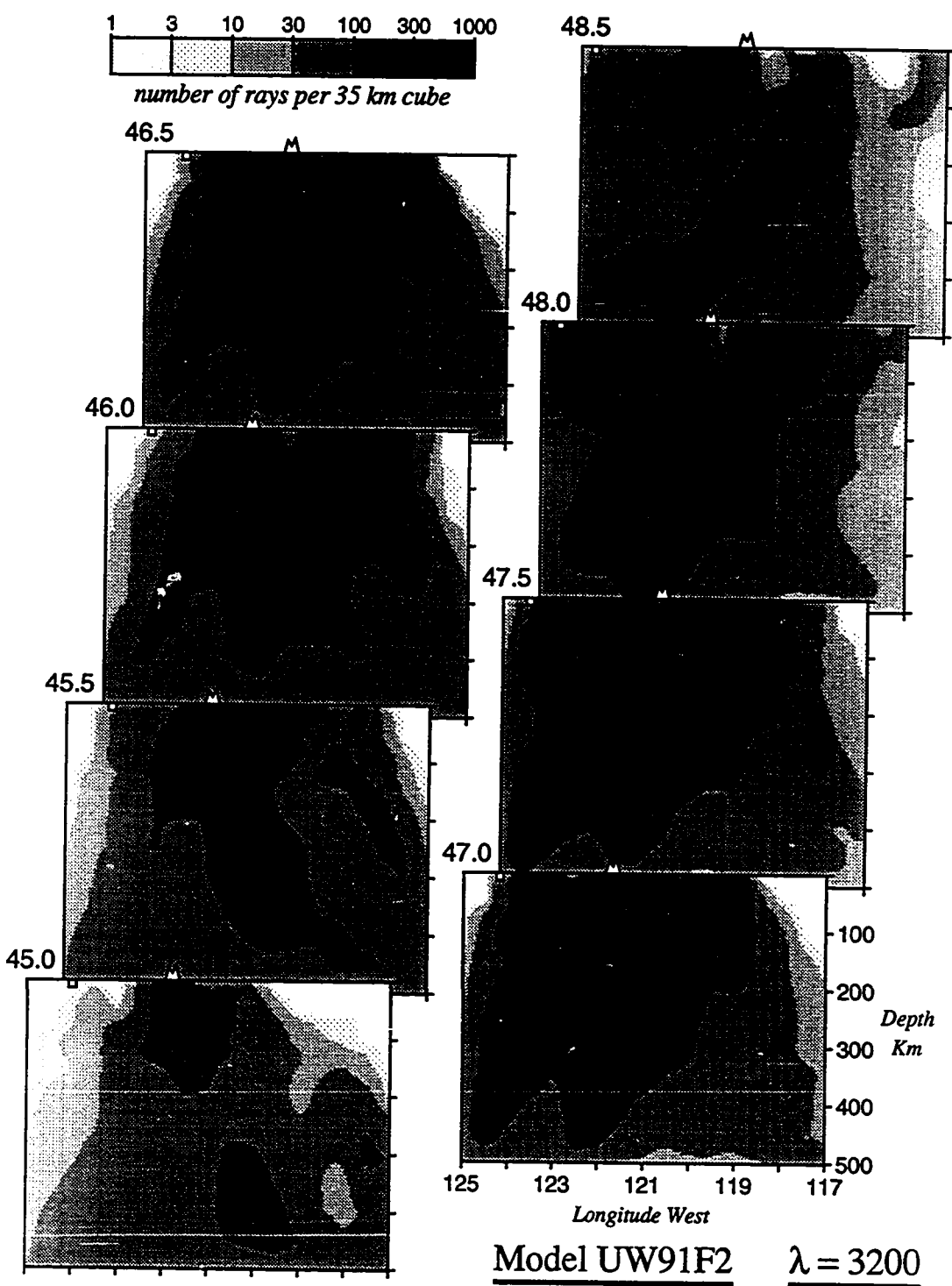


Figure 5.1a,b Constant latitude slices of ray density for (a) radially symmetric Herrin model and (b) model UW91F2 obtained from nonlinear travel-time inversion. See text for interpretation.

Figure 5.1 (continued)



(b)

not critically dependent on the use of the correct ray paths. This is not to say, however, that the model itself is not dependent on obtaining correct rays paths. The rays are unusually well distributed compared to those in most tomography experiments and, in particular, experiments in subduction zone environments [e.g. *Spakman and Nolet* 1988, *Zhou* 1990, *Zhou and Clayton* 1990]. This arises from the fact that the events used all lie outside the model region and therefore are not clustered along fault zones (Wadati-Benioff zones in the case of subduction zones). Model UW91F2 has a 2% loss rays due to the ray-tracing procedure (Appendix C).

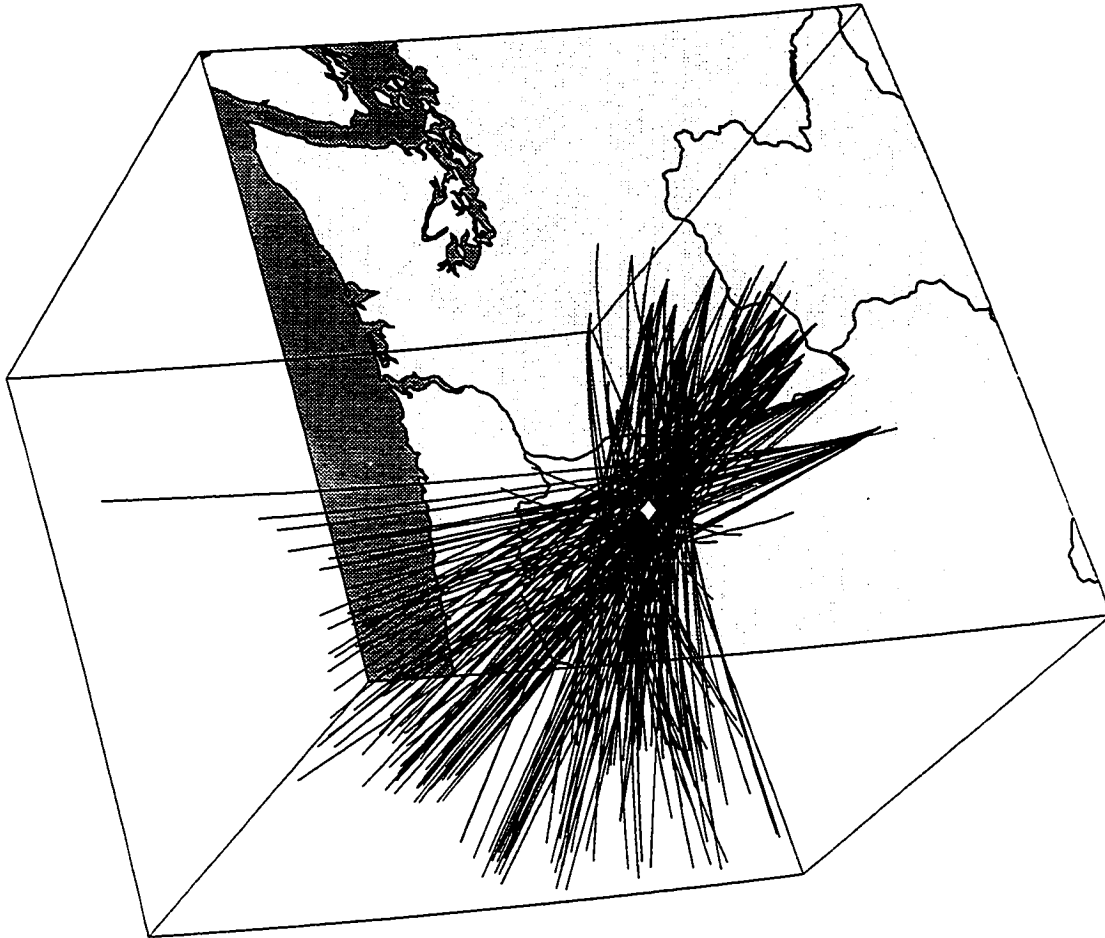
In Figures 5.2a-c we plot in perspective view all rays which effect a given knot at several key positions. The rays are only plotted within the region of relatively high resolution to give a more detailed view of their distribution and only rays which have a 2 km or greater effective ray length in the region of the knot are shown. The effective ray length is determined by the partial derivative (P_{ij}) associated with each ray and knot (in inversions employing block parametrization these partial derivatives are simply the ray length within each block). Although it is sometimes difficult to observe individual ray positions in detail, we can quite easily discern whether or not a region is well covered by crossing rays. We will refer back to these plots when analyzing our ability to resolve key features of our models, but from examining this figure alone we can expect to be able to reasonably well resolve features at each of these knots.

5.2.2 Spike Resolution Test

As discussed above, linear resolution estimation may be made through the following process:

- create an artificial or *phantom* slowness perturbation model (Δs_{spike}) with ‘spikes’ sufficiently separated to avoid overlap,
- simulate travel-time anomaly data through the operation $\Delta t_{spike} = \mathbf{A}\Delta s_{spike}$ with \mathbf{A} the matrix of partial derivatives associated with the reference slowness model,
- invert the constrained system of (4.5.3) with Δt_{spike} substituted for the real data vector Δt .

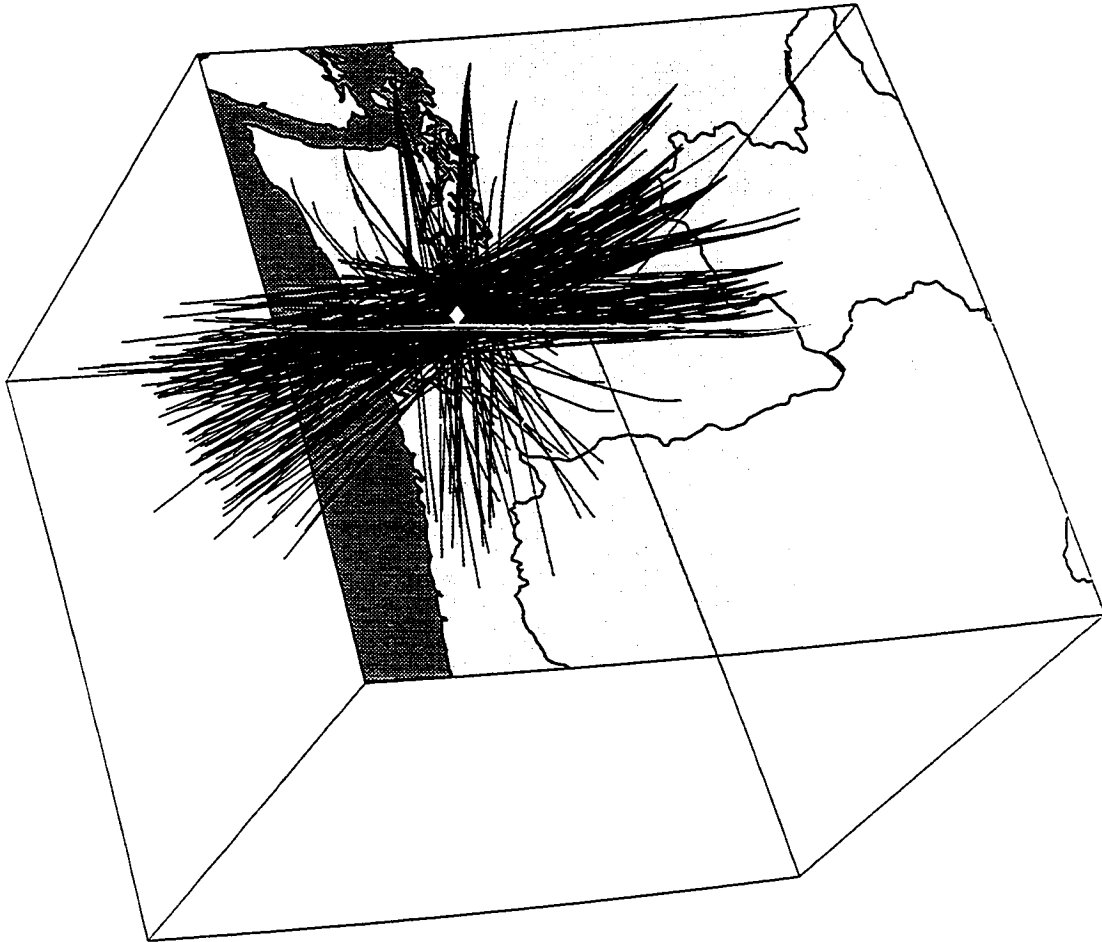
Whereas this process will produce an estimate of the resolution kernel defined in equation (5.2.4) it is a ‘best-case scenario’ in that, not only are we assuming that



Model UW91F2 $\lambda = 3200$

(a)

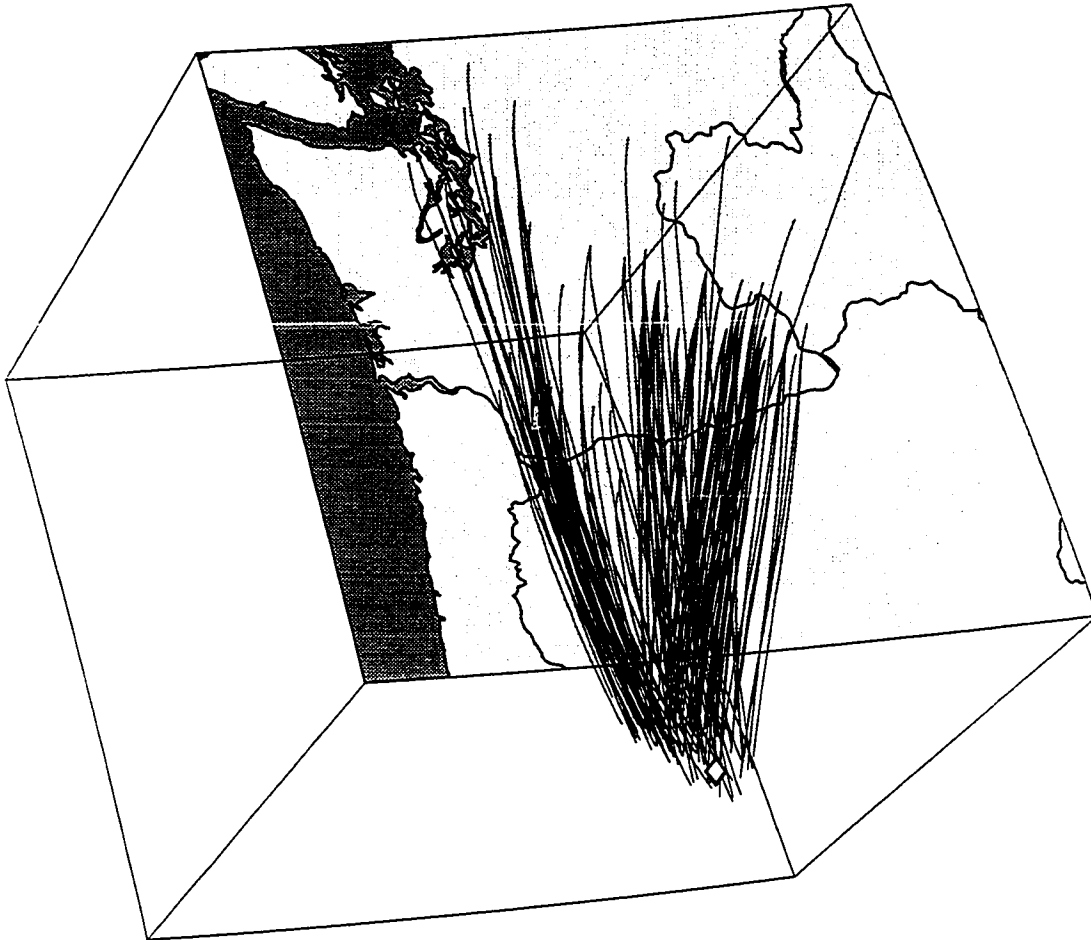
Figure 5.2a-c A plot of all rays which significantly effected the node at (a) 46N, 120E and 200 km depth (197 rays), (b) 48N, 121E, and 250 km depth (269 rays) and (c) 45N, 118E, and 500 km depth (155 rays). The open diamond represents the position of each node. Rays which had the effect of a 2 km or greater 'ray length' in the region of the knot are plotted.

Figure 5.2 (continued)

Model UW91F2 $\lambda = 3200$

(b)

Figure 5.2 (continued)



Model UW91F2 $\lambda = 3200$

(c)

there are no errors in our ‘theory’ (e.g. that ray theory and our parameterization are adequate), but also no errors in our data. We can take a step toward making this exercise more realistic by adding noise to the simulated data [e.g. *Spakman* 1988]. This can be accomplished at no extra cost, and gives us a better idea of what the sensitivity of the model is to a more realistic data structure. Although the true noise structure is, no doubt, not purely Gaussian (and perhaps more importantly not independently distributed), we will limit ourselves to adding only normally distributed error to our simulated data. This is an area where more research is certainly warranted.

Shown in Figure 5.3a is the entire phantom model of Δs_{spike} which we will use for purposes of discussion. Spikes which are 5% fast are located every degree in latitude, every one and a half degrees in longitude, and every third knot in depth (see Figure 4.2 for knot distribution). Being single knot spikes, these are then the smallest feature which can be imaged by this parameterization. We have inverted for many such structures (both with single and multiple spikes) and found our interpretation of all to be similar. By performing the analysis on multiple spikes we tend to achieve a somewhat pessimistic resolution estimate for any given knot due to tradeoffs with the static station and event parameters. It is, however, not a strong effect for spike spacings such as shown and is much more efficient than performing the analysis separately for each spike. The regularization that we employ (penalizing model roughness) is weighted against a spike slowness model, therefore the inversion procedure will tend to distribute as much structure as possible into the un-regularized station and event statics producing a smoother slowness model. By removing the static parameters we can retrieve an inversion model much closer to the phantom, but we then do not obtain a valid analog to the real data inversion procedure.

An inversion of this synthetic data is shown in Figure 5.3b at intervals of one degree in latitude with plots of the higher resolution interior region plotted at intervals of one half degree in latitude in Figures 5.3c and 5.3d for the phantom and inversion models, respectively. Compared with the ray density diagrams discussed in §5.2.1, we can see that, at least for the lower portions of the model, the best resolution is obtained in regions of high ray coverage. For the shallow structure, however, despite a high ray density we do not retrieve the phantom spikes but rather single vertically blurred spikes in their place. This is due to the fact that all

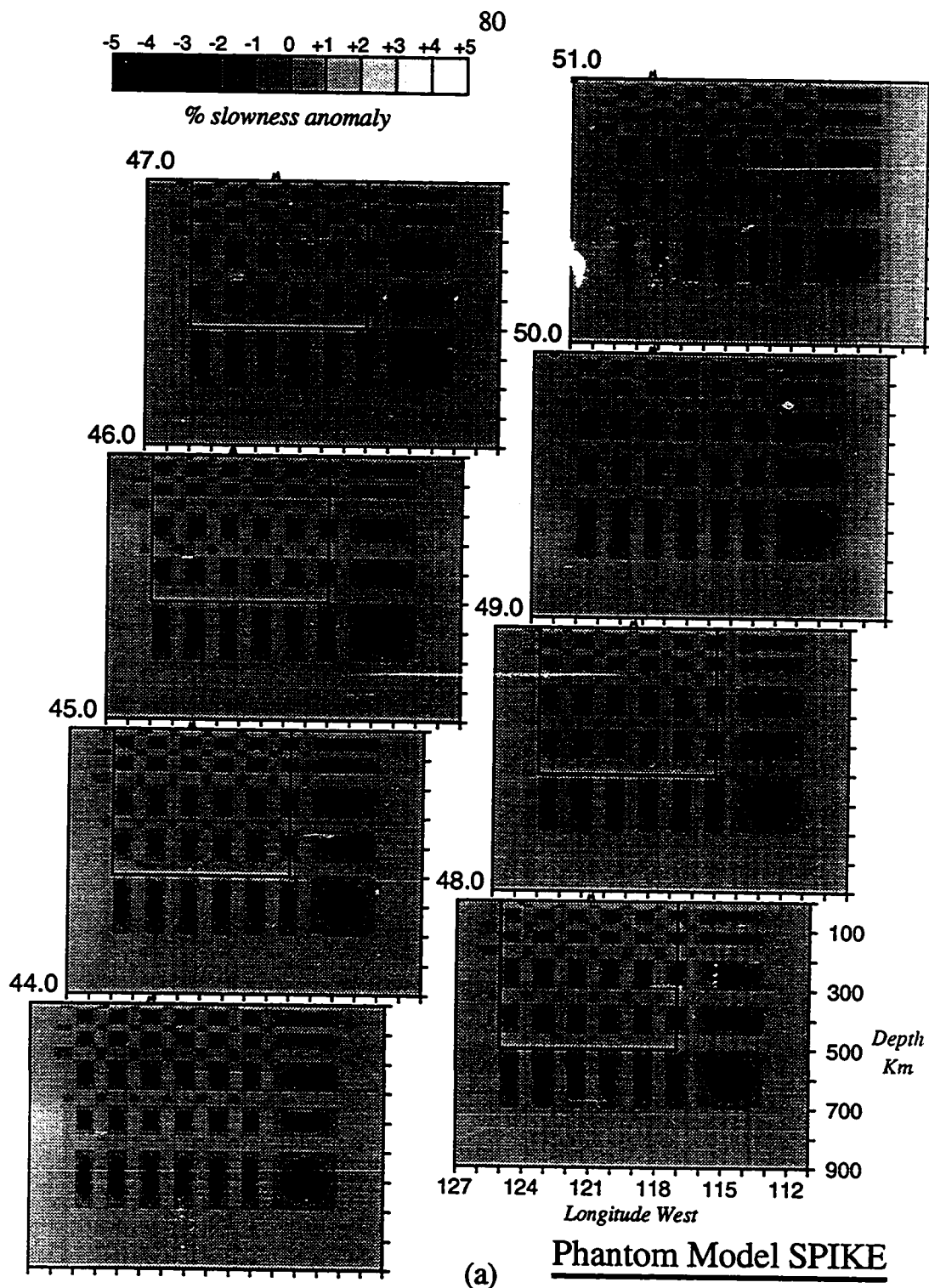
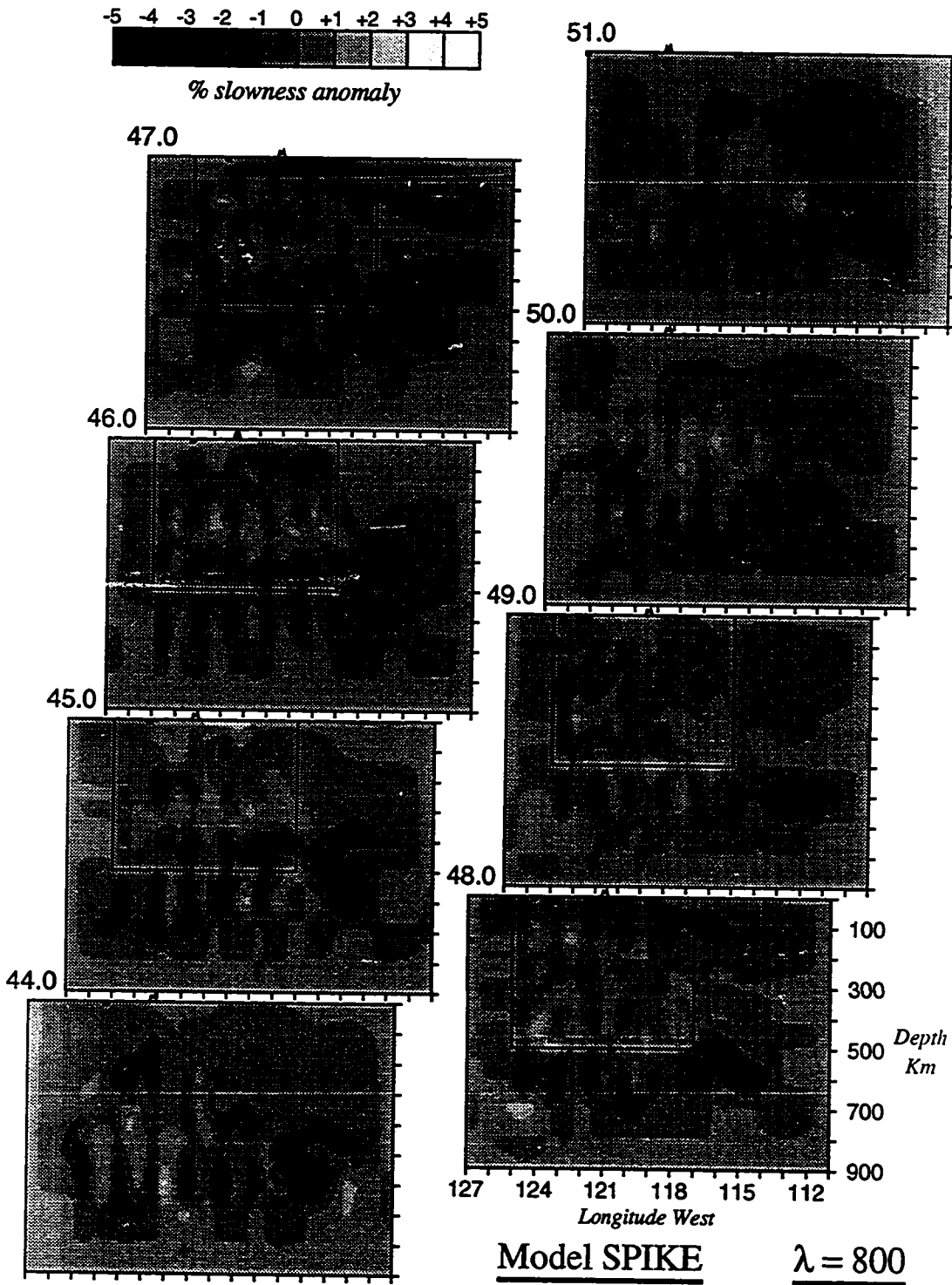


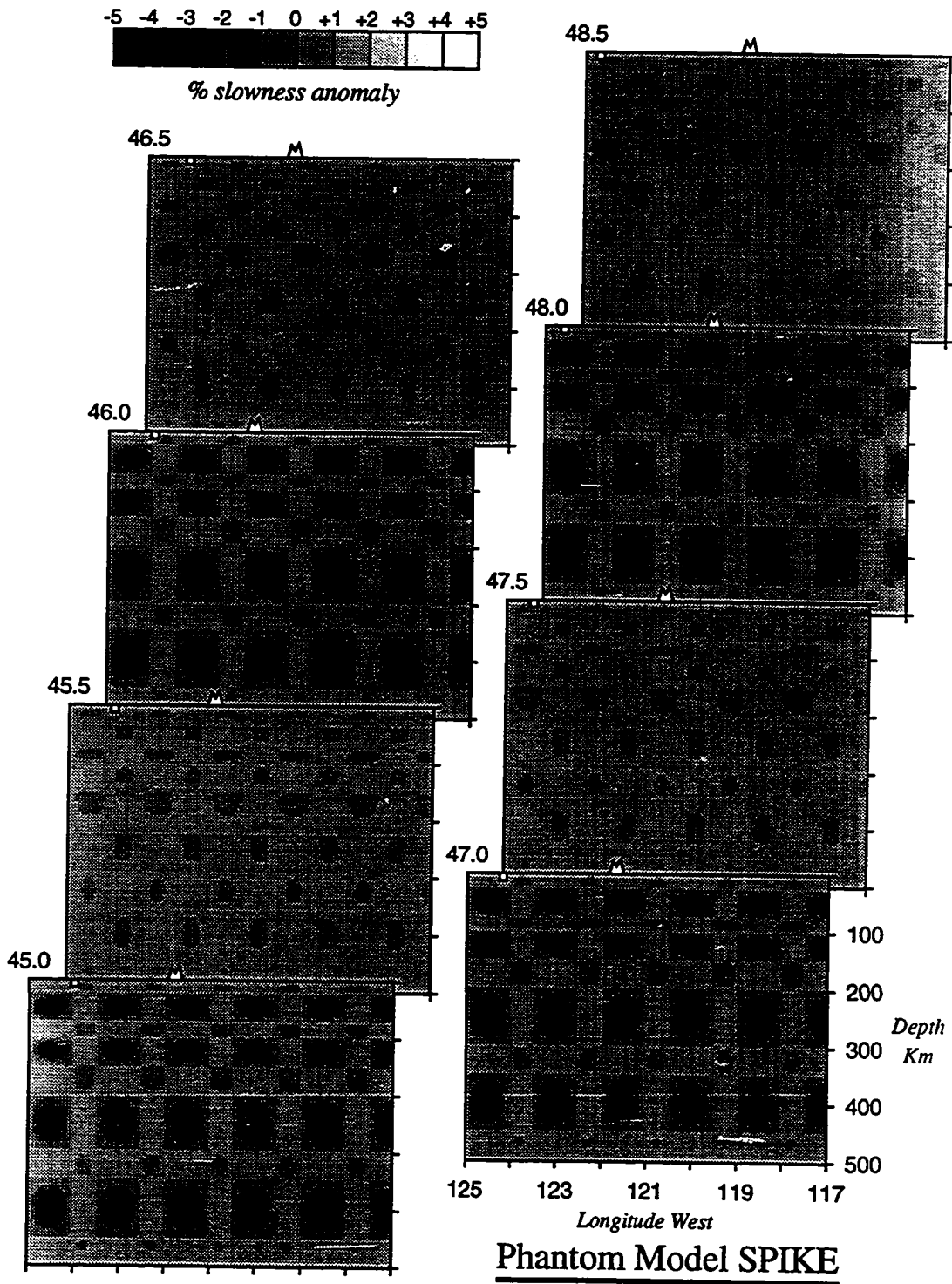
Figure 5.3a-d Latitudinal cross-sections for multiple spike resolution tests for (a) the entire phantom model, (b) entire inverted model, (c) interior of phantom model, and (d) interior of inverted model. Random error with a standard deviation of 0.10 sec was added to artificial data. Interior models are shown at 0.5 degree intervals (as opposed to 1.0).

Figure 5.3 (continued)



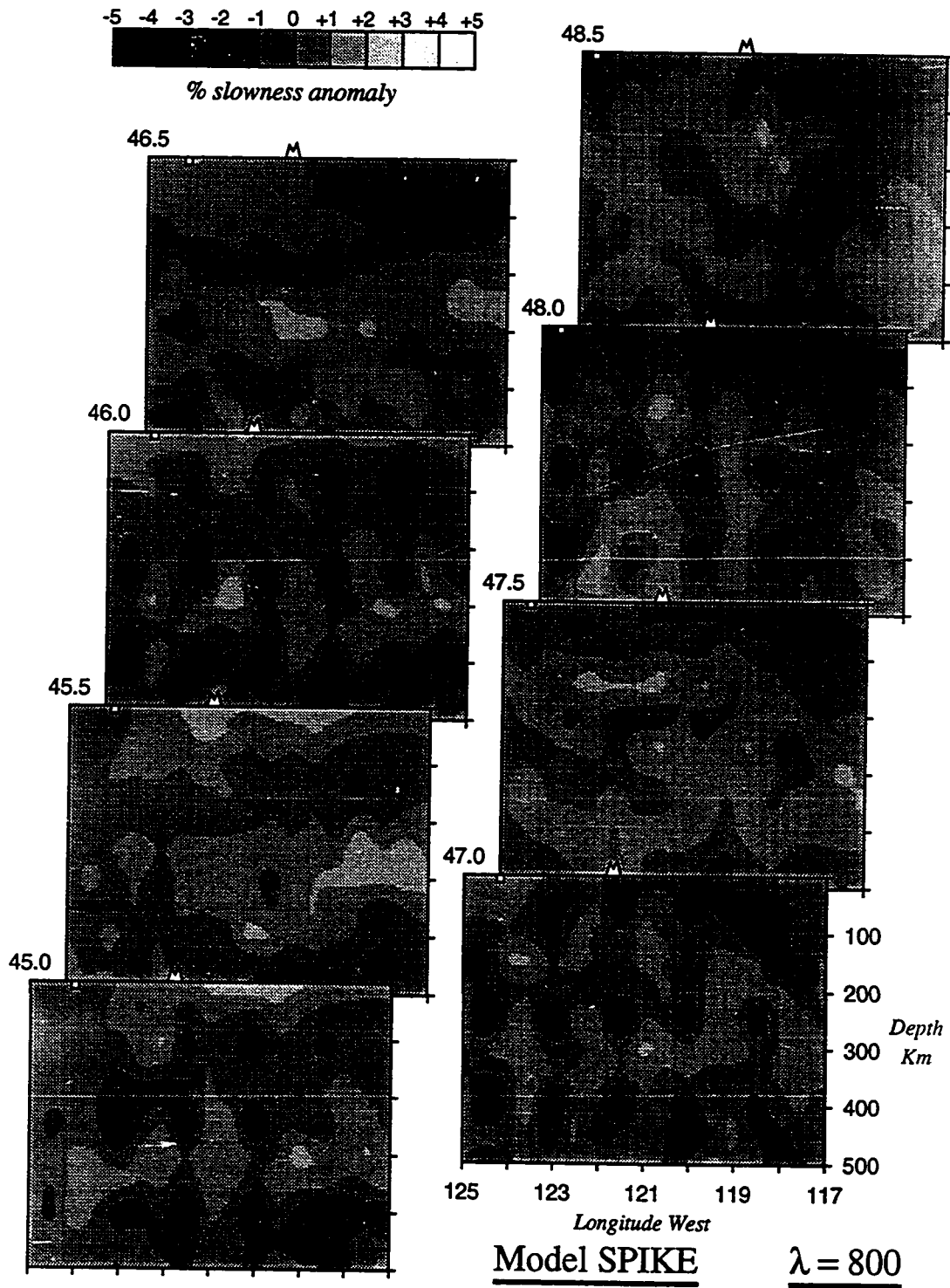
(b)

Figure 5.3 (continued)



(c)

Figure 5.3 (continued)



(d)

the rays are traveling nearly vertically in these shallow regions and much of the signal can be explained by station statics. We therefore should not expect to be able to resolve vertical structure with any confidence in these shallow regions. What is somewhat surprising is the ability of the data set to resolve to a high degree knots at 600 km depth. From Figure 5.2c we can see that there are indeed a good number of crossing rays even at the edges of our interior model region to provide this resolution.

We have shown that, despite relatively high noise and unfavorable regularization constraints, the spikes, for the most part, have not shifted position. No spikes were placed on the outside edge of the exterior region due to fact that the inversion process heavily damps these areas (as discussed in §3.5). The importance of adding noise arises from the observation that not all knot resolution estimates are effected equally. Compared with the same experiment done without noise (not shown) some knots seem to be highly susceptible to this level of noise while others appear fairly robust (at least to purely random, independently distributed noise). Next, we examine the same process applied to a phantom model of a subducting slab. Although the slab model is fairly smooth, we can simulate the non-linear case with this model.

5.2.3 Resolution of a Synthetic Slab Model

In Figure 5.4a we have plotted constant latitude cross-sections through the phantom model of a slab dipping at an angle of 55 degrees to the east with a Gaussian shaped variation of slowness from a peak amplitude that is 4.0% lower than background (with a standard deviation of 35 km). We have chosen this model to mimic in a simple fashion the type of anomaly observed in this region (with several key differences which will be discussed in §5.3). We will first form synthetic travel-time data by assuming the radial Earth ray paths are correct and then inverting those data also keeping the rays fixed.[†] The result of this process is shown in Figure 5.4b (where random noise with a standard deviation of 0.10 sec was added

[†] The final two letters of each model name indicate the type of forward and inverse problem solved. The next to last letter is either an N if the forward problem was not ray traced, or an R if it was ray traced. The final letter is either an L if the inversion was linear, or an N if it was non-linear.

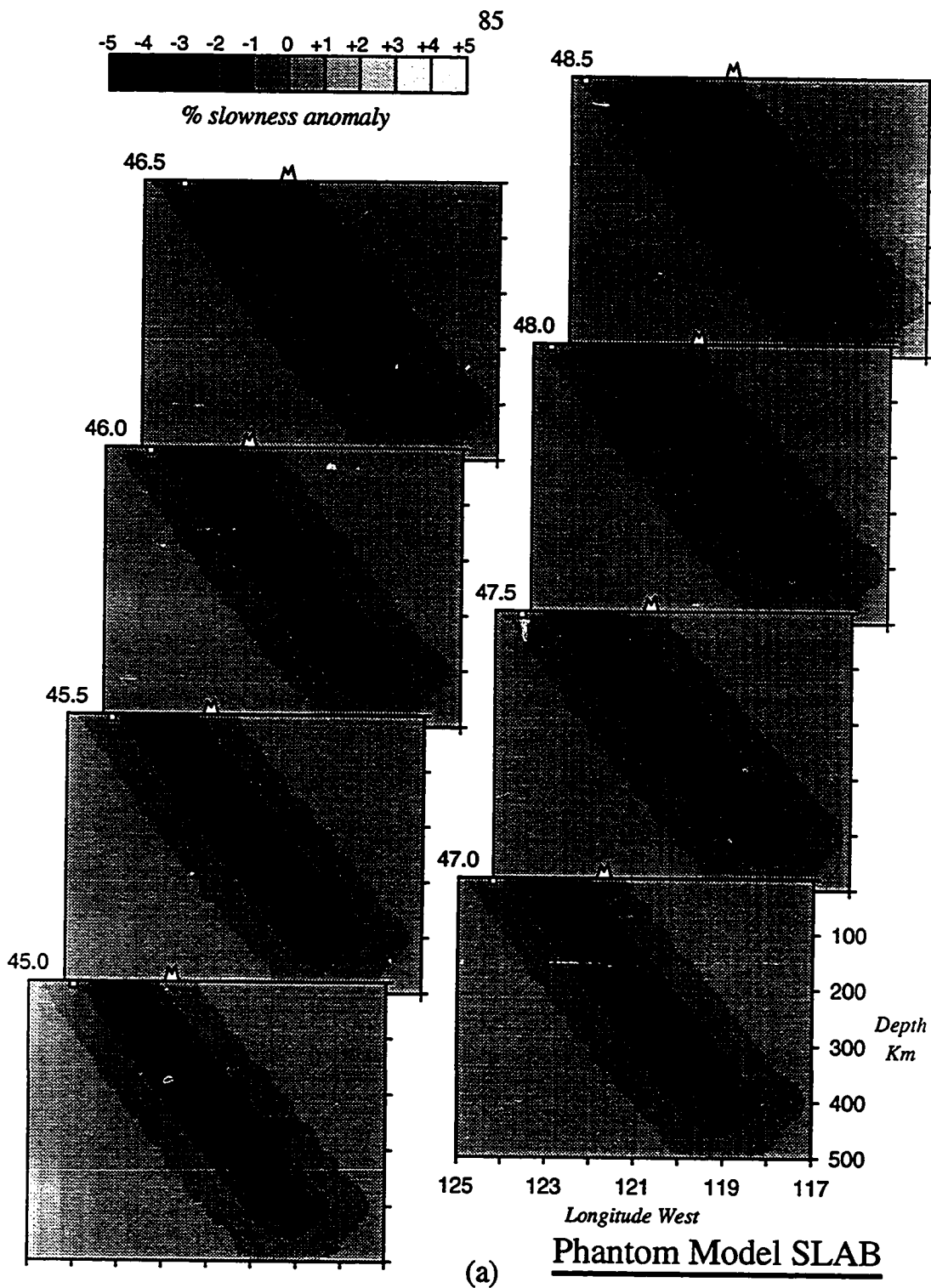
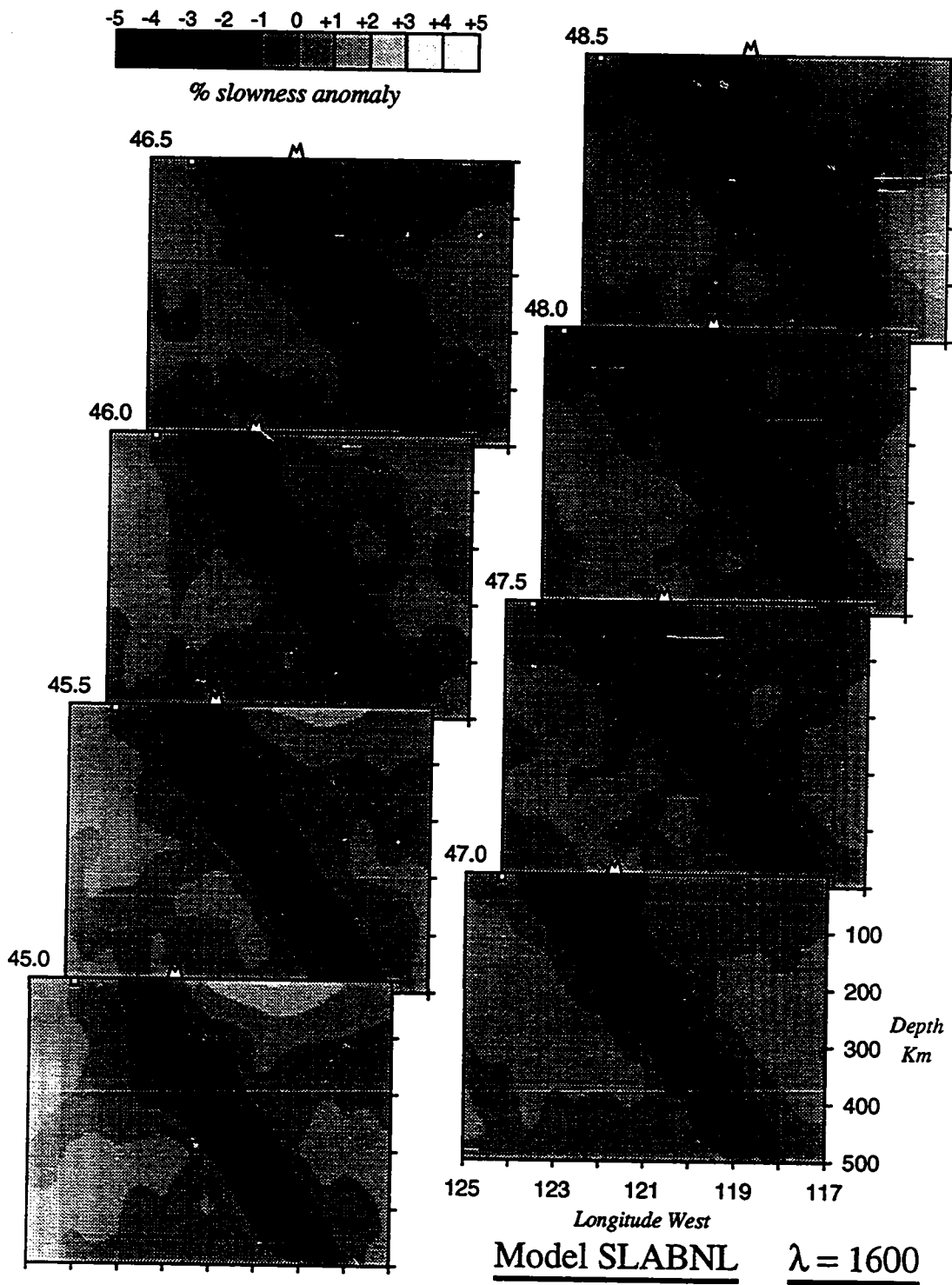


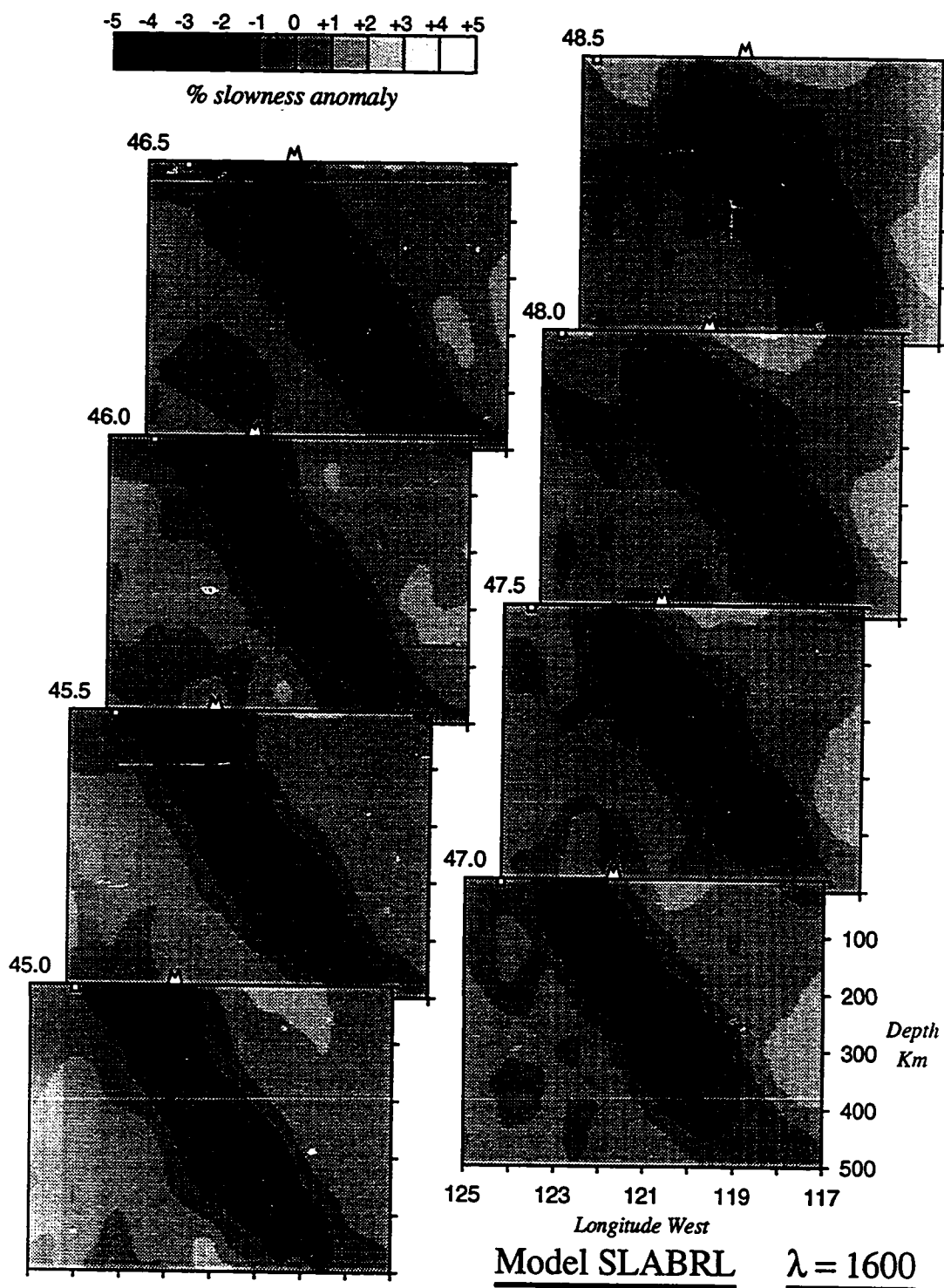
Figure 5.4a-d Latitudinal cross-sections for subducting slab resolution tests for (a) the phantom model, (b) non-raytraced data with linear inversion, (c) raytraced data with linear inversion, (d) raytraced data with non-linear inversion (with ray paths obtained from (c)). Random error with a standard deviation of 0.10 sec added to all artificial data.

Figure 5.4 (continued)



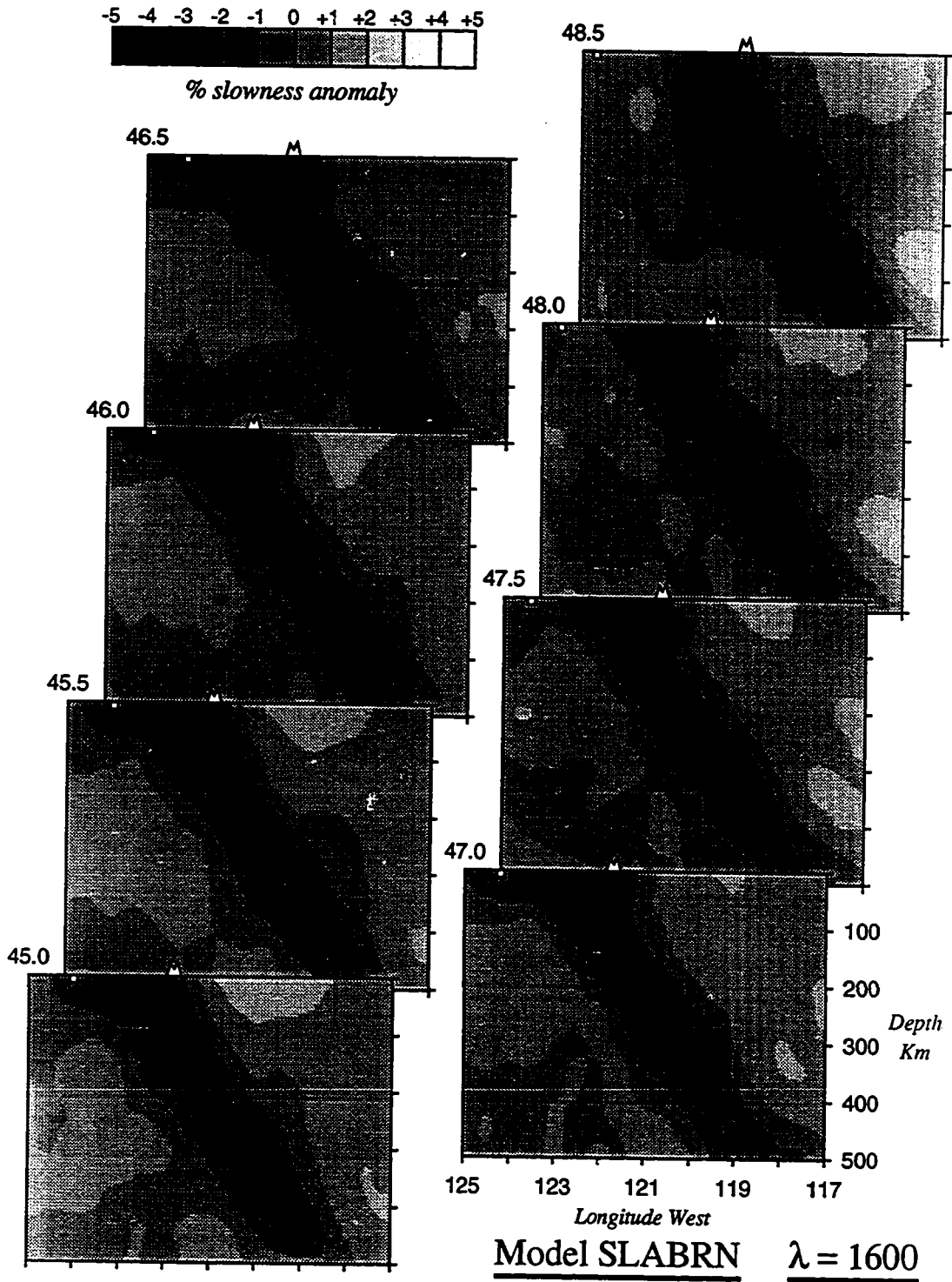
(b)

Figure 5.4 (continued)



(c)

Figure 5.4 (continued)



(d)

to all synthetic data). Even with a relatively large amount of random noise added (compared to that estimated for our data set, see Chapter 3), we see that the structure is still well resolved, with only a small amount of smearing and few artifacts produced. This success results from the completeness of the data set and the our assumption of no modeling errors.

The non-linear nature of the travel-time inversion problem is widely recognized but often not treated (particularly in large scale inversions). If the ray paths which we first assumed are not close enough to the true ray paths, then the linearization may remain adequate in that theoretical travel-time errors are small, but not adequate in that the partial derivatives are wrong, so structure is put in the wrong place. This has been recognized to arise in the case of regional phases where ray paths are critically dependent on radial Earth structure [*van der Hilst and Spakman 1989, Zielhuis et al. 1989*] but may also provide a strong effect for teleseismic phases in regions of large-scale lateral velocity anomalies with steep gradients. It has long been known that subduction zone structure, in particular, can severely effect ray paths [e.g. *Jacob 1970, Sleep 1973*].

To test the effect of ray bending and therefore attain a more realistic estimate of the resolution capabilities of our travel-time data we must perform three-dimensional ray-tracing through the phantom model. We have done this for the phantom model shown in Figure 5.4a and then used these times to perform a linear inversion with the (incorrect) radial Earth ray paths (since for real data we would not have known the true ray paths). The result of this exercise is shown in Figure 5.4c. It is readily apparent that our resolution test using non-raytraced data overestimated our ability to accurately image a subducting slab. No longer do we obtain either an anomaly level near that of the truth nor an accurate estimate of the width of the anomaly. This is explained by the effect of the slab structure on rays traveling up the dip of the slab which are focused toward its core. When this focusing is not taken into account (i.e. when we assume radial Earth ray paths) we then need a much wider slab anomaly to explain the observed travel-time pattern. Rays traveling perpendicularly through the slab constrain the wider anomaly to have a lower amplitude.

Next we test how well ray-tracing through the result of our linear inversion can improve our estimates of the ray paths and therefore improve the accuracy of

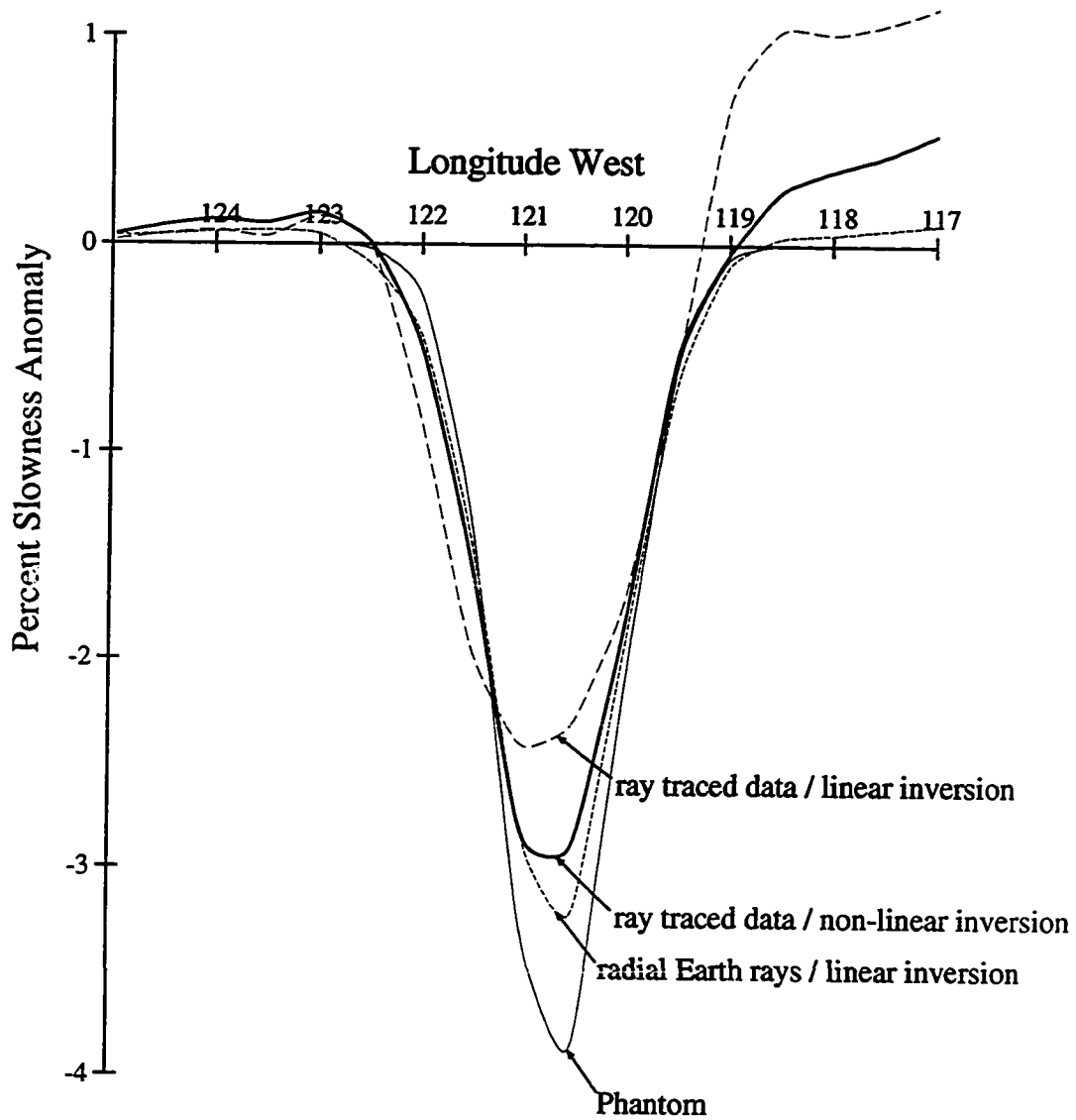
our model. Performing this ray tracing and then using the resulting ray paths and travel time patterns for a second inversion iteration results in the model shown in Figure 5.4*d*. In all cases random noise with a standard deviation of 0.10 sec was added to synthetic data. We can see that this process does reduce the width of the slab anomaly and also slightly increase its amplitude. These results are summarized in Figure 5.5 where the average anomaly values versus longitude for the models at 250 km depth are plotted for both the case of no noise added to the data (Figure 5.5*a*) and noise added as in Figure 5.4 (Figure 5.5*b*). For the case of no noise added to the synthetic data, for the non-linear model from ray traced data (Figure 5.4*d*), the ray paths used to produce this model were ray traced through the linear model constructed from noisy data (Figure 5.4*c*), so this model is still somewhat effected by noise.

5.3 Slowness Perturbation Models

In this section we present the results of inverting real data. First we examine model UW91F1, the ‘linear’ first iteration of the inversion process described in Chapter 4. We then move on to two iterations of the non-linear perturbations arrived at by the algorithm described in §4.6. We will be comparing these images to the results of the linear and non-linear resolution tests and also referring back to the ray distribution plots in order to judge the validity of the results.

Each model below is shown at different levels of regularization (smoothing) represented by the trade-off parameter λ (see §4.4).[†] Large λ represents more smoothing at the expense of fitting the data. In classical resolution-covariance analysis we would plot a ‘trade-off’ curve for each model parameter representing estimated model covariance versus resolution for various levels of regularization. In this case, resolution is usually measured in terms of the half-width of the resolution kernel or the magnitude of the diagonal elements of the resolution matrix (see §5.2). We will, however, use the global statistics of residual variance reduction and model ‘roughness’ as measures for our trade-off between resolution and accuracy or reliability. The model roughness, $\sigma_f^{(k)}(\lambda)$ is simply the rms misfit to the constraint equations (without weighting by λ), for a given iteration k and smoothing

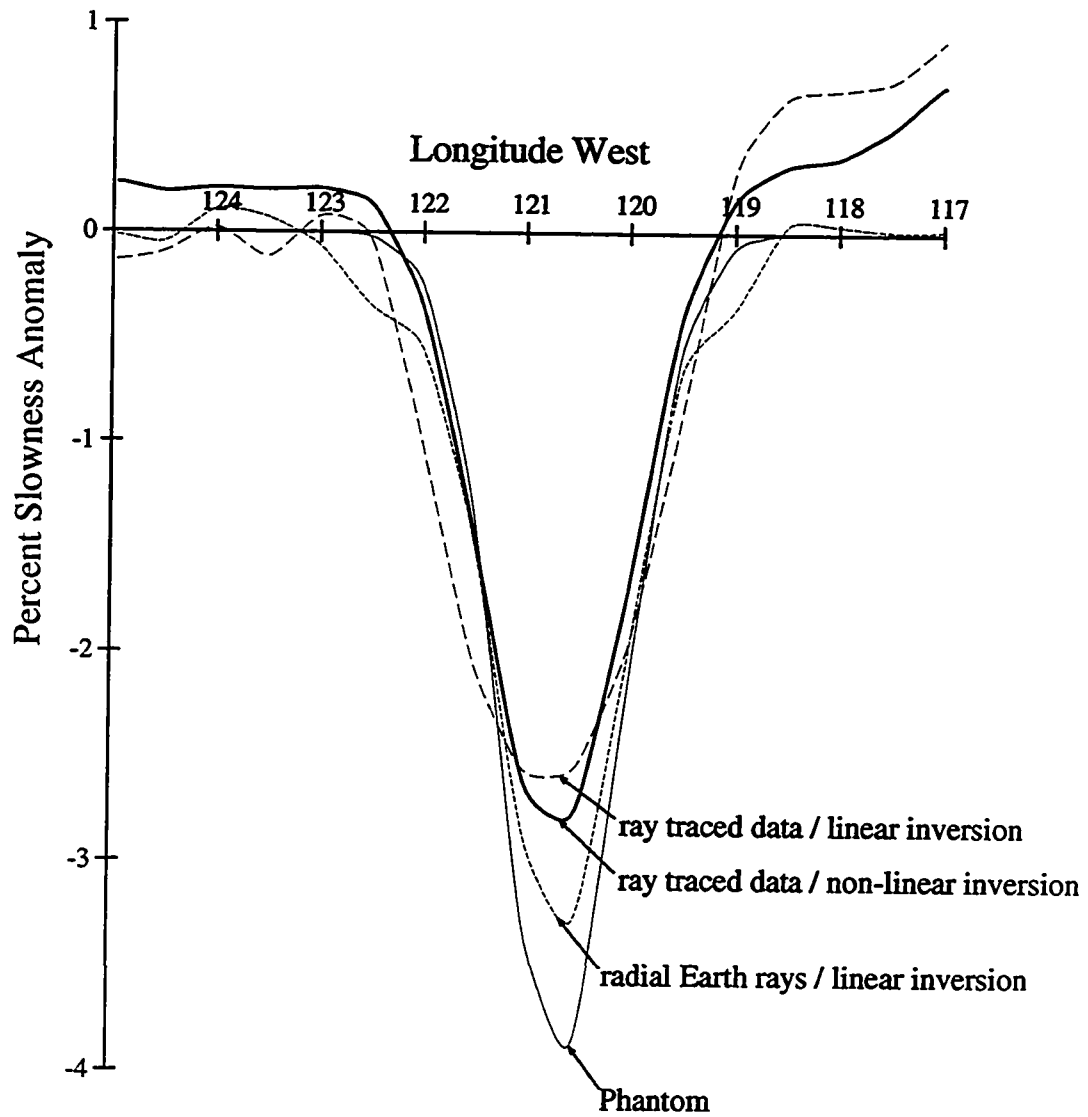
[†] The display of both the higher-resolution interior and complete model is described in §5.1.



(a)

Figure 5.5a,b Slowness Anomalies at 250 km depth as a function of longitude averaged over latitude from 43N to 49N, for synthetic slab models with (a) no noise added to data and (b) noise with a standard deviation of 0.10 sec added to all data.

Figure 5.5 (continued)



(b)

parameter λ ,

$$\sigma_f^{(k)}(\lambda) = \sqrt{\frac{1}{m} \sum_{i=1}^m [F_{ij} \Delta s_j^{(k)}(\lambda)]^2} . \quad (5.3.1)$$

The rms travel-time residual reduction is the percent difference between the initial (weighted) rms misfit to the travel-time equations (with each event initially having a zero mean arrival time),

$$\sigma_{rr}^{(0)} = \sqrt{\frac{1}{n} \sum_{i=1}^n [W_{ij} \Delta t_j^{(0)}]^2} , \quad (5.3.2)$$

and the (weighted) rms misfit to the travel-time equations for a given iteration k and smoothing parameter λ ,

$$\sigma_{rr}^{(k)}(\lambda) = \sqrt{\frac{1}{n} \sum_{h=1}^n \left[W_{hi} \left[P_{ij}^{(k-1)} \Delta s_j^{(k)}(\lambda) + h_r^{(k)}(\lambda) + e_q^{(k)}(\lambda) - \Delta t_i^{(k-1)} \right] \right]^2} , \quad (5.3.3)$$

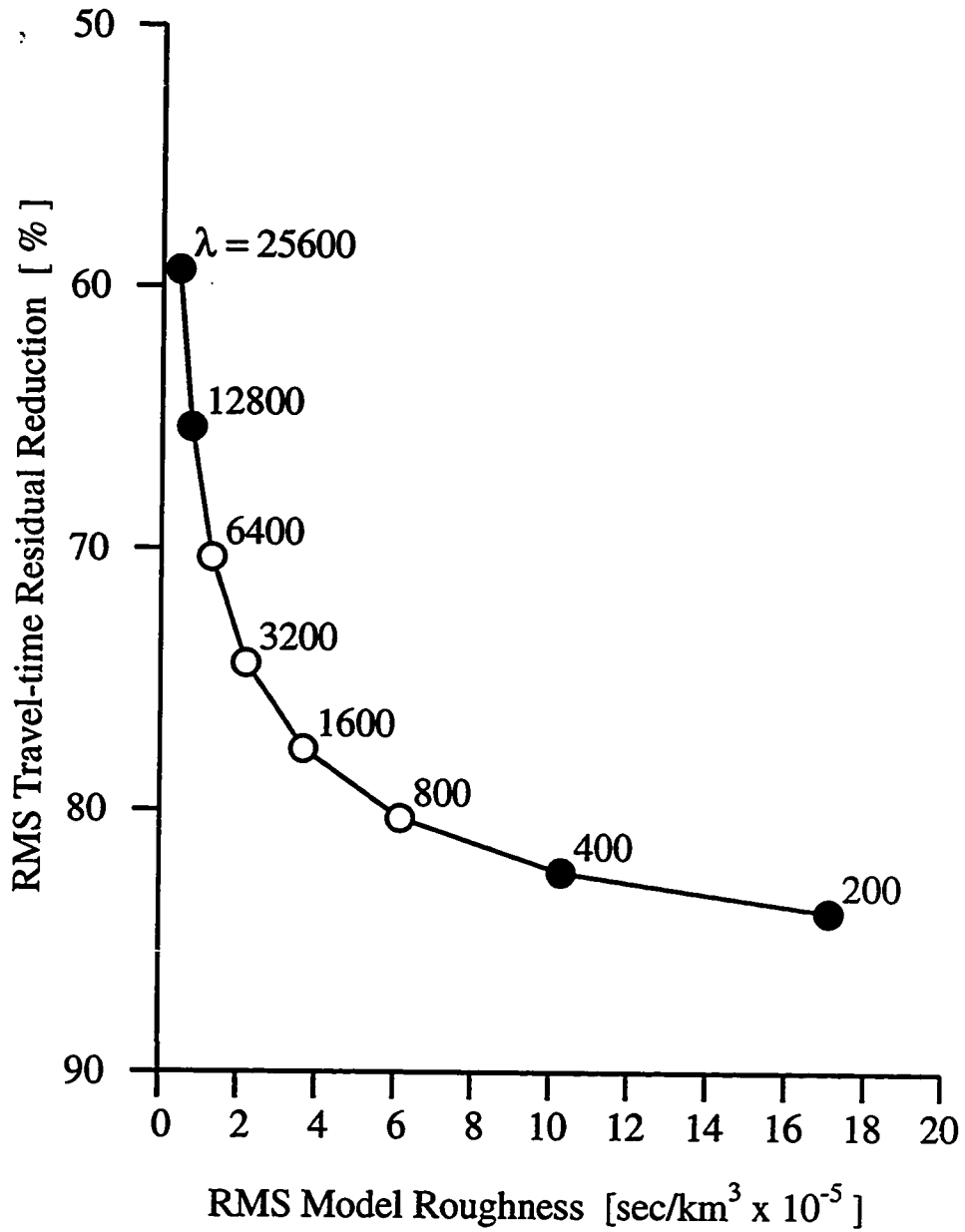
where r and q are completely determined by i . This then gives, for the percent difference,

$$\frac{\sigma_{rr}^{(0)} - \sigma_{rr}^{(k)}(\lambda)}{\sigma_{rr}^{(0)}} . \quad (5.3.4)$$

The initial (un-weighted) rms travel-time residual for our data set was 0.458 sec. While the measure of rms residual reduction is sensitive to original data selection and in itself does not directly provide an estimate of model covariance, its relative value for various levels of regularization can give us a valuable sense of at what level the addition of more high frequency model features is providing diminishing returns with respect to the fitting of the data.

5.3.1 First Iteration ‘Linear’ Model UW91F1

Figure 5.6 is a plot of the trade-off between data fitting and model roughness, as described above, for model UW91F1. As mentioned previously the absolute scale of the residual variance reduction is sensitive to the initial data selection (if we had chosen to use more events from azimuths with rays traveling up the dip of the slab the percent reduction would be inflated). It is therefore the shape of the trade-off curves (the relative values) that is important rather than the isolated value at any given point. We can see from Figure 5.6 that it is within the range of λ



Model UW91F1

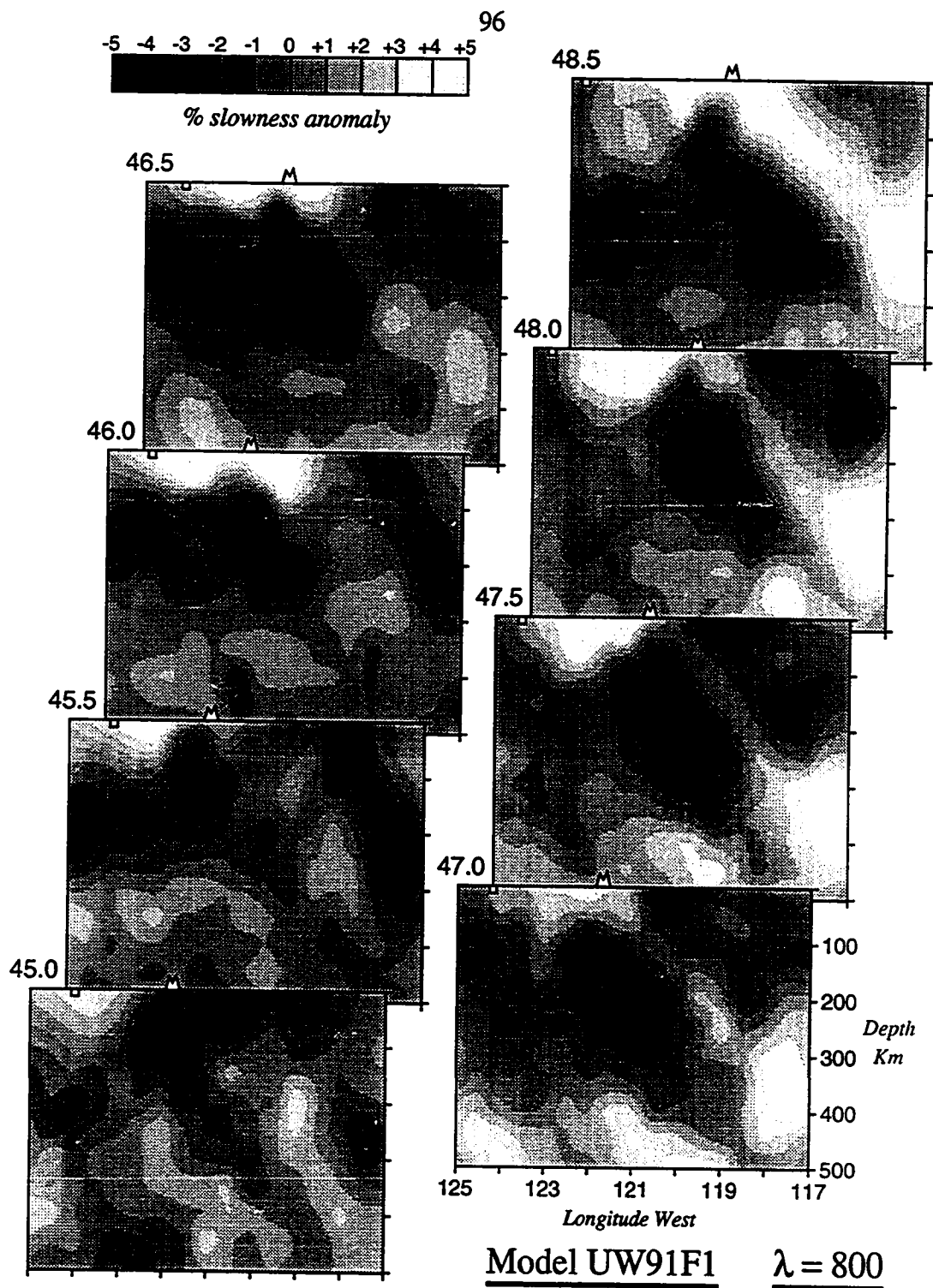
Figure 5.6 Trade-off between data fitting and model roughness. The open symbols delineate models shown in text. The roughness represents the rms misfit of the constraint equations (5.3.1). Equation (5.3.3) describes rms travel-time residuals.

from 800 to 6400 that the major tradeoff between these parameters occurs. At lower values the model rapidly increases in roughness while minimally improving the fit to the data while at higher values the fit to the data becomes dramatically worse for small changes in smoothness. We will therefore confine our analysis in this thesis to these values (indicated by open symbols in Figure 5.6).

Displayed in Figure 5.7*a-d* is the ‘linear’ model UW91F1 at different levels of regularization (smoothing) represented by the trade-off parameter λ (see §4.4). As described above, relatively large λ represents more emphasis being placed on our obtaining a smooth model at the expense of fitting the data. By examining the effect of differing levels of regularization on the inversion we can get a sense of which model features are most robust. As can be readily seen at all levels of regularization, the dominant feature within this interior region is a high velocity anomaly dipping steeply eastward. From our slab resolution analysis in §5.2.3 we expect certain distortions to arise from the linear inversion of such a feature. We therefore expect the slab to be artificially widened and for the peak-to-peak amplitude of the anomaly to be under estimated. The other robust feature of these inversions is a high velocity anomaly in the shallow southeast corner of the region. This anomaly lies below the Blue Mountains of eastern Oregon and has been recognized previously as a region of anomalously high velocity [*Rasmussen and Humphreys* 1988].

In Figure 5.8 we have taken a cross-section through model UW91F1 at a constant depth of 200 km to better analyze the lateral variation of the model (with a regularization of 3200). Plotted for reference are both surface features (coastlines and major rivers) and the contours of shallow slab structure (at 30, 40, 50 and 60 km) described in §1.3.1. These intermediate depths (from approximately 150 to 450 km) are, in general, the best resolved. We see from this figure that the slab appears to lie in a reasonable position relative to our knowledge of shallow structure and that, except for the Blue Mountains anomaly on the right-hand side of the plot, the slab is clearly the dominant feature at this depth.

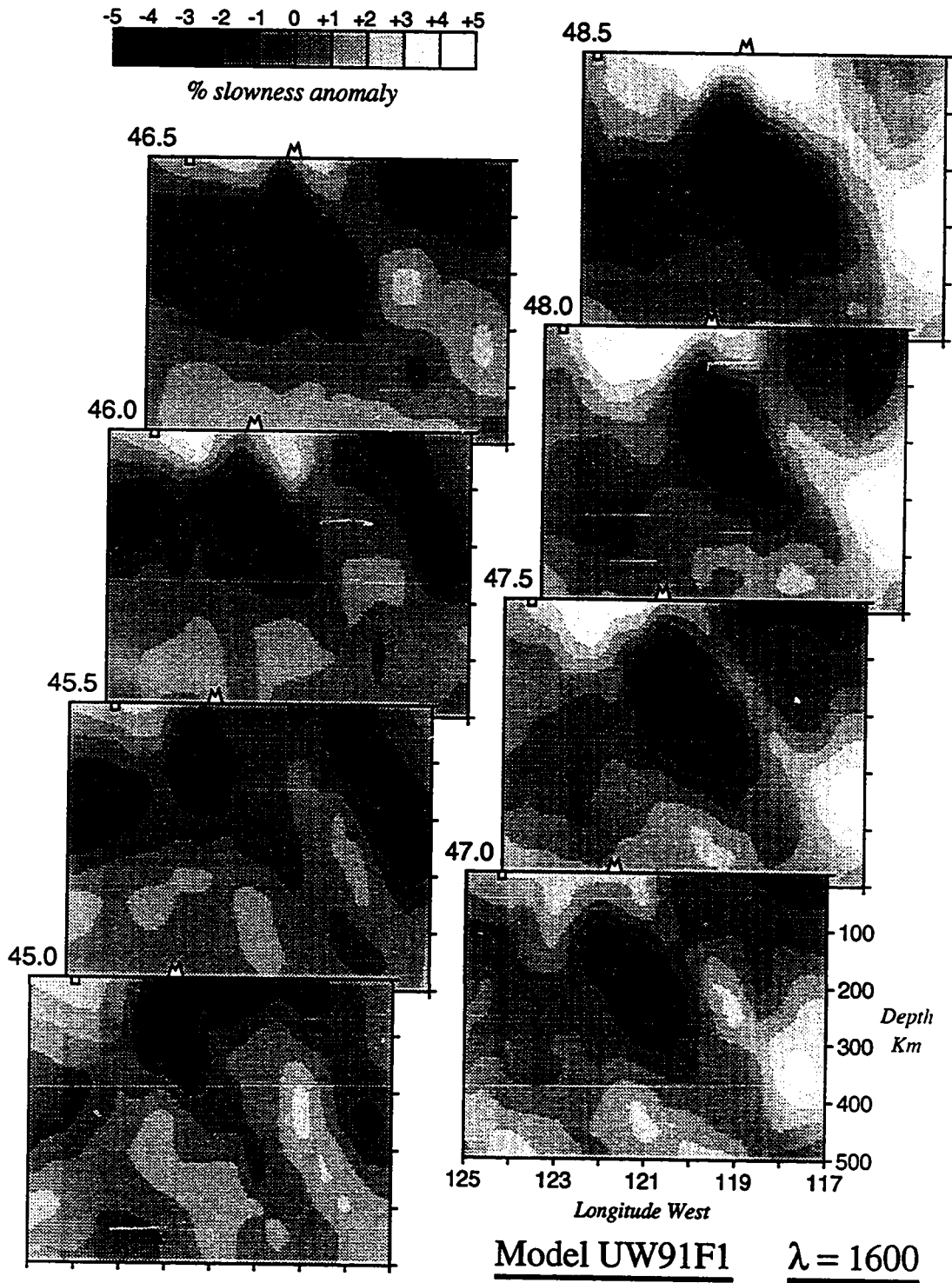
Outside of the region of relatively high resolution (shown for a regularization of 3200 in Figure 5.9) the only stable feature is a high velocity blob in the down-dip direction of the Northern portion of the inferred slab anomaly. Some resolution exists in this region as is indicated in the spike resolution tests of §5.2.2, and while



(a)

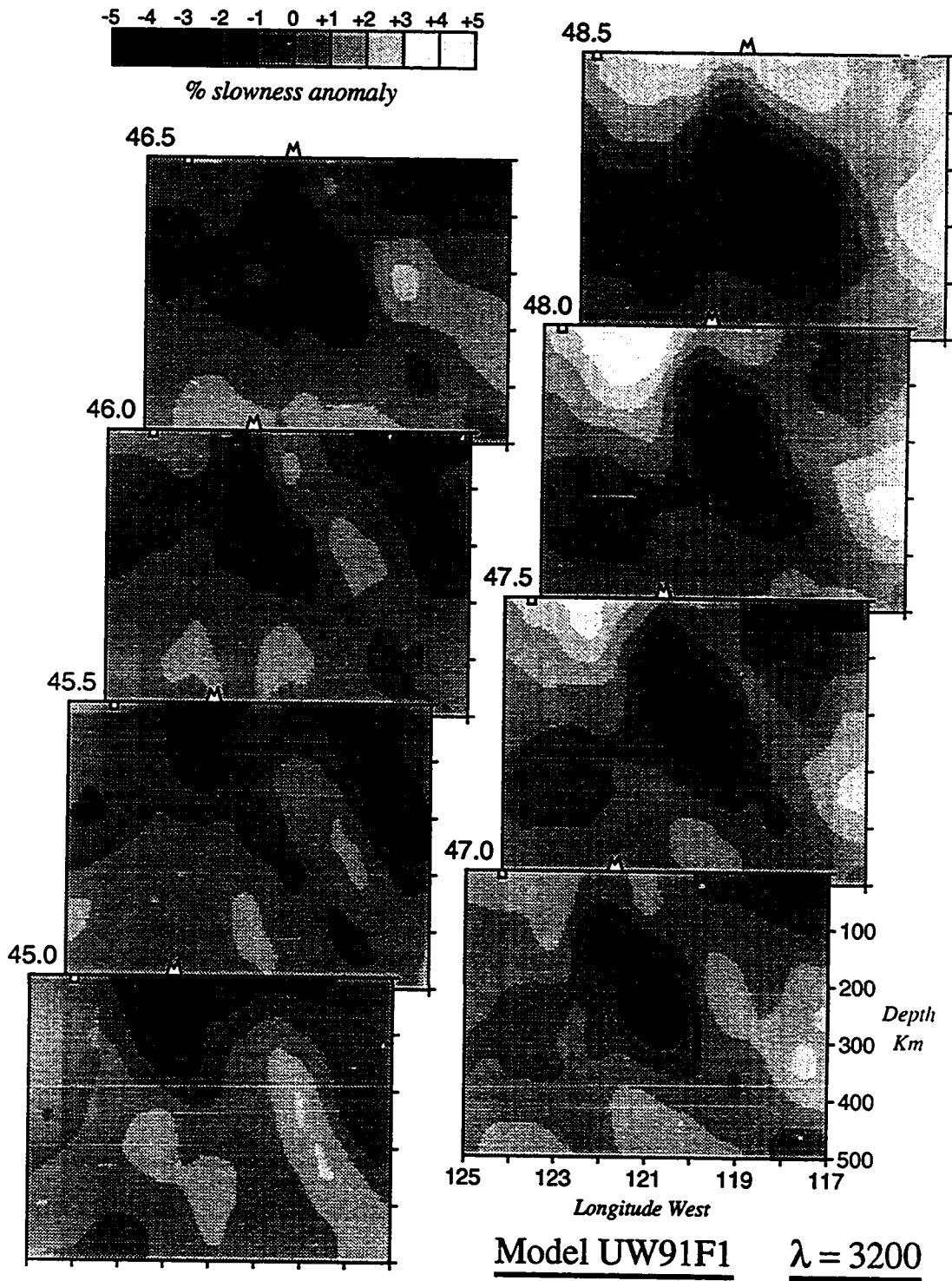
Figure 5.7(a-d) Latitudinal slices through the interior of slowness model UW91F1 for regularizations of (a) 800, (b) 1600, (c) 3200, and (d) 6400. This model represents a linear inversion (i.e. radial Earth ray paths were assumed). See text for interpretation.

Figure 5.7 (continued)



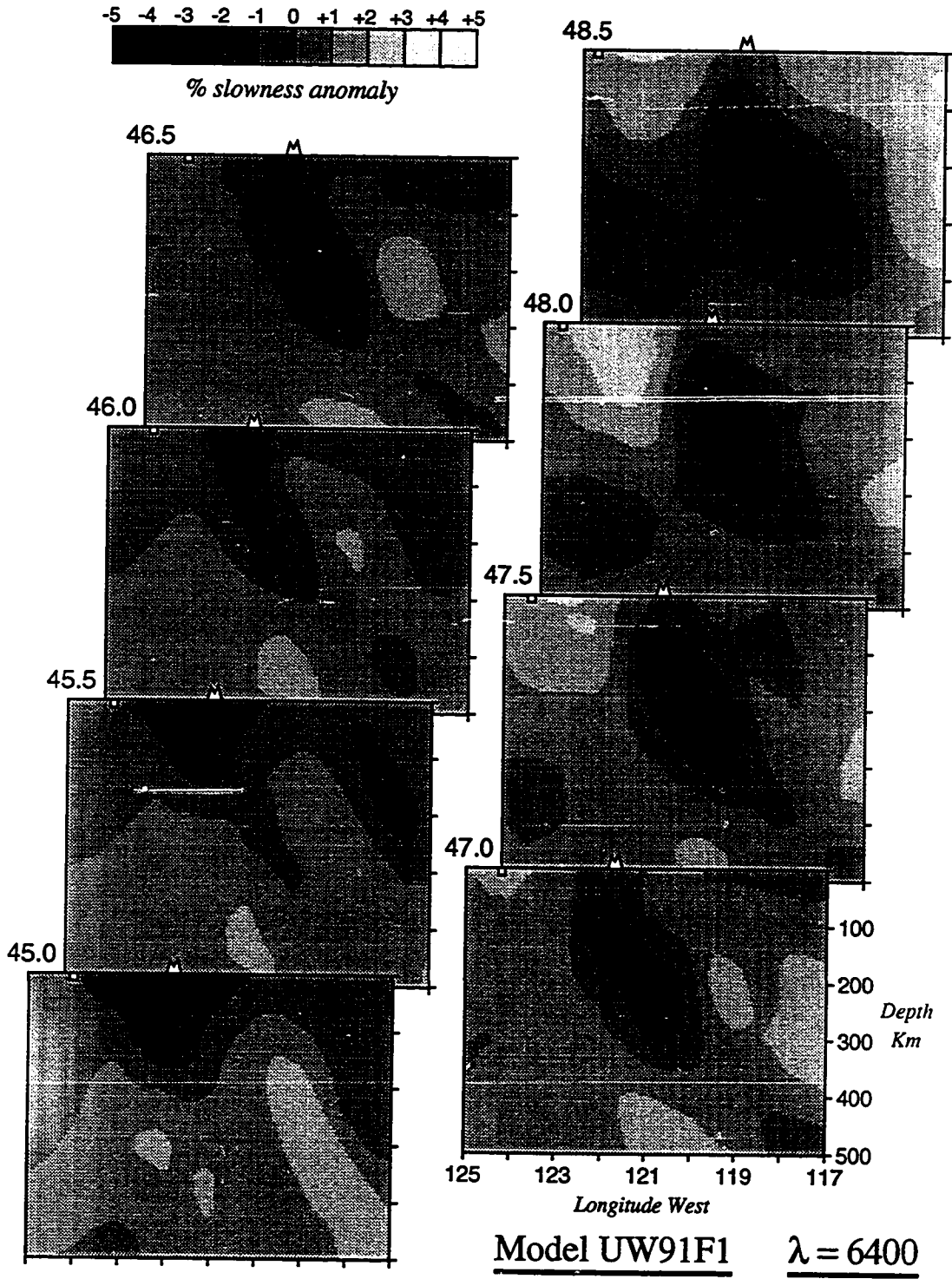
(b)

Figure 5.7 (continued)

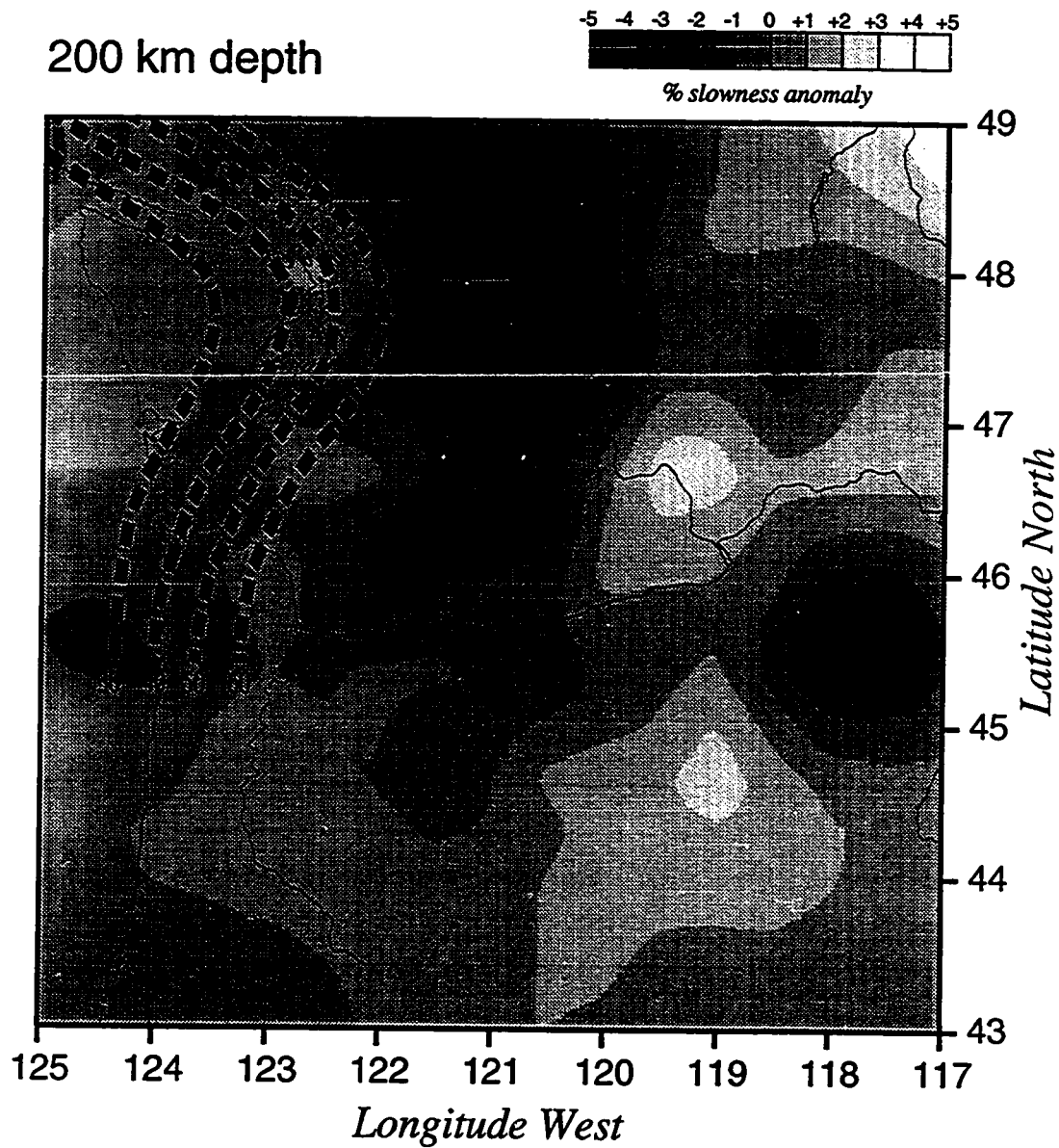


(c)

Figure 5.7 (continued)



(d)



Model UW91F1 $\lambda = 3200$

Figure 5.8 Slice through non-linear slowness perturbation model UW91F1 at 200 km depth with map of region and contours of shallow slab structure superimposed (see section 1.3.1 for description and origin of contours).

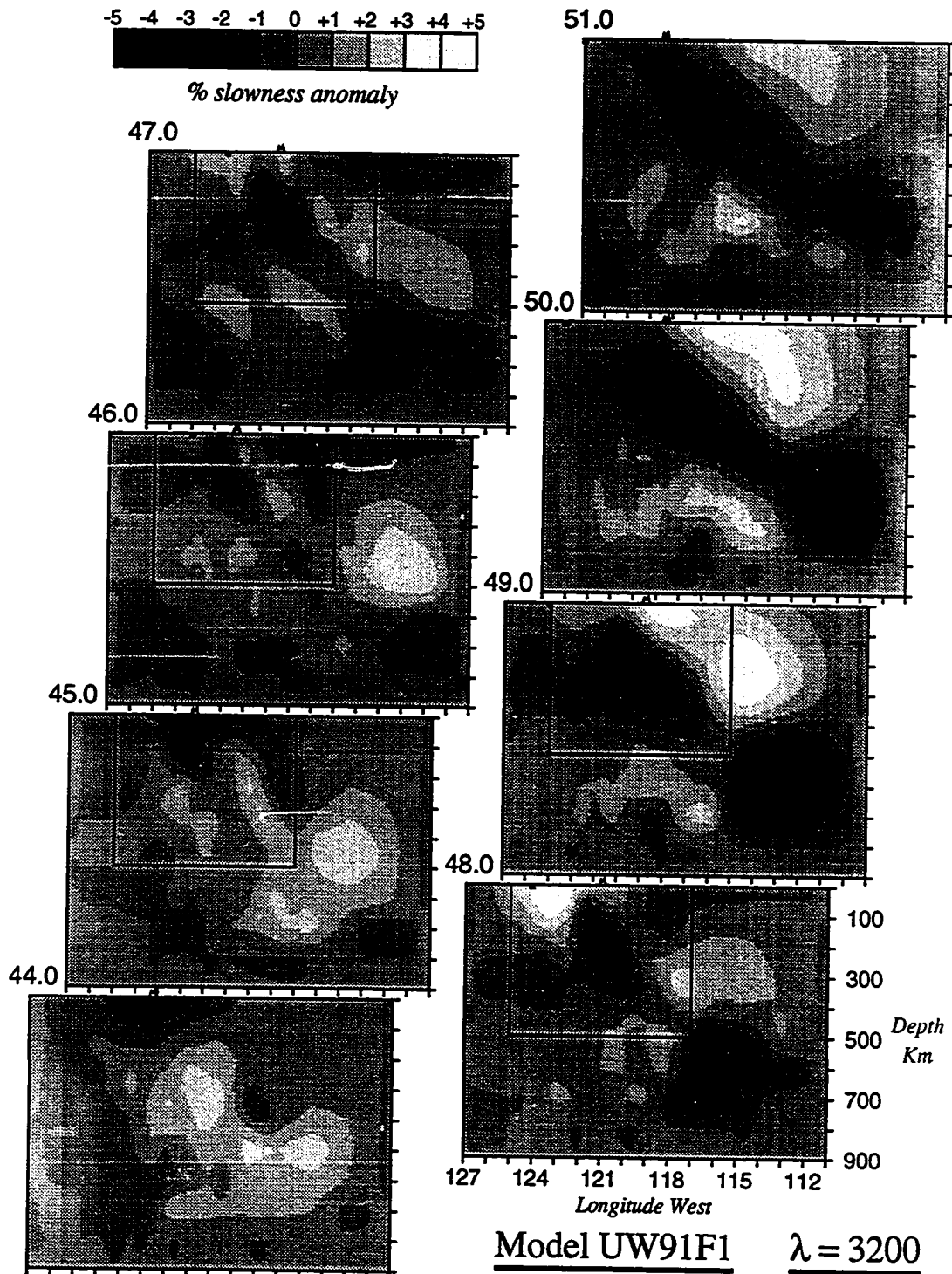


Figure 5.9 Latitudinal slices through the entirety of slowness model UW91F1 for a regularization of 3200. This model represents a linear inversion. The region outside of the interior boxes is not well resolved. See text for interpretation.

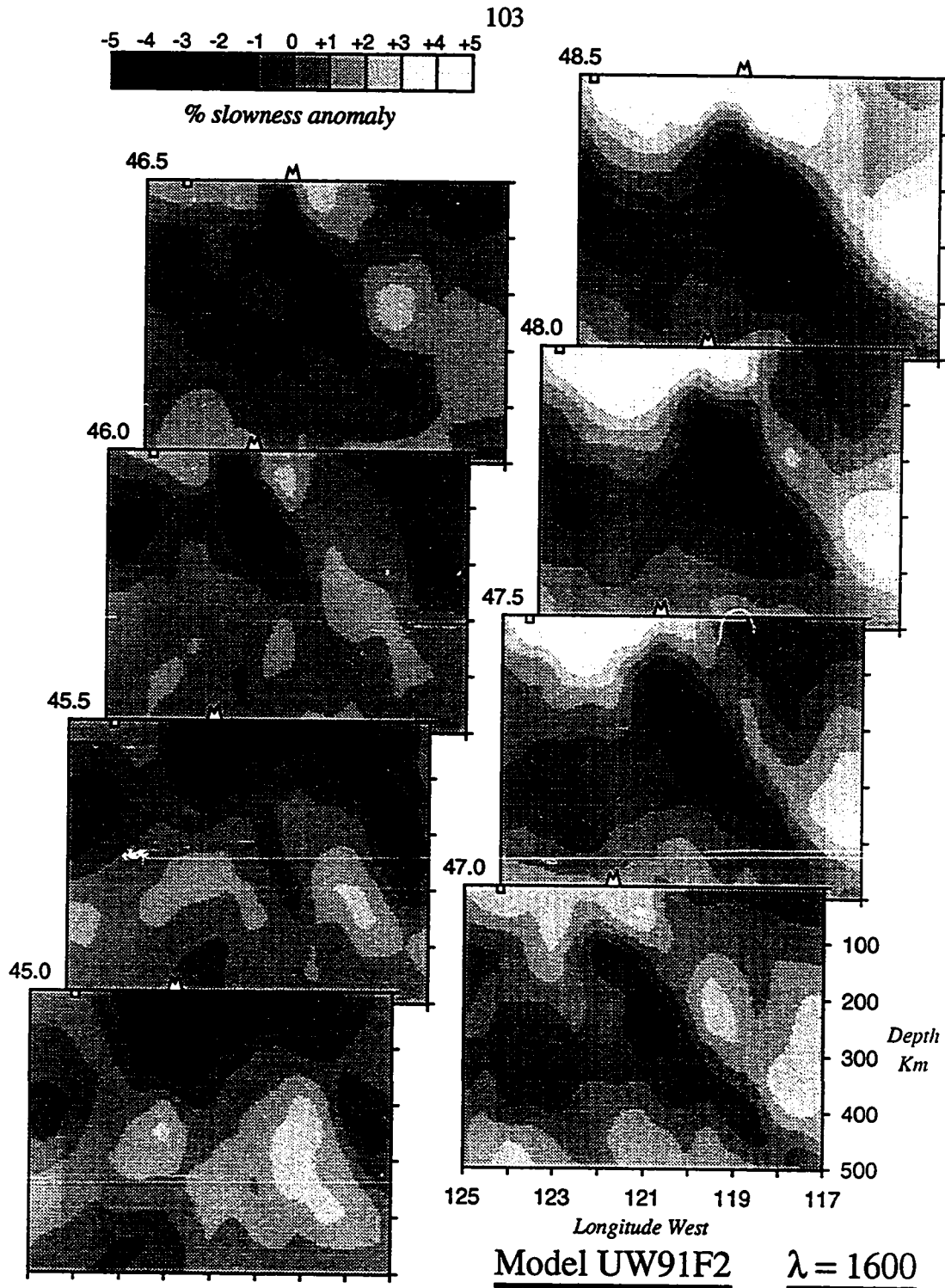
this feature appears rather large it is limited in size by our parameterization in this region (see Figure 4.2). Whether or not this is an artifact of performing only a linear inversion, we will try to test in the following sections, but for the case of a phantom slab model with realistic data, we saw in §5.2.3 that artifacts of such amplitude and shape were not produced merely due to ray geometry and the non linearity of the problem.

5.3.2 Second Iteration Model UW91F2

In this section we examine the effect of performing a second iteration of inversion with an improved knowledge of appropriate starting model gained from ray tracing through the first iteration model UW91F1 (with $\lambda = 1600$). Since our starting model now varies three-dimensionally we will require the solution of the general two-point ray tracing problem for each of our station-event pairs (except for core phase data as described in Appendix C). Our method of accomplishing this is described in detail in Chapter 4 and Appendix C.

The tradeoff curve for Model UW91F2 has nearly the same shape as that for the previous iteration but the data can now be fit slightly better for each level of regularization. In Figure 5.10*a,b* we will once again examine models with various levels of regularization, but now that we know what to expect in terms of this variation we will restrict ourselves to the central values of λ equal to 1600 and 3200. By comparing the model at these levels of regularization to their equivalent models in Figure 5.7 we can see that, as expected, the ray tracing through model UW91F1 (with $\lambda = 1600$) has produced a thinner, higher amplitude anomaly with, in general, less structure outside of the slab anomaly and the anomaly beneath the Blue Mountains of NE Oregon. Comparing Figure 5.11 to Figure 5.8 of model UW91F1 illustrates, perhaps, the most dramatic change between these models, the thinning of the slab in the northern portion of the interior model.

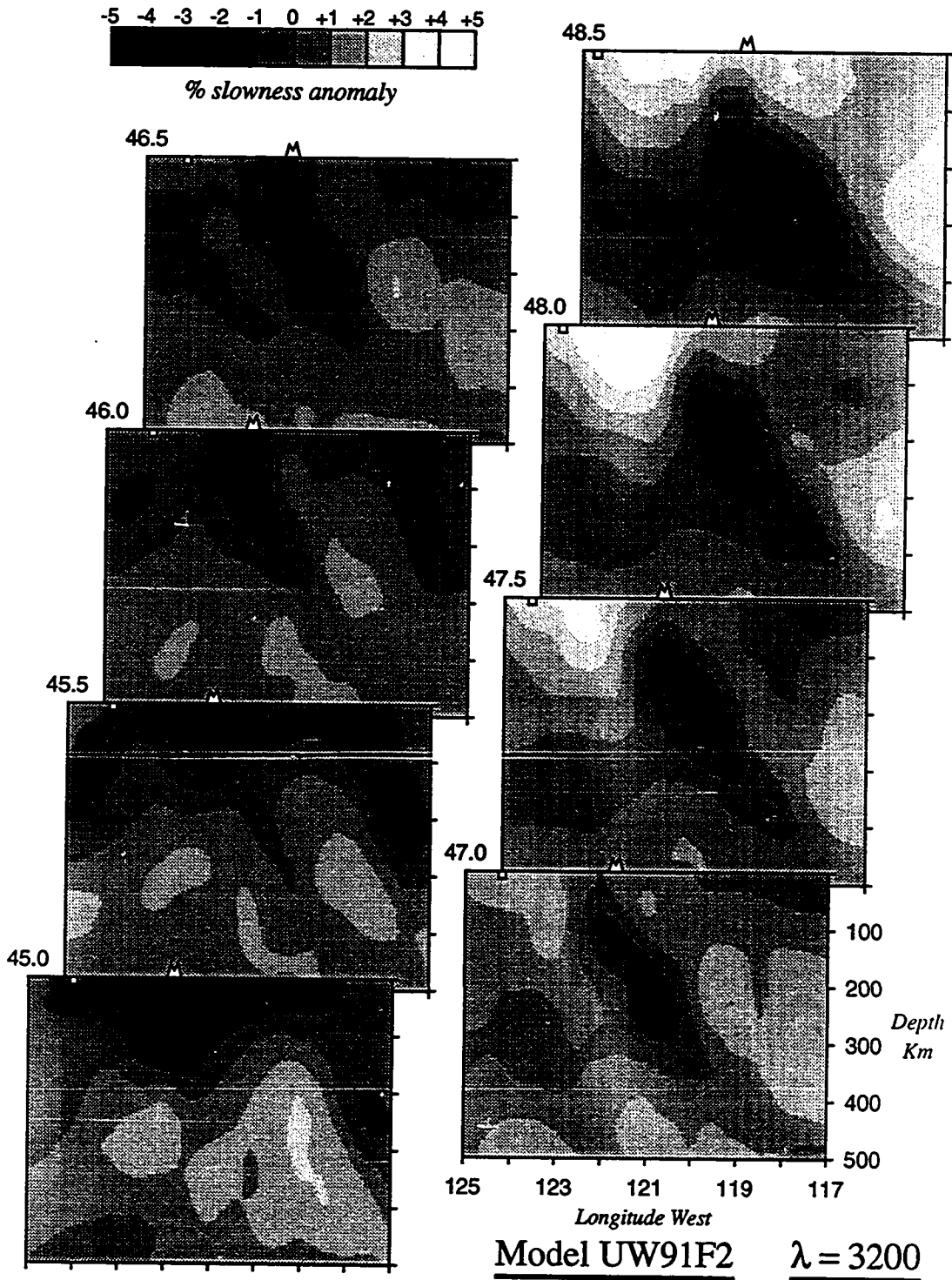
The effect of this second iteration on the exterior region is shown in Figure 5.12. The high velocity blob seen in the previous iteration is still present but has thinned slightly. The size of this anomaly is on the order the smallest possible with our parameterization (compare with the phantom spike model in Figure 5.3*a*) and therefore we know not expect any further significant decrease in its size. It does, however, appear that a high velocity feature of some sort is required by the data in



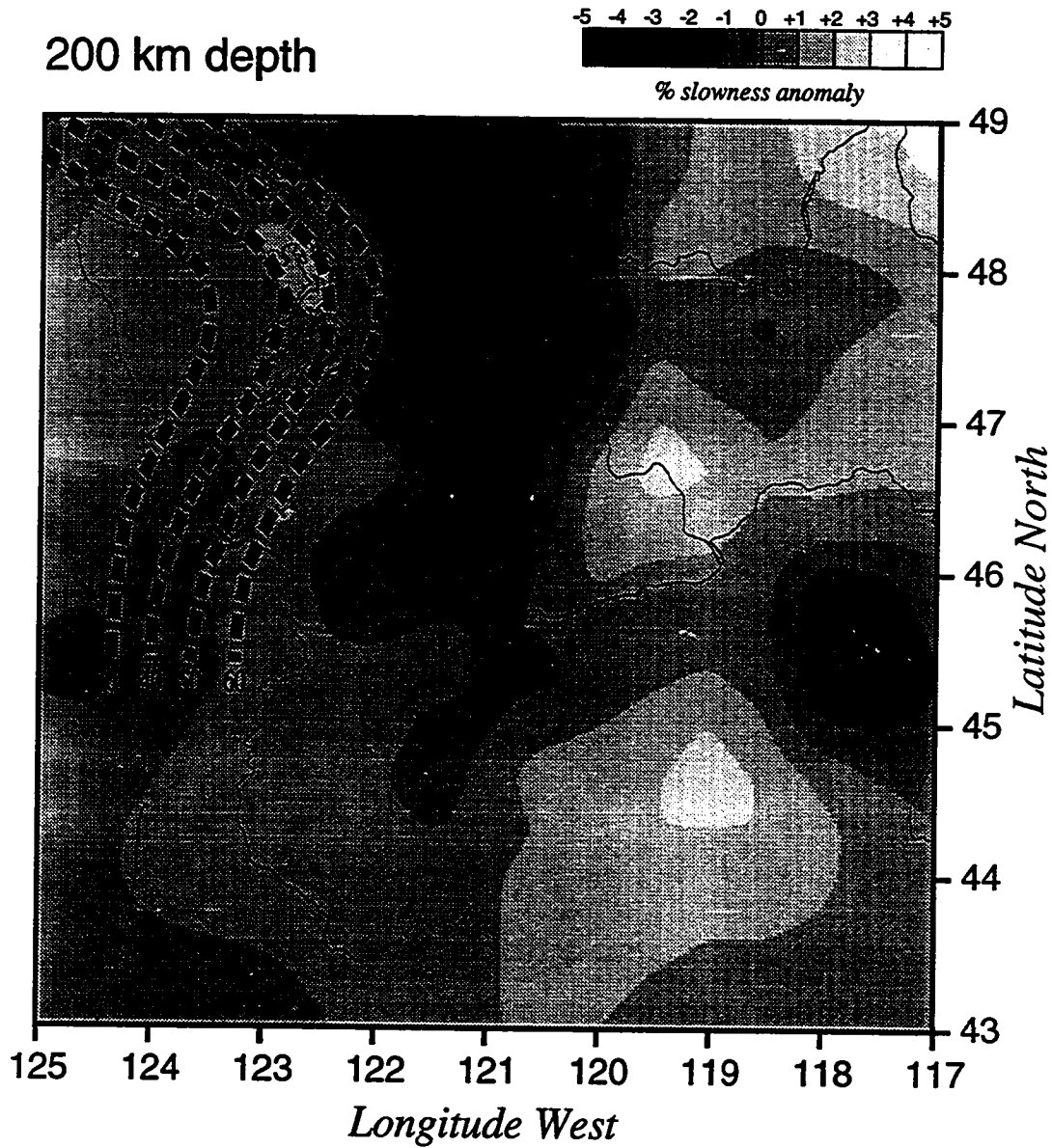
(a)

Figure 5.10a,b Latitudinal slices through the interior of slowness model UW91F2 for regularizations of (a) 1600 and (b) 3200. This model represents a non-linear inversion (ray paths were obtained from model UW91F1). See text for interpretation.

Figure 5.10 (continued)



(b)



Model UW91F2 $\lambda = 3200$

Figure 5.11 Slice through non-linear slowness perturbation model UW91F2 at 200 km depth with map of region and contours of shallow slab structure superimposed (see section 1.3.1 for description and origin of contours).

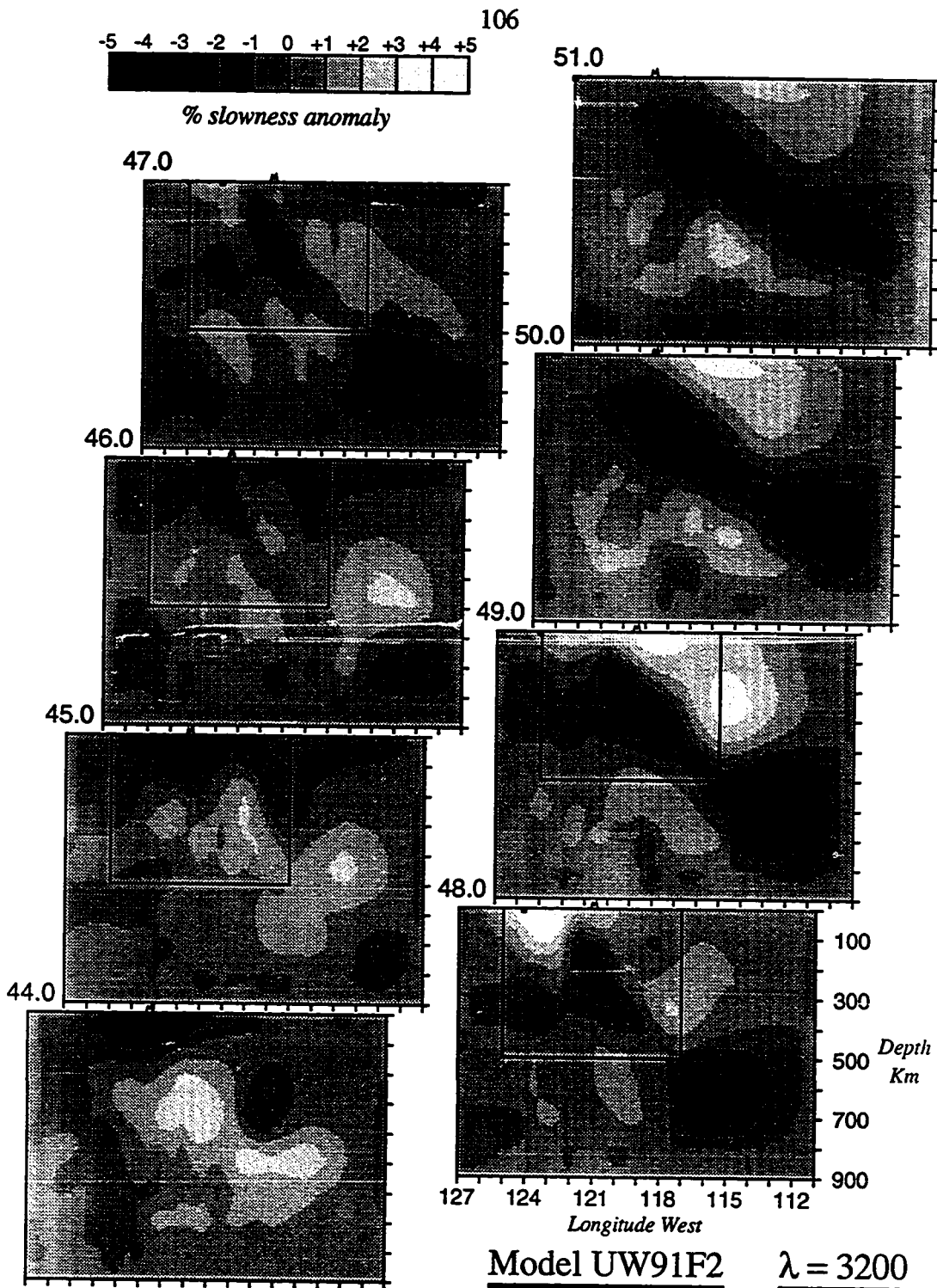


Figure 5.12 Latitudinal slices through the entirety of slowness model UW91F2 for a regularization of 3200. This model represents a non-linear inversion. The region outside of the interior boxes is not well resolved. See text for interpretation.

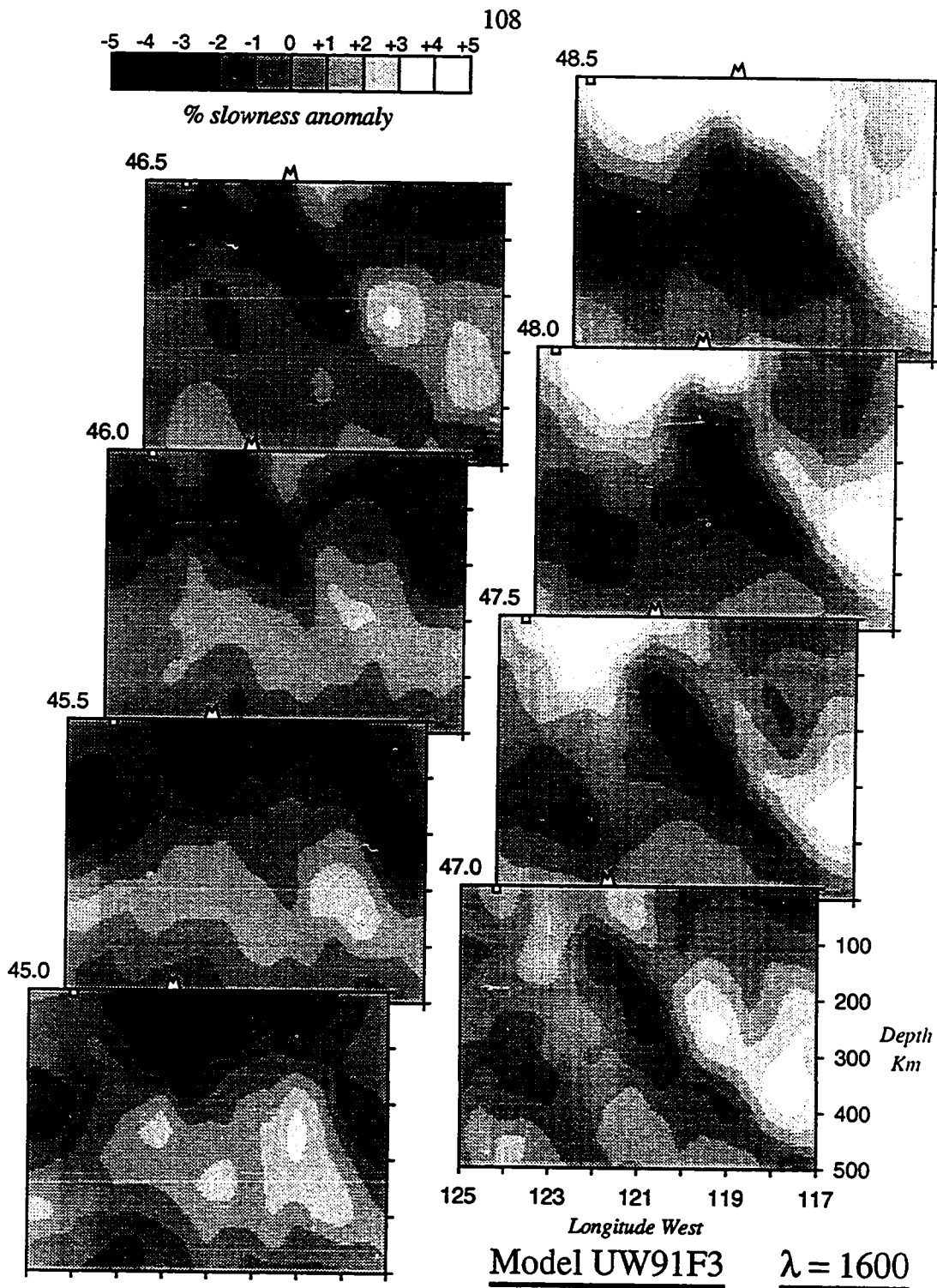
this region. Although the overall shapes and placement of anomalies do not change dramatically between these iterations, we now hopefully have a more reliable basis on which to make inferences about geodynamical forces and processes which may control the tectonic development of the region.

5.3.3 Third Iteration Model UW91F3

We have ray traced through model UW91F2 with λ equal to 3200 and calculated the associated partial derivatives and predicted travel times to invert for the series of models represented as latitudinal cross-sections in Figures 5.13*a,b* (for λ once again equal to 1600 and 3200). The 'trade-off' curve between smoothness and data fit is not substantially different than that for model UW91F2 and, in fact, the effect of using a smoother model ($\lambda = 3200$) in ray tracing through UW91F2 than we did through UW91F1 (where we used $\lambda = 1600$) seems to have a larger overall effect than the additional iteration. In detail, however, where the model gradients were large such as around the inferred position of the subducting Juan de Fuca plate, we do see a further reduction in the slab anomaly width.

This can be seen best by comparing the depth sections of the previous iteration's models (Figures 5.8 and 5.11) to the depth section at 200 km for model UW91F3 (Figure 5.14). We see that there indeed is a further focusing of structure, but the effect is not as great as in the previous iteration and we therefore do not expect further iterations of this process to substantially alter this structure. By comparing the outside model structure shown in Figures 5.9 and 5.12 to that for Figure 5.15 we see that there is not a large enough change in this down dip high velocity to alter our interpretation of it or its origin (which will be discussed further in Chapter 7). We have found through ray tracing tests through model UW91F3 for selected rays that, as expected, the ray paths did not change significantly from their previous positions. We therefore conclude that two iterations of the non-linear procedure are sufficient to bring the ray paths as close to being in agreement with the inverted model as our travel-time data can constrain.

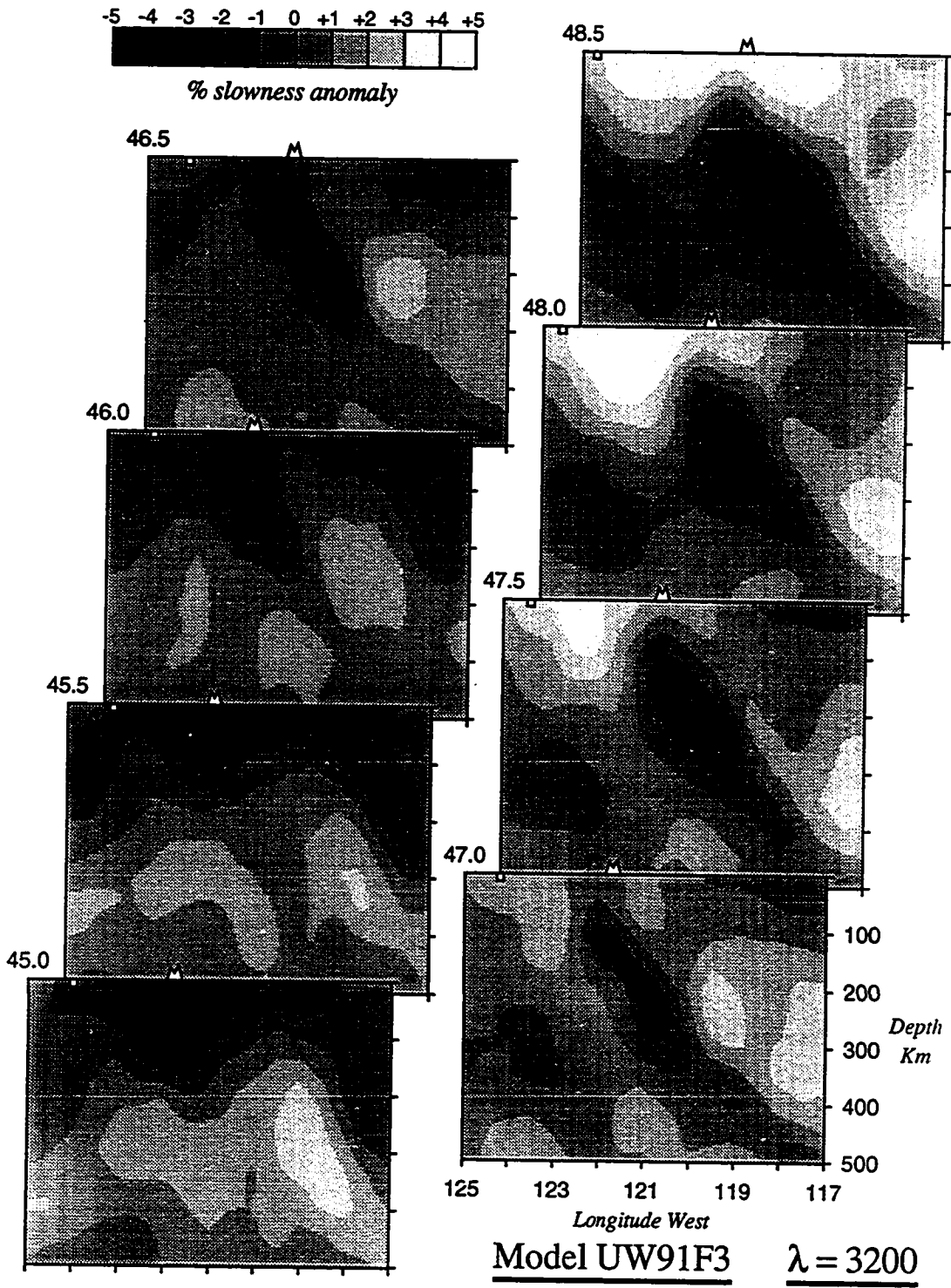
To aid in our comparison of these three models we have plotted in Figure 5.16 the slowness anomalies at 200 km depth as a function of longitude averaged from latitudes 47 N to 48 N. Although the mean value along this strip has changed over these inversion iterations, we can easily compare the peak-to-peak anomaly



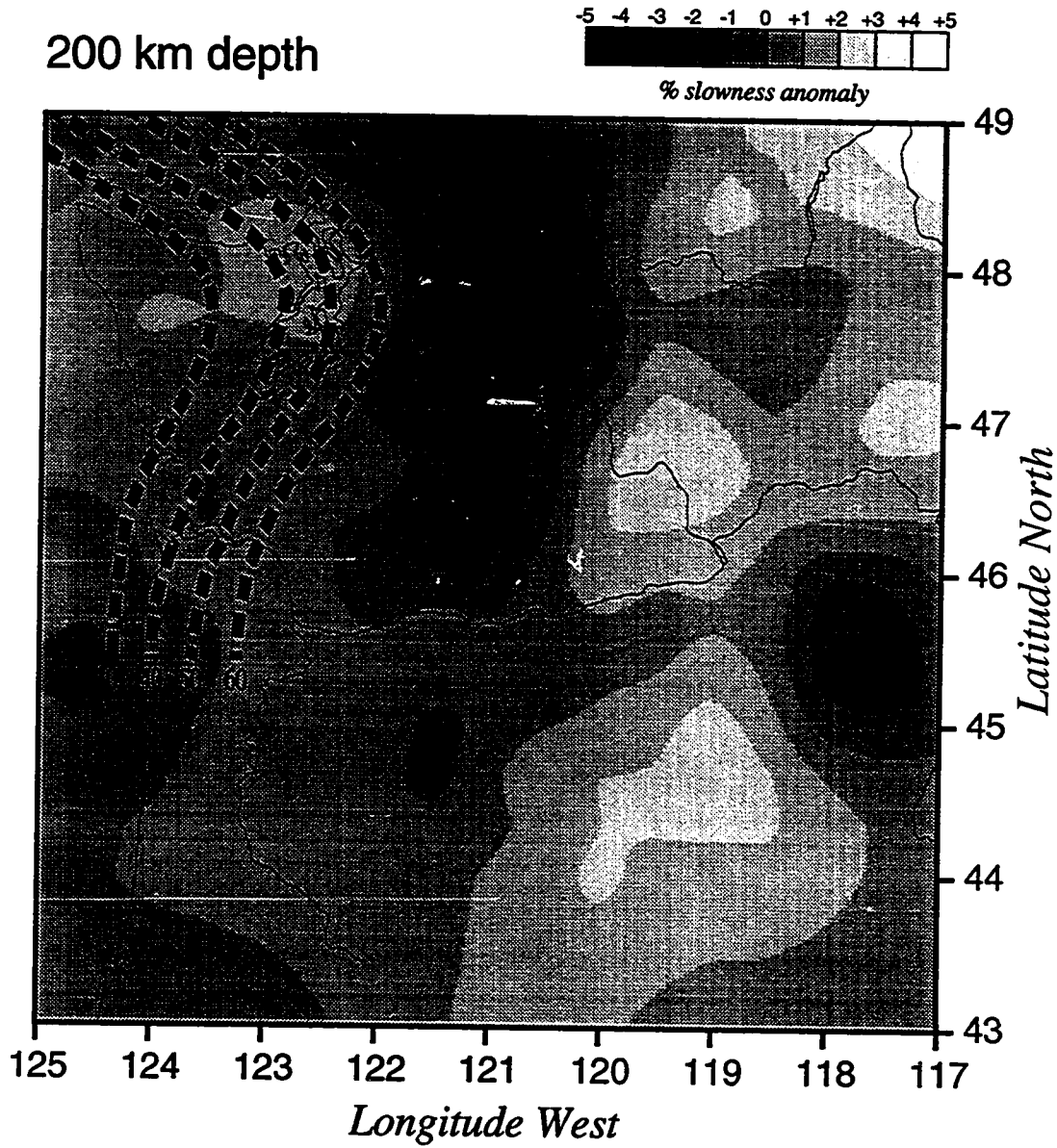
(a)

Figure 5.13a,b Latitudinal slices through the interior of slowness model UW91F3 for regularizations of (a) 1600 and (b) 3200. This model represents a non-linear inversion (ray paths were obtained from model UW91F2). See text for interpretation.

Figure 5.13 (continued)



(b)



Model UW91F3 $\lambda = 3200$

Figure 5.14 Slice through non-linear slowness perturbation model UW91F3 at 200 km depth with map of region and contours of shallow slab structure superimposed (see section 1.3.1 for description and origin of contours).

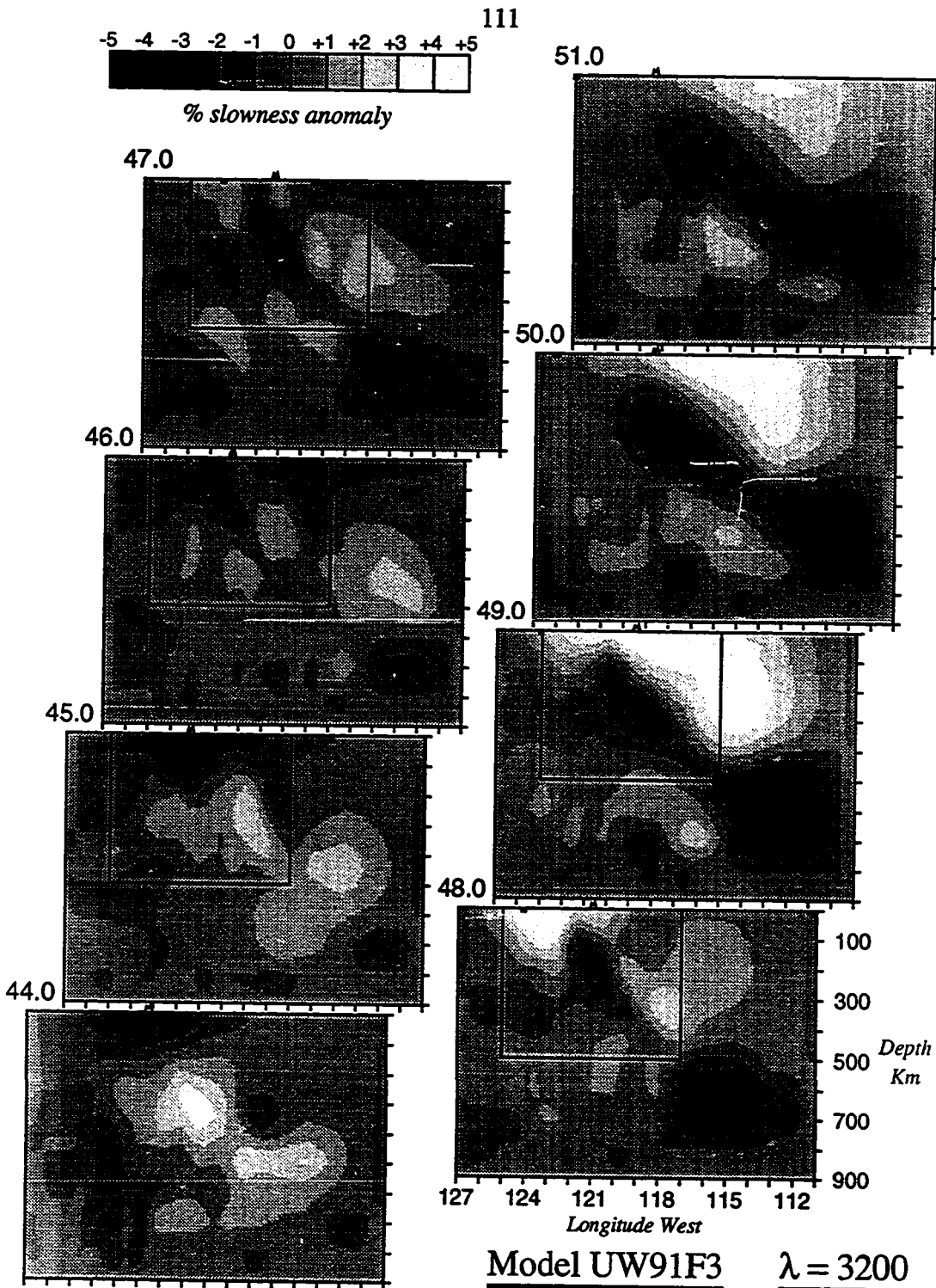


Figure 5.15 Latitudinal slices through the entirety of slowness model UW91F3 for a regularization of 3200. This model represents a non-linear inversion. The region outside of the interior boxes is not well resolved. See text for interpretation.

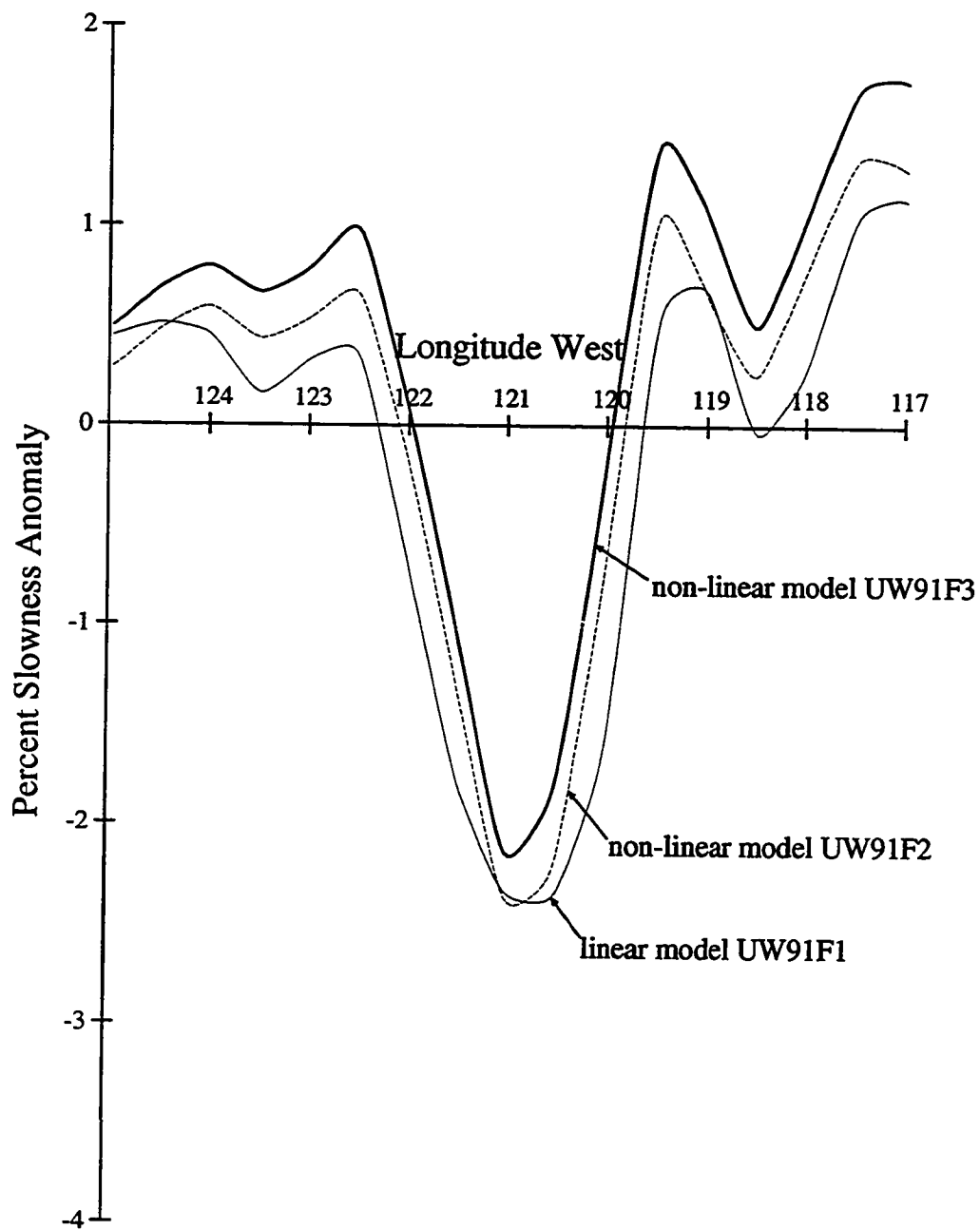


Figure 5.16 Slowness Anomalies at 200 km depth as a function of longitude averaged over latitude from 47N to 48N, for models UW91F1, UW91F2, and UW91F3, with $\lambda = 3200$.

variations and associated half widths to see that the anomaly has narrowed and increased in magnitude. These changes are more prominent between iterations 1 and 2 (represented by models UW91F1 and UW91F2) than between iterations 2 and 3 (represented by model UW91F3). Once again it should be noted that this is a cut through the model at equal depth (not perpendicular to the slab) and therefore the true width of the anomaly is less than it appears here.

Chapter 6

P-wave Amplitude Analysis

6.1 Introduction

The use of teleseismic phase travel times alone to invert for subduction zone velocity structure may lead to an ambiguous characterization of slab thickness [e.g. *Fischer et al.* 1988]. We have shown how this ambiguity arises from the effect of ray-bending on waves traveling up-dip along the subducting slab. For thin slabs (with appropriately large velocity gradients) the rays remain within the slab longer and defocus more on emergence producing low amplitude arrivals at the surface relative to thick slabs. However, only small changes in travel time are calculated. This makes the use of the amplitudes of first arrivals a promising data set to distinguish slab thickness. A significant challenge to using amplitude data, however, is to properly calibrate the stations for both instrument and local site response.

At the Washington Regional Seismic Network (WRSN) we have found that a large portion of the variation in local site response can be attributed to geologic factors as well as instrumental effects. We have generated a set of calibration values for the WRSN by averaging the P-wave amplitudes of many events from western azimuths whose ray paths travel approximately perpendicular to the slab and are therefore minimally affected by this deep structure. We discuss this calibration in §6.2. In §6.3 we then use these values to normalize amplitudes observed from wavefronts propagating *up* the dip of the slab in order to compare this observation with what we would expect from the structure of a subducting slab. Finally in §6.4 we will compare these observations with the amplitude response calculated from our models with Chapter 5.

6.2 Inversion for Site Amplitude Responses

Since we are dealing with a band-limited data set, we consider the origin of the amplitude of a *P*-wave first arrival to be simply decomposable into the following product,

$$\alpha_k = \rho_k \varepsilon_j \sigma_i, \quad (6.2.1)$$

where

α_k = the measured amplitude of the k^{th} arrival,

ρ_k = regional propagation effect for k^{th} ray (within 3D model),

ϵ_j = the earthquake source term for j^{th} event, and

σ_i = site response term for i^{th} station,

with i and j completely determined by k . Since many of our instruments are uncalibrated and instrumental and local geologic effects are, for practical purposes, unresolvable from one another with the use of data alone, we have simply combined these two effects into the *site response* term, σ_i . We also have assumed that the earthquake source term ϵ will absorb any path effects originating near the source or outside of our three-dimensional model, as these too are unresolvable from one another. Taking the log (base 10) of both sides of (6.2.1) we obtain

$$\log \alpha_k = \log \rho_k + \log \epsilon_j + \log \sigma_i \quad (6.2.2)$$

which is now amenable to matrix manipulation.[†] For the simple case of two events and four stations (with all events recorded at all stations), we can express (6.2.2) as the matrix product

$$\begin{bmatrix} 1 & . & . & . & 1 & . \\ 1 & . & . & . & . & 1 \\ . & 1 & . & . & 1 & . \\ . & 1 & . & . & . & 1 \\ . & . & 1 & . & 1 & . \\ . & . & 1 & . & . & 1 \\ . & . & . & 1 & 1 & . \\ . & . & . & 1 & . & 1 \\ 1 & . & . & . & . & . \end{bmatrix} \begin{bmatrix} \log \sigma_1 \\ \log \sigma_2 \\ \log \sigma_3 \\ \log \sigma_4 \\ \log \epsilon_1 \\ \log \epsilon_2 \end{bmatrix} = \begin{bmatrix} \log \alpha_1 \\ \log \alpha_2 \\ \log \alpha_3 \\ \log \alpha_4 \\ \log \alpha_5 \\ \log \alpha_6 \\ \log \alpha_7 \\ \log \alpha_8 \\ 0 \end{bmatrix} - \begin{bmatrix} \log \rho_1 \\ \log \rho_2 \\ \log \rho_3 \\ \log \rho_4 \\ \log \rho_5 \\ \log \rho_6 \\ \log \rho_7 \\ \log \rho_8 \\ 0 \end{bmatrix}$$

[†] Log notation here represents log base 10. Thomson and Gubbins [1982] and others have found amplitude data to have a lognormal distribution.

where a ‘.’ represents a zero matrix element, or symbolically as

$$\Omega \begin{bmatrix} \log \sigma \\ \log \varepsilon \end{bmatrix} = \begin{bmatrix} \log \alpha \\ 0 \end{bmatrix} - \begin{bmatrix} \log \rho \\ 0 \end{bmatrix}. \quad (6.2.3)$$

In order to make inferences about the regional structure's effect on the amplitude measurements, α , we must correct for event and site responses, ε and σ . One way which we might attempt this is to collect event's from many different back azimuths and distances, assume that the regional effect on the amplitudes from this range of directions will vary randomly, and then invert for σ and ε with ρ simply considered noise. Given no *a priori* knowledge of the regional structure this would seem a logical course to take. Since we have good reason, however, to believe that the amplitude response from certain back azimuths will have a large regional anomaly while that from others will not, it makes more sense to discard high anomaly directions to avoid biasing our inversion results. In a subduction zone we expect a relatively large anomaly from waves traveling ‘up’ or parallel to the plate as opposed to perpendicularly through it. We will therefore use only events with rays arriving sub-perpendicular to the subducting slab (from western back azimuths) to solve for the site calibration factors, σ . Our inversion for the event calibration terms, ε , is necessary, but incidental to our current purpose since we will be using different events (from eastern back azimuths) to actually investigate regional (slab) structure.

In order to solve (6.2.3) for σ and ε we will implement a robust inversion technique of iterative residual down-weighting [Huber 1981, Egbert and Booker 1986]. We do this to stabilize our inversion process, for the amplitude data tend to contain a larger number of outliers than, for instance, travel-time data. This is due to the fact that there is no stationarity principle for amplitude data which is dependent on *gradients* of velocity. Therefore first order perturbations in the slowness field and hence ray paths will cause first order perturbations in measured amplitude. While this is ‘good’ in the sense that our data are very sensitive to our model, it does create a less stable data base from which to extract information. However, the effects of diffraction in producing ‘wavefront healing’ should smooth out some of this effect.

The iterative technique works by scaling each equation by a function of its residual obtained from the previous iteration. Such a function is shown in Figure 6.1 which has the effect, in the limit, of minimizing the residuals within 1.5 standard errors by the L_2 or least-squares norm while minimizing residuals which lie beyond 1.5 standard errors with the more robust L_1 norm [see *Huber* 1981]. Our method of calculating the standard errors with which to implement this method follows that of *Egbert and Booker* [1986]. The effect is to minimize the influence of 'outliers' - data which are effected by biases or noise beyond the Gaussian errors assumed in standard least-squares analysis. The results of such an inversion for the calibration factors, σ , after 5 iterations is shown contoured in map view in Figure 6.2 (we have found that this inversion procedure converges with 4-5 iterations for our data set). The scale in Figure 6.2 represents one order of magnitude.

6.3 Observed Amplitude Signature over the WRSN

With the station corrections obtained from the process described in §6.2 we may now scale amplitude data to eliminate, to some degree, the effect of local structure and instrument gain variations. If we consider equation (6.2.2) for the case of a series of events from approximately the same location we now expect the portion of the amplitude response arising from regional structure, ρ , to be the nearly the same at each station. We therefore have

$$\log \alpha_k = \log \rho_i + \log \varepsilon_j \quad (6.3.1)$$

where α has now been calibrated by dividing it by the previously calculated σ . Explicitly, for the case of 4 events and 2 stations, this becomes

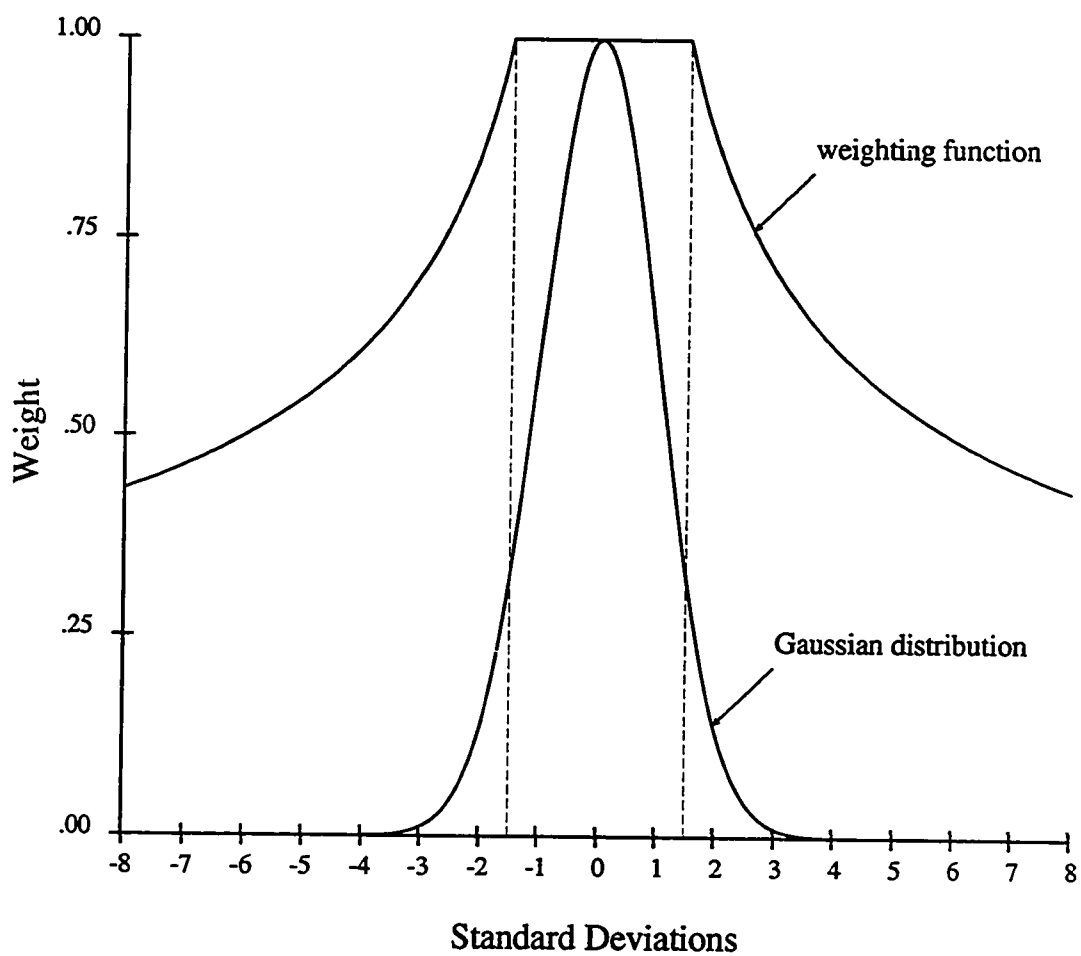
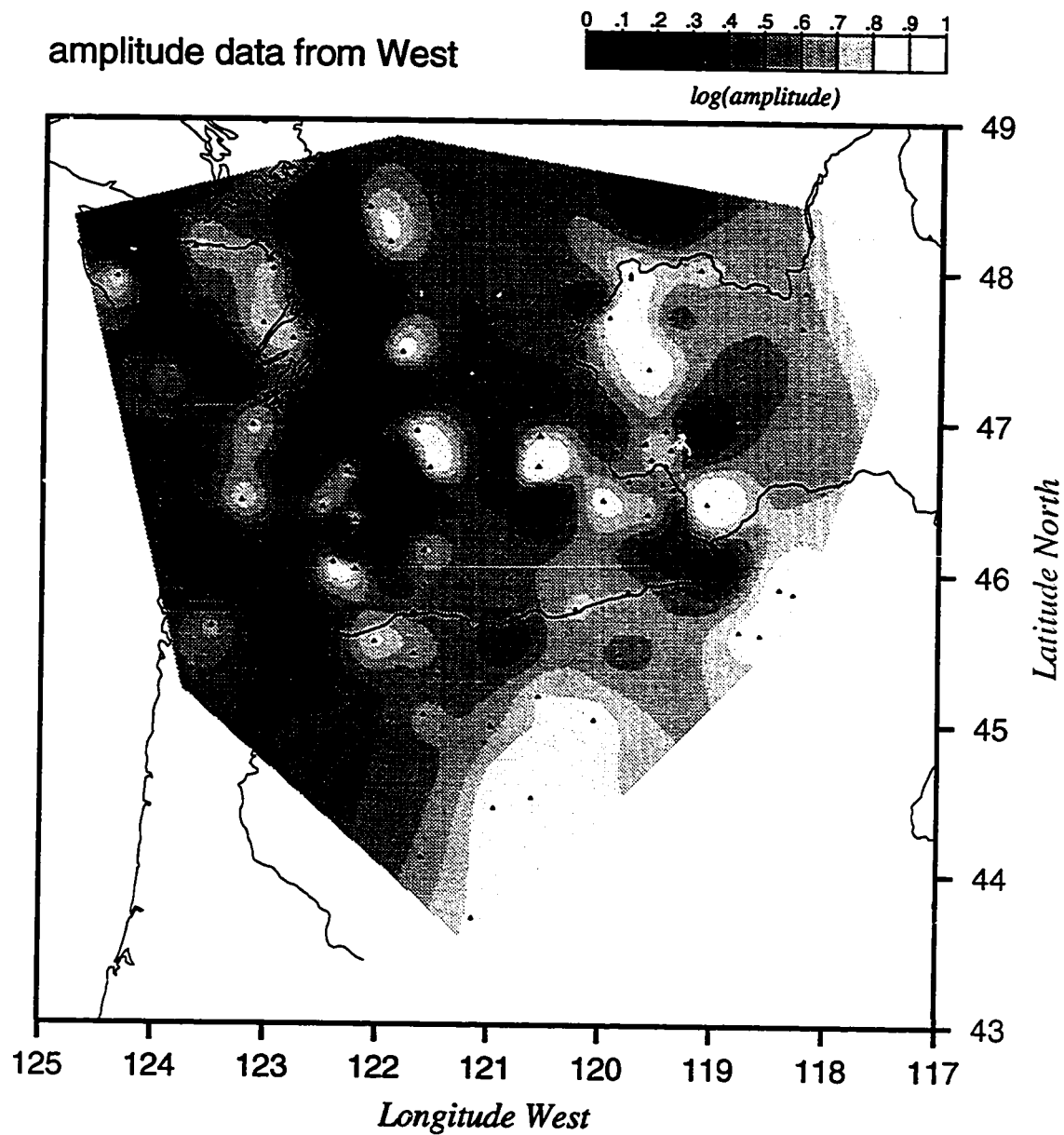


Figure 6.1 Weighting function used in robust iterative inversion technique. Residuals within 1.5 standard deviations are not weighted and therefore minimized with a least-squares norm while residuals outside are minimized, in the limit, as $|r|$.



Site Calibrations

Figure 6.2 Amplitudes of P-wave data from western azimuths inverted for with a robust iterative inversion technique to obtain site calibrations. See text for details.

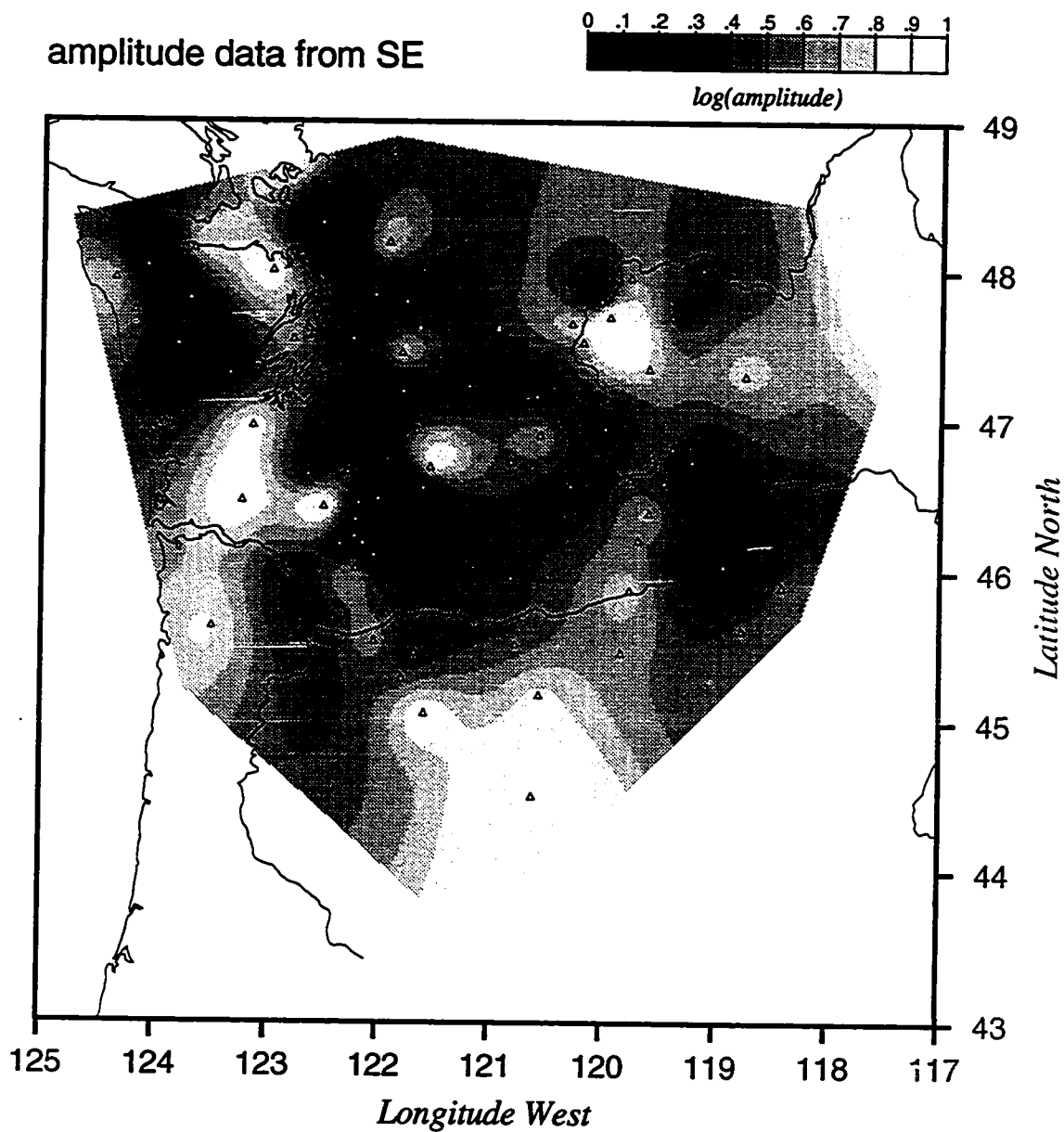
$$\begin{bmatrix} 1 & . & 1 & . & . & . \\ . & 1 & . & 1 & . & . \\ 1 & . & . & . & 1 & . \\ . & 1 & . & . & . & 1 \\ 1 & . & 1 & . & . & . \\ . & 1 & . & 1 & . & . \\ 1 & . & . & . & 1 & . \\ . & 1 & . & . & . & 1 \\ 1 & . & . & . & . & . \end{bmatrix} \begin{bmatrix} \log \rho_1 \\ \log \rho_2 \\ \log \varepsilon_1 \\ \log \varepsilon_2 \\ \log \varepsilon_3 \\ \log \varepsilon_4 \end{bmatrix} = \begin{bmatrix} \log \alpha_1 \\ \log \alpha_2 \\ \log \alpha_3 \\ \log \alpha_4 \\ \log \alpha_5 \\ \log \alpha_6 \\ \log \alpha_7 \\ \log \alpha_8 \\ 1 \end{bmatrix} .$$

Symbolically this may be written as

$$\Psi \begin{bmatrix} \log \rho \\ \log \varepsilon \end{bmatrix} = \begin{bmatrix} \log \alpha \\ 1 \end{bmatrix} . \quad (6.3.2)$$

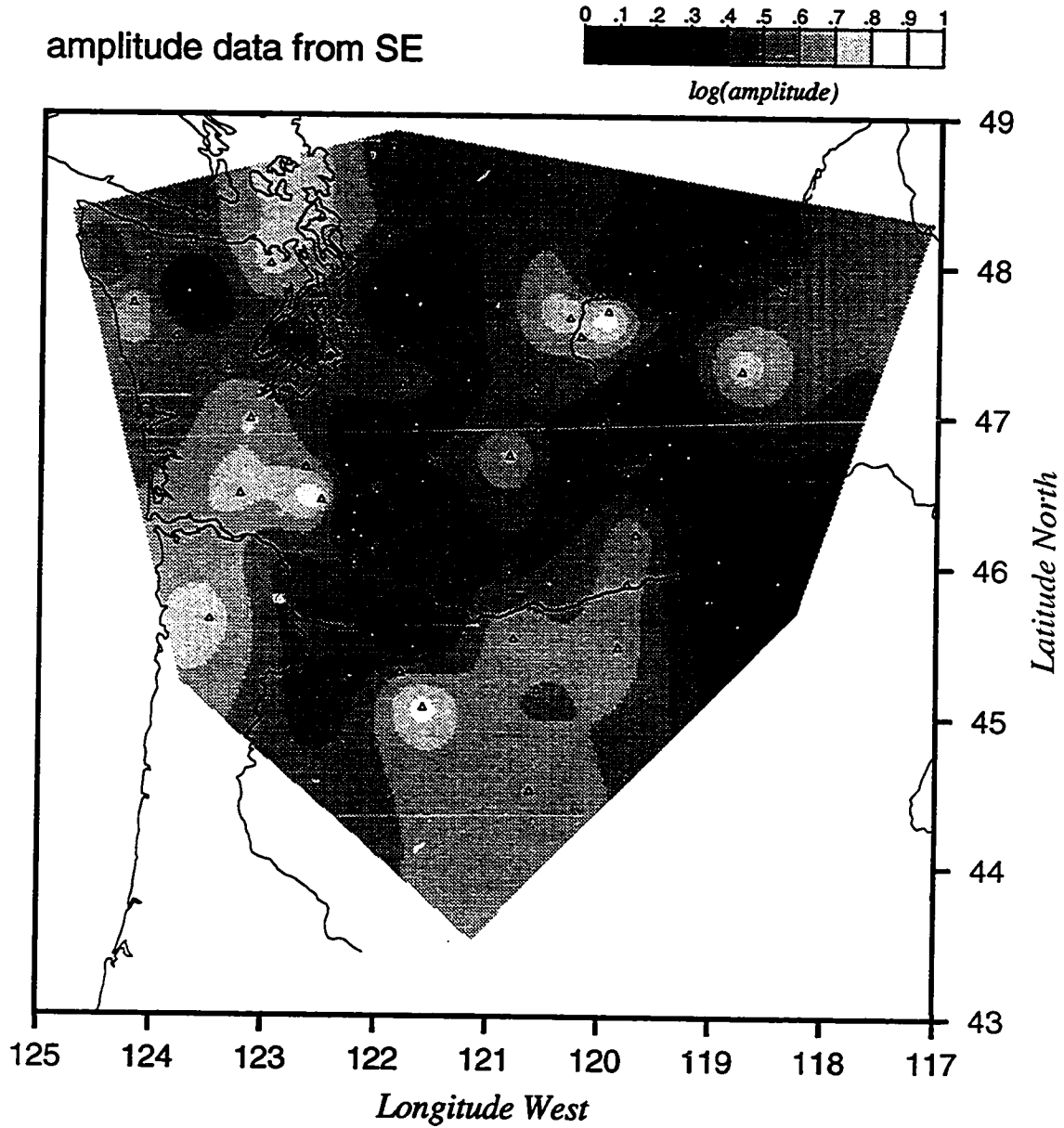
Our task is to now solve (6.3.2) for the effect of regional structure ρ and, of course, a scaler for each event, ε , given the calibrated amplitude data, α . Once again we will apply a robust iterative inversion technique to our problem due now both to the stability of the amplitude measurements and the calibration factors, σ . The results of such an inversion, with the use of 9 high quality events located near the Peru-Chile border (back azimuth $\approx 120^\circ$, $\Delta \approx 80^\circ$), is shown in Figures 6.3 and 6.4 for un-calibrated and calibrated data, respectively.

It is readily apparent that a large portion of the signal from these southeast back azimuths is consistent with that from western back azimuths as obtained from the calibration procedure. What is left after calibrating this data, however, is qualitatively consistent with what we expect from our knowledge of regional structure obtained from travel-time inversion. The low amplitude region to the east of Puget Sound continuing to the south, and that above northeastern Oregon are consistent with projections of the high velocity regions of our regional model, where we expect ray divergence to occur. In the next section we will examine quantitatively the amplitude anomalies produced by these velocity models. There remains in our amplitude data, however, more high frequency information than we expect to be able to obtain with a long wavelength regional velocity structure. This high spatial



Un-calibrated Data

Figure 6.3 Observed amplitudes of P-waves from South-east back azimuths, without amplitude calibrations applied, inverted for with a robust inversion technique.



Calibrated Data

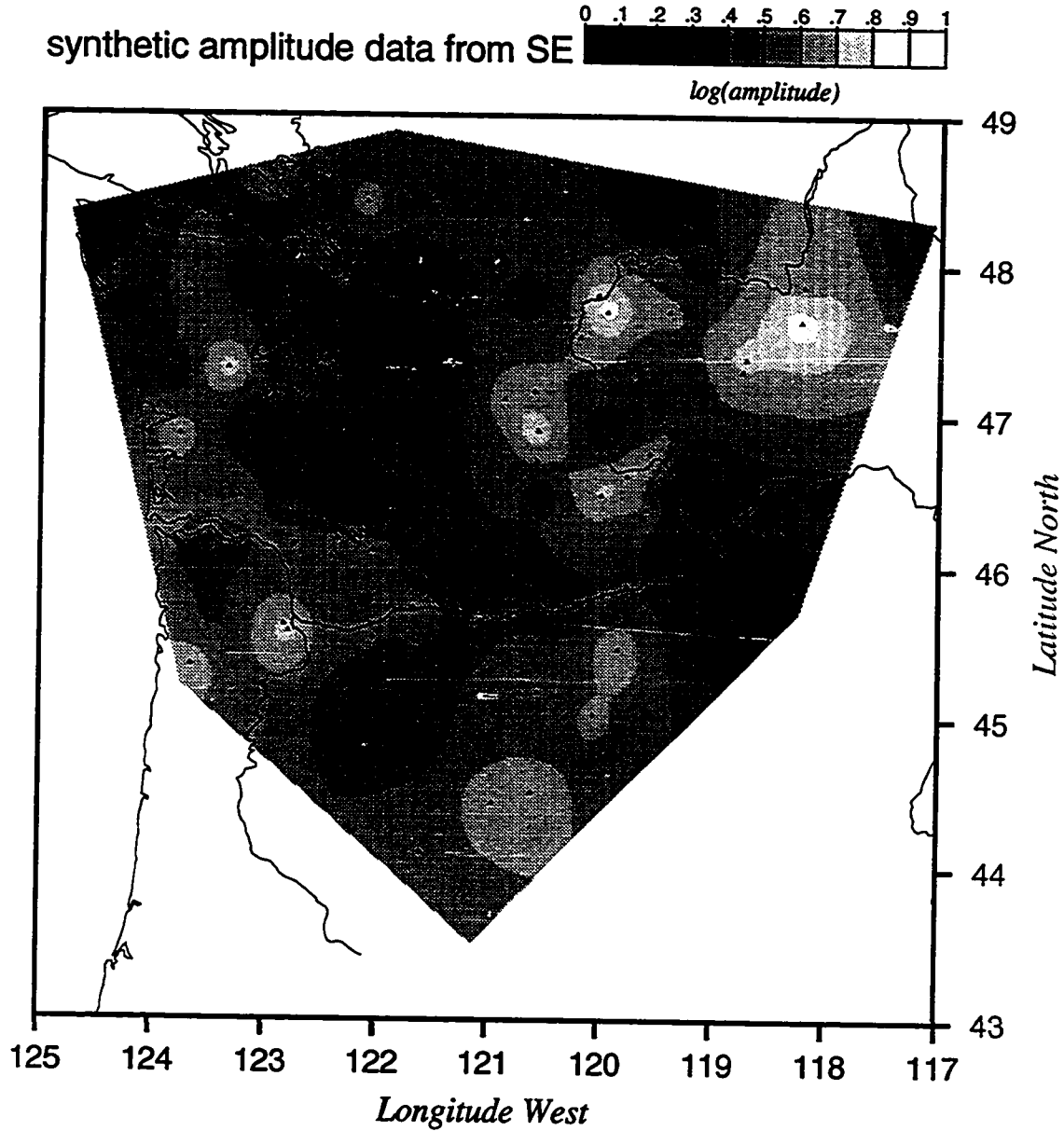
Figure 6.4 Observed amplitudes of P-waves from South-east back azimuths, after applying calibration correction, inverted for with a robust inversion technique.

frequency anomaly most likely arises both from intermediate and shallow depth anomalies not properly treated by our calibration procedure and from our use of too few events in both the calibration and southeast back azimuth analyses. There are many events available to be used in both analyses and the inclusion of further data no doubt will help stabilize these results.

6.4 Amplitude Response of the Cascadia Subduction Zone

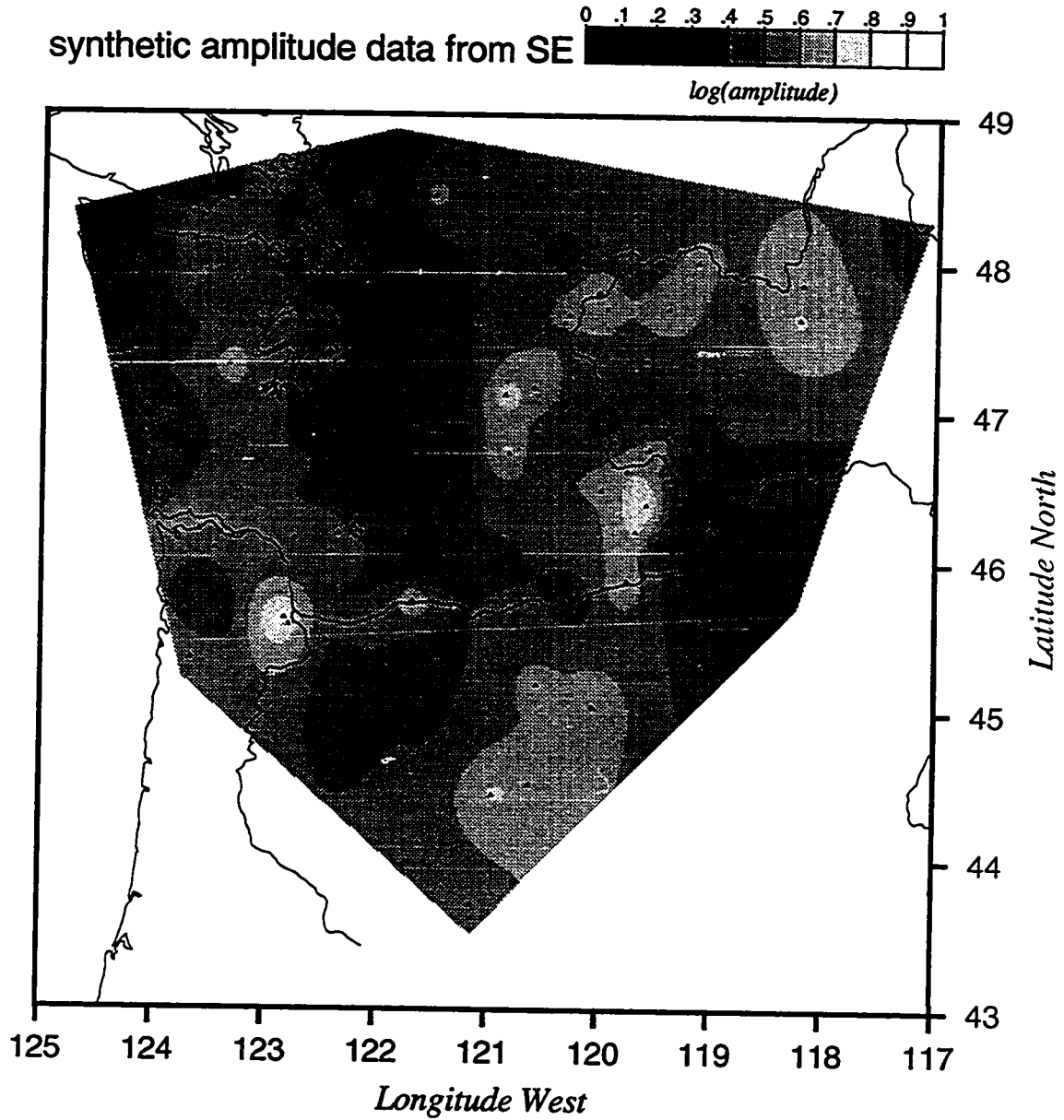
We estimate the amplitude anomalies expected from the models which we derived in Chapter 5 from travel-time inversion by calculating the degree of ray convergence and divergence through these models. We calculate the ray divergence by simply shooting two additional rays (in slightly different directions) after solving the two point ray tracing problem and then comparing the angles which they subtend near the receiver and at the source. Since we ray trace from receiver to source, we are here taking advantage of the reciprocity which exists between source and receiver responses [see *Aki and Richards* 1980]. In order to obtain reliable estimates of amplitude and also simulate the averaging nature of our observations, we perform this analysis on a grid of 16 event locations spanning approximately the same range as the events used in the previous section (approximately 4 degrees). We then perform the same inversion procedure as described above treating these calculations as our new 'data.'

The results of such an inversion can be seen in Figures 6.5 and 6.6 representing the amplitude response of slowness models UW91F1 and UW91F2, respectively. The non-linear model produces a narrower and more pronounced amplitude anomaly over the projected inferred position of the subducting slab as well as over the Blue Mountain anomaly in northeastern Oregon. Qualitatively these results indicate that the improvement made in performing the non-linear inversion produce a more believable structure, or at least one more consistent with other data sets.



Model UW91F1 $\lambda = 3200$

Figure 6.5 Predicted amplitudes of P-waves calculated from three-dimensional ray tracing through slowness model UW91F1 derived from travel-time inversion. See text for a detailed model interpretation.



Model UW91F2 $\lambda = 3200$

Figure 6.6 Predicted amplitudes of P-waves calculated from three-dimensional ray tracing through slowness model UW91F2 derived from travel-time inversion. See text for a detailed model interpretation.

Chapter 7

Summary and Conclusions

Our goal in this research was to obtain better resolution of the upper-mantle structure of the Cascadia subduction zone. To accomplish this we attacked on several fronts where we felt that substantial progress was feasible. The first of these was to obtain an 'optimal' data set, both in terms of coverage and quality. In this respect we were lucky enough to have over 10 years of high quality digital data available to us (over 3200 events) and the facilities and support to access, analyze, and archive this data in an efficient manner. Over this time span the range of data in terms of azimuth and distance with respect to the WRSN has been spanned to an extent well beyond that available to previous studies. We have described the distribution of this data set and the culling of the events used for further study in Chapter 2.

Our second challenge was to improve on the method of extraction of parameters from teleseismic data. Up to this point many researchers were using visually chosen arrival times and qualitative estimates of errors. We felt that this could be substantially improved and to do so developed a multi-channel cross correlation procedure to semi-automatically provide robust estimates of both relative arrival times and associated quantitative data variance. This analysis is detailed in Chapter 3 and in *VanDecar and Crosson [1990]*. The improvements in data analysis and quality probably have played a major role in achieving improved resolution.

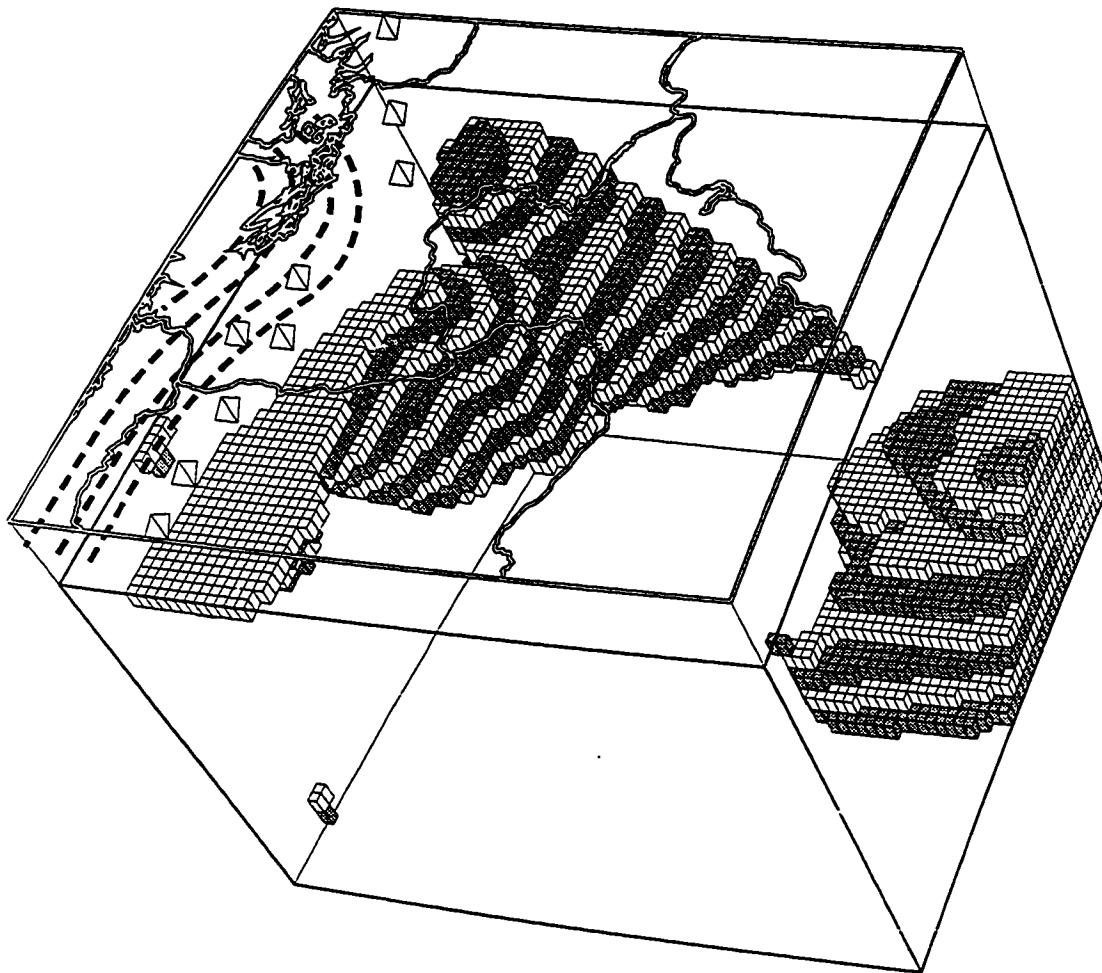
It has been common in structure inversion to assume linearity in the travel-time equations. While this may be justified in regions of low amplitude and relatively uncorrelated velocity anomalies, we have shown both with synthetic examples and actual data that for environments such as subduction zones that ignoring the non-linearity due to ray bending has an appreciable effect on the structure obtained. If we wish to use our inverted models to make quantitative inferences about tectonic processes then obtaining the best possible estimate of shape, location and *magnitude* of the velocity anomalies is essential. We therefore have taken into account the effects of ray bending by performing iterations of linear inversion employing three-dimensional ray tracing between iterations. This procedure appears to converge quickly for the case of the Cascadia subduction zone indicating that

after only 2 iterations the rays paths are linearly close to being consistent with the models obtained.

In order to judge our resolution over various parts of the model we have employed several methods of examining ray distribution and density. We have also performed both linear and 'non-linear' synthetic tests for various spike and slab-like structures. The results have indicated that our resolution is high over much of the upper mantle beneath the Cascadia subduction zone and sufficient, when combined with auxiliary data, to make inferences concerning the tectonic development of the region.

As discussed in the introduction on regional tectonics (§1.2), the Juan de Fuca plate system and presumably the Cascadia subduction zone have undergone dramatic changes over the past 7-10 Ma. The implications of this complicated tectonic history must be taken into account in order to predict what sort of structure one should expect for the *subducted* portion of the Juan de Fuca plate. A reduction in subduction rate of 45% or more over these time periods is sure to have effects at depth. Does the deep slab also slow by 45%? This would not seem logical if the forces of 'slab pull' play a major role in subduction zone dynamics. We therefore might expect this deeper portion of the slab to exert a sizable tensional stress on the upper part, possibly enough to pull it apart. This may even be a positive feedback process in that once the deep part of the slab is no longer providing a downward force, the upper portions may have that much more of a tendency to slow down.

These factors along with the 'direct' evidence from our images of current upper mantle structure, lead us to the conclusion that the older slab material that would now be beneath Oregon possibly ripped free from the shallow slab and continued to sink into the mantle at the rate it had prior to ≈ 10 Ma. In Figure 7.1a-c we have plotted in three-dimensional perspective (from various viewing points) the regions of our third iteration non-linear model UW91F3 (with $\lambda = 3200$) that have anomalies greater than 1% fast (the anomaly beneath the Blue Mountains of northeast Oregon has been removed for clarity). These figures illustrates the lack of deep slab material in the southern portions of our model and also hint that the deep fast material at approximately 600 km depth might be associated with this missing older portion of the slab. As we pointed out in Chapter 5, our resolution in this

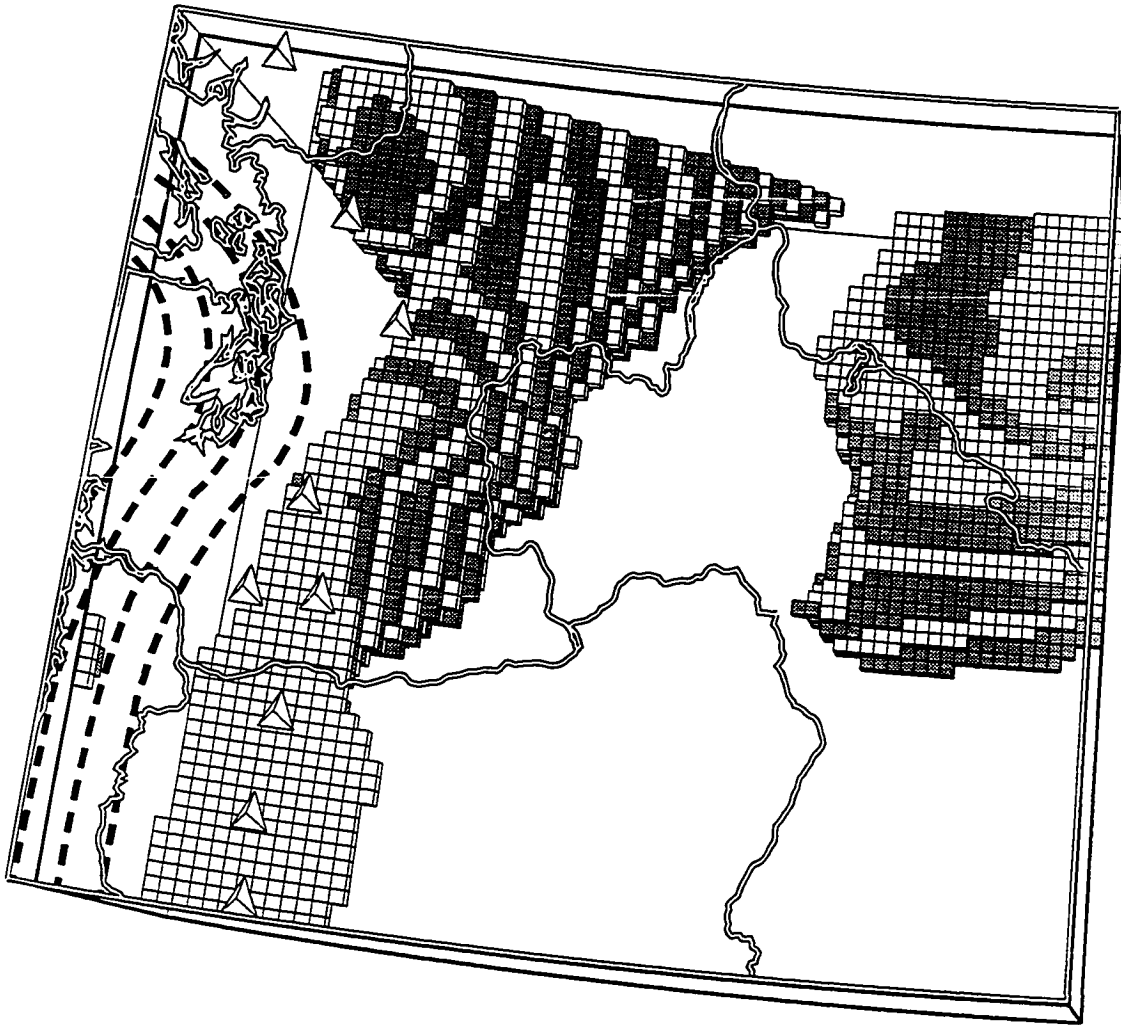


Model UW91F3 $\lambda = 3200$

(a)

Figure 7.1a-c Three-dimensional perspective of slowness model with regions of greater than 1% negative slowness (high velocity) within boxed regions. Viewing points are from above (a) Texas, (b) southern Idaho and (c) Kansas. The boxed region extends from 100 to 600 km in depth, 44N to 50N and 124W to 114W. Boxes are for plotting purposes only. An anomaly beneath the Blue Mtns. of NE Oregon has been removed for clarity. The pyramids at the surface represent Quaternary strato-volcanos.

Figure 7.1 (continued)

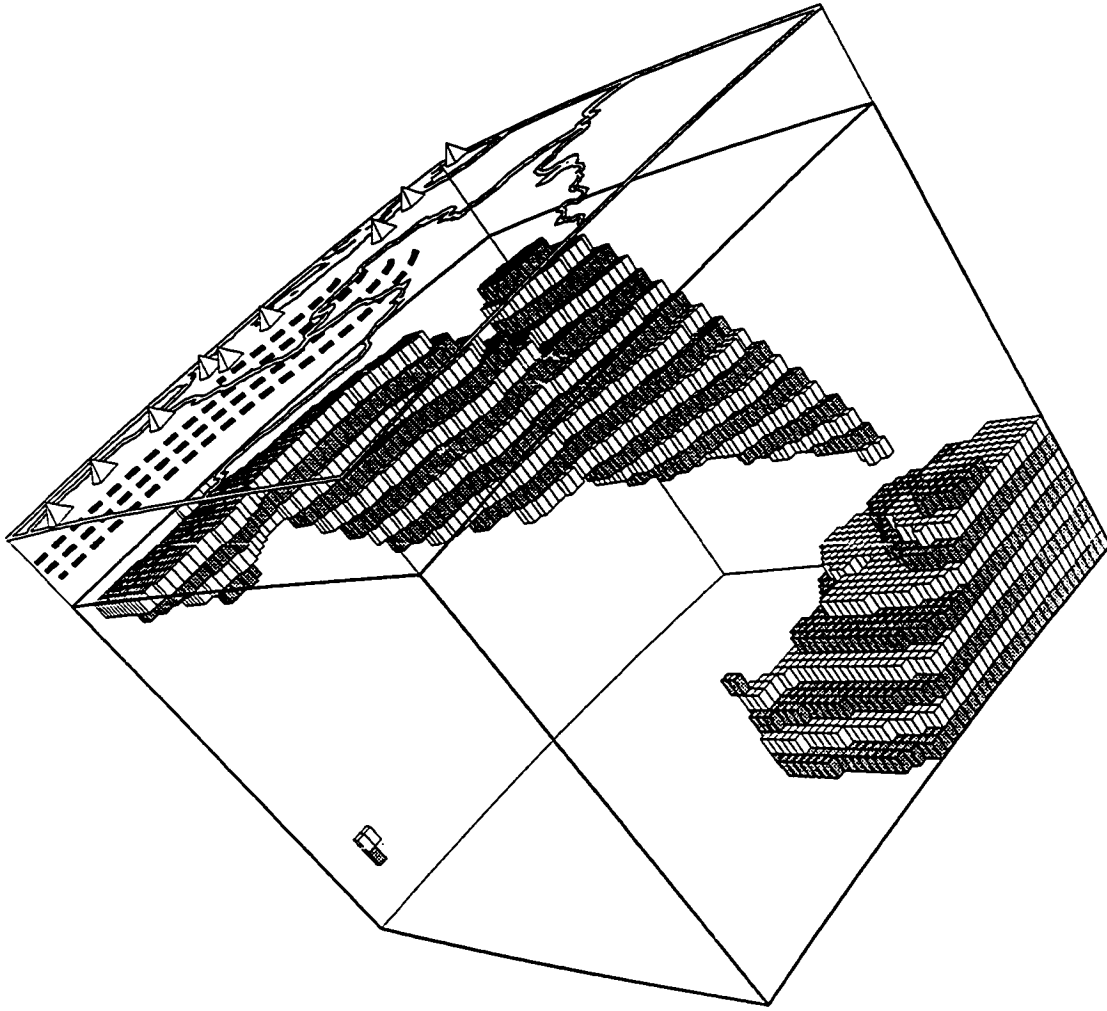


Model UW91F3

$\lambda = 3200$

(b)

Figure 7.1 (continued)



Model UW91F3

$\lambda = 3200$

(c)

deep region is poor so that we can not say whether this is really an isolated blob of material (possibly piling up at the 670 discontinuity) or whether it would continue deeper if our model parameterization allowed deeper structure.

This 'tear' that we are postulating presumably would propagate to the north, where the changes in subduction rate were less dramatic, possibly leaving only shallow slab material beneath Oregon. If the slab were rising buoyantly in the area where it has no deep root, we might expect the zone of magmatic activity at the surface to migrate eastward. This is consistent with the behavior reported by Priest [1990]. The well-recognized change in character of volcanism from Oregon and southern Washington to further north is such that to the south the number of volcanic vents is much greater and their distribution more widespread, while to the north volcanism is tightly centered around isolated strato-volcanos [e.g. *Guffanti and Weaver* 1988]. There also appear to be changes in volcanic composition from south to north. There are trace elements rarely found in arc volcanics yet common to ocean island and mid-ocean ridge basalts found in southern Washington and Oregon [e.g. *Leeman et al.* 1990]. Heat flow, too, is observed to be higher to the south.

It is tempting to postulate how such mantle material and high heat flow might arise from a 'window' to the mantle caused by a slab tear, but a more detailed synthesis of these varied observations must be done to make any positive statements. In Figure 7.1*b* we see that the upper portion of this upper mantle material is consistent with a steeply dipping slab to the north, but if the contours of shallow slab structure are correct, the transition from shallow to steep dip changes character from south to north. To the south, beneath Oregon, there is no need for a bend or knee in the subducting slab according to our images. This may help to explain the lack of seismicity within the subducted slab beneath Oregon. These images are in general consistent with the arc of recent Cascade volcanism that is thought to derive from the loss of volatiles from the subducting slab at approximately 100 to 120 km depth (as in other subduction zone regions). Finally, our model may also help to explain the locations and focal mechanisms of large earthquakes within the subducting slab that are concentrated below the Puget Sound and have down-dip tension axes [*Baker and Langston* 1987], since this structure would predict that the slab

might only be connected to a deep root beneath the northern portion of the subduction zone.

Bibliography

- Achauer, U., L. Green, J.R. Evans, and H.M. Iyer (1986). Nature of the magma chamber underlying the Mono Craters area, eastern California, as determined from teleseismic travel-time residuals, *J. Geophys. Res.*, **91**, 13,873-13,891.
- Achauer, U., J.R. Evans, and D.A. Stauber (1988). High resolution seismic tomography of compressional-wave velocity structure at Newberry Volcano, Oregon Cascade range, *J. Geophys. Res.*, **93**, 10,135-10,147.
- Aki, K., A. Christoffersson, and E.S. Husebye (1977). Determination of the three-dimensional seismic structure of the lithosphere, *J. Geophys. Res.*, **82**, 277-296.
- Aki, K. and P.G. Richards (1980). *Quantitative seismology - Theory and methods: I and II*, W.H. Freeman and Co., San Francisco, 932 pp.
- Allen, R.V. (1978). Automatic earthquake recognition and timing from single traces, *Bull. Seism. Soc. Am.*, **68**, 1521-1532.
- Allen, R.V. (1982). Automatic phase pickers: their present use and future prospects, *Bull. Seism. Soc. Am.*, **72**, 225-242.
- Anderson, D.L. (1987). Thermally induced phase changes, lateral heterogeneity of the mantle, continental roots, and deep slab anomalies, *J. Geophys. Res.*, **92**, 13,968-13,980.
- Archambeau, C.B., J.C. Bradford, P.W. Broome, W.C. Dean, E.A. Flinn, and R.L. Sax (1965). Data processing techniques for the detection and interpretation of teleseismic signals, *Proc. IEEE*, **53**, 1860-1884.
- Atwater, T. (1970). Implications of plate tectonics for the Cenozoic tectonic evolution of western North America, *Geol. Soc. Am. Bull.*, **81**, 3513-3536.
- Backus, G.E. and J.F. Gilbert (1967). Numerical applications of a formalism for geophysical inverse problems, *Geophys. J. Roy. Astr. Soc.*, **13**, 247-276.
- Backus, G.E. and J.F. Gilbert (1968). The resolving power of gross Earth data, *Geophys. J. Roy. Astr. Soc.*, **16**, 169-205.
- Backus, G.E. and J.F. Gilbert (1970). Uniqueness in the inversion of inaccurate gross Earth data, *Proc., Roy. Soc. London, Ser. A*, **266**, 123-192.
- Backus, G.E. (1988). Comparing hard and soft prior bounds in geophysical inverse problems, *Geophys. J.*, **94**, 249-261.
- Backus, M.M., J.P. Burg, D. Baldwin, and E. Bryan (1964). Wide-band extraction

- of mantle P-waves from ambient noise, *Geophysics*, **29**, 672-692.
- Baker, G.E. and C.A. Langston (1987). Source parameters of the 1949 magnitude 7.1 South Puget Sound, Washington, earthquake as determined from long-period body waves and strong motions, *Bull. Seis. Soc. Am.*, **77**, 1530-1557.
- Baldwin, R. (1965). Engineering aspects of multichannel processing based on measured noise correlations, *Proc. IEEE*, **53**, 1884-1889.
- Barton, P.J. (1986). The relationship between seismic velocity and density in the continental crust - a useful constraint?, *Geophys. J. Roy. Astr. Soc.*, **87**, 195-208.
- Ben-Menahem, A. and W.B. Beydoun (1985). Range of validity of seismic ray and beam methods in general inhomogeneous media - I. General theory, *Geophys. J. R. Astr. Soc.*, **82**, 207-234.
- Berteussen, K.-A. (1975). Crustal structure and P-wave travel time anomalies at NORSAR, *J. Geophys.*, **41**, 71-84.
- Berteussen, K.A., A. Christoffersson, E.S. Husebye, and A. Dahle (1975). Wave scattering theory in analysis of P-wave anomalies at NORSAR and LASA, *Geophys. J. Roy. Astr. Soc.*, **42**, 403-417.
- Beydoun, W.B. and A. Ben-Menahem (1985). Range of validity of seismic ray and beam methods in general inhomogeneous media - II. A canonical problem, *Geophys. J. R. Astr. Soc.*, **82**, 235-262.
- Birtill, J.W. and F.E. Whiteway (1965). The application of phased arrays to the analysis of seismic body waves, *Proc., Roy. Soc. London, Ser. A*, **258**, 421-493.
- Bjorck, A. (1976). Methods for sparse linear least squares problems, in *Sparse Matrix Computations*, edited by J.R. Bunch and D.J. Rose, Academic Press, Inc., New York, 177-199.
- Bostrom, R.C. (1980). Tectonic sequence in the western states: Abbreviation of east limb, *EPR, Modern Geol.*, **7**, 67-74.
- Bostrom, R.C. (1984). Is Pacific NW subduction active, decaying or incipient? The 2-m geoid (abstract), *EOS*, **65**.
- Botros, M. and H.P. Johnson (1988). Tectonic evolution of the Explorer-Northern Juan de Fuca region from 8 Ma to the present, *J. Geophys. Res.*, **93**,

10,421-10,437.

- Bungum, H. and E.S. Husebye (1971). Errors in time delay measurements, *Pure Appl. Geophys.*, **91**, 56-70.
- Bungum, H., E.S. Husebye, and F. Ringdahl (1971). The NOR&SAR array and preliminary results of data analysis, *Geophys. J. Roy. Astr. Soc.*, **25**, 115-126.
- Bungum, H. and E.S. Husebye (1974). Analysis of the operational capabilities for the detection and location of seismic events at NOR&SAR, *Bull., Seis. Soc. Am.*, **64**, 637-656.
- Burg, J.P. (1964). Three-dimensional filtering with an array of seismometers, *Geophysics*, **29**, 693-713.
- Capon, J., R.J. Greenfield, and R.J. Kolker (1967). Multidimensional maximum-likelihood processing of a large aperture seismic array, *Proc. IEEE*, **55**, 192-211.
- Capon, J., R.J. Greenfield, R.J. Kolker, and R.T. Lacoss (1968). Short-period signal processing results for the Large Aperture Seismic Array, *Geophysics*, **33**, 452-472.
- Carlson, R.L. (1976). *Cenozoic Plate convergence in the vicinity of the Pacific Northwest: A synthesis and assessment of plate tectonics in the Northeastern Pacific*, Ph.D. thesis, Univ. of Washington, Seattle, .
- Carson, B.J., J. Yuan, P.B. Meyers, and W.D. Bernard (1974). Initial deep-sea sediment deformation at the base of the Washington continental margin, *Geology*, **2**, 561-564.
- Catchings, R.D. and W.D. Mooney (1988). Crustal structure of the Columbia Plateau: Evidence for continental rifting, *J. Geophys. Res.*, **93**, 459-474.
- Cervený, V. and I. Psencik (1979). Ray amplitudes of seismic body waves in laterally inhomogeneous media, *Geophys. J. Roy. Astr. Soc.*, **57**, 91-106.
- Cervený, V. and J. Jansky (1983). Ray amplitudes of seismic body waves in inhomogeneous radially symmetric media, *Studia Geoph. et geod.*, **27**, 9-18.
- Chapman, C.H. and J.A. Orcutt (1985). Least-squares fitting of marine seismic refraction data, *Geophys. J. R. Astr. Soc.*, **82**, 339-374.
- Chiao, L.Y. and K.C. Creager (1990). Geometric constraints on Cascadia subduction (abstract), *EOS*, **71**, 1574.

- Chiu, J.M., B.L. Isacks, and R.C. Cardwell (1985). Propagation of high-frequency seismic waves inside the subducted lithosphere from intermediate-depth earthquakes recorded in the Vanuatu arc, *J. Geophys. Res.*, **90**, 12,741-12,754.
- Claerbout, J.F. (1964). Detection of P-waves from weak sources at great distances, *Geophysics*, **29**, 197-211.
- Cline, A.K. (1981). *FITPACK - Software package for curve and surface fitting employing splines under tension*, Department of Computer Sciences, University of Texas, Austin, Texas., .
- Clowes, R.M. (1987). LITHOPROBE: Exploring the subduction zone of Western Canada, *The Leading Edge*, **6**, 12-19.
- Constable, S.C., R.L. Parker, and C.G. Constable (1987). Occam's inversion: A practical algorithm for generating smooth models from electromagnetic sounding data, *Geophysics*, **52**, 289-300.
- Creager, K.C. (1984). *Geometry, velocity structure, and penetration depths of descending slabs in the western Pacific*, Ph.D. thesis, Univ. of California, San Diego, 205 pp.
- Creager, K.C. and T.H. Jordan (1984). Slab penetration into the lower mantle, *J. Geophys. Res.*, **89**, 3031-3049.
- Creager, K.C. and T.H. Jordan (1986). Slab penetration into the lower mantle beneath the Mariana and other island arc of the Northwest Pacific, *J. Geophys. Res.*, **91**, 3573-3589.
- Crosson, R.S. (1972). Small earthquakes, structure, and tectonics of the Puget Sound region, *Bull. Seis. Soc. Am.*, **62**, 1133-1171.
- Crosson, R.S. (1976a). Crustal structure modeling of earthquake data 1. Simultaneous least squares estimation of hypocenter and velocity parameters, *J. Geophys. Res.*, **81**, 3036-3046.
- Crosson, R.S. (1976b). Crustal structure modeling of earthquake data 2. Velocity structure of the Puget Sound region, Washington, *J. Geophys. Res.*, **81**, 3047-3054.
- Crosson, R.S., E.T. Endo, S.M. Malone, L.L. Noson, and C.S. Weaver (1980). Eruption of Mt. St. Helens: Seismology, *Nature*, **285**, 529-536.
- Crosson, R.S. (1983). Review of seismicity in the Puget Sound region from 1970

- through 1978, in *Proceedings of Workshop XIV, Earthquake Hazards of the Puget Sound Region, Washington, USGS Open File Rept. 83-19*, edited by J.C. Yount and R.S. Crosson, U.S. Geol. Survey, 6-18.
- Crosson, R.S. (1986). Comment on 'Geodetic strain measurements in Washington' by J.C. Savage, M. Lisowski, and W.H. Prescott, *J. Geophys. Res.*, **91**, 7555-7557.
- Crosson, R.S. and T.J. Owens (1987). Slab geometry of the Cascadia subduction zone beneath Washington from earthquake hypocenters and teleseismic converted waves, *Geophys. Res. Letts.*, **14**, 824-827.
- Crosson, R.S. and E.L. Crosson (1988). A new detection algorithm for phase arrivals using a regional seismograph network (abstract), *EOS*, **69**, 1307.
- Davies, D. and R.M. Sheppard (1972). Lateral heterogeneity in the Earth's mantle, *Nature*, **239**, 318-323.
- Dickinson, W.R. (1970). Relations of andesites, granites, and derivative sandstones to arc-trench tectonics, *Rev. Geophys.*, **8**, 813-860.
- Dragert, H., A. Lambert, and J. Liard (1981). Repeated precise gravity measurements on Vancouver Island, British Columbia, *J. Geophys. Res.*, **86**, 6097-6106.
- Dziewonski, A.M. and D.L. Anderson (1981). Preliminary Reference Earth Model, *Phys. Earth Plan. Int.*, **25**, 297-356.
- Dziewonski, A.M. (1984). Mapping the lower mantle: determination of lateral heterogeneity in P velocity up to degree and order 6, *J. Geophys. Res.*, **89**, 5929-5952.
- Dziewonski, A.M. and J.H. Woodhouse (1987). Global images of the Earth's interior, *Science*, **236**, 37-48.
- Egbert, G.D. and J.R. Booker (1986). Robust estimation of geomagnetic transfer functions, *Geophys. J. Roy. Astr. Soc.*, **87**, 173-194.
- Enayatollah, M.A. (1972). Travel times of P-waves for the Swedish-Finnish seismograph network, *Pure Appl. Geophys.*, **94**, 101-123.
- Engdahl, E.R. (1977). Seismicity and plate subduction in the central Aleutians, in *Island Arcs, Deep Sea Trenches and Back-arc Basins*, edited by M. Talwani and W.C. Pitman, American Geophysical Union Maurice Ewing Series, number 1, 259-271.

- Engebretson, D.C., A. Cox, and R.C. Gordon (1984). Relative motions between oceanic plates of the Pacific basin, *J. Geophys. Res.*, **89**, 10,291-10,310.
- Engebretson, D.C., A. Cox, and R.C. Gordon (1985). *Relative motions between oceanic and continental plates in the Pacific basin*, Geological Society of America, Boulder, 59 pp.
- Fawcett, J.A. and R.W. Clayton (1984). Tomographic reconstruction of velocity anomalies, *Bull., Seis. Soc. Am.*, **74**, 2201-2219.
- Fischer, K.M., T.H. Jordan, and K.C. Creager (1988). Seismic constraints on the morphology of deep slabs, *J. Geophys. Res.*, **93**, 4773-4783.
- Fletcher, J.B. and H.P. Lui (1985). Research note: Precise measurement of seismic travel times from an air gun source, *Geophys. J. R. Astr. Soc.*, **82**, 549-557.
- Franklin, J.N. (1970). Well-posed stochastic extensions of ill-posed linear problems, *J. Math. Anal. Appl.*, **31**, 682-716.
- Giardini, D. and J.H. Woodhouse (1984). Deep seismicity and modes of deformation in Tonga subduction zone, *Nature*, **307**, 505-509.
- Giardini, D. and J.H. Woodhouse (1986). Horizontal shear flow in the mantle beneath Tonga arc, *Nature*, **319**, 551-555.
- Gilbert, F. (1971a). The diagonal sum rule and averaged eigenfrequencies, *Geophys. J. R. Astr. Soc.*, **23**, 119-123.
- Gilbert, F. (1971b). Ranking and winnowing gross earth data for inversion and resolution, *Geophys. J. R. Astr. Soc.*, **23**, 125-128.
- Golizdra, G.Y. (1980). Statement of problems of comprehensive interpretation of gravity field and seismic observations, *Izvestiya, Earth Physics*, **16**, 535-539.
- Golub, G.H. and C.F. VanLoan (1983). *Matrix Computations*, The Johns Hopkins Univ. Press, Baltimore, 476 pp.
- Green, A.G., R.M. Clowes, C.J. Yorath, C. Spencer, E.R. Kanasewich, M.T. Brandon, and A.S. Brown (1986). Seismic reflection imaging of the subducting Juan de Fuca plate, *Nature*, **319**, 210-213.
- Green, P.E. Jr., R.A. Frosch, and C.F. Romney (1965). Principles of an experimental Large Aperture Seismic Array (LASA), *Proc. IEEE*, **53**, 1821-1833.

- Gubbins, D. and R. Snieder (1991). Dispersion of P waves in subducted lithosphere: Evidence for an Eclogite layer, *J. Geophys. Res.*, **96**, 6321-6333.
- Gudmundsson, O., J.H. Davies, and R.W. Clayton (1990). Stochastic analysis of global travelttime data: mantle heterogeneity and random errors in the ISC data, *Geophys. J. Int.*, **102**, 25-43.
- Guffanti, M. and C.S. Weaver (1988). Distribution of late Cenozoic volcanic vents in the Cascade Range: Volcanic arc segmentation and regional tectonic considerations, *J. Geophys. Res.*, **93**, 6513-6529.
- Haddon, R.A.W. and E.S. Husebye (1978). Joint interpretation of P-wave time and amplitude anomalies in terms of lithospheric heterogeneities, *Geophys. J. Roy. Astr. Soc.*, **55**, 19-43.
- Hager, B.H. (1978). Oceanic plate motions driven by lithospheric thickening and subducting slabs, *Nature*, **276**, 156-159.
- Hager, B.H. and R.J. O'Connell (1978). Subduction zone dip angles and flow driven by plate motion, *Tectonophysics*, **50**, 111-133.
- Hager, B.H. and R.J. O'Connell (1979). Kinematic models of large-scale flow in the Earth's mantle, *J. Geophys. Res.*, **84**, 1031-1048.
- Hamburger, M.W. and B.L. Isacks (1987). Deep earthquakes in the southwest Pacific: a tectonic interpretation, *J. Geophys. Res.*, **92**, 13,841-13,854.
- Harper, J.R. (1975). On the driving forces of plate tectonics, *Geophys. J. Roy. Astron. Soc.*, **40**, 465-474.
- Heaton, T.H. and H. Kanamori (1984). Seismic potential associated with subduction in the Northwestern United States, *Bull. Seis. Soc. Am.*, **74**, 933-941.
- Heaton, T.H. and H. Kanamori (1985). Reply to Acharya's "Comment on 'Seismic potential associated with subduction in the Northwestern United States'", *Bull. Seis. Soc. Am.*, **75**, 891-892.
- Heaton, T.H. and S.H. Hartzell (1986). Source characteristics of hypothetical subduction earthquakes in the northwestern United States, *Bull. Seis. Soc. Am.*, **76**, 675-708.
- Heaton, T.H. and S.H. Hartzell (1987). Earthquake hazards on the Cascadia Subduction Zone, *Science*, **236**, 162-168.
- Helfrich, G.R., S. Stein, and B.J. Wood (1989). Subduction zone thermal structure

- and minerology and their relation to seismic wave reflections and conversions at the slab/mantle interface, *J. Geophys. Res.*, **94**, 753-763.
- Hendrickson, M.A. (1986). *The determination of seismic structure from teleseismic P waveforms on the Washington continental margin*, M.Sc. thesis, Univ. of Washington, Seattle, 74 pp.
- Herrin, E. (1968). 1968 seismological tables for P phases, *Bull. Seis. Soc. Am.*, **58**, 1196-1241.
- Hesser, D.H. (1982). *Linear predictive processing and pattern recognition for automated classification of local seismic events*, M.Sc. thesis, Univ. of Washington, Seattle, 240 pp.
- Hestenes, M.R. and E. Stiefel (1952). Methods of conjugate gradients for solving linear systems, *J. Res. Nat. Bur. Standards*, **49**, 409-436.
- Ho-liu, P., H. Kanamori, and R.W. Clayton (1988). Applications of attenuation tomography to Imperial Valley and Coso-Indian Wells region, southern California, *J. Geophys. Res.*, **93**, 10,501-10,520.
- Holdahl, S.R., F. Faucher, and H. Dragert (1989). Contemporary vertical crustal motion in the Pacific Northwest, in *Slow deformation and transmission of stress in the Earth*, edited by S.C. Cohen and P. Vanicek, AGU/IUGG Geophysics Monograph Series No. 49, IUGG Vol. 4, 17-29.
- Huber, P.J. (1981). *Robust Statistics*, John Wiley & Sons, New York, .
- Humphreys, E.D., R.W. Clayton, and B.H. Hager (1984). A Tomographic image of mantle structure beneath southern California, *Geophys. Res. Letts.*, **11**, 625-627.
- Humphreys, E.D. (1985). *Studies of the crust-mantle system beneath southern California*, Ph.D. thesis, Cal. Inst. Tech., Pasadena, 189 pp.
- Humphreys, E.D. and R.W. Clayton (1985). Adaption of back-projection tomography to seismic travel-time problems, *J. Geophys. Res.*, **93**, 1073-1085.
- Husebye, E.S. and B. Jansson (1966). Application of Array Data Processing Techniques to the Swedish Seismograph Network, *Pure Appl. Geophys.*, **63**, 82-104.
- Hyndman, R.D., C.J. Yorath, R.M. Clowes, and E.E. Davis (1990). The northern Cascadia subduction zone at Vancouver Island: seismic structure and tectonic history, *Can. J. Earth Sci.*, **27**, 313-329.

- Ihnen, S.M. and D.M. Hadley (1986). Prediction of strong ground motion in the Puget Sound region: the 1965 Seattle earthquake, *Bull. Seis. Soc. Am.*, **76**, 905-922.
- Ito, A. (1985). High resolution relative hypocenters of similar earthquakes by cross-spectral analysis method, *J. Phys. Earth*, **33**, 279-294.
- Iyer, H.M. (1968). Determination of frequency-wave-number spectra using seismic arrays, *Geophys. J. Roy. Astr. Soc.*, **16**, 97-117.
- Iyer, H.M. and J.H. Healy (1972). Teleseismic residuals at the LASA-USGS extended array and their interpretation in terms of crust and upper-mantle structure, *J. Geophys. Res.*, **77**, 1503-1527.
- Iyer, H.M., J.R. Evans, G. Zandt, R.M. Stewart, J.M. Coakley, and J.N. Roloff (1981). A deep low-velocity body under the Yellowstone caldera, Wyoming: Delineation using teleseismic P-wave residuals and tectonic interpretation, *Geol. Soc. Am. Bull.*, **92**, 792-798.
- Iyer, H.M. (1984). Geophysical evidence for the locations, shapes and sizes, and internal structures of magma chambers beneath regions of Quaternary volcanism, *Proc., Roy. Soc. London, Ser. A*, **310**, 473-510.
- Jackson, D.D. (1972). Interpretation of inaccurate, insufficient and inconsistent data, *Geophys. J. Roy. Astr. Soc.*, **28**, 97-109.
- Jackson, D.D. (1976). Most squares inversion, *J. Geophys. Res.*, **81**, 1027-1030.
- Jackson, D.D. (1979). The use of a priori data to resolve non-uniqueness in linear inversion, *Geophys. J. Roy. Astr. Soc.*, **57**, 137-157.
- Jacob, K.H. (1970). Three-dimensional seismic ray tracing in a laterally heterogeneous spherical earth, *J. Geophys. Res.*, **75**, 6675-6689.
- Jacob, K.H. (1972). Global tectonic implications of anomalous seismic P traveltimes from the nuclear explosion Longshot, *J. Geophys. Res.*, **77**, 2556-2573.
- Jacob, K.H., K. Nakamura, and J.N. Davies (1977). Trench-volcano gap along the Alaska-Aleutian Arc: facts, and speculations on the role of terrigenous sediments for subduction, in *Island Arcs, Deep Sea Trenches and Back-arc Basins*, edited by M. Talwani and W.C. Pitman, American Geophysical Union Maurice Ewing Series, number 1, 243-258.
- Jansky, J. and V. Cerveny (1981). Computation of ray integrals and ray amplitudes in radially symmetric media, *Studia Geoph. et Geod.*, **25**, 288-292.

- Jansson, B. and E.S. Husebye (1968). Application of array data processing techniques to a network of ordinary seismograph stations, *Pure Appl. Geophys.*, **69**, 80-99.
- Jeffreys, H. and K.E. Bullen (1940). *Seismological tables*, British Association, London, .
- Jeffreys, H. (1970). *The Earth*, University Press, Cambridge, 525 pp.
- Jordan, T.H. and J.N. Franklin (1971). Optimal solutions to a linear inverse problem in geophysics, *Proceedings of the National Academy of Sciences*, **68**, 291-293.
- Jordan, T.H. (1981). Global tectonic regionalization for seismological data analysis, *Bull., Seis. Soc. Am.*, **71**, 1131-1141.
- Jordan, T.H. and K.A. Sverdrup (1981). Teleseismic location techniques and their application to earthquake clusters in the South-Central Pacific , *Bull., Seis. Soc. Am.*, **71**, 1105-1130.
- Julian, B.R. and D. Gubbins (1977). Three-dimensional seismic ray tracing, *J. Geophys.*, **43**, 95-113.
- Jupp, D.L.B. and K. Vozoff (1975). Stable iterative methods for the inversion of geophysical data, *Geophys. J. Roy. Astr. Soc.*, **42**, 957-976.
- Jurkevics, A., R. Wiggins, and L. Canales (1980). Body-wave inversion using travel time and amplitude data, *Geophys. J. Roy. Astr. Soc.*, **63**, 75-93.
- Kanamori, H. (1977). Seismic and aseismic slip along subduction zones and their tectonic implications, in *Island Arcs, Deep Sea Trenches and Back-arc Basins*, edited by M. Talwani and W.C. Pitman, American Geophysical Union Maurice Ewing Series, number 1, 163-174.
- Keach, R.W., C.J. Potter, J.E. Oliver, and L.D. Brown (1986). Cenozoic active margin and shallow Cascades structure: COCORP results from western Oregon (abstract), *Geol. Soc. Am. Abstr. Prog.*, **19**, 652.
- Kennett, B.L.N. (1978). Some aspects of non-linearity in inversion, *Geophys. J. Roy. Astr. Soc.*, **55**, 373-391.
- Kincaid, C. and P. Olson (1987). An experimental study of subduction and slab migration, *J. Geophys. Res.*, **92**, 13,832-13,840.
- Kissling, E. (1988). Geotomography with local earthquake data, *Rev. Geophys.*, **26**,

659-698.

- Knapp, C.H. and G.C. Carter (1976). The generalized correlation method for estimation of time delay, *IEEE Trans. Acoust., Speech, Signal Processing*, **24**, 320-327.
- Knopoff, L. (1967). Density-velocity relations for rocks, *Geophys. J. Roy. Astr. Soc.*, **13**, 1-8.
- Koch, M. (1985). A numerical study on the determination of the 3-D structure of the lithosphere by linear and non-linear inversion of teleseismic travel times, *Geophys. J. R. astr. Soc.*, **80**, 73-93.
- Langston, C.A. (1981). Evidence for the subducting lithosphere under Vancouver Island and western Oregon from teleseismic P-wave conversions, *J. Geophys. Res.*, **86**, 3857-3866.
- Lapp, D.B., T.J. Owens, and R.S. Crosson (1990). P-waveform analysis for local subduction geometry south of Puget Sound, Washington, *Pure Appl. Geophys.*, **133**, 349-365.
- Lawson, C.L. and R.J. Hanson (1974). *Solving least squares problems*, Prentice-Hall, New Jersey, 340 pp.
- Leary, P.C. and P.E. Malin (1982). Millisecond accurate monitoring of seismic travel times over 13- and 18-kilometer baselines, *J. Geophys. Res.*, **87**, 6919-6930.
- Leeman, W.P., D.R. Smith, W. Hildreth, Z. Palacz, and N. Rogers (1990). Compositional diversity of late Cenozoic basalts in a transect across the southern Washington Cascades: Implications for subduction zone magmatism, *J. Geophys. Res.*, **95**, 19,561-19,582.
- Lees, J.M. (1989). *Seismic tomography in western Washington*, Ph.D. thesis, Univ. of Washington, Seattle, 173 pp.
- Lees, J.M. and R.S. Crosson (1989). Tomographic inversion for three-dimensional velocity structure at Mount St. Helens using earthquake data, *J. Geophys. Res.*, **94**, 5716-5728.
- Lees, J.M. and J.C. VanDecar (1989). Seismic tomography constrained by Bouguer gravity anomalies (abstract), *Seis. Res. Letts.*, **60**, 11.
- Lees, J.M. and R.S. Crosson (1990). Tomographic imaging of local earthquake delay times for three-dimensional velocity variation in western

- Washington, *J. Geophys. Res.*, **95**, 4763-4776.
- Lees, J.M. and J.C. VanDecar (1991). Seismic tomography constrained by Bouguer gravity anomalies: applications in Western Washington, *Pure Appl. Geophys.*, **135**, 31-52.
- Lees, J.M. and R.S. Crosson (1991). Bayesian ART versus conjugate gradient methods in tomographic seismic imaging: An application at Mount St. Helens, Washington, in *Spatial statistics and imaging: Proceedings of the 1988 AMS-IMS-SIAM summer research conference*, edited by A. Posollo, (in press).
- Lerner-Lam, A.L. and T.H. Jordan (1987). How thick are the continents?, *J. Geophys. Res.*, **92**, 14,007-14,026.
- Levenberg, K. (1944). A method for the solution of certain non-linear problems in least squares, *Quart. Appl. Math.*, **2**, 164-168.
- Lewis, T.J., W.H. Bentkowski, E.E. Davis, R.D. Hyndman, J.G. Souther, and J.A. Wright (1988). Subduction of the Juan de Fuca plate: Thermal consequences, *J. Geophys. Res.*, **93**, 15,207-15,225.
- Ligdas, C.N., I.G. Main, and R.D. Adams (1990). Three-dimensional structure of the lithosphere in the Aegean region, *Geophys. J. Int.*, **102**, 219-229.
- Lin, J.W. (1973). *A study of upper mantle structure in the Pacific Northwest using P-waves from teleseisms*, Ph.D. thesis, Univ. of Washington, Seattle, 98 pp.
- Lin, J.W. and R.S. Crosson (1974). Upper mantle structure of Western Washington (abstract), *EOS*, **55**, 75.
- Lister, C.R.B. (1989). Plate tectonics at an awkward junction: rules for the evolution of Sovanco Ridge area, NE Pacific, *Geophys. J.*, **96**, 191-201.
- Ludwin, R.S., C.S. Weaver, and R.S. Crosson (1991). Seismicity of Washington and Oregon, in *Neotectonics of North America*, edited by D.B. Slemmons, E.R. Engdahl, D. Blackwell, D. Schwartz and M. Zoback, DNAG associated volume GSMV-1,.
- Ma, L. (1988). *Regional tectonic stress in Western Washington from focal mechanisms of crustal and sub-crustal earthquakes*, M.Sc. thesis, Univ. of Washington, Seattle, 84 pp.
- Mack, H. (1969). Nature of short-period P-wave variations at LASA, *J. Geophys.*

- Res.*, **74**, 3161-3170.
- Marquardt, D.W. (1963). An algorithm for least-squares estimation of nonlinear parameters, *J. Soc. Ind. Appl. Math.*, **11**, 431-441.
- Marquardt, D.W. (1970). Generalised inverses, ridge regression, biased linear estimation, and non-linear estimation, *Technometrics*, **12**, 591-612.
- McCamy, K. and R.P. Meyer (1964). A correlation method of apparent velocity measurement, *J. Geophys. Res.*, **69**, 691-699.
- McKenzie, D.P. and R.L. Parker (1967). The North Pacific: An example of tectonics on a sphere, *Nature*, **216**, 1276-1280.
- Menke, W. (1984). *Geophysical data analysis: Discrete inverse theory*, Academic Press, Inc., Orlando, 260 pp.
- Meyerholtz, K.A., G.L. Pavlis, and S.A. Szpakowski (1989). Convolutional quelling in seismic tomography, *Geophysics*, **54**, 570-580.
- Michaelson, C.A. and C.S. Weaver (1986). Upper mantle structure from teleseismic P-wave arrivals in Washington and Northern Oregon, *J. Geophys. Res.*, **91**, 2077-2094.
- Molnar, P., D. Freedman, and J.S.F. Shih (1979). Lengths of intermediate and deep seismic zones and temperatures in downgoing slabs of lithosphere, *Geophys. J. Roy. Astr. Soc.*, **56**, 41-54.
- Mundal, I., M. Ukawa, and R.S. Crosson (1991). Normal and anomalous P phases from local earthquakes, and slab structure of the Cascadia subduction zone, (*in preparation*),.
- Murtagh, B.A. and M.A. Saunders (1978). Large-scale linearly constrained optimization, *Math. Prog.*, **14**, 41-72.
- Nakanishi, I. and K. Yamaguchi (1986). A numerical experiment on nonlinear image reconstruction from first arrival times for two-dimensional island arc structure, *J. Phys. Earth*, **34**, 195-201.
- Nataf, H.-C., I. Nakanishi, and D.L. Anderson (1984). Anisotropy and shear-velocity heterogeneities in the upper mantle, *Geophys. Res. Letts.*, **11**, 109-112.
- Nercessian, A., A. Hirn, and A. Tarantola (1984). Three-dimensional seismic transmission prospecting of the Mont Dore volcano, France, *Geophys. J. Roy. Astr. Soc.*, **76**, 307-315.

- Nishimura, C., D.S. Wilson, and R.N. Hey (1984). Pole of rotation analysis of present-day Juan de Fuca plate motion, *J. Geophys. Res.*, **89**, 10,283-10,290.
- Nolet, G. (1985). Solving or resolving inadequate and noisy tomographic systems, *J. Comp. Physics*, **61**, 463-482.
- Nolet, G. (1987). Seismic wave propagation and seismic tomography, in *Seismic Tomography*, edited by G. Nolet, D. Reidel Publ. Co., Dordrecht, The Netherlands, 1-23.
- Nolet, G. and M.J.R. Wortel (1989). Structure of the Upper Mantle, in *Encyclopedia of Geophysics*, edited by David E. James, Van Nostrand Reinhold Publ., New York, 775-788.
- Nolet, G. (1990). Partitioned wave-form inversion and 2D structure under the NARS array, *J. Geophys. Res.*, **95**, 8499-8512.
- Nolet, G. and R. Snieder (1990). Research note: Solving large linear inverse problems by projection, *Geophys. J. Int.*, **103**, 565-568.
- Ocola, L.C. (1972). A nonlinear least-squares method for seismic refraction mapping - Part I: algorithm and procedure, *Geophysics*, **37**, 260-272.
- Oppenheimer, D.H. and K.E. Herkenhoff (1981). Velocity-density properties of the lithosphere from three-dimensional modeling at the Geysers-Clear Lake region, California, *J. Geophys. Res.*, **86**, 6057-6065.
- Owens, T.J. and R.S. Crosson (1988). Shallow structure effects on broadband teleseismic P waveforms, *Bull. Seis. Soc. Am.*, **78**, 96-108.
- Owens, T.J., R.S. Crosson, and M.A. Hendrickson (1988). Constraints on the subduction geometry beneath western Washington from broadband teleseismic waveform modeling, *Bull. Seis. Soc. Am.*, **78**, 1319-1334.
- Paige, C.C. and M.A. Saunders (1982). LSQR: An algorithm for sparse linear equations and sparse least squares, *ACM Trans. Math. Software*, **8**, 43-71.
- Parker, R.L. (1970). The inverse problem of electrical conductivity in the mantle, *Geophys. J. Roy. Astr. Soc.*, **22**, 121-138.
- Parker, R.L. (1972). Inverse theory with grossly inadequate data, *Geophys. J. Roy. Astr. Soc.*, **29**, 123-138.
- Parker, R.L. (1974). Best bounds on density and depth from gravity data,

- Geophysics*, **39**, 644-649.
- Parker, R.L. (1975). The theory of ideal bodies for gravity interpretation, *Geophys. J. Roy. Astr. Soc.*, **42**, 315-334.
- Parker, R.L. (1977a). Linear inference and underparameterized models, *Rev. Geophys. Space Phys.*, **15**, 446-456.
- Parker, R.L. (1977b). Understanding inverse theory, *Ann. Rev. Earth Planet. Sci.*, **5**, 35-64.
- Paulssen, H. (1988). Evidence for a sharp 670-km discontinuity as inferred from P-to-S converted waves, *J. Geophys. Res.*, **93**, 10,489-10,500.
- Pavlis, G.L. and J.R. Booker (1980). The mixed discrete-continuous inverse problem: application to the simultaneous determination of earthquake hypocenters and velocity structure, *J. Geophys. Res.*, **85**, 4801-4810.
- Pavlis, G.L. and J.R. Booker (1983). Progressive multiple event location (PMEL), *Bull., Seis. Soc. Am.*, **73**, 1753-1777.
- Phadke, S. and E.R. Kanasevich (1990). Seismic tomography to obtain velocity gradients and three-dimensional structure and its application to reflection data on Vancouver Island, *Can. J. Earth Sci.*, **27**, 104-116.
- Priest, G.R. (1990). Volcanic and tectonic evolution of the Cascade volcanic arc, central Oregon, *J. Geophys. Res.*, **95**, 19,583-19,600.
- Qamar, A., A. Rathbun, R. Ludwin, and R.S. Crosson (1986). Earthquake hypocenters in Washington and northern Oregon - 1980, *Washington Dept. of Natural Resources, Division of geology and earth resources.*,.
- Ram, A. and R.F. Mereu (1975). A comparison of adaptive processing techniques with nth root beam forming methods, *Geophys. J. Roy. Astr. Soc.*, **42**, 653-670.
- Rasmussen, J.R. and E.D. Humphreys (1988). Tomographic image of the Juan de Fuca plate beneath Washington and western Oregon using teleseismic P-wave travel times, *Geophys. Res. Letts.*, **15**, 1417-1420.
- Rea, D.K. and R.A. Duncan (1986). North Pacific plate convergence: A quantitative record of the past 140 m.y., *Geology*, **14**, 373-376.
- Richards, M.A. and B.H. Hager (1985). *The Earth's geoid and the large-scale structure of mantle convection*, Proceedings of the NATO ASI: "Physics of the Earth", Univ. of Newcastle Upon Tyne, .

- Riddihough, R. (1984). Recent movements of the Juan de Fuca plate system, *J. Geophys. Res.*, **89**, 6980-6994.
- Robinson, R. and H.M. Iyer (1981). Delineation of a low-velocity body under Roosevelt Hot Springs geothermal area, Utah, using teleseismic P-wave data, *Geophysics*, **46**, 1456-1466.
- Rodi, W.L., T.H. Jordan, J.F. Masso, and J.M. Savino (1980). Determination of three-dimensional structure of Eastern Washington from the joint inversion of gravity and earthquake travel time data, *Systems, Science and Software, Technical Report, Project No. 40094*.
- Rogers, G.C. (1983). *Seismotectonics of British Columbia*, Ph.D. thesis, University of British Columbia, Vancouver, 227 pp.
- Romanowicz, B.A. (1979). Seismic structure of the upper mantle beneath the United States by three-dimensional inversion of body wave arrival times, *Geophys. J. Roy. Astr. Soc.*, **57**, 479-506.
- Ryall, A. (1964). Improvement of array seismic recordings by digital processing, *Bull., Seis. Soc. Am.*, **54**, 277-294.
- Sabatier, P.C. (1977a). On geophysical inverse problems and constraints, *J. Geophys.*, **43**, 115-137.
- Sabatier, P.C. (1977b). Positivity constraints in linear inverse problems: I. General Theory, *Geophys. J. Roy. Astr. Soc.*, **48**, 415-441.
- Sabatier, P.C. (1977c). Positivity constraints in linear inverse problems: II. Applications, *Geophys. J. Roy. Astr. Soc.*, **48**, 443-459.
- Sambridge, M.S. (1990). Non-linear arrival time inversion: constraining velocity anomalies by seeking smooth models in 3-D, *Geophys. J. Int.*, **102**, 653-677.
- Savage, J.C. and M. Lisowski (1991). Strain measurements and the potential for a great subduction earthquake off the coast of Washington, *Science*, **252**, 101-103.
- Scales, J.A. (1987). Tomographic inversion via the conjugate gradient method, *Geophysics*, **52**, 179-185.
- Shaw, P.R. and J.A. Orcutt (1985). Waveform inversion of seismic refraction data and applications to young Pacific crust, *Geophys. J. R. Astr. Soc.*, **82**, 375-414.

- Shaw, P.R. (1986). The accuracy of models derived by WKBJ waveform inversion, *Geophys. J. R. Astr. Soc.*, **85**, 291-313.
- Sleep, N.H. (1973). Teleseismic *P*-wave transmission through slabs, *Bull. Seis. Soc. Am.*, **63**, 1349-1373.
- Snedecor, G.W. (1956). *Statistical Methods*, Iowa State Press, Ames, Iowa, 173-180.
- Snieder, R. (1987). Surface wave holography, in *Seismic Tomography*, edited by G. Nolet, D. Reidel Publ. Co., Dordrecht, The Netherlands, 323-337.
- Snieder, R. (1988a). Large-scale waveform inversions of surface waves for lateral heterogeneity: 1. Theory and numerical examples, *J. Geophys. Res.*, **93**, 12055-12065.
- Snieder, R. (1988b). Large-scale waveform inversions of surface waves for lateral heterogeneity: 2. Application to surface waves in Europe and the Mediterranean, *J. Geophys. Res.*, **93**, 12067-12080.
- Snieder, R. (1990). A perturbative analysis of non-linear inversion, *Geophys. J. Int.*, **101**, 545-556.
- Snieder, R., J. Beckers, and F. Neele (1991). The effect of small-scale structure on normal mode frequencies and global inversions, *J. Geophys. Res.*, **96**, 501-516.
- Spakman, W. (1988). *Upper mantle delay time tomography*, Ph.D. thesis, Univ. of Utrecht, Utrecht, The Netherlands, 200 pp.
- Spakman, W. and G. Nolet (1988). Imaging algorithms, accuracy and resolution in delay time tomography, in *Mathematical Geophysics*, edited by N.J. Vlaar, G. Nolet, M.J.R. Wortel and S.A.P.L. Cloetingh, D. Reidel Publ. Co., Dordrecht, The Netherlands, 155-187.
- Spakman, W., M.J.R. Wortel, and N.J. Vlaar (1988). The Hellenic subduction zone: A tomographic image and its geodynamic implications, *Geophys. Res. Letts.*, **15**, 60-63.
- Spakman, W., S. Stein, R. van der Hilst, and R. Wortel (1988). Resolution experiments for the NE Pacific subduction zone tomography, *EOS*, **69**, 1308.
- Spence, W. (1987). Implications of the slowing of subduction at Cascadia (abstract), *EOS*, **68**, 1467.

- Spence, W. (1989). Stress origins and earthquake potentials in Cascadia, *J. Geophys. Res.*, **94**, 3076-3088.
- Spencer, C. and D. Gubbins (1980). Travel-time inversion for simultaneous earthquake location and velocity structure determination in laterally varying media, *Geophys. J. Roy. Astr. Soc.*, **63**, 95-116.
- Spencer, C. (1985). The use of partitioned matrices in geophysical inversion problems, *Geophys. J. Roy. Astr. Soc.*, **80**, 619-629.
- Stewart, R.R. (1988). Short note: Derivation of an algebraic reconstruction technique to determine weakly anisotropic velocity, *Geophysics*, **53**.
- Stork, C. (1988). A non-linear velocity inversion of a moderately difficult synthetic cross-hole model using ray-trace tomography, *EOS*, **69**.
- Stork, C. and R.W. Clayton (1991). Linear aspects of tomographical velocity analysis, *Geophysics*, **56**, 483-495.
- Stuart, D.J., J.C. Roiler, W.H. Jackson, and G.B. Mangan (1964). Seismic propagation paths, regional traveltimes, and crustal structure in the Western United States, *Geophysics*, **29**, 178-187.
- Taber, J.J. and S.W. Smith (1985). Seismicity and focal mechanisms associated with the subduction of the Juan de Fuca plate beneath the Olympic Peninsula, Washington, *Bull. Seis. Soc. Am.*, **75**, 237-249.
- Taber, J.J. and B.T.R. Lewis (1986). Crustal structure of the Washington continental margin from refraction data, *Bull. Seis. Soc. Am.*, **76**, 1011-1024.
- Tanimoto, T. and D.L. Anderson (1984). Mapping convection in the mantle, *Geophys. Res. Letts.*, **11**, 287-290.
- Tanimoto, T. (1985). The Backus-Gilbert approach to the three-dimensional structure in the upper mantle - I. Lateral variation of surface wave phase velocity and its error and resolution, *Geophys. J. R. Astr. Soc.*, **82**, 105-123.
- Tarantola, A. and B. Valette (1982). Inverse problems = quest for information, *J. Geophys.*, **50**, 159-170.
- Tarantola, A. and A. Nercessian (1984). Three-dimensional inversion without blocks, *Geophys. J. Roy. Astr. Soc.*, **76**, 299-306.
- Tarantola, A. (1987a). *Inverse problem theory: Methods for data fitting and model parameter estimation*, Elsevier, Amsterdam, .

- Tarantola, A. (1987b). Inversion of travel times and seismic waveforms, in *Seismic Tomography*, edited by G. Nolet, D. Reidel Publ. Co., Dordrecht, The Netherlands, 135-157.
- Thomson, C. (1983). Ray-theoretical amplitude inversion for laterally varying velocity structure below NORSAR, *Geophys. J. Roy. Astr. Soc.*, **74**, 525-558.
- Thomson, C.J. and D. Gubbins (1982). Three-dimensional lithospheric modelling at NORSAR: linearity of the method and amplitude variations from the anomalies, *Geophys. J. Roy. Astr. Soc.*, **71**, 1-36.
- Thomson, C.J. and C.H. Chapman (1985). An introduction to Maslov's asymptotic method, *Geophys. J. Roy. Astr. Soc.*, **83**, 143-168.
- Toomey, D.R., S.C. Solomon, and G.M. Purdy (1988). Microearthquakes beneath median valley of mid-Atlantic ridge near 23 degrees north: Tomography and tectonics, *J. Geophys. Res.*, **92**, 9093-9112.
- Uyeda, S. and H. Kanamori (1979). Back-arc opening and the mode of subduction, *J. Geophys. Res.*, **84**, 1049-1061.
- VanDecar, J.C. and R.S. Crosson (1990). Determination of teleseismic relative phase arrival times using multi-channel cross correlation and least squares, *Bull. Seis. Soc. Am.*, **80**, 150-169.
- VanDecar, J.C., R.S. Crosson, and K.C. Creager (1990). Teleseismic arrivals recorded over the Cascadia Subduction Zone: amplitude variation and calibration of the Washington Regional Seismic Network (abstract), *Seis. Res. Letts.*, **61**, 32.
- VanDecar, J.C., R.S. Crosson, and K.C. Creager (1991). Teleseismic travel-time inversion for Cascadia Subduction Zone structure employing three-dimensional ray tracing, *Proceedings of the European Seismological Commission XXII General Assembly, Barcelona, Spain.*
- van der Hilst, R.D. and W. Spakman (1989). Importance of the reference model in linearized tomographic inversions: Images of subduction below the Caribbean plate, *Geophys. Res. Letts.*, **16**, 1093-1097.
- van der Sluis, A. and H.A. van der Vorst (1987). Numerical solution of large sparse linear algebraic systems arising from tomographic problems, in *Seismic Tomography*, edited by G. Nolet, D. Reidel Publ. Co., Dordrecht, The Netherlands, 49-83.
- Vasco, D.W. (1991). Bounding seismic velocities using a tomographic method,

Geophysics, **56**, 472-482.

- Verplanck, E.P. and R.A. Duncan (1987). Temporal variations in plate convergence and eruption rates in the western Cascades, Oregon, *Tectonics*, **6**, 197-209.
- Vine, F.J. and J.T. Wilson (1965). Magnetic anomalies over a young ocean ridge off Vancouver Island, *Science*, **150**, 485-489.
- Vine, F.J. (1966). Spreading of the ocean floor: New evidence, *Science*, **154**, 1405-1415.
- Vozoff, K. and D.L.B. Jupp (1975). Joint inversion of geophysical data, *Geophys. J. Roy. Astr. Soc.*, **42**, 977-991.
- Walck, M.C. and R.W. Clayton (1987). P wave velocity variations in the Coso region, California derived from local earthquake data, *J. Geophys. Res.*, **92**, 393-406.
- Walck, M.C. (1988). Three-dimensional variations in shear structure and V_p/V_s for the Coso region, California, *J. Geophys. Res.*, **93**, 2047-2052.
- Weaver, C.S. and C.A. Michaelson (1985). Seismicity and volcanism in the Pacific Northwest: evidence for the segmentation of the Juan de Fuca plate, *Geophys. Res. Letts.*, **12**, 215-218.
- Weaver, C.S. and G.E. Baker (1988). Geometry of the Juan de Fuca plate beneath Washington and northern Oregon from seismicity, *Bull. Seis. Soc. Am.*, **78**, 264-275.
- Weber, M. (1990). Subduction zones - their influence on traveltimes and amplitudes of P-waves, *Geophys. J. Int.*, (in press).
- Wilson, D.S., R.N. Hey, and C. Nishimura (1984). Propagation as a mechanism of ridge reorientation: a model for the tectonic evolution of the Juan de Fuca Ridge, *J. Geophys. Res.*, **89**, 9215-9225.
- Woodhouse, J.H. and A.M. Dziewonski (1984). Mapping the upper mantle: three-dimensional modeling of earth structure by inversion of seismic waveforms, *J. Geophys. Res.*, **89**, 5953-5986.
- Yelin, T.S. (1982). *The Seattle earthquake swarms and puget basin focal mechanisms and their tectonic implications*, M.Sc. thesis, Univ. of Washington, Seattle, 96 pp.
- Zervas, C.E. (1984). *A time term analysis of P_n velocities in Washington*, M.Sc. thesis, Univ. of Washington, Seattle, 134 pp.

- Zervas, C.E. and R.S. Crosson (1986). P_n observation and interpretation in Washington, *Bull., Seis. Soc. Am.*, **76**, 521-546.
- Zhou, H.W. (1990). Mapping of P -wave slab anomalies beneath Tonga, Kermadec and New Hebrides arcs, *Phys. Earth Planet. Inter.*, **61**, 199-229.
- Zhou, H.W. and R.W. Clayton (1990). P and S wave travel time inversions for the subducting slab under the island arcs of the Northwest Pacific, *J. Geophys. Res.*, **95**, 6829-6852.
- Zielhuis, A., w. Spakman, and G. Nolet (1989). A reference model for tomographic imaging of the upper-mantle shear velocity structure beneath Europe, in *Digital seismology and modeling the lithosphere*, edited by R. Cassinis, G. Panza, and G. Nolet, Plenum Press, London, 333-340.

Appendix A
Station Locations

Table A.1: Location of those stations of the Washington Regional Seismograph Network used in this study. (MSH = Mt. St. Helens)

Station Locations - Washington Regional Seismograph Network				
Name	Latitude (North)	Longitude (West)	Elevation (km)	Approximate Location
APW	46° 39' 06.00"	122° 38' 51.00"	0.4570	Alpha Peak
ASR	46° 09' 02.40"	121° 35' 33.60"	1.2800	Stagman Ridge
AUG	45° 44' 10.00"	121° 40' 50.00"	0.8650	Augspurgen Mtn.
BDG	46° 13' 59.10"	119° 19' 03.00"	0.6500	Badger Mtn.
BHW	47° 50' 12.60"	122° 01' 55.80"	0.1980	Bald Hill
BLN	48° 00' 26.50"	122° 58' 18.64"	0.5850	Blyn Mtn.
BOW	46° 28' 30.00"	123° 13' 41.00"	0.8700	Boisfort Mtn.
BPO	44° 39' 06.86"	121° 41' 19.20"	1.9570	Bald Peter
BRV	46° 29' 07.20"	119° 59' 29.40"	0.9250	Black Rock Valley
BVW	46° 48' 37.75"	119° 52' 54.10"	0.7070	Beverly
CBS	47° 48' 16.70"	120° 02' 27.60"	1.0730	Chelan Butte
CBW	47° 48' 25.50"	120° 01' 57.60"	1.1600	Chelan Butte
CDF	46° 06' 58.20"	122° 02' 51.00"	0.7800	Cedar Flat
CHO	45° 35' 27.00"	118° 34' 45.00"	1.0760	Cabbage Hill
CMM	46° 26' 07.00"	122° 30' 21.00"	0.6200	Crazyman Mtn.
CMW	48° 25' 25.30"	122° 07' 08.40"	1.1900	Cultus Mtn.
COW	46° 29' 27.60"	122° 00' 43.60"	0.3050	Cowlitz River
CPW	46° 58' 25.80"	123° 08' 10.80"	0.7920	Capitol Peak
CRF	46° 49' 30.60"	119° 23' 18.00"	0.2600	Corfu
DAV	47° 38' 18.00"	118° 13' 33.60"	0.7580	Davenport
DPW	47° 52' 14.30"	118° 12' 10.20"	0.8920	Davenport
DY2	47° 59' 06.91"	119° 46' 13.03"	0.8840	Dyer Hill
DYH	47° 57' 37.80"	119° 46' 09.60"	0.8200	Dyer Hill
EDM	46° 11' 50.40"	122° 09' 00.00"	1.6090	MSH East Dome
ELK	46° 18' 20.00"	122° 20' 27.00"	1.2700	MSH Elk Rock
ELL	46° 54' 35.00"	120° 34' 06.00"	0.8050	Ellensburg
EPH	47° 21' 12.80"	119° 35' 46.20"	0.6280	Ephrata
EST	47° 14' 16.80"	121° 12' 21.80"	0.7560	Easton

Table A.1: (continued)

Name	Latitude (North)	Longitude (West)	Elevation (km)	Approximate Location
ETP	46° 27' 53.40"	119° 03' 32.40"	0.2500	Eltopia
ETT	47° 39' 18.00"	120° 17' 36.00"	0.4390	Entiat
ETW	47° 36' 16.20"	120° 19' 51.60"	1.4750	Entiat
FL2	46° 11' 47.00"	122° 21' 01.00"	1.3780	MSH Flattop
FLT	46° 11' 21.30"	122° 21' 22.50"	1.3870	MSH Flattop
FMW	46° 56' 29.60"	121° 40' 11.30"	1.8590	Mt. Fremont
FOR	45° 58' 14.00"	121° 45' 30.00"	1.1520	Forlorn Lakes
FOX	48° 19' 50.00"	119° 42' 29.00"	0.8960	Fox Mtn.
FPW	47° 58' 09.00"	120° 12' 46.50"	0.3520	Fields Point
GBL	46° 35' 51.60"	119° 27' 35.40"	0.3300	Gable Mtn.
GHW	47° 02' 30.00"	122° 16' 21.00"	0.2680	Garrison Hill
GL2	45° 57' 50.00"	120° 49' 15.00"	1.0000	Goldendale
GLD	45° 50' 13.00"	120° 48' 46.00"	0.6100	Goldendale
GLK	46° 33' 50.20"	121° 36' 30.70"	1.3200	Glacier Lake
GMO	44° 26' 20.80"	120° 57' 22.30"	1.6890	Grizzly Mtn.
GMW	47° 32' 52.50"	122° 47' 10.80"	0.5060	Gold Mtn.
GRO	45° 21' 04.50"	123° 39' 43.00"	0.9450	Grindstone Mtn.
GSM	47° 12' 11.40"	121° 47' 40.20"	1.3050	Grass Mtn.
GUL	45° 55' 27.00"	121° 35' 44.00"	1.1890	Guler Mtn.
HDW	47° 38' 54.60"	123° 03' 15.20"	1.0060	Hoodspout
HH2	46° 10' 18.00"	119° 23' 01.00"	0.4900	Horse Heaven Hills
HHW	46° 10' 59.00"	119° 22' 59.00"	0.4150	Horse Heaven Hills
HSR	46° 10' 07.50"	122° 11' 43.13"	1.7740	MSH South Ridge
HTW	47° 48' 12.50"	121° 46' 08.65"	0.8290	Haystack Mtn.
JBO	45° 27' 41.68"	119° 50' 13.28"	0.6450	Jordan Butte
JCW	48° 11' 36.60"	121° 55' 46.20"	0.6160	Jim Creek
JUN	46° 08' 48.00"	122° 09' 10.80"	1.0490	June Lake
KMO	45° 38' 07.80"	123° 29' 22.20"	0.9750	Kings Mtn.
KOS	46° 27' 40.80"	122° 11' 25.80"	0.8280	Kosmos
LMW	46° 40' 04.80"	122° 17' 28.80"	1.1950	Ladd Mtn.
LNO	45° 52' 15.80"	118° 17' 06.00"	0.7680	Linton Mtn.
LO2	46° 45' 00.00"	121° 48' 36.00"	0.8530	Longmire

Table A.1: (continued)

Name	Latitude (North)	Longitude (West)	Elevation (km)	Approximate Location
LOC	46° 43' 04.80"	119° 25' 54.60"	0.2010	Locke Island
LVP	46° 04' 06.00"	122° 24' 30.00"	1.1700	Lakeview Peak
MBW	48° 47' 02.40"	121° 53' 58.80"	1.6760	Mt. Baker
MCW	48° 40' 46.80"	122° 49' 56.40"	0.6930	Mt. Constitution
MDW	46° 36' 48.00"	119° 45' 39.00"	0.3300	Midway
MFW	45° 54' 10.80"	118° 24' 21.00"	0.3950	Milton-Freewater
MJ2	46° 33' 28.00"	119° 21' 50.00"	0.1500	May Junction
MOW	47° 50' 46.90"	122° 02' 52.90"	0.1800	Monroe
MOX	46° 34' 38.00"	120° 17' 35.00"	0.5400	Moxie City
MTM	46° 01' 31.80"	122° 12' 42.00"	1.1210	Mt. Mitchell
NAC	46° 44' 03.80"	120° 49' 33.20"	0.7380	Naches
NCO	43° 42' 18.20"	121° 08' 06.30"	1.9080	Newberry Crater
NEL	48° 04' 41.80"	120° 20' 17.70"	1.4900	Nelson Butte
NEW	48° 15' 50.00"	117° 07' 13.00"	0.7600	Newport
NLO	46° 05' 18.00"	123° 27' 00.00"	0.9000	Nicolai Mtn.
OBC	48° 02' 07.10"	124° 04' 39.00"	0.9380	Bonidu Creek
OBH	47° 19' 34.50"	123° 51' 57.00"	0.3830	Burnt Hill
OCT	47° 44' 57.00"	124° 10' 25.80"	0.7430	Mt. Octopus
OD2	47° 23' 27.60"	118° 42' 38.40"	0.5900	Odessa
ODS	47° 18' 24.00"	118° 44' 42.00"	0.5230	Odessa
OEM	48° 07' 46.50"	124° 18' 13.50"	0.7120	Ellis Mtn.
OFK	47° 57' 00.00"	124° 21' 28.10"	0.1340	Forks
OHW	48° 19' 24.00"	122° 31' 54.60"	0.0540	Oak Harbor
OLQ	47° 30' 58.10"	123° 48' 31.50"	0.1210	Lake Quinault
OMK	48° 28' 49.20"	119° 33' 39.00"	0.4210	Omak
ONR	46° 52' 37.50"	123° 46' 16.50"	0.2570	North River
OOW	47° 44' 12.00"	124° 11' 22.00"	0.7430	Mt. Octopus
OSD	47° 49' 15.00"	123° 42' 06.00"	2.0100	Mt. Olympus
OSP	48° 17' 05.46"	124° 35' 23.30"	0.5850	Sooes Peak
OT2	46° 43' 17.00"	119° 14' 05.00"	0.3550	Othello
OTH	46° 44' 20.40"	119° 12' 59.40"	0.2600	Othello
OTR	48° 05' 00.08"	124° 20' 39.00"	0.7120	Tyee Ridge
PAT	45° 52' 50.10"	119° 45' 40.10"	0.3000	Paterson

Table A.1: (continued)

Name	Latitude (North)	Longitude (West)	Elevation (km)	Approximate Location
PEN	45° 36' 43.20"	118° 45' 46.50"	0.4300	Pendleton
PGO	45° 28' 00.00"	122° 27' 10.00"	0.2370	Gresham
PGW	47° 49' 24.50"	122° 37' 25.20"	0.1220	Port Gamble
PHO	45° 37' 07.80"	122° 49' 50.20"	0.2990	Portland Hills
PLN	47° 47' 04.80"	120° 37' 58.82"	0.7000	Plain
PRO	46° 12' 45.60"	119° 41' 09.00"	0.5520	Prosser
RC1Z	46° 57' 00.00"	119° 26' 00.00"	0.5000	Royal City
RMW	47° 27' 34.95"	121° 48' 19.20"	1.0240	Rattlesnake Mtn.
RPK	45° 45' 42.00"	120° 13' 50.00"	0.3300	Roosevelt Peak
RPW	48° 26' 54.00"	121° 30' 49.00"	0.8500	Rockport
RSW	46° 23' 28.20"	119° 35' 19.20"	1.0370	Rattlesnake Mtn.
RVC	46° 56' 34.50"	121° 58' 17.30"	1.0000	Voight Creek
RVW	46° 08' 58.20"	122° 44' 37.20"	0.4600	Rose Valley
SAW	47° 42' 06.00"	119° 24' 03.60"	0.6900	St. Andrews
SBL	46° 20' 25.20"	122° 02' 19.80"	1.6650	Strawberry Lake
SBO	45° 01' 42.00"	120° 03' 33.48"	1.3900	Squaw Butte
SH2	46° 11' 33.00"	122° 14' 12.00"	1.4230	MSH West
SHW	46° 11' 33.00"	122° 14' 12.00"	1.4230	MSH West
SMW	47° 19' 10.20"	123° 20' 30.00"	0.8400	South Mtn.
SOS	46° 14' 38.50"	122° 08' 12.00"	1.2700	Smith River
SPW	47° 33' 13.30"	122° 14' 45.10"	0.0080	Seward Park
STD	46° 14' 16.00"	122° 13' 21.90"	1.2680	Studebaker Ridge
STW	48° 09' 02.90"	123° 40' 13.10"	0.3080	Striped Peak
SYR	46° 51' 46.80"	119° 37' 04.20"	0.2670	Smyrna
TBM	47° 10' 10.00"	120° 35' 58.00"	1.0640	Table Mtn.
TCO	44° 06' 27.00"	121° 36' 00.00"	1.9750	Three Creek Meadows
TDH	45° 17' 23.40"	121° 47' 25.20"	1.5410	Tom, Dick, Harry Mtn.
TDL	46° 21' 03.00"	122° 12' 57.00"	1.4000	Tradedollar Lske
TWW	47° 07' 17.20"	120° 52' 04.50"	1.0460	Teanaway
VBE	45° 03' 37.20"	121° 35' 12.60"	1.5440	Beaver Butte
VCR	44° 58' 58.18"	120° 59' 17.35"	1.0150	Criterion Ridge
VFP	45° 19' 05.00"	121° 27' 54.30"	1.7160	Flag Point

Table A.1: (continued)

Name	Latitude (North)	Longitude (West)	Elevation (km)	Approximate Location
VG2	45° 09' 20.00"	122° 16' 15.00"	0.8230	Goat Mtn.
VGB	45° 30' 56.40"	120° 46' 39.00"	0.7290	Gordon Butte
VGT	45° 08' 59.40"	122° 15' 55.20"	0.9930	Goat Mtn.
VIP	44° 30' 29.40"	120° 37' 07.80"	1.7310	Ingram Point
VLL	45° 27' 48.00"	121° 40' 45.00"	1.1950	Laurance Lake
VLM	45° 32' 18.60"	122° 02' 21.00"	1.1500	Larch Mtn.
VTG	46° 57' 28.80"	119° 59' 14.40"	0.2080	Vantage
VTH	45° 10' 52.20"	120° 33' 40.80"	0.7730	The Trough
WA2	46° 45' 24.20"	119° 33' 45.50"	0.2300	Wahluke Slope
WAT	47° 41' 55.00"	119° 57' 15.00"	0.9000	Waterville
WBW	48° 01' 04.20"	119° 08' 13.80"	0.8250	Wilson Butte
WEN	47° 31' 46.20"	120° 11' 39.00"	1.0610	Wenatchee
WG2	46° 01' 50.25"	118° 51' 19.95"	0.5110	Wallula Gap
GW	46° 02' 40.80"	118° 55' 57.60"	0.1580	Wallula Gap
WIW	46° 25' 48.80"	119° 17' 13.40"	0.1300	Wooded Island
WNS	46° 42' 37.00"	120° 34' 30.00"	1.0000	Wenas
WPO	45° 34' 24.00"	122° 47' 22.38"	0.3340	Portland
WPW	46° 41' 53.40"	121° 32' 48.00"	1.2500	Whitepass
WRD	46° 58' 11.40"	119° 08' 36.00"	0.3780	Warden
YAK	46° 31' 15.80"	120° 31' 45.20"	0.6190	Yakima
YEL	46° 12' 35.00"	122° 11' 16.00"	1.7500	MSH Yellow Rock

Appendix B
Event Locations

Table B.1: Event parameters from the NOAA data base for the earthquakes used in this study. The great circle azimuth and angular distance (Δ) to each event are calculated with respect to WRSN (latitude 46 N and longitude 121 W). Angular distances of less than 100° represent mantle phases (P) while those with $\Delta > 100^\circ$ result in core phases (PKP).

Events Used in Present Study								
Date yy/mm/dd	Time (UTC)	Location		Depth (km)	Magnitude		Azimuth (w.r.t. WRSN)	Δ
		Latitude	Longitude		m_b	M_{sz}		
80/07/20	21:20	17.865S	178.625W	591	6.0		234°	82°
80/10/10	14:44	36.246N	1.493E	10	5.3		43°	83°
81/04/28	21:14	23.721S	179.981E	540	6.0		232°	88°
81/05/08	23:34	42.660N	139.129E	200	6.0		308°	66°
81/09/30	23:03	4.798S	112.008W	10	5.9	5.2	169°	51°
81/10/01	12:14	73.317N	54.812E	0	5.9	3.8	1°	61°
81/10/22	13:59	63.789N	97.548E	0	4.9		342°	66°
82/01/04	06:05	18.014N	145.626E	590	6.1		285°	79°
82/03/22	06:04	6.650N	175.064E	33	5.6	5.4	255°	67°
82/10/16	06:14	46.743N	48.213E	0	5.4	3.1	7°	87°
82/12/31	19:46	42.796N	77.423E	24	5.8	5.1	347°	90°
83/01/15	00:39	33.268N	136.040E	435	5.5		302°	75°
83/01/16	22:10	5.458S	147.046E	235	6.0		268°	95°
83/02/14	00:23	10.504N	140.924E	39	5.8	5.7	283°	88°
83/03/08	13:21	3.471S	177.628E	33	5.8	5.0	246°	73°
83/03/19	21:41	35.081N	25.350E	65	5.7		27°	93°
83/04/12	12:07	4.843S	78.103W	104	6.5		131°	63°
83/04/15	10:08	5.979S	75.663W	118	5.6		129°	66°
83/05/25	17:30	21.895S	138.918W	0	5.9	4.1	198°	70°
83/06/21	17:06	29.718N	129.395E	158	5.9		304°	81°
83/07/31	10:26	20.127S	126.931W	10	5.9	5.3	186°	66°
83/08/02	02:17	20.435N	122.101E	158	6.1		303°	92°
83/08/05	06:21	3.596S	62.153W	23	5.6	5.3	116°	72°
83/09/04	20:52	20.998S	169.801E	112	5.5		241°	92°
83/09/15	10:39	16.103N	93.153W	115	5.6		133°	38°
83/09/28	08:04	41.170N	132.455E	513	5.1		310°	71°
83/10/08	07:45	44.229N	130.741E	558	5.7		314°	70°

Table 2.1: (continued)

Date yy/mm/dd	Time (UTC)	Location		Depth (km)	Magnitude		Azimuth (w.r.t. WRSN)	Δ
		Latitude	Longitude		m_b	M_{sz}		
83/10/13	12:22	24.457N	46.279W	10	5.5	5.4	83°	62°
83/12/11	09:13	8.137N	137.239E	24	6.2	6.3	284°	92°
83/12/15	04:22	33.099S	70.120W	100	5.9		139°	91°
83/12/22	04:11	11.866N	13.529W	11	6.4	6.2	69°	93°
84/01/19	16:34	5.988N	146.533E	30	5.7	5.8	276°	87°
84/03/06	02:17	29.384N	138.935E	457	6.2		298°	76°
84/03/11	13:42	26.653S	108.507W	10	5.7	4.4	168°	74°
84/03/11	22:22	38.392N	135.482E	351	5.3		306°	71°
84/03/19	20:28	40.320N	63.350E	15	6.5	7.0	357°	94°
84/03/30	07:59	17.362N	59.633W	26	5.8	5.0	98°	58°
84/04/20	06:31	50.120N	148.745E	582	6.0		310°	57°
84/04/23	21:40	47.450N	146.692E	414	6.0		308°	59°
84/06/11	02:05	30.707S	71.179W	46	6.3	5.8	139°	89°
84/06/15	14:22	15.816S	174.831W	247	6.1		232°	79°
84/06/18	11:20	15.705S	72.491W	117	5.8		132°	76°
84/09/17	20:59	55.870N	87.446E	0	4.9		344°	75°
84/10/23	22:28	13.714N	144.917E	123	5.4		282°	83°
84/10/26	20:22	39.155N	71.328E	33	6.0	6.1	350°	94°
84/11/06	07:58	18.876S	67.352E	10	6.2	5.8	343°	152°
84/11/22	13:52	68.532N	140.883E	33	5.4	4.9	332°	51°
85/01/02	23:08	53.490N	171.531W	235	4.8		302°	33°
85/02/23	13:41	10.254S	161.126E	85	6.0		254°	89°
85/05/01	13:27	9.196S	71.230W	600	6.0		127°	71°
85/06/26	23:44	6.854N	72.980W	154	5.2		118°	57°
85/07/07	06:01	22.577N	141.982E	260	5.4		291°	79°
85/08/11	09:59	54.139N	168.731E	50	5.9	5.8	307°	44°
85/08/11	16:06	36.126N	95.632E	33	5.4	4.4	331°	91°
85/09/10	06:39	27.208N	139.848E	501	5.8		296°	77°
85/09/26	07:27	34.693S	178.656W	52	6.3	7.0	224°	96°
85/10/06	12:00	18.961S	169.432E	273	5.7		242°	90°
85/11/12	03:34	36.514S	97.918W	10	4.6		162°	85°
86/02/15	21:37	14.774N	91.414W	136	5.3		132°	40°
86/04/14	10:52	4.865S	151.268E	216	5.4		265°	92°
86/04/30	07:07	18.404N	102.973W	27	6.2	7.0	146°	31°

Table 2.1: (continued)

Date yy/mm/dd	Time (UTC)	Location		Depth (km)	Magnitude		Azimuth (w.r.t. WRSN)	Δ
		Latitude	Longitude		m_b	M_{sz}		
86/05/11	01:24	26.743N	125.205E	194	5.9		305°	86°
86/06/24	03:11	4.448S	143.943E	102	6.6	7.1	271°	97°
86/07/07	16:26	10.389N	56.832E	8	6.4	6.2	3°	124°
86/07/18	17:22	10.770N	69.428W	7	5.9	4.9	112°	56°
86/10/22	08:59	10.569S	166.040E	165	5.9		250°	86°
86/10/28	15:04	26.978S	26.676E	5	5.2	5.3	65°	148°
86/10/30	01:28	21.702S	176.616W	188	6.4		230°	84°
87/01/07	18:19	34.259N	103.405E	33	5.5	5.5	325°	90°
87/02/23	02:43	57.922S	25.350W	27	5.9	5.7	136°	130°
87/04/03	01:17	49.928N	78.829E	0	6.2	4.7	347°	83°
87/04/16	01:10	54.957N	157.985E	310	5.0		312°	49°
87/05/07	03:05	46.736N	139.232E	430	6.0		311°	64°
87/06/05	04:59	41.584N	88.737E	0	6.2	4.4	338°	88°
87/07/06	23:59	61.501N	112.803E	0	5.1		335°	64°
87/07/11	06:15	82.229N	17.556W	10	5.5	5.0	10°	46°
87/08/03	07:37	86.906N	63.095E	10	5.0	4.5	360°	47°
87/08/04	22:15	29.292S	176.202W	33	5.5	5.2	226°	90°
87/08/06	15:15	5.417S	105.015W	10	5.6	5.2	160°	53°
87/09/01	04:26	23.052S	66.529W	199	6.0		131°	85°
87/09/03	06:40	58.893S	158.513E	33	5.9	7.3	218°	124°
87/09/13	11:20	14.272N	89.979W	123	5.1		130°	41°
87/09/18	21:58	47.017N	89.658E	33	5.3	4.8	340°	83°
87/10/03	03:35	17.950S	69.247W	149	5.8		130°	79°
87/10/12	13:57	7.288S	154.371E	25	6.3	6.8	261°	92°
87/11/06	18:47	22.801S	63.583W	538	5.8		129°	86°
88/02/05	18:49	24.893S	70.554W	31	6.0	6.1	135°	84°
88/02/24	02:54	51.723N	176.797W	60	5.5		300°	36°
88/02/24	15:43	0.507S	91.653W	10	5.5	4.5	142°	53°
88/02/26	06:17	37.319S	47.989E	10	6.1	6.7	47°	168°
88/03/21	23:31	77.601N	125.451E	10	6.0	6.0	345°	50°
88/04/22	04:03	17.062N	61.543W	61	5.0		100°	57°
88/04/25	10:10	7.791S	158.255E	44	6.1	6.0	258°	89°
88/05/20	14:58	8.116N	38.413W	10	5.8	5.9	90°	79°
88/06/05	18:22	15.397S	167.578E	110	6.0		246°	89°

Table 2.1: (continued)

Date yy/mm/dd	Time (UTC)	Location		Depth (km)	Magnitude		Azimuth (w.r.t. WRSN)	Δ
		Latitude	Longitude		m_b	M_{sz}		
88/08/08	19:59	63.501N	2.611E	10	5.6		25°	62°
88/08/10	11:46	28.165S	112.695W	10	5.9		172°	75°
88/08/14	10:56	54.601N	152.657E	644	5.5		313°	52°
88/08/14	17:53	27.431S	70.937W	38	6.0		137°	86°
88/08/17	01:59	7.657S	107.263E	58	6.0		297°	124°
88/08/22	16:19	66.307N	78.474E	0	5.3		352°	67°
88/08/27	07:04	31.071N	64.838W	10	5.1		89°	45°
88/09/09	23:07	6.943S	81.335W	33	5.7		135°	64°
88/09/15	18:48	1.403S	77.895W	189	5.8		128°	61°
88/09/22	22:28	23.980N	167.144W	10	5.4		255°	43°
88/10/13	00:32	61.888N	169.548E	33	5.3		318°	41°
88/11/25	23:46	48.123N	71.245W	20	5.9		68°	33°
88/12/04	05:19	73.405N	54.902E	0	5.8		1°	61°
88/12/24	10:39	27.446S	63.008W	570	5.7		131°	90°
89/02/04	19:24	5.928N	82.807W	33	5.8		129°	52°
89/04/02	10:35	10.644N	85.504W	113	4.9		128°	46°
89/04/15	14:26	8.429N	61.069W	25	5.8		107°	63°
89/04/29	06:25	57.193N	122.087E	33	5.3		328°	64°
89/05/02	09:30	16.750N	99.364W	10	5.4		141°	34°
89/05/13	03:35	50.141N	105.411E	33	5.5		331°	76°
89/05/19	02:21	54.323N	165.580W	104	6.0		303°	29°
89/06/10	17:29	22.201S	138.830W	0	5.5		198°	70°
89/06/18	14:06	17.767N	68.837W	71	5.9		105°	51°
89/06/20	05:41	52.260N	174.204E	50	5.1		303°	41°
89/06/25	11:15	32.892N	39.572W	10	5.2		71°	61°
89/06/26	03:27	19.388N	155.192W	10	6.0		238°	39°
89/06/26	10:38	39.278N	28.229W	10	5.8		59°	65°
89/07/30	09:29	52.532S	13.076E	10	5.6		119°	150°
89/08/12	15:31	18.445N	100.735W	97	5.4		142°	32°
89/08/14	17:51	18.923S	176.403E	114	5.7		237°	86°
89/08/21	18:25	4.066S	154.392E	500	6.0		263°	89°
89/09/16	23:20	16.560N	93.659W	110	5.9		133°	37°
89/09/17	00:53	40.188N	51.794E	33	6.0		6°	94°
89/10/18	18:20	40.094N	114.019E	10	5.5		321°	81°

Appendix C

Three-dimensional Ray Tracing

In order to obtain the correct path of integration for the integrals described §4.2 we must solve the two-point ray-tracing problem through arbitrarily varying three-dimensional media. Equations for accomplishing this, formulated in terms of accumulated travel time along the ray path, were derived by *Julian and Gubbins* [1977]. The appropriate equations for solving the resultant differential equations as an initial value problem, as given in Appendix A of *Julian and Gubbins* [1977], contained certain typographical which were corrected by *Creager* [1984] and are therefore restated (corrected) here. They are

$$\frac{dr}{dt} = -v \cos i , \quad (\text{C.1a})$$

$$\frac{d\theta}{dt} = -\frac{v}{r} \sin i \cos j , \quad (\text{C.1b})$$

$$\frac{d\phi}{dt} = \frac{v}{r \sin \theta} \sin i \sin j , \quad (\text{C.1c})$$

$$\frac{di}{dt} = -\left(v_r - \frac{v}{r}\right) \sin i + \left(\frac{v_\theta}{r} \cos j - \frac{v_\phi}{r \sin \theta} \sin j\right) \cos i , \quad (\text{C.1d})$$

and

$$\frac{dj}{dt} = -\frac{1}{\sin i} \left(\frac{v_\theta}{r} \sin j + \frac{v_\phi}{r \sin \theta} \cos j\right) + \frac{v}{r} \sin i \sin j \cot \theta , \quad (\text{C.1e})$$

where subscripts indicate partial derivatives with respect to the subscripted variable. All variables are represented as functions of accumulated travel time, t , with (r, θ, ϕ) representing the standard polar spherical coordinate system (with $\theta = 0$ representing the North pole), $i(t)$ the angle between the ray tangent and the vertical and $j(t)$ the angle between the ray tangent projected onto the $\theta\phi$ -plane and the northward direction (positive clockwise). The variables i and j therefore simply represent take-off angle and azimuth, respectively, as commonly used in seismological problems.

Solving these equations as a initial value problem is known as the *shooting* method of ray tracing. This is due to the fact that given the initial values of the above variables (r, θ, ϕ, i , and j) we can simply integrate along the path defined by equations C.1a-e until passing by the desired end point. We then have a *true* ray path through the velocity field (within the limits of our numerical accuracy) but

probably not a path that connects to the desired end point and possibly a non-unique path as well. We will attack these two problems following the formulation of *Creager* [1984].

The latter of these problems (non-uniqueness) arises in our situation due to triplications in travel-time surfaces. We seek a true ray path that connects our station locations to a certain earthquake hypocenter by finding a minimum travel-time path, yet any given path which we find may only represent a local minima. To attack this problem *Creager* [1984] devised a scheme of calculating the travel-time surfaces from a given event to the surface of the Earth in a sufficiently dense grid to define these triplications and therefore be able to choose the ray path representing the global travel-time minimum. We have altered these routines for our purposes to use an arbitrarily varying three-dimensional velocity field and to integrate to a given source depth rather than the Earth's surface, but essentially the methods are identical (see *Creager* [1984] for a detailed description). A table is created from each of the 146 station locations to cover the teleseismic distance range from approximately 30 to 100 degrees. Rays are traced to a depth of 100 km for the purposes of the initial table.

Once we have decided on which branch of the travel-time surface the first arrival lies, we must then iterate shooting rays until we find one close enough (within 0.1 degrees) to the desired end point (hypocenter). The method of accomplishing this is also given in detail in *Creager* [1984] but in essence we simply choose the closest rays from the previously calculated table which surround the desired endpoint and then use Newton's method of false position to zero in on the hypocenter (each of the three initial rays are re-calculated for the depth of the event in question before beginning the iterative procedure). For each of the models through which we ray traced we were able to locate approximately 98% of the ray paths to within the desired accuracy, usually within 3-5 iterations. Many of the remaining 2% could probably be located with the use of a denser table of initial values.

The final ray paths are then saved for use in calculating the partial derivatives necessary for performing the travel-time inversion. The travel-times are corrected for the difference between the final ray's end point and the hypocenter through the use of the time difference between these two points calculate from the radially symmetric reference model [*Herrin*, 1968]. The travel-time *residuals* are not changing

dramatically over these distances (less than 11 km) and therefore we have found empirically that this correction is accurate to within approximately .02 seconds.

Vita

John Callaway VanDecar

Date of birth: 2 August 1963

Place of Birth: Boise, Idaho

Educational background:

Boise Senior High School, Boise, Idaho, diploma, May 1982

Texas A&M University, College Station, Texas, B.S. Geophysics, May 1986

University of Washington, Seattle, Washington, Ph.D. Geophysics, June 1991